

GROWTH OF GALLIUM NITRIDE AND INDIUM NITRIDE FILMS AND
NANOSTRUCTURED MATERIALS BY HYDRIDE-METALORGANIC VAPOR
PHASE EPITAXY

By

HYUN JONG PARK

A DISSERTATION PRESENTED TO THE GRADUATE SCHOOL
OF THE UNIVERSITY OF FLORIDA IN PARTIAL FULFILLMENT
OF THE REQUIREMENTS FOR THE DEGREE OF
DOCTOR OF PHILOSOPHY

UNIVERSITY OF FLORIDA

2006

Copyright 2006

by

Hyun Jong Park

To Cathy, who endured and enjoyed our life in Gainesville, Florida

ACKNOWLEDGMENTS

I would like to thank Dr. Tim Anderson for being my advisor and chairman.

Although the expectations placed on me were always challenging, it led me to a level of academic excellence that was unthinkable without his expectations.

I want to sincerely thank Dr. Olga Kryliouk for being a coadvisor and cochair. Dr. Kryliouk showed me new ways of thinking in our daily discussions. She was a mentor, friend, and sometime critic, who allowed me to attain a higher level of research. I am in debt for her the effort and creativity she provided throughout my time at UF.

I thank Dr. Fan Ren, Dr. Cammy Abernathy, and Dr. Jason Weaver for being my committee members. Their thoughtful advice is greatly appreciated.

Without the senior students' contributions, this work would not be possible. I am truly in debt to Dr. Mike Reed who greatly modified the Hydride-Metalorganic Vapor Phase Epitaxy system in Microfabritech from RCA hydride for VPE of InP. The optimism and kindness he provided helped even after leaving the group were crucial to me in solving numerous technical problems.

I would like to thank Dr. Mike Mastro for being my mentor and teaching me how to operate the H-MOVPE system. He gave me valuable advice during my first year in Dr. Anderson's group.

Dr. Sang Won Kang opened a new door for InN growth using the H-MOVPE system. His creative thinking, logical approach, experience, and kindness have influenced me. He is the best colleague I have ever had.

I am thankful for the enormous help of Woo Kyoung Kim, from whom I learned to organize things and how to work effectively. He also helped to perform HT-XRD and analyze the data. He was a counselor, friend, and mentor who has permanently influenced my life.

YongSun Won is the smartest person that I have known who understands matters in a scientific way. His way of thinking was always beyond my knowledge. I appreciate his help and valuable discussions.

Josh Mangum embodies the right attitude towards research and people. He is a good communicator and friend. His willingness to help was essential for me to complete this project.

Dr. Jang Yeon Hwang and Young Seok Kim helped me with Raman spectroscopy and hydrodynamics simulations. Their thorough understanding of the physical world deeply influenced me.

Dr. Seokhyun Yoon helped me with SEM and EDS when I did not know how to use them. He also shared with me a happiness of a loving family when I was alone.

Dr. Byoung Sam Kang and Hung-Ta Wang in Dr. Fan Ren's group fabricated InN nanorods based gas sensor. The completeness of my work would not be possible without their help.

I would like to thank my colleagues, KeeChan Kim, Oh-Hyun Kim, and Do Jun Kim for providing helpful discussions and encouragement during my research. KeeChan Kim and Oh Hyun Kim especially helped me automate the H-MOVPE system. Their way of working effectively was very influential.

Without the great staff at UF, this work would not have been possible. I would like to acknowledge James Hinnant and Dennis Vince in Chemical Engineering, Scott Gapinski, Di Badylak, and Chuck Rowland in Microfabritech. I sincerely thank Valentin Craciun for HR-XRD, Eric Lambers for AES and XPS, Maggie Puga-Lambers for SIMS, Kerry Siebein for TEM at the Major Analytical Instrument Center, UF.

I also would like to acknowledge my collaboration outside UF. The support and discussion with Dr. Chinho Park (Yeung Nam University) was greatly appreciated. He and his students, Seok-Ki Yeo, helped analyze the Raman spectroscopy data and gave me valuable advice. Dr. Jianyun Shen taught me how to use Thermo-Calc and strain energy modeling. Drs. Albert Davydov and Igor Levin helped me verify the thermochemical data and did excellent characterization samples at NIST by FE-SEM, TEM, and CBED. Drs. Dmitry Khokhlov at Moscow State University and Timur Burbaev at Physical Institute, Moscow carried out the PL measurements for the InN films and nanorods. Dr. Jaime Freitas at Naval Research Lab performed the Raman spectroscopy and PL on the InN nanorod samples. Dr. Zuzanna Liliental-Weber at Lawrence Berkeley Lab characterized InN nanorods by HR-TEM. Dr. Talmage Tyler at the International Technology Center measured the field emission properties of InN nanorods. Dr. Mee Yi Ryu at the Air Force Institute of Technology performed CL and Hall measurements of InN films and nanorods. I would not have reached this point without their enormous help.

I thank Drs. Seong-Geun Oh, Yeong Koo Yeo, and Hong-Woo Park in Chemical Engineering, Hanyang University for recommending me for studying in the University of Florida. I would not have this great opportunity without their kind and thoughtful help.

I also would like to thank Andrew Wislocki for proofreading this dissertation. He corrected grammatical errors and made the contents clearer by helpful discussions.

I cannot thank my family enough for their boundless love. My father (Jong Soo Park), mother (Sun Kyoung Kim), and sister (Soo Kyoung Park) have been an essential part of my life. Although they were far away in Korea, they were always with me in my heart throughout my life as a graduate student in Gainesville.

My sons, David and Justin Park, showed me what true love is. Although I needed more time and effort to balance family life and research, I would not trade their love for anything in the world.

Finally, I would like to thank my wife, Catherine Park, for her endless support and trust. I was always happy for her presence and I will feel this way forever.

TABLE OF CONTENTS

	<u>page</u>
ACKNOWLEDGMENTS	iv
LIST OF TABLES	xii
LIST OF FIGURES	xiv
ABSTRACT	xxii
CHAPTER	
1 INTRODUCTION	1
1.1 History of GaN and InN Development	1
1.1.1 GaN Development	1
1.1.2 InN Development	3
1.2 Literature Review	9
1.2.1 Equilibrium Analysis of GaN and InN	9
1.2.1.1 Thermochemical Data for GaN and InN	9
1.2.1.2 Equilibrium Calculations of GaN Growth by HVPE	10
1.2.2 Stress in GaN Films	14
1.2.2.1 <i>In situ</i> Stress Measurements	16
1.2.2.2 <i>Ex situ</i> Stress Measurements	18
1.2.3 GaN Growth on Si	21
1.2.4 Growth of InN Films and Nanostructured Materials	25
1.2.4.1 Growth of InN Films	25
1.2.4.2 Growth of InN Nanostructured Materials	29
2 CHEMICAL EQUILIBRIUM ANALYSIS OF H-MOVPE SYSTEM	32
2.1 Introduction	32
2.2 Thermochemical Data Collections	33
2.3 Chemical Equilibrium Calculations	35
2.3.1 Thermochemical Data Verification	35
2.3.2 Complex Chemical Equilibrium Calculations	38
2.3.2.1 Ga-C-H-Cl-Inert System	38
2.3.2.2 Ga-C-H-Cl-N System	45
2.3.2.3 In-C-H-Cl-Inert System	47
2.3.2.4 In-C-H-Cl-N-Inert System	53

2.3.2.5 NH ₃ Partial Decomposition	60
2.4 Conclusions.....	62
3 STRESS DETERMINATION STUDIES OF GALLIUM NITRIDE FILM ON SAPPHIRE	64
3.1 Introduction.....	64
3.2 Effects of Lattice and Thermal Expansion Mismatches	67
3.2.1 Lattice Mismatch at Growth Temperature	67
3.2.2 Thermal Expansion Mismatch.....	69
3.2.3 Combination of Lattice and Thermal Expansion Mismatches	70
3.3 Stress Measurements of GaN Films on Sapphire	71
3.3.1 GaN Structural and Compositional Studies.....	72
3.3.2 Stress Measurements by Raman Spectroscopy	77
3.3.2.1 Curvature Calculations.....	79
3.3.2.2 Lattice Parameter Calculations.....	80
3.3.3 Lattice Parameter Measurements by XRD Reciprocal Space Mapping	81
3.3.4 Curvature Measurements by XRD Rocking Curve.....	84
3.4 Stress Modeling of GaN on Sapphire	89
3.4.1 Frank-van der Merwe's Semi-infinite Model.....	89
3.4.2 Layer-by-Layer Growth Model	91
3.4.2.1 Strain Energy (Homogeneous Stress) Calculations	92
3.4.2.2 Dislocation Energy (Periodic Strain Energy) Calculation	94
3.4.2.3. Total Strain Energy Calculations	95
3.5 Conclusions.....	97
4 GROWTH OF GALLIUM NITRIDE ON SILICON BY H-MOVPE.....	100
4.1 Introduction.....	100
4.2 H-MOVPE Growth Technique	101
4.2.1 Chemical Reactions of H-MOVPE Technique.....	101
4.2.2 H-MOVPE Reactor Schematics	102
4.3 Thick GaN Growth on Al ₂ O ₃	106
4.4 GaN Growth on Si	111
4.4.1 Growth of Thin and Thick GaN on Si.....	111
4.4.1.1 Nitronex GaN/Si template.....	111
4.4.1.2 Growth of Thin GaN Using Nitronex Template	114
4.4.1.3 Growth of Thick GaN Using the Nitronex Template.....	115
4.4.2 Growth of Thick GaN on Si Using InN Interlayers	118
4.4.2.1 InN Growth on Si(111)	119
4.4.2.2 LT-GaN Growth on InN Buffer Materials/Si(111).....	120
4.4.2.3 Thick HT-GaN Growth on LT-GaN/InN/Si(111).....	123
4.5 Conclusions.....	126
5 GROWTH OF INDIUM NITRIDE NANORODS BY H-MOVPE.....	128

5.1	Introduction.....	128
5.2	Chemical Reactions for InN Growth by H-MOVPE.....	130
5.3	InN Nanorods Growth Optimization	130
5.3.1	Experimental Procedure	131
5.3.2	Results	131
5.3.2.1	Effects of Growth Temperature and HCl/TMI Molar Ratio	131
5.3.2.2	Effects of NH ₃ /TMI Molar Ratio and Substrate Material	134
5.3.2.3	Equilibrium Analysis.....	135
5.4	Properties of InN Nanorods	138
5.4.1	Morphology	138
5.4.2	Crystallinity	139
5.4.3	Self-alignment	141
5.4.4	Growth Axis and Structural Properties.....	145
5.4.5	Polarity	150
5.4.6	Chemical Composition	151
5.4.7	Photoluminescence	153
5.4.8	Cathodoluminescence.....	156
5.4.9	Raman Spectroscopy	157
5.4.10	Electrical Properties.....	158
5.4.11	Field Emission Properties.....	159
5.5	Pt-dispersed InN Nanorods for Selective Detection of Hydrogen at Room Temperature	163
5.5.1	Experimental Procedure	163
5.5.2	Results	164
5.6	Conclusions.....	167
6	EXPLORATORY STUDY OF INDIUM NITRIDE FILMS GROWTH BY H- MOVPE	169
6.1	Experimental Procedure.....	169
6.2	Results.....	170
6.2.1	Effect of HCl/TMIn Molar Ratio	170
6.2.2	Effect of Growth Temperature	172
6.2.3	Effect of NH ₃ /TMIn Molar Ratio	174
6.2.4	Effect of Buffer Layer	177
6.2.4.1	Surface Morphology of InN Films without Buffer Layer	177
6.2.4.2	Growth of InN Films with Low Temperature Buffer Layer	177
6.2.5	Growth of InN Films on Al ₂ O ₃ and Si.....	179
6.3	Conclusions.....	181
7	EXPLORATORY STUDY OF GALLIUM NITRIDE NANORODS GROWTH BY H-MOVPE.....	183
7.1	Experimental Procedure.....	183
7.2	Results.....	183
7.3	Conclusions.....	189

8	FUTURE WORK AND RECOMMENDATIONS	190
	8.1 Nucleation and Growth Mechanism Studies of InN Nanorods	190
	8.2 Self-aligned InN Nanorods as Buffer Material for GaN on Si	190
	8.3 Buffer Layer Optimization for GaN growth on Si Substrate.....	191
	8.4 Use of Negative Thermal Expansion Materials.....	192
	8.5 Double-sided Growth of GaN on Si and Sapphire	195
	APPENDIX: THERMOCHEMICAL DATA FOR AL-IN-GA-C-H-CL-N SYSTEM.....	196
	LIST OF REFERENCES	222
	BIOGRAPHICAL SKETCH	243

LIST OF TABLES

<u>Table</u>	<u>page</u>
1-1 Reported values of thermochemical data for solid GaN and InN	12
1-2 Reported values of the Raman $E_2^{(high)}$ peak positions	20
1-3 Techniques used for growth of crack-free GaN on Si.....	23
2-1 Commonly considered species in Ga-In-H-C-Cl-N system	34
2-2 Additionally included gas phase species.....	35
2-3 Base inlet conditions for sources for GaN growth and atomic mole fractions for calculation	39
2-4 Typical growth conditions for InN and atomic mole fractions for calculation.....	48
3-1 Lattice parameters of GaN and widely used substrates at 300 and 1300 K.....	68
3-2 Lattice constants at 1300 and 300 K and thermal strain ($\Delta T = 1000$ K) of GaN and widely used substrates	70
3-3 The growth conditions of the two samples for stress measurements	72
3-4 GaN a and c lattice parameters measured at 300 K (\AA)	84
3-5 Stress, lattice parameter, and curvature of the H-MOVPE GaN with depth.....	86
3-6 Calculated misfit dislocation density of GaN on widely used substrates with Vernier period	90
3-7 Lattice constants (\AA) of GaN, AlN, and Al_2O_3	93
3-8 Elastic stiffness coefficients c_{ij} (GPa) and compliances s_{ij} (1/GPa) of GaN, AlN, and Al_2O_3	93
3-9 Shear moduli, Poisson's ratios, and lattice parameters of GaN, AlN, and Al_2O_3	94
3-10 Calculated lattice constants and total energy	96
4-1 Electrical properties of GaN film grown on GaN/ Al_2O_3 template.....	111

4-2	Sheet resistance and resistivity measured by four-point probe	111
4-3	Growth conditions for InN buffer interlayer on Si.....	119
5-1	Base conditions of InN nanorods growth	131
5-2	Intensity ratio comparison with XRD powder pattern with different substrates	140
5-3	Electrical properties of InN films and nanorods	159
6-1	Base conditions of InN film growth.....	169
7-1	Base conditions for GaN micro/nanorods growth.....	183
8-1	Lists of NTE materials	192
A-1	Gas Phase	197
A-2	Gas Phase (Metalorganics, Adducts, Oligomers, etc).....	217
A-3	Liquid Phase	218
A-4	Solid Phase	220
A-5	Carbon (Graphite)	221
A-6	GaN and InN	221

LIST OF FIGURES

<u>Figure</u>	<u>page</u>
1-1	Reported values of electric properites of InN (a) Hall mobility and (b) Carrier concentration with calendar year.....6
1-2	Reported bandgap energy of InN as a function of carrier concentration7
1-3	Examples of equilibrium calculations. (a) Driving force for the deposition as a function of growth temperature with various parameters for F (b) Comparison between calculated growth rates and experimental data11
1-4	Driving force for the deposition of InN (ΔP_{In}) using InCl (HVPE) and InCl ₃ (THVPE) as a function of growth temperature.13
1-5	Schematic of GaN growth on SiC (a) GaN/SiC and (b) GaN/AlN/SiC growth16
1-6	<i>In situ</i> curvature measurements during the growth of a ~ 6 μ m thick GaN layer showing the influence of AlN interlayers on the curvature. The sample was crack-free after growth18
1-7	Raman peak shifts of 2 μ m thick GaN with different LT-GaN buffer layer thickness; LT-GaN buffer layer thickness (a) 10 nm, (b) 50 nm, (c) 75 nm, and (d) 85 nm21
2-1	Phase diagram of In-N systems at P = 0.1 MPa and experimental InN decomposition data.....36
2-2	Calculated ΔG^{rxn} for GaN(s) and (GaN) ₃ (g) formation reactions37
2-3	Phase diagram of Ga-N systems at P = 0.1 MPa.....38
2-4	Schematic of the inlet of H-MOVPE technique for GaN growth38
2-5	Equilibrium partial pressures of gas phase molecules and mole fractions of condensed phases with respect to the temperature in Ga-C-H-Cl-Inert system.....40
2-6	Equilibrium partial pressures of gas phase molecules and mole fractions of condensed phases with respect to $X(H)/\{X(Inert) + X(H)\}$ in Ga-C-H-Cl-Inert system.....42

2-7	Equilibrium partial pressures of gas phase molecules and mole fractions of condensed phases with respect to X(Cl)/X(Ga) ratio in Ga-C-H-Cl-Inert system.....	44
2-8	Schematic of H-MOVPE for GaN growth: Ga-C-H-Cl-N system. N is present and H ₂ is used as a carrier gas in the system compared to Figure 2-4	45
2-9	Calculated growth-etch transition temperature as a function of Cl/Ga ratio.....	46
2-10	Calculated transition of growth-etch and Ga(l) formation as a function of temperature and Cl/Ga ratio	47
2-11	Schematic of the inlet of H-MOVPE technique for InN growth.....	48
2-12	Equilibrium partial pressures of gas phase molecules and mole fractions of condensed phases with respect to the temperature in In-C-H-Cl-Inert system	50
2-13	Equilibrium partial pressures of gas phase molecules and mole fractions of condensed phases with respect to X(H)/{X(Inert) + X(H)} in In-C-H-Cl-Inert system.....	51
2-14	Equilibrium partial pressures of gas phase molecules and mole fractions of condensed phases with respect to X(Cl)/X(In) ratio in In-C-H-Cl-Inert system	52
2-15	Schematic of H-MOVPE inlet with In-C-H-Cl-N-Inert system for thermodynamic calculations. N is present in the system compared to Figure 2-11	54
2-16	Calculated growth and etch regime with respect to temperature and Cl/In ratio. N/In ratio was varied from 100 to 7000	55
2-17	Calculated growth and etch regime with respect to temperature and Cl/In ratio. Cl/In ratio was varied from 1.1 to 10	56
2-18	Calculated results of the growth, no growth (etch), and In droplet regimes (a) Cl/In = 0 to 0.5, N/In = 4.0 x 10 ⁴ to 7.0 x 10 ⁴ , (b) Cl/In = 0 to 1, N/In = 1.0 x 10 ³ to 7.8 x 10 ⁴ , and (c) In droplet etching conditions at T = 1153 K, P = 10 ⁵ Pa.....	57
2-19	Calculated growth-etch transition temperatures (a) In droplet etch conditions when no HCl was present (b) growth-etch transition temperature at high N/In ratios: 10 ⁵ , 10 ⁶ , and 10 ⁷	59
2-20	Equilibrium partial pressures for decomposition of NH ₃ at 1 atm total pressures calculated by Thermo-Calc	60
2-21	Magnitude of the Gibbs energy correction required to achieve a value for partial decomposition (α) at 950 °C.....	61

2-22	NH ₃ mole fraction with respect to temperature at different values of α	62
3-1	Substrates for GaN plotted with thermal strain versus lattice parameters at room temperature	70
3-2	XRD ω and ω -2 θ rocking curve of MOCVD and H-MOVPE grown GaN on sapphire, XRD FWHM; ω -rocking curve (MOCVD: 1261 arcsec, H-MOVPE: 1790 arcsec); ω -2 θ rocking curve (MOCVD: 92 arcsec, H-MOVPE: 122 arcsec)	72
3-3	Pole figures for the (116) sapphire substrate (2 theta = 57.490°) and (112) GaN by MOCVD (2 theta = 69.185°). The GaN in-plane axis is rotated by 30° with respect to the sapphire axis.....	73
3-4	Pole figures for the (116) sapphire substrate (2 theta = 57.490°) and (112) GaN by H-MOVPE (2 theta = 69.185°). The GaN in-plane axis is rotated by 30° with respect to the sapphire axis	74
3-5	AES surface scan and depth profile of GaN on sapphire grown by MOCVD	75
3-6	AES surface scan and depth profile of GaN on sapphire grown by H-MOVPE	76
3-7	Raman E ₂ peak shifts at the surface (a) MOCVD, (b) H-MOVPE, and (c) depth profile	78
3-8	XRD reciprocal space mapping of H-MOVPE grown GaN (002) and (114) peaks	82
3-9	XRD reciprocal space mapping of MOCVD grown GaN(002) and (114) peaks.....	83
3-10	The procedure of determining curvature by measurements of XRD rocking curves	85
3-11	Curvature measurements by XRD rocking curve by displacing the H-MOVPE grown GaN/c-Al ₂ O ₃ sample in x-direction by 5 mm	86
3-12	SIMS oxygen depth profiles of MOCVD and H-MOVPE grown GaN films	88
3-13	Frank-van der Merwe's semi-infinite overgrowth model	90
3-14	Shen-Dann's layer-by-layer model	91
3-15	Minimum energy calculation of stress + dislocation energy.....	96
3-16	In-plane lattice constants of GaN on AlN/sapphire	97

4-1	Schematics of H-MOVPE (a) bird eye view of the entire reactor, (b) the source and growth zones with temperature profile in the source zone.....	103
4-2	Process Flow Diagram (PFD) of H-MOVPE system.....	105
4-3	XRD θ -2 θ scan and ω -rocking curve of as received GaN/Al ₂ O ₃ template from Uniroyal Optoelectronics. * denotes the secondary peak due to Cu K β radiation	107
4-4	SEM images of GaN film (a) Cross-sectional SEM of 125 μ m thick H-MOVPE GaN film on GaN/Al ₂ O ₃ template, (b) SEM plan-view of the same sample. (c) Plan-view of LT-HVPE smoothing layer.....	108
4-5	XRD of GaN film (a) XRD θ -2 θ scan of thick (45 μ m) GaN on GaN/Al ₂ O ₃ , (b) XRD ω -rocking curve of GaN (002) peak; FWHM = 780 arcsec	109
4-6	Auger Electron Spectroscopy of 45 μ m thick GaN film (a) surface scan (b) sputtering depth profile (c) surface scan after sputtering	110
4-7	X-SEM image of GaN on Si using AlGa _n graded layer	112
4-8	XRD θ -2 θ scan and HR-XRD ω -rocking curve of as received GaN/Si from Nitronex, FWHM = 0.222 $^{\circ}$ (800 arcsec).....	113
4-9	SEM plan and cross sectional views of 2 μ m H-MOVPE + 1 μ m MOVPE crack-free GaN grown on AlGa _n /Si graded layer	114
4-10	XRD θ -2 θ scan of 2 μ m H-MOVPE + 1 μ m MOVPE crack-free GaN grown on AlGa _n /Si graded layer	114
4-11	SEM plan-views of thick (55 μ m) GaN films grown on GaN/Si templates (4 hr) with (a) fast cooling and (b) slow cooling. Note two micrographs are at different magnification.....	115
4-12	Schematic of crack generation of GaN on Si and GaN on Nitronex template. Cracking penetration to Si were observed in both cases.....	116
4-13	XRD θ -2 θ scan of thick (55 μ m) GaN film on GaN/Si template for 4 hr.....	117
4-14	XRD ω -rocking curve of GaN (002) peak of 55 μ m thick GaN. FWHM = 0.248 $^{\circ}$ (892 arcsec).....	117
4-15	The schematic to obtain thick GaN on Si(111) using InN buffer materials.....	119
4-16	SEM plan-view of InN columnar film, small nanorods (d = 250 nm), large nanorods (d = 500 nm), and microrods grown on Si(111)	120

4-17	SEM plan-view of 10, 20, and 30 min LT-GaN grown on (a) InN columnar film, (b) smaller nanorods ($d = 250$ nm), (c) larger nanorods ($d = 500$ nm), and (d) microrods.....	121
4-18	LT-GaN deposited on InN nanorods ($d = 500$ nm) on Si(111) for 30 min (~ 4 μm) (a) plan-view of LT-GaN on InN nanorods, (b) cross-sectional view (c) XRD θ - 2θ scan.....	122
4-19	HT-GaN/LT-GaN growth on various InN structures (a) InN columnar film, (b) small nanorods ($d = 250$ nm), (c) large nanorods ($d = 500$ nm), and (d) microrods. The right figures show expanded views of the surface of HT-GaN films.....	123
4-20	Thick (28 μm) and freestanding (self-separated) GaN grown on InN nanorods/Si (a) SEM plan-view of the GaN film, (b) XRD θ - 2θ scan.....	124
4-21	Cross-sectional view of thick GaN grown on InN nanorods/Si(111). The surface was covered by LT-HVPE layer grown after thick HT-HVPE.....	125
4-22	SEM plan-view of thick GaN grown on InN nanorods ($d=500$ nm)/Si(111). (a) as grown HT-GaN surface, (b) covered LT-GaN surface.....	126
5-1	The growth map of InN at different HCl/TMI ratio with growth temperature; N/In = 250; Growth time = 1 hr; Substrate = c-Al ₂ O ₃	132
5-2	Scanning electron micrographs of InN film and nanorods. NH ₃ /TMIn were varied from 100 to 7000; Other growth conditions are HCl/TMIn = 4, T = 600 °C; Growth time = 1 hr.....	134
5-3	The calculated boundary of the growth and etch regimes and experimental observations. (a) deposition temperature vs. HCl/TMIn ratio for selected N/In atom ratios; (b) deposition temperature vs. N/In atomic ratio for selected HCl/TMIn ratios.....	136
5-4	Scanning electron micrographs of InN nanorods grown at optimal conditions; Cl/In = 4, N/In = 250, T = 600 °C, for 1 hr growth on Si(111)	138
5-5	XRD θ - 2θ scan of InN nanorods grown on various substrates (a) a-Al ₂ O ₃ , (b) c-Al ₂ O ₃ , (c) r-Al ₂ O ₃ , (d) Si(100), (e) Si (111), (f) GaN/c-Al ₂ O ₃ , and (g) PDF#50-1239 (powder diffraction file).....	139
5-6	Scanning Electron Micrographs of aligned InN nanorods grown on GaN/Al ₂ O ₃ substrates. (a) sparse nanorods with sharp tips (b) dense nanorods with sharp tips (c) dense nanorods with flat tips	142
5-7	XRD scan of aligned InN nanorods on GaN/c-Al ₂ O ₃ substrates	143
5-8	XRD ω -rocking curve of aligned InN nanorods on GaN/Al ₂ O ₃	143

5-9	XRD pole figure of self-aligned InN nanorods (Substrate: GaN/c-Al ₂ O ₃).....	144
5-10	InN (103) plane and ϕ -axis for pole figure measurement	144
5-11	Transmission electron micrographs of an InN nanorod (a) splitting of reflections and (BF) bright field image at the bottom, (b) sparse planar defects by dark- and bright-field image.....	146
5-12	TEM and SAD of InN nanorods (WZ) with growth axes (a) [0002], (b) [1010], and (c) [1124].....	147
5-13	SEM image of wurtzite InN nanorod grown on the side wall of a nanorod	148
5-14	TEM and SAD of InN and In ₂ O ₃ nanorods (a) InN (ZB) growth axis = a few degrees off [220] (b) In ₂ O ₃ (BCC) growth axis = [402]	149
5-15	CBED of the InN nanorod.....	151
5-16	AES spectrum of surface scan of as grown InN nanorods at T = 600 °C, HCl/TMIn = 4, NH ₃ /TMIn = 250, 1 hr growth on c-sapphire	152
5-17	Scanning electron micrographs with AES of InN nanorods before and after AES sputtering damage	152
5-18	EDS line-scan of an InN nanorod grown on Si substrate.....	153
5-19	Room temperature (300 K) PL of InN nanorods grown on Si substrate and InN film on GaN substrate, maximum intensity observed around 1.08 eV	154
5-20	Low Temperature (6 K to 300 K) PL of InN nanorods on Si substrate (a) whole detection range, (b) magnified range between 730 to 850 meV from 23 to 100 K region.....	155
5-21	CL spectra of InN nanorods grown on sapphire	156
5-22	Room-temperature Raman scattering of InN nanorods deposited on Si and GaN/Si substrates	158
5-23	Scanning Electron Micrograph of sharp edge InN nanorods grown on Si (single NR on the left) and on GaN/Al ₂ O ₃ substrates.....	160
5-24	I-V curves and Fowler-Nordheim plots of InN nanorods on Si.....	161
5-25	SEM images and schematic of hydrogen gas sensor made of Pt nanoparticle dispersed InN nanorods.....	163
5-26	I-V characteristics from uncoated and Pt-coated InN nanorods	164

5-27	I-Time plot of 10 to 250 ppm H ₂ test by Pt-InN nanorods (left) and $ \Delta R /R(\%)$ -Time plot of 10 to 250 ppm H ₂ test by Pt-InN nanorods (right)	165
5-28	N ₂ , N ₂ O, ND ₃ , and O ₂ test for InN nanorods	166
6-1	Scanning electron micrographs of InN films (a) HCl/TMIn = 0, (b) HCl/TMIn = 0.3, (c) HCl/TMIn = 1, and (d) HCl/TMIn = 4. Other growth conditions: T = 560 °C; P = 760 Torr; N/In ratio = 2500; substrate: GaN/Al ₂ O ₃ ; growth time = 1 hr	170
6-2	Growth rate and XRD of InN (a) InN growth rate and (b) XRD scan with respect to HCl/TMIn ratio	171
6-3	SEM plan-views of InN films grown at different temperatures (a) 500, (b) 525, (c) 560, and (d) 600 °C; Other growth conditions Cl/III ratio = 1; P = 760 Torr; N/In ratio = 2500; Substrate = GaN/c-Al ₂ O ₃ ; growth time = 1 hr	172
6-4	Growth rate and XRD scans with respect to the growth temperature (a) Log _e (Normalized growth rate) vs 1000/T (K), (b) XRD scans in 2 theta ranges from 30° to 32°; growth temperature 300 to 700 °C; growth time = 1 hr.....	173
6-5	Scanning electron micrographs of InN films grown in different NH ₃ /TMIn ratios; other growth parameters Cl/In ratio = 1; P = 760 Torr; Growth T = 560 °C; growth time = 1 hr.....	175
6-6	Growth rate and XRD scans with respect to NH ₃ /TMIn ratio (a) Growth rate vs. N/In (NH ₃ /TMIn) ratio, (b) XRD scans of 2 theta range from 30 to 32° when N/In was 100 to 50000, (c) enlarged view of XRD for N/In range 7000 to 50000; Cl/In ratio = 1; P=760 Torr; Growth T = 560 °C; growth time = 1 hr	176
6-7	AFM images of the InN films. NH ₃ /TMI = 10000, HCl/TMI = 0.3, T=560 °C; Substrate = GaN/c-Al ₂ O ₃ ; growth time = 1 hr	177
6-8	SEM plan-view and cross-sectional of InN films on GaN/Al ₂ O ₃ substrate; N/In = 5000, Cl/In = 1, T = 560 °C, and growth time = 1 hr with 450 °C buffer layer growth for 30 min.....	178
6-9	XRD θ -2 θ scan of InN grown on GaN/Al ₂ O ₃ substrate; N/In = 5000, Cl/In = 1, T = 560 °C, and growth time = 1 hr with 450 °C buffer layer growth for 30 min.....	178
6-10	XRD ω -rocking curve of InN grown on GaN/Al ₂ O ₃ substrate; N/In = 5000, Cl/In = 1, T = 560 °C, and growth time = 1 hr with 450 °C buffer layer growth for 30 min	179
6-11	XRD θ -2 θ scan of InN film grown on c-Al ₂ O ₃	180
6-12	XRD θ -2 θ scan of InN film grown on Si(111)	180

6-13	XRD θ - 2θ scan comparison of InN film grown on different substrates	181
7-1	SEM plan-view micrographs of GaN grown at Cl/Ga ratio 2 and 3 on c-Al ₂ O ₃ , GaN/c-Al ₂ O ₃ , and Si at N/Ga = 250 without nitridation in N ₂	184
7-2	SEM micrographs of GaN grown at Cl/Ga ratio of 2.5 and 2.75, N/Ga = 250, and in H ₂ with nitridation	185
7-3	SEM plan-view of GaN with Cl/Ga ratio 2, 2.5, 4, and 6 on c-Al ₂ O ₃ , GaN/c-Al ₂ O ₃ , and Si(111).....	186
7-4	SEM plan-view of GaN at Cl/Ga = 19, N/Ga = 800, T = 850 °C on various substrates	187
8-1	Schematic of crack-free GaN growth on Si substrate using self-aligned InN or GaN nanorods.....	191
8-2	Lattice parameters of ZrW ₂ O ₈ (◇) and HfW ₂ O ₈ (○) as a function of temperature.....	193
8-3	Crystal structures of NTE materials (a) Unit cell of ZrW ₂ O ₈ , with 90% thermal ellipsoids drawn. (b) Polyhedral representation of the structure. ZrO ₆ octahedra shown in white, WO ₄ tetrahedra shaded.....	193
8-4	An array of linked triangles as found in tridymite. Rotation of one triangle causes the local environment to be pulled inwards	194

Abstract of Dissertation Presented to the Graduate School
of the University of Florida in Partial Fulfillment of the
Requirements for the Degree of Doctor of Philosophy

GROWTH OF GALLIUM NITRIDE AND INDIUM NITRIDE FILMS AND
NANOSTRUCTURED MATERIALS BY HYDRIDE-METALORGANIC VAPOR
PHASE EPITAXY

By

Hyun Jong Park

December 2006

Chair: Timothy Anderson

Cochair: Olga Kryliouk

Major Department: Chemical Engineering

Chemical equilibria analyses in the Ga/In-H-C-Cl-N-inert system were performed to predict gas and condensed phase species that might exist in H-MOVPE of GaN and InN. It was found that carbon co-deposition and metal droplets (Ga or In) formation can be eliminated by providing a threshold level of H₂ and HCl, respectively. The transitions between deposition and etching, and between 2-phase (Ga or In)N and pure (Ga or In) metal and single-phase (Ga or In)N were predicted as a function of N/III and Cl/III molar ratios and temperature.

Stress was measured by Raman spectroscopy in two GaN films (grown by MOCVD and H-MOVPE, respectively) on sapphire and a difference of 2 cm⁻¹ in the E₂ mode was observed. Subsequent measurement by XRD-SM, rocking-curves, AES, and SIMS showed inconsistent results compared to the Raman result suggesting that the Raman E₂ shift may not be only related to biaxial or hydrostatic stress.

Controlled growth of InN nanorods (NR) was achieved by varying the Cl/In and N/In molar ratios and growth temperature. The NRs were grown on a, c, r-Al₂O₃, GaN/c-Al₂O₃, Si (100), and Si (111) without a template or external catalyst. Well-faceted wurtzite and threading dislocation-free NRs were observed by SEM and TEM. The diameters and lengths of nanorods ranged 100 to 300 nm and ~ 1 μm for 1 hr growth. XRD patterns indicated the nanorods were textured in the [002] direction and TEM-DP confirmed the growth axis was predominantly [002]. Nanorods grown on GaN/c-Al₂O₃ occasionally showed vertical self-alignment and were epitaxially grown as judged by XRD pole-figure analysis. The nanorods had N-polarity as characterized by CBED, while RT PL showed a predominant peak at 1.08 eV. Raman spectroscopy showed three phonon lines (451, 496, and 596 cm⁻¹) that were assigned to A₁(TO), E₂², and E₁(LO), respectively. InN NRs-based gas sensor was fabricated that could detect H₂ to 10 ppm.

Crack-free, 3 μm GaN films were grown on GaN/AlGaN/Si template at 850 °C although cracks developed when the thickness exceeded 7 μm. It was possible, however, to grow crack-free polycrystalline 40 μm thick GaN on Si using InN NRs as a buffer material.

CHAPTER 1 INTRODUCTION

1.1 History of GaN and InN Development

The technology related to GaN and InN is highly developed. Both are currently used as host materials in optoelectronics and electronics devices. It is informative to review the history of those materials to properly understand the current issues that require more study.

1.1.1 GaN Development

The history of GaN crystal growth originates in 1938 [Juz38] when GaN was first synthesized by flowing NH_3 through gallium at high temperatures. The standard crystals for GaN powder X-ray diffraction file (*i.e.*, PDF# 02-1078) were obtained then and this data is still in use. Grimmeriss and Koelmans used the same method to grow small GaN crystals and measured PL for the first time back in 1959 [Gri59].

GaN film was first deposited by Maruska and Tietjen on sapphire substrate by CVD [Mar69]. Little attention, however, was paid to GaN's use as a semiconductor because of the difficulty in doping it p-type. GaN regained its attention in 1980s with need to develop blue emitters.

Yoshida reported improvement of GaN quality by using LT-AlN buffer layer in 1983 [Yos83]. In 1986, Amano reported improved GaN surface morphology and electrical and optical properties by using LT-AlN buffer layer [Ama86]. The buffer layer acted as a nucleation layer and decreased interfacial free energy to facilitate two-dimensional growth by changing the properties of the surface.

To fabricate GaN based devices, electronic properties such as carrier concentrations must be controlled. The doping of wide band gap materials is known to be difficult in part the probability of forming native defects that can dominate the electronic point defect chemistry. Intrinsic GaN grows n-type with a direct wide (3.4 eV) bandgap. The long belief in the native n-type nature of GaN is due to N-vacancy donor behavior. High conductivity p-type GaN was not achieved until 1989. It was observed that p-type conductivity drastically improved (from 10^8 to $35 \Omega\text{cm}$) after low electron energy beam irradiation (LEEBI).

Utilizing LEEBI treated Mg doped p-type GaN and intrinsic n-type GaN, Amano fabricated the first UV-LED [Ama89]. Nakamura later established that a simple annealing in inert or vacuum environment will improve p-type conductivity similar to the LEEBI treatment [Nak92]. The reason of great p-type conductivity improvement by LEEBI or annealing was not clear then, but it was later discovered that an Mg-H neutral species prevents Mg activation [Got95].

GaN-based Field Effect Transistors (FET) [Kha93] and Heterojunction Bipolar Transistors (HBT) [Pan94] were also fabricated in the early 1990s, enabled by the improved crystal quality and conductivity.

The threading dislocation density of these transistors, however, was about 10^9 to 10^{10} cm^{-2} , or about 10^6 times higher than typical semiconductors. Although devices could be fabricated with the high density of dislocations, their long-term reliability was questioned.

In 1994, a significant reduction of the dislocation density was achieved by adopting lateral epitaxial overgrowth that used either a SiO_2 or Si_3N_4 mask [Kat94]. Because

threading dislocations tend to form parallel to the growth axis, vertical blocking of the threading dislocations improved crystal quality drastically (from $10^9 - 10^{10}$ to $10^4 - 10^5$ cm^{-2}).

GaN-based devices began to be fabricated more routinely beginning in 1994. It is worth mentioning that Nakamura's two-flow reactor design significantly improved crystal quality [Nak94]. In this process, inert or hydrogen gas is injected vertically onto the substrate to modulate local concentrations of precursors by reducing the boundary layer thickness. Following the invention and breakthroughs, Nakamura reported an InGaN based 1 cd LED in 1994 [Nak94], a 10 cd LED in 1995 [Nak95a, Nak95b], a laser diode in 1996 [Nak96a], and continuous wave (CW) lasing at room temperature in 1997 [Nak97]. The intensity and life time improved in consecutive years and Nichia Corporation reported estimated 10,000 hr life time of blue laser diodes in 1998 [Nak98].

Research related to GaN has continued, as a result of the major breakthroughs made during the 80s and 90s. The lack of a suitable substrate material continues to create problems and the growth of large ($> 2''$) diameter freestanding GaN has not been easily achieved due to cracking and bowing problems. Also the heat generated from LED devices is still problematic due to the low thermal conductivity of the sapphire substrate. Undoubtedly, the integration of GaN technology with Si would be another important step for GaN-based device development. Furthermore the use of 12'' diameter Si wafer would improve device throughput and lower unit device fabrication cost.

1.1.2 InN Development

The first report on InN crystal growth originates from 1938 and used $\text{InF}_6(\text{NH}_4)_3$ for crystallographic study just as for GaN growth [Juz38]. The powder X-ray diffraction file for InN was collected and is in current use as PDF#02-1450. Several reports are

found from the 1950s and 1960s about synthesis of InN [Juz56, Ren58, Pas63, Sam69]. The growth methods were mainly interaction of In compounds with ammonia or thermal decomposition of complex single precursors containing direct bonding between In and N. InN powder or small crystals were usually obtained as a result. In 1972, Hovel and Cuomo [Hov72] deposited InN films on sapphire and silicon by reactive RF sputtering in the growth temperature range 25 to 600 °C. Hall mobility, n-type carrier concentration, and resistivity were measured as $250 \pm 50 \text{ cm}^2/\text{Vs}$, $5 \text{ to } 8 \times 10^{18} \text{ cm}^{-3}$, and $3 \text{ to } 5 \times 10^{-3} \text{ } \Omega\text{cm}$, respectively. Trainor and Rose grew InN by reactive evaporation and a bandgap of 1.7 eV was measured [Tra74]. Osamura reported the entire range of InGaN by an electron beam plasma technique that used an electron beam to heat and evaporate In and Ga and a plasma to create a nitrogen dc discharge [Osa72, Osa75]. The grown InN showed bandgap energy of 1.95 eV at room temperature and 2.11 eV at 78 K. Puychevriier and Menoret [Puy76] grew InN by reactive cathodic sputtering and the bandgap of InN was measure as 2.07 eV at room temperature and 2.21 eV at 77 K.

Then, in 1984, Tansley and Foley [Tan84] reported RF sputtering growth of InN with N_2 . Very high Hall mobility at room temperature and very low background carrier concentration were measured as $2700 \text{ cm}^2/\text{Vs}$ and $5.3 \times 10^{16} \text{ cm}^{-3}$, respectively. It should be noted that even with today's advanced techniques of MOVPE and MBE, these values are not easy to obtain. In addition, there is no other report of InN grown by RF sputtering that demonstrated such high Hall mobility and low carrier concentration. The typical mobility and carrier concentration of InN grown by sputtering is $100 \text{ cm}^2/\text{Vs}$ and 10^{20} 1/cm^3 , respectively. The problem of Hall measurement is that sometimes it can give

inconsistent values when the film is not uniformly deposited. However, the reason is unclear at this point.

Epitaxy of InN by HVPE was first reported in 1977 [Mar77]. Indium trichloride powder was used as the indium source and ammonia was used as the nitrogen source. The obtained epitaxial InN film showed background carrier concentration and Hall mobility as 2×10^{20} to $8 \times 10^{21} \text{ cm}^{-3}$ and 30 to $50 \text{ cm}^2/\text{Vs}$, respectively. The optimal growth temperature was found to be $600 \text{ }^\circ\text{C}$ and there was no growth at temperature higher than $670 \text{ }^\circ\text{C}$. Indium trichloride powder [Tak97b, Mar77, Sun96], indium monochloride, or both form *in situ* by flowing HCl over In metal depending on the source temperature [Tak97a, Sat94] grew InN by HVPE using predominantly InCl_3 , or InCl and showed ambiguous results on the superior precursors.

Kang reported successful H-MOVPE growth of InN in a chlorinating environment [Kan04]. In this approach, the conditions for selective etching condition of In metal in addition to protecting InN film were found by thermodynamic analysis and experiments. As a result growth of InN film without evidence of In metal droplets was achieved at a relatively low (2500) V/III ratio. During this study, columnar structured InN crystals were observed. It demonstrated the possibility of InN nanorods growth and greatly influenced the present study.

MOVPE and MBE have been widely used to grow InN since the late 1980s. Single crystal InN growth by MOVPE was reported using trimethylindium (TMIn) and NH_3 as the precursors [Mat89, Wak89, Wak90]. However, high Hall mobility (*i.e.*, $> 300 \text{ cm}^2/\text{Vs}$) and low background carrier concentration (*i.e.*, $< 10^{19} \text{ cm}^{-3}$) were not achieved until recent years.

InN was also grown by MOMBE using TMIn instead of pure In metal source [Abe93]. Electron Cyclotron Resonance (ECR) was used to generate a nitrogen plasma. The obtained Hall mobility and electron carrier concentration were $100 \text{ cm}^2/\text{Vs}$ and 10^{20} cm^{-3} , respectively. Aderhold [Ade01] reported improved InN film quality by MOMBE. Hall mobility and background carrier concentration were $500 \text{ cm}^2/\text{Vs}$ and $8.8 \times 10^{18} \text{ cm}^{-3}$, respectively. The reported Hall mobility and carrier concentration were plotted in Figure 1-1 with recent MOVPE data [Bhu03, Yam02, Yam04, Yam06]. Hall mobility and the carrier concentration of MOVPE grown InN were $1100 \text{ cm}^2/\text{Vs}$ and $4.5 \times 10^{18} \text{ cm}^{-3}$, respectively [Yam06].

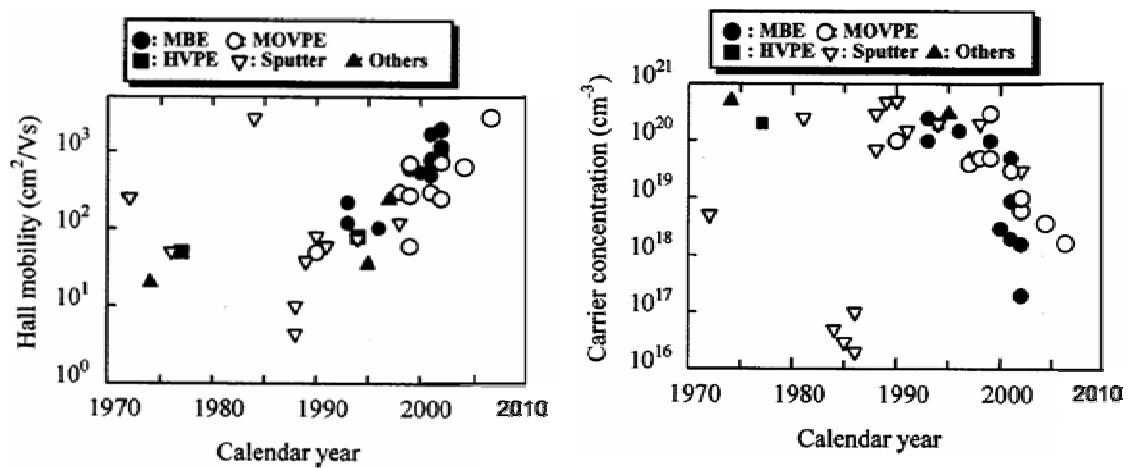


Figure 1-1. Reported values of electric properties of InN (a) Hall mobility and (b) Carrier concentration with calendar year [Bhu03, Yam02, Yam04, Yam06].

Interest in InN has increased since 2002 due to the ambiguous fundamental energy bandgap. The reported bandgap energy value of InN has a wide spread: ~ 0.7 [Inu01, Dav02, Wu02, Sug03, Bri04, But05], ~ 1.1 eV [Inu01, This work], and ~ 1.9 eV [Hov72, Tya77, Nat80, Tan86, Wes88, Sul88, But02, Mot02, Had03] are commonly reported values. Figure 1-2 shows some of the InN bandgap data representing the spread of the values [But05b].

The reason for the controversial bandgap is not well established, although many believe the inclusion of oxygen (In_2O_3 or any form) may be responsible. High crystalline quality InN is therefore essential to determine the controversial property and clarify this ambiguity.

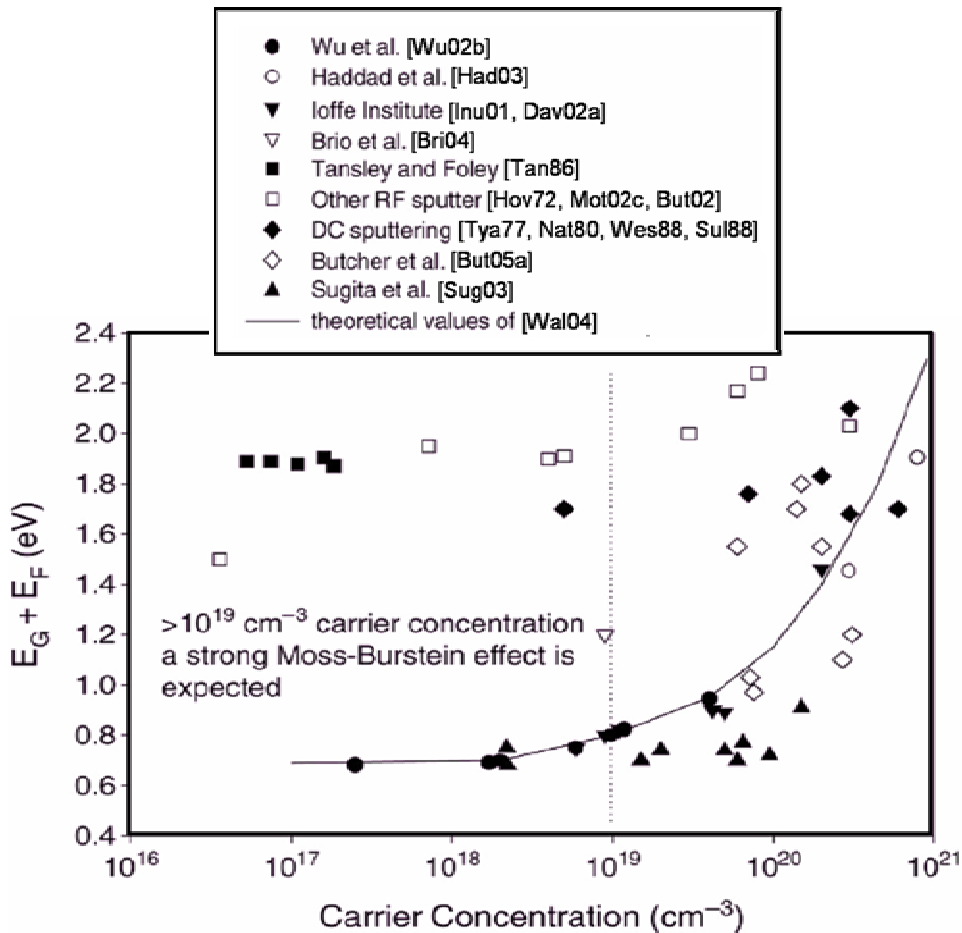


Figure 1-2. Reported bandgap energy of InN as a function of carrier concentration [But05b].

The best reported InN films grown by MOVPE demonstrated Hall mobility and background doping as $1100 \text{ cm}^2/\text{Vs}$ and $4.5 \times 10^{18} \text{ cm}^{-3}$, respectively [Yam06]. MBE grown InN films showed better values of Hall mobility and carrier concentration as $2050 \text{ cm}^2/\text{Vs}$ and $3.49 \times 10^{17} \text{ cm}^{-3}$, respectively [Lu02a].

InN-based electronic devices were fabricated and preliminary evidence of two-dimensional electron gas (2DEG) in a field effect transistor (FET) was reported [Sch00, Lu02b]. Problems growing high quality InN overlap with those for GaN in that lattice and thermal expansion matched substrates are absent and that efficient doping, especially p-type, is difficult.

The growth of InN, however, is more challenging because of the low growth temperature and the formation of In metal droplets. The growth temperature and V/III ratio seem to be the most important growth parameters. Yamamoto investigated the effects of growth temperature and V/III ratio [Yam01]. They found that V/III ratio could be lowered at higher temperature due to the enhancement of the active nitrogen concentration. The suggested growth temperature was 550 to 650 °C. The Hall mobility and carrier concentration were reported as 200 to 400 cm²/Vs and 10¹⁸ to 10²⁰ cm⁻³, respectively [Yam01b, Yam02, Yam04]. The Hall mobility and carrier concentration are improving with increasing temperature up to 600 °C and then showed worse results at higher temperatures.

To enhance the decomposition of NH₃, several techniques have been used. It is well known that the reactor geometry is very important to grow high quality material primarily for MOVPE, as demonstrated by improvement of GaN quality by the two-flow design [Nak91]. Flow modulation [Kel00] was used to leverage the advantages of Atomic Layer Deposition (ALD). TMIn and NH₃ were provided in turn, or NH₃ was kept flowing and TMIn was provide in a pulsed manner. Plasma-assisted MBE and MOVPE [Wan06, Che06, Wu06, Wak89, Wak90, Sat97] and laser-assisted MOVPE

[Yam06, Li94, Bhu02, Bhu03] were also utilized to enhance ammonia decomposition and showed some promising results.

This overview of GaN and InN thin film growth and the corresponding electrical and optical properties demonstrates the advances that have been made and their potential commercial applications. It is also clear that GaN has received considerably more study than InN.

1.2 Literature Review

1.2.1 Equilibrium Analysis of GaN and InN

1.2.1.1 Thermochemical Data for GaN and InN

Studying phase stability is essential for predicting process limits because semiconductors grown at high temperature often experience thermal annealing processes for metallization, remedying implantation damage, or dopant activation. In addition, GaN, AlN and their alloy have applications for high temperature devices thanks to their high temperature stability.

Equilibrium calculations can provide preliminary information on appropriate processing conditions. These calculations require thermodynamic property values for all species and phases. Unfortunately, the properties for Ga-In-N system are not that well defined, especially the standard enthalpy of formation. The reported heats of formations of GaN and InN are quite scattered [Sed06]. The reported heat of formation of GaN ranges from -109.62 [Hah40] to -156.8 kJ/mole [Ran00] and that of InN from -71.0 [Lei04] to 138.072 [Bin02].

Unland and coworkers recently reported thermochemical data for GaN powder and measured the decomposition temperature as 1110 ± 10 K by dynamic oscillation Thermogravimetric Analysis (TGA) and isothermal stepping TGA [Unl03]. Based on

their assessment relative to other reported values, the experimental data from Unland *et al.* [Unl03] were adopted in this study for the GaN–base calculations.

A similar method (TGA) was applied to InN and the $\Delta H_f^0(298.15K)$, $S_m^0(298.15K)$, C_p , and decomposition temperature of InN were determined [Ond02]. The equilibrium decomposition temperature may be lower than the experimentally observed temperature because of the kinetic barriers; however, the equilibrium decomposition temperature cannot be higher than experimental data unless there is measurement error. The InN decomposition temperature (773 K) as measured with TGA by Onderka [Ond02] is higher than Leitner’s drop calorimetry value (686 K) [Lei04]. Considerable uncertainty, however, still exists in the thermochemical data for InN. The data from SUB94 and [Lei04] will be cautiously used for InN in this study since rigorously assessed data is still not available. The reported thermochemical values for GaN and InN are tabulated in Table 1-1.

1.2.1.2 Equilibrium Calculations of GaN Growth by HVPE

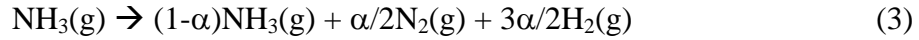
Koukitu [Kou98] performed chemical equilibrium calculations analytically by considering only a limited number of species. They calculated partial pressures of the gaseous species in equilibrium with GaN during HVPE growth with respect to temperature, input GaCl partial pressure, input V/III ratio, and H₂/inert ratio. By comparing the equilibrium of Ga containing gas phase concentration with input GaCl partial pressure, the driving force for the deposition was calculated with the definition:

$$\Delta P_{Ga} = P_{GaCl}^0 - (P_{GaCl} + P_{GaCl_3}) \quad (1)$$

The factor that represents the ratio of the H₂ carrier with the inert carrier was defined as F and was given as:

$$F = \frac{1/2(2P_{H_2} + 3P_{NH_3} + P_{HCl})}{P_{H_2} + 3/2P_{NH_3} + 1/2P_{HCl} + P_{IG}} \quad (2)$$

It should be noted that a way of dealing with NH_3 partial decomposition was introduced here with a factor α such as:



where α is the mole fraction of the decomposed NH_3 . The value of α was measured as $\alpha = 0.03$ at $950^\circ C$ by mass spectroscopy [Ban72], but is a strong function of temperature.

Figure 1-3 (a) shows plots of the driving force for the deposition with temperature with different F values [Kou98]. It was observed that ΔP_{Ga} (the driving force) decreased with increasing F.

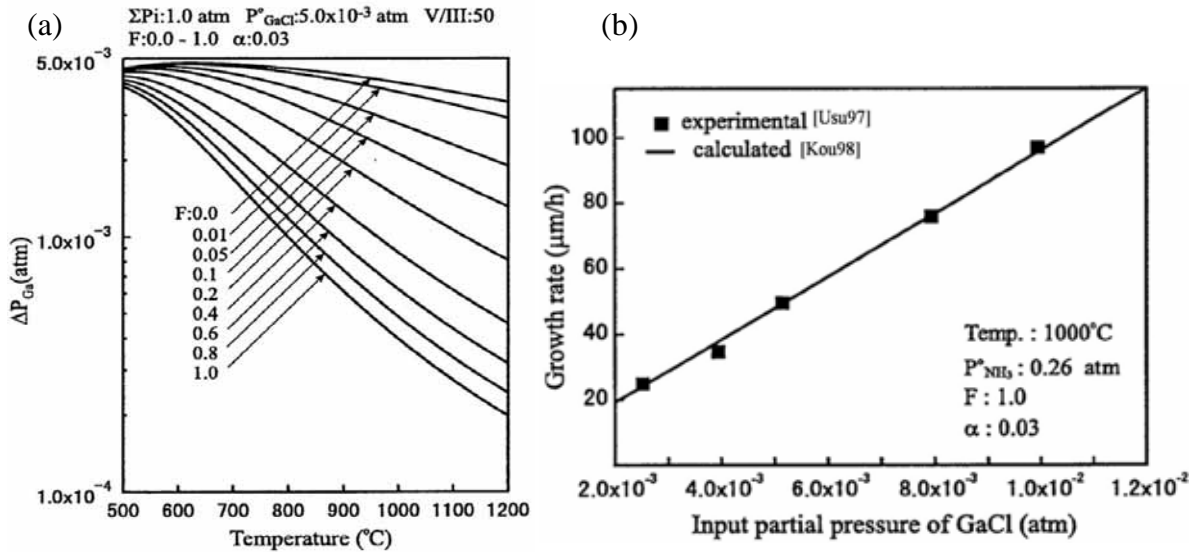


Figure 1-3. Examples of equilibrium calculations. (a) Driving force for the deposition as a function of growth temperature with various parameters for F. Total pressure: 1.0 atm, input partial pressure of GaCl: 5×10^{-3} atm, input V/III ratio: 50 and $\alpha: 0.03$. (b) Comparison between calculated growth rates [Kou98] and experimental data [Usu97].

The growth rate with driving force for the deposition was defined as the following formula:

Table 1-1. Reported values of thermochemical data for solid GaN and InN.

Material	$\Delta H_f^0(298.15K)$ (kJ/mole)	Method	$S_m^0(298.15K)$ (J/mole K)	Method	Tdecomp (K)
GaN	-109.62 [Hah40]	Combustion calorimetry			920 [SUB94]
	-156.8 [Ran00]	Drop calorimetry			1052 [Dav01] 1435 [Lei03]
	-156.8 ± 16 [Unl03]	TGA	30 ± 4 [Unl03]	Debye-Einstein	1110 ± 10 [Unl03]
	-161.56 [Sed06]	DFT calc	36.1 [Sed06]	DFT calc	
InN	-144.6 [Mac70]	High pressure equilibria			
	-133.8 ± 6.3 [Vor71]	Knudsen effusion MS	53.7 ± 7.1 [Vor71]		
	-137.2 ± 18.8 [Vor73]	Knudsen effusion MS	32.3 ± 20.9 [Vor73]		
	-130.6 [Gor77]	Knudsen effusion MS	51.6 [Gor77]		
			54.4 ± 8.0 [Hon87]		
	-132.7 ± 6.7 [Jon87]	Static pressure measurement			1211 [SUB94]
	-138.07 [Bin02]				
			31.6 ± 3 [Ond02]	Debye-Einstein	773 ± 5 [Ond02]
-71.0 [Lei04]	Drop calorimetry	42.51 [Lei04]	PDOS/assessed	638 [Lei04]	
-78.64 [Sed06]	DFT calc	42.5 [Sed06]	DFT calc		

$$r = K_g \Delta P_{Ga} \quad (4)$$

where r = growth rate, and K_g is the mass transfer coefficient.

By adjusting the mass transfer coefficient (*i.e.*, $K_g = 1.18 \times 10^5 \mu\text{m/h atm}$ in this case), the growth rate results matched well with experimental data as seen in Figure 1-3 (b). Thus, it was concluded that GaN growth by HVPE is thermodynamically controlled under these ranges of growth conditions.

Following similar procedures, Kumagai analyzed HVPE growth of InN by InCl and InCl₃ precursors [Kum01]. The results showed that InN growth is difficult using InCl but possible with InCl₃ along with inert or low H₂/inert carrier gas as shown in Figure 1-4 [Kum01]. It could be seen that the driving force has negative values in an H₂ carrier ($F = 1.0$), while it has slightly positive values in an inert carrier ($F = 0.0$).

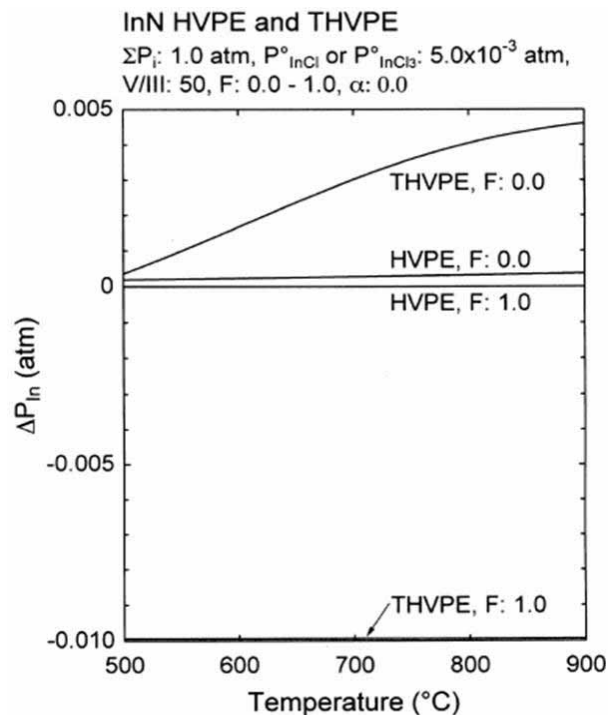


Figure 1-4. Driving force for the deposition of InN (ΔP_{In}) using InCl (HVPE) and InCl₃ (THVPE) as a function of growth temperature. The calculation was performed for growth under inert gas ($F = 0.0$) and hydrogen carrier gas ($F = 1.0$) conditions. [Kum01].

It should be noted that no report was found that dealt with adjustable Cl/III ratio, but only at fixed values since either monochloride ($\text{Cl/III} = 1$) or trichloride ($\text{Cl/III} = 3$) was used in HVPE and THVPE techniques. Continuous variation of Cl/III ratio is possible in H-MOVPE by simply adding an independent stream of a Cl containing species (*i.e.*, HCl). Thermodynamic analysis of H-MOVPE technique including various Cl/III ratios is presented in Chapter 2.

1.2.2 Stress in GaN Films

Stress measurements and modeling of GaN films is important because GaN is usually grown on foreign substrates due to the lack of bulk GaN crystals. The traditional approach to analyze the stress in GaN films was not satisfactory because there were some cases when the expected stress occurred in an exactly opposite manner. For example, both compressive and tensile stressed GaN can be grown on SiC [Per97, Dav97, Dew98, Rie96, Wal99]. Therefore, it could be concluded that the stress in the GaN film is not only related to the lattice and thermal expansion mismatch, since both give stress in GaN, but also to other important factors.

The stress in GaN is mainly related to the lattice and thermal expansion mismatches with the substrate and the initial surface properties, which result in a growth mode change. The origins of tensile stress were identified as lattice and thermal expansion mismatches between GaN and substrate, Si or Mg doping, or grain boundaries of island coalescence [Kro03]. Likewise, the origin of compressive stress can be lattice and thermal expansion mismatches between GaN and substrate. The island growth mode should be avoided as it often creates polycrystalline materials. A buffer layer is usually used to enhance crystal quality by uniform coverage of the surface to prevent island growth.

The traditional approach to modeling the residual stress in GaN film by lattice and thermal expansion mismatches has a flaw because GaN films are typically grown on buffer layers or by a nitridation process. The pregrowth processes change the surface properties significantly. The buffer layers are usually amorphous and the nitridated surface of sapphire is also an amorphous AlO_xN_y layer. Therefore, the traditional heteroepitaxy modeling such as Frank-van der Merwe and Matthews [Mer50, Mat75] cannot be applied since the existence of an amorphous interface was not considered. In addition, the lattice mismatch (*i.e.*, $\sim 14\%$ for sapphire, $\sim 21\%$ for Si, or even $\sim 3.5\%$ for SiC) is very large; dislocations will form at the interface immediately.

A visible product of the incorporation of significant stress in a film is cracking. Etzkorn and Clarke investigated the cracking of thick GaN films on sapphire substrate [Etz01]. A viable mechanism for cracking was identified as island coalescence. A model was developed to deduce the maximum thickness of crack formation with given stress. According to the model, $16\ \mu\text{m}$ thick crack-free GaN could be grown on sapphire with tensile stress in $0.14\ \text{GPa}$. Strain energy calculations related to crack generations were carried out by measuring the bending moment of GaN and sapphire. It was argued that tensile stress in GaN film was generated at the growth temperature after reaching a critical thickness. Kinetically limited crack healing mechanism was suggested after crack generation.

Waltreit reported that GaN films grown directly on 6H-SiC showed no stress, while GaN films grown on AlN/6H-SiC showed compressive stress, although the lattice parameters and thermal expansion coefficients of AlN and SiC are similar [Wal99]. The lattice mismatch induced 3.4% compressive stress was fully relieved in GaN directly

grown on SiC, whereas 0.3 % compressive stress still remained in GaN grown on AlN/SiC even beyond 1 μm thick. It was concluded that the stress in GaN film was mainly determined by its growth mode rather than lattice mismatch in this case. The growth mode is mainly related to the initial surface properties of the substrate. The results suggested that the advantage of the buffer layer is not only in averaging the lattice and thermal mismatches, but also enhancing the surface property. Schematic of GaN directly grown on 6H-SiC and using AlN buffer layer is shown in Figure 1-5.

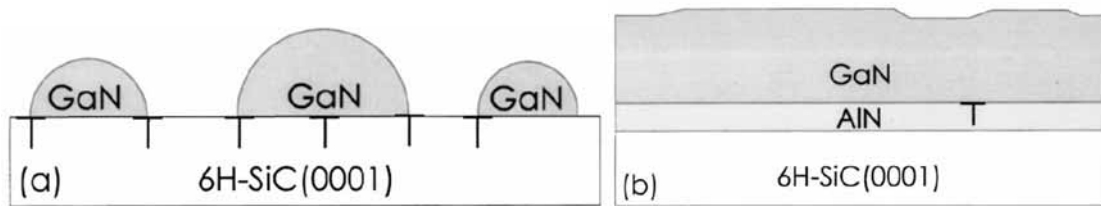


Figure 1-5. Schematic of GaN growth on SiC: (a) GaN/SiC and (b) GaN/AlN/SiC growth. Note that the strain is fully relieved in (a), whereas it is only partially relaxed in (b) [Wal99].

Three dimensional growth (Volmer-Weber) governed the GaN growth without buffer layer and a number of dislocations were shown, while two dimensional growth (Frank-van der Merwe) can occur with few dislocations with AlN buffer layer [Wal99].

1.2.2.1 *In situ* Stress Measurements

To understand the stress evolution in GaN films, *in situ* stress measurements have been carried out using a Multibeam Optical Stress Sensor (MOSS) system [Flo97, Hea99]. This method determines the wafer curvature by measuring a laser beam deflection, which is proportional to the stress. It was used to *in situ* measure the stress in AlGaIn film grown on AlN/SiC [Aco04]. They found that AlGaIn film was initially under compressive stress and evolved into tensile stress as the film thickness increased. The transition (from compressive to tensile stress) thickness of AlGaIn film depended on

the AlN buffer layer growth conditions and AlGaN film Al mole fraction. For example, when V/III ratio was varied from 750 to 10600, the AlGaN initial compressive stress was varied from 1.9 to 8.7 GPa. GaN film did not show a transition to tensile stress up to 3.8 μm thick, whereas more Al content AlGaN showed rapid transition to tensile stress. The persistent tensile stress in MOCVD GaN on sapphire using both LT-AlN and LT-GaN buffer layers were observed by MOSS at growth temperature [Hea99]. The origin of tensile stress may be from the grain boundaries of islands. It was also found that thermal annealing or temperature cycling does not reduce tensile stress in the film. Because the thermal expansion mismatch effect is much larger, eventually the GaN film on sapphire showed compressive stress after cooling.

Raghavan and Redwing [Rag04] measured the persistent tensile stress in AlN grown on Si *in situ* across the wide temperature range 600 to 1100 °C. A sharp drop in the tensile stress was observed from 1 to 0.4 GPa while decreasing the AlN growth temperature below 800 °C. This represented the transition of epitaxial AlN film to polycrystalline. GaN film was consecutively grown on AlN/Si. The GaN film showed slightly compressive stress at 1100 °C.

Krost *et al.* measured the stress in the GaN films on Si(111) *in situ* and successfully grew crack-free 7 μm thick GaN on Si(111) with multiple AlN interlayers [Kro05, Dad04, Clo04, Kro03]. The sources of tensile stress were identified as grain boundaries from island coalescence (0.2 GPa/ μm) and Si-doping (1.6 GPa/ μm) [Kro05]. The non-uniformly deposited SiN was called an “*in situ* mask” and high quality GaN could be obtained on the *in situ* SiN mask/AlN/Si. The *in situ* curvature measurement results for GaN grown on SiN/AlN/Si are shown in Figure 1-6 [Kro03].

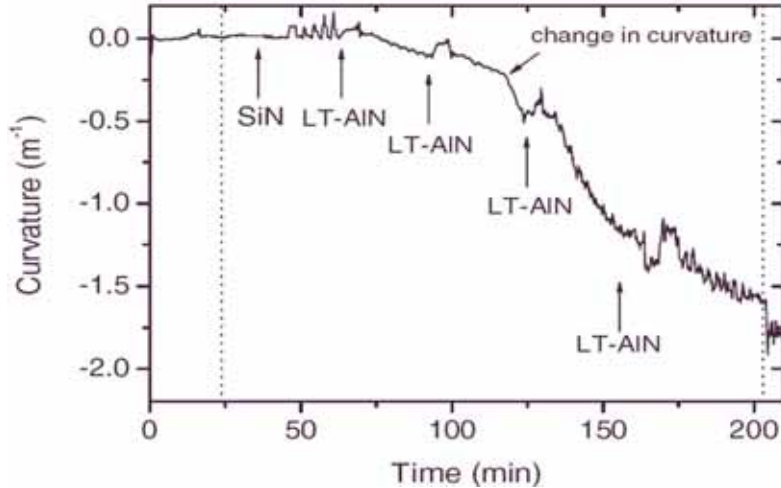


Figure 1-6. *In situ* curvature measurements during the growth of a $\sim 6 \mu\text{m}$ thick GaN layer showing the influence of AlN interlayers on the curvature. The sample was crack-free after growth [Kro03].

Evolution of the curvature was observed with inclusion of LT-AlN interlayers. When LT-AlN was applied, a temporary compressive stress was observed as shown in Figure 1-6. Nevertheless, the film was under persistent tensile stress as the thickness increased. Based on the results presented in Figure 1-6, it is evident that AlN has an impact for only a small amount of subsequent growth. Although this AlN interlayers may improve the crack-free thickness, the growth of thick ($> 100 \mu\text{m}$) crack-free GaN in this way should have inherent limit.

1.2.2.2 *Ex situ* Stress Measurements

The surface of HVPE and H-MOVPE grown GaN is often very rough. Commonly used non-destructive methods to measure the stress in rough films or the films that have structures on them are XRD reciprocal space mapping and Raman spectroscopy. In this case, the stress measurement is taken after the sample has cooled to room temperature.

XRD Reciprocal Space Mapping. The lattice parameters of a film can be precisely measured using an XRD reciprocal space mapping. It was observed that GaN showed strong in-plane strain although out-of-plane strain was negligible [Eip05]. Considerable

thermal compressive stress was found from GaN grown by ion beam assisted MBE on γ -LiAlO₂ (100). It was found that there was 3 times greater compressive stress in the in-plane than out-of-plane during measurement by HT-XRD in the temperature range 25 to 600 °C (HT-XRD chamber temperature) [Eip05]. Stress in GaN was also measured on ZnO substrate by HR-XRD [Min04]. In accordance with the *in situ* stress measurement results, the change of buffer layer thickness changed the film stress significantly. Thus, buffer layer material should be carefully selected and the thickness of the buffer layer should be controlled to reduce stress in the final film.

Raman Spectroscopy. Raman spectroscopy is a well-established, non-destructive, and convenient technique to detect the stress in the film, although the typical accuracy of stress measured by Raman spectroscopy compared to ~ 5 % for HR-XRD is about 20 % [Dav97]. Among the all allowed Raman modes, it is known that the E₂ mode is strongly related to biaxial stress in GaN [Dav97]. Between the two E₂ peaks, the higher frequency mode is usually used due to the higher intensity. Biaxial stress in GaN sample can be measured by comparing the position of E₂^(high) peak with that of a stress-free sample.

Table 1-2 lists the Raman E₂^(high) peak positions reported in the literature [Dav97, Mel97, Gil00, Kry99a, Dav97, Yam00, Dem96, Yoo97, Ben02]. It is noticed that even freestanding or high pressure grown bulk GaN samples do not have unanimous Raman E₂^(high) peak that can be used for stress-free standard. The E₂ mode of freestanding GaN ranged from 565 to 570 cm⁻¹. Therefore, deciding the value of stress-free E₂^(high) peak position is impossible at this point. Generally 568 cm⁻¹ is considered as the stress-free GaN E₂^(high) peak position because it is about average value from freestanding GaN samples. Therefore the stress in GaN can be determined by comparing the E₂ value with

568 cm^{-1} . If the measured E_2 frequency is higher than 568 cm^{-1} , the film is under compressive stress qualitatively, and vice versa.

Table 1-2. Reported values of the Raman $E_2^{(\text{high})}$ peak positions.

Sample description	Raman $E_2^{(\text{high})}$ peak position (cm^{-1})	Reference
Freestanding (300 μm) by HVPE Substrate: Al_2O_3	568	[Dav97]
Freestanding (100 μm) by HVPE Substrate: SiC, no buffer	565	[Mel97]
Freestanding by high N_2 pressure	565	[Gil00]
Freestanding on LiGaO_2 by H-MOVPE	570	[Kry99a]
0.5 to 3 μm GaN/AlN(AlGaIn)/SiC	565	[Dav97]
1.8 μm on AlN/ Al_2O_3 by MOCVD	566	[Yam00]
V/III (2000 to 6000) MOCVD	569 (V/III = 6000) to 571 (V/III = 2000)	[Dem96]
1.5 μm GaN/(10 to 85 nm)LT-GaN/c- Al_2O_3 by MBE	565 to 572	[Yoo97]
GaN/misoriented Al_2O_3 by MOCVD	570 to 571	[Ben02]

The quantitative value of stress can be obtained using a linear proportionality factor. This quantitative argument may be meaningless in some sense since the stress-free value is unknown. However, two samples can be quantitatively compared by assuming one sample is stress-free. The reported value of this proportionality factor ranges from 2.4 to 4.2 $\text{cm}^{-1}/\text{GPa}$ [Dav97, Kis96]. Thus, further study is required to conclusively determine the stress from Raman peak shift quantitatively.

One may expect compressive stress to be present in GaN grown on Al_2O_3 because the lattice and thermal expansion mismatches leads to compressive stress. However, it is not straightforward to predict whether the overgrown GaN will have compressive or tensile stress. The Raman spectroscopy results showed that the grown GaN film on c- Al_2O_3 is less compressively stressed with increasing V/III ratio [Dem96].

Moreover, the Raman E_2 peak significantly shifted from 572.0 (compressive) to 565.2 cm^{-1} (tensile) while changing the buffer layer thickness from 10 to 85 nm as shown in Figure 1-7 [Yoo97].

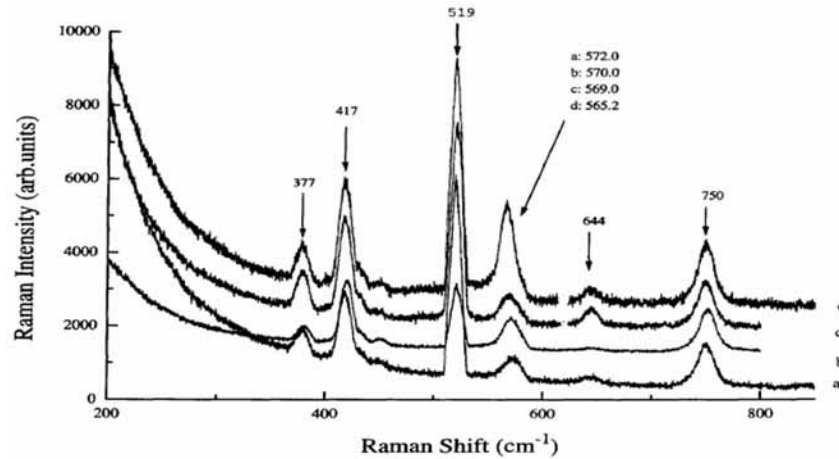


Figure 1-7. Raman peak shifts of 2 μm thick GaN with different LT-GaN buffer layer thickness; LT-GaN buffer layer thickness (a) 10 nm, (b) 50 nm, (c) 75 nm, and (d) 85 nm. [Yoo97].

This tensile to compressive stress change is expected because uniform coverage of the surface at an optimal buffer layer thickness will lead to compressive stress from 2-D growth rather than 3-D island growth that create tensile stress at the grain boundary.

Since Raman spectroscopy is sensitive to the stress in the GaN film, it was used as a major technique to measure the stress in the GaN films grown on sapphire substrate and the results will be presented in Chapter 3.

1.2.3 GaN Growth on Si

One of the advantages of using Si substrate instead of sapphire is its availability in large diameters. Another advantage of Si is that the heat generated from the device can more easily drain because Si has much higher thermal conductivity (145 W/m K) than sapphire (5.43 W/m K). GaN films are usually grown on Si (111) substrate because the hexagonal geometry (*i.e.*, three-fold symmetry) of the Si (111) surface is better matched

with the basal plane of GaN. The growth of GaN on Si (100) would be more challenging due to the different crystallographic structures. For example, it was often observed that a mixture of cubic and hexagonal GaN grown on Si (100) substrate by MBE [As00]. GaN grown on Si (100) shows multiple in-plane alignments mainly composed of two in-plane domains rotated by 30° [Leb00, Sch04b].

GaN is usually grown by MOCVD on Si since it gives the most promising results and is suitable for mass production. HVPE can also be used to grow GaN on Si. The report of HVPE GaN growth on Si is, however, limited [Mas06, Zha05, Mes05, Yu05]. A maximum crack-free thickness of HVPE GaN film grown on Si is $1.5\ \mu\text{m}$ on 2 inch Si(111) [Zha05]. The results suggested that the crack generation is not much related to growth chemistry, growth rate, or reactor geometry. Instead, it is more related to lattice mismatch and thermal expansion coefficient mismatch among GaN, buffer layer, and Si.

The driving force for crack is the strong tensile stress in the film caused by lattice and thermal expansion differences between GaN and Si. The origin of tensile stress within GaN film on Si substrate is not only from lattice and thermal expansion mismatches, but also from island coalescence boundaries due to the initial growth from small crystallites [Dad03]. Along with the brittleness of Si, sometimes cracks can penetrate into Si over $1\ \mu\text{m}$ depth [Zam02].

A number of techniques such as AlN buffer layer [Dad03, Lia00, Sch05], AlN/SiC buffer [Lia00], AlGaIn buffer layer [Wan05], multiple AlN interlayers [Kro03], AlGaIn graded layer [Mar01, Abl05], AlGaIn/HT-AlN [Sch05], AlGaIn/GaN superlattice [Lia01], SiO₂ patterning [Det01, Zam01, Zam02, Nao03], and Si doping in GaN [Yu06] were

used to reduce the crack density in GaN on Si. Table 1-3 lists some of the techniques used for crack-free GaN growth on Si.

Table 1-3. Techniques used for growth of crack-free GaN on Si.

Crack reduction technique for GaN grown on Si	Growth T (°C)	Crack-free thickness (Crack-free area)	Ref
AlN/SiC buffer layer	1050	1.3 to 1.5 μm	[Lia00]
AlGaIn/GaN superlattice on AlN/SiC/Si		(10 cm diameter)	[Lia01]
Multiple AlN interlayer on AlN buffer layer with in situ curvature measurement	1145	7 μm	[Kro03]
AlGaIn graded layer on HT(1160 °C)AlN (100 nm) buffer layer	1050	2 μm	[Abl05]
In situ SiN mask (1.5 mono layer) on Si doped AlN buffer layer(25 nm)	1165	0.75 μm	[Dad03]
Al _{0.58} Ga _{0.42} N buffer layer (180 nm) at 800 °C	1000	0.4 μm	[Wan05]
AlGaIn graded layer on AlN buffer layer (10 to 500 nm)	1050	0.7 to 1.6 μm	[Mar01]
SiO ₂ patterning	1100	9 μm (5 μm x 10 μm)	[Det01]
		10 μm (100 μm x 100 μm)	
Lateral confined epitaxy (prepatterned Si)	1020	0.7 μm (100 μm x 100 μm)	[Zam02]
Si doped GaN on AlN buffer layer (100 nm)	1000	< 1 μm	[Yu06]

Crack-free 1.3 to 1.5 μm GaN was successfully grown on 10 cm diameter Si (111) using AlN and SiC buffer layers [Lia00]. Further study showed that high crystal quality and smooth surface were achieved by insertion of AlGaIn/GaN superlattice interlayers [Lia01]. The results showed that large diameter GaN growth on Si is promising.

The typical crack-free thickness of GaN grown on large area Si is < 2 μm except one report showed 7 μm crack-free GaN grown on Si [Kro03]. However, the growth of large area (> 2" diameter) freestanding (> 100 μm thick) GaN on Si was not reported to date.

An AlN buffer layer between GaN and Si is most widely used because the thermal expansion difference between AlN and Si is less than GaN and Si. In addition, GaN

films on AlN will possess compressive stress during cooling that may compensate for the tensile stress.

Unlike many reports of GaN growth on sapphire that uses either LT-AlN or LT-GaN as a buffer layer, reports of LT-GaN buffer layer usage of GaN on Si were rarely found (*i.e.*, [Mas06b]). The benefit of LT-GaN buffer layer on sapphire may be the change of the surface property resulting in two-dimensional growth. On the other hand, GaN on Si is under significant tensile stress. Therefore, changing the surface property is necessary, and, in addition, artificial compressive stress generation is required to grow crack-free GaN film on Si. It is evident that AlN and AlGaN are promising buffer layer materials between GaN and Si due to the compensation of tensile and compressive stress. It was found that the higher Al concentration in AlGaN buffer layer is better for subsequent GaN growth [Wan05].

Table 1-4 lists the structural properties of various substrates for GaN epitaxy. It can be predicted that what kind of stress the GaN film will be under by comparing the lattice parameter and thermal expansion coefficient. Tensile and compressive stress induced by lattice mismatch and thermal expansion mismatch are drawn in Figure 3-1.

The other widely used technique is the growth of an AlGaN graded layer. This method creates gradual changes in the stress in GaN films. In addition, AlGaN graded layers reduce threading dislocations significantly [Mar01].

Other than stress engineering by buffer and interlayers, SiO₂ patterning was also used to reduce cracking problems [Det01, Nao03, Zam01, Zam02]. Adopted from Epitaxial Lateral Overgrowth (ELO), grooved Si substrate was used as the substrate and a thin GaN layer was grown, followed by SiO₂ patterning [Det01]. The growth of GaN on

prepatterned Si, termed Lateral Confined Epitaxy (LCE) [Zam01] was also studied.

However, this technique did not create more promising results since GaN films tend to bend upwards (concave), although a crack-free region of 100 μm x 100 μm was reported [Zam02].

Table 1-4. Structural Properties of Various Substrates for GaN Epitaxy [Kan04].

Substrate	E_g (eV)	Lattice parameter a (\AA)	Lattice parameter c (\AA)	Lattice mismatch with GaN (%)	Thermal expansion coefficient (10^{-6}K^{-1})	
					a	c
GaN – wurtzite	3.36	3.189	5.18	0	5.6	3.17
InN - wurtzite	0.7	3.537	5.704	9.8	4.0	3.0
AlN – wurtzite	6.2	3.112	4.98	2.5	4.2	5.3
6H-SiC – wurtzite	2.9	3.08	15.1	3.5	4.2	4.7
Al₂O₃ – wurtzite	6.8	4.758	12.991	16.1	7.5	8.5
ZnO - wurtzite	3.35	3.21	5.21	1.94	2.9	4.8
LiAlO ₂ – tetragonal	6.1	5.1687	6.2679	1.5	7.1	7.5
LiGaO ₂ – orthorhombic	4.1	5.402	5.007	0.9	6	7
3C-SiC – diamond	2.3	4.36		3.9	2.7	
GaAs – zinc blende	1.42	5.65		19.87	6.0	
Si (111) – cubic	1.12	5.83		17.0	6.2	
BP – zinc blende	2.0	4.54		0.63		

Another way of reducing cracks would involve creating weak cohesion between GaN and Si, so that the film can separate during the cooling process. For example, ion implantation (N^+) was carried out to intentionally create defective layer of AlN/Si substrate [Jam05]. This partially isolated the III-nitride layer and Si substrates and helped reduce the strain by up to 84 %. A novel approach of creating weak cohesion between GaN and Si using InN as buffer material will be presented in Chapter 4.

1.2.4 Growth of InN Films and Nanostructured Materials

1.2.4.1 Growth of InN Films

InN is the least studied material among the group III nitrides that are relevant to UV-visible-IR optoelectronics. InN has high drift velocity at room temperature, which is

a good characteristic for high speed FET applications [Ole98]. In addition, tandem solar cells with Si at the bottom cell and a higher bandgap material (*i.e.*, $\text{In}_x\text{Ga}_{1-x}\text{N}$ 1.85 eV) on the top cell can achieve a maximum efficiency of 32.1 % [Mat87].

Efforts have been made to grow InN crystals by MOCVD [Wak90, Sat97, Guo99, Yam94, Yam97, Yam99, Pan99, Yan02, Dra06, Mal04, Cha04, Sin04, Yam05, Yam04, Jai04, Los04, Yam05, Mal05, Hua05, Kel00, Yam01, Sug03], MBE [Abe93, Dav99, Lu01], HVPE [Iga92], laser assisted CVD [Bu93], as well as other less used processes. Most InN films were grown by MOCVD because MOCVD is a well-established technique especially when mass production is considered.

The growth of high quality InN, however, was impeded by several factors. Low (< 700°C) growth temperature is required due to the very high nitrogen vapor pressure and strong tendency to form In metal droplets. It is difficult to grow high quality material due to the reduced adatom mobility on the surface at low growth temperature. In addition, due to the high kinetic barrier for breaking N-H bonds of NH_3 [Seg04, Yum81, Liu78], excessive NH_3 flow is required to compensate for the amount of active nitrogen. Excessive NH_3 will form H_2 , and H_2 is known to make InN growth less thermodynamically favorable [Kou99, Hua05, Dra06, Joh04j]. Thus, the growth rate of InN is very low compared to other group III nitrides.

Another obstacle is the lack of suitable substrate for InN growth. Sapphire and Si have been widely used substrates for InN because sapphire is a good substrate for group III nitrides in that the surface of sapphire can be changed to AlO_xN_y by nitridation. Si has numerous advantages including the possibility of fabricating tandem solar cells. The lattice mismatch between InN (0001) and Si (111) is about 8 %, while the lattice

mismatch between InN (0001) and c-Al₂O₃ is about 26 %. It should be noted that when a lattice mismatch is greater than 0.8 %, dislocations will form at the interface. Thus stating that an 8 % lattice mismatch is better than a 26 % mismatch with InN does not have much significance when critical thickness is concerned.

It was found in early work that although Si has a smaller lattice mismatch than sapphire, the films grown on sapphire had superior quality after nitridation [Yam94]. Nitridation process formed AlN on sapphire substrate [Ven99] and AlN has a 13 % lattice mismatch (c.f. Al₂O₃ has 26 % lattice mismatch with InN). Si_xN_y formation is known to prevent epitaxial growth of GaN on Si [Plo99]. Thus nitridation of Si substrate should be avoided.

InN films were grown on Si(111) substrate without nitridation [Yan02]. To avoid SiN layer formation, TMIn was first introduced before NH₃. MOCVD with double zone heating was used to facilitate thermal cracking of NH₃. Growth temperature was varied from 350 to 600 °C and a maximum of 6 μm/hr growth rate was achieved although the films over 1 μm thick cracked.

For InN growth on sapphire, the optimal nitridation temperature and times were ambiguous. For example, one report showed best results with 1000 °C for 30 min [Pan99] and the other report proclaimed 1075 °C for 5 min gave best results [Dra06].

To elucidate the effect of nitridation, the most useful method may be to observe the surface evolution during the growth *in situ*. From *in situ* spectroscopic ellipsometry study of InN growth by MOVPE [Dra06], it was found that the nitridation at 1050 °C for 45 sec, or 1000 °C for 300 sec would give the best quality film. It may be concluded that lower nitridation temperature requires longer nitridation time.

The optimal growth temperature of InN is another ambiguity. In fact, the temperature is not an exact value in practice because it depends on the places of thermocouples, thermocouple types, or the temperature measurement methods. Therefore, ~ 25 to 50 °C of temperature error is possible. The highest reported growth temperature for InN was 750 °C [Tak97]. The lowest growth temperature is not clearly reported because of the low quality of the material, but it may be approximately 350 °C [Yan02] for MOCVD. Typical InN growth temperature is around 450 to 650 °C.

It seems that the crystal grower's golden rule, "the higher growth temperature, the better crystal quality," holds for InN case as well. The highest Hall mobility was reported from the sample grown at 600 °C [Kel00]. The growth temperature at 650 °C gave the best surface morphology [Yam01]. InN films grown at 620 °C showed the best optical properties, whereas the samples grown at 600 °C exhibited the best electrical properties. Some reported that high growth temperature is destructive to InN because it begins to decompose. For example, surface morphology of the InN was best at 550 °C during the 520 to 590 °C experiments [Yan02]. According to the other experiments, 560 °C grown samples showed the best quality among the 540 to 580 °C [Jai04]. Thus, the optimal growth temperature determination is not clear yet. It should be noted that optimal growth temperature is well above the decomposition temperature of InN as in the GaN case. This result showed that InN decomposition and growth temperatures have a wide range of overlaps, about 230 °C (520 °C decomposition [Dra06] to 750 °C growth [Tak97]).

To find optimal growth conditions for InN film by H-MOVPE, exploratory study was carried out and the results are presented in Chapter 6. It should be noted that during

the growth study in chlorinating environment [Kan04], InN columnar structured materials were observed and the growth conditions provided a good starting point for the growth of nanostructured materials.

1.2.4.2 Growth of InN Nanostructured Materials

The growth of InN nanostructured material is interesting since the hope is that devices made of nanostructures will have superior efficiency due to quantum confinement effects. The growths of InN nanorods and nanowires have been reported by several researchers [Ji05, Kim03, Che05, Qia05, Luo05, Cha05, Lia02, Yin04, Sch04, Lan04, Tan04, Sar05, Joh04, Yin04, Lan04, Vad05, Zha05, Shi05, Tak97].

InN nanowires have usually been grown by thermal catalytic CVD that usually uses Au as a catalyst. For example, Liang *et al.* [Lia02] synthesized InN nanowires on gold patterned p-type Si (100). Pure indium foil and NH₃ were used as an indium and nitrogen sources, respectively. The growth was performed at 500 °C for 8 hrs and 40 to 80 nm diameter nanowires were created. The band gap was 1.85 eV measured by PL.

Zhang *et al.* [Zha02] fabricated anodic alumina membranes (AAM) and deposited Au catalyst to grow InN nanowires by electrodeposition. The indium and nitrogen sources were pure indium powder and ammonia. Despite the complex substrate preparation and the rather long growth time (12 hr), the InN nanowires were polycrystalline with rough surface morphology.

Lan *et al.* [Lan04] produced InN nanorods using pure indium powder and NH₃ as the indium and nitrogen sources in a hot wall quartz reactor. Au was sputtered on Si(100) substrates as the catalyst and good quality single crystal InN nanorods were produced. The band gaps of 0.766 eV and 1.9 eV were observed depending on the diameter of nanorods. It was still arguable why there exist two distinct values.

The typical sources of In were In metal [Vad05, Zha05, Joh04, Tan04, Lan04, Lia02], In_2O_3 [Tan04, Sch04, Lan04, Yin04, Luo05], InCl_3 [Tak97, Kim03], or TMIIn [This work]. Sometimes a novel precursor, such as indium acetylacetonate, was used [Sar05]. Ammonia was mainly used as the nitrogen source since most other nitrogen sources are extremely flammable. A less flammable nitrogen source, monomethylhydrazine (MMHy), was occasionally used [Tak97].

An external catalyst was not used to grow InN nanostructures in some cases [Che05, Luo05, Joh04, Vad05]; however it is possible that In liquid acted as a self-catalyst. For example, Johnson *et al.* [Joh04] reported InN nanowires on the quartz surface and indium metal surface. Indium metal and NH_3 were also used as the indium and nitrogen sources, respectively. The growth was carried out at 700 °C for 2 hrs and 50 to 100 nm diameter nanowires were generated. Although the morphology of the nanowires shows rather rough surface, the nanowires were single crystal and the band gap was 0.80 eV as measured by PL.

The growth axis was usually along the [110] direction [Lia02, Yin04, Lan04, Tan04] and sometimes the [001] direction [Kim03, Joh04], suggesting that there was more than one growth mechanism that governs nanostructure growth.

Nanostructures can be grown in a relatively wide range of temperature. For example, nanowires were grown at $T = 600$ to 750 °C [Luo05, Sch04, Tak97], 565 to 590 °C [Yin04], 525 °C [Tan04], 500 °C [Lan04].

Since InN nanowires may be of higher quality than InN films, there was strong motivation to determine the bandgap. However, the bandgap measured from InN nanowires still showed wide ranges, although a majority of the results centered at 0.8 eV.

Both 1.9 eV and 0.8 eV bandgaps were detected as evidenced by the brown colored (30 to 50 nm diameter) and black colored (50 to 100 nm diameter) nanowires [Lan04]. In another case, both room temperature PL and optical absorption spectrum showed 0.8 eV of bandgaps from InN nanowires [Joh04a]. The bandgap was also measured from InN nanowires and two distinctive peaks of 0.8 eV and 1.9 eV were detected from the InN and In₂O₃ mixture [Vad03]. A higher bandgap (1.9 eV) was still detected from InN nanowires grown on Anodic Alumina Membrane (AAM), using direct reaction of In metal with NH₃ [Zha05]. Nanowires grown by nitridation of In₂O₃ powders without catalyst showed a 1.7 eV bandgap [Luo05]. Another medium bandgap of 1.1 eV (FWHM 105 meV) was measured by PL from aligned wurtzite polycrystalline InN nanofingers [Ji05]. A bandgap of 1.1 eV was also obtained by calculation from InN nanotubes based on Density Functional Theory (DFT) considering stability and electronic structures of single walled (SW) InN nanotubes [Qia05]. On the other hand, other calculations showed 0.8 to 0.9 eV [Bec02] from wurtzite InN.

Further investigation is required to conclude the correct bandgap of InN as well as the reasons for the wide range of bandgap values.

In this study, InN nanostructured material growth optimizations were carried out by H-MOVPE and the results are presented in Chapter 5.

As an exploratory work, GaN nanostructured material was tested to grow by H-MOVPE and some results are shown in Chapter 7 followed by recommended future work in Chapter 8.

CHAPTER 2 CHEMICAL EQUILIBRIUM ANALYSIS OF H-MOVPE SYSTEM

2.1 Introduction

Although the Hydride Metalorganic Vapor Phase Epitaxy (H-MOVPE) technique has proven to be a promising and versatile technique to synthesize III-V compound semiconductors, the chemistry of H-MOVPE is not currently well understood. Experimental definition of the gas phase and heterogeneous reactions are noticeably absent, mainly due to the difficulty of dealing with corrosive gases, such as HCl. In addition, hot furnace walls and wall deposition during growth also obstruct the use of optical *in situ* measurements. An alternative way to study the chemical reactions involving the H-MOVPE technique is through simulations, and the most straightforward is chemical equilibrium analysis.

Thermodynamic analysis can give insight into which gas phase and condensed phase species will be present without detailed knowledge of molecular structures or reaction kinetics. Because reaction kinetics is excluded, the result in some cases may not represent the actual chemistry. It can, however, give an approximate idea of which species will be dominant under various conditions.

Reed [Ree02] calculated the mole fractions of gas and condensed phase species at equilibrium in the H-MOVPE system for GaN growth by varying temperature, Cl/Ga ratio, and NH₃ flow rates. It was found that the calculated results matched well with experiments when Ga(l) is excluded from the system. It was also found that Cl acted as a gallium sink and H (from NH₃) acted as a carbon scavenger.

In this chapter, more species have been added into Reed's database. The newly incorporated species includes not only Ga, but also In containing species. The database also contains metalorganics and adducts. The aspects of two main reactions can be compared: Group III chloride formation versus metalorganic decompositions. One of the goals for this study is to see whether H-MOVPE is closer to MOVPE or HVPE after metalorganics + HCl reactions. If the results are known, the consecutive chemistry will be clearer because both MOVPE and HVPE chemistry are well studied.

2.2 Thermochemical Data Collections

Great care should be taken when selecting and adding new thermochemical data. The inclusion of one erroneous data point or exclusion of one important species may render the calculation results inapplicable. Most data for well-identified traditional species in the Ga-In-C-H-Cl-N system are from the Thermo-Calc SUB94 database. Most data for well-known species from SUB94 have passed the self consistency test as well as 2nd and 3rd law verifications with experimental data.

Species that are commonly included in a complex equilibrium analysis of subsystems in the Ga-In-H-C-Cl-N system are listed in Table 2-1. In this Table, a number of gas phase species are categorized by Ga, In, and Cl containing species, with other species such as hydrocarbons, and the species that are only composed of C, N, or H. Condensed phases are also organized in the same way as the gas phase. It should be noted that although some species may not exist in the H-MOVPE system, they were not excluded from the database. Trace species were traditionally excluded to save computation time. Now, with advancements in computing power, there is no need to exclude non-significant species, as long as the correct thermochemical data are used. In

addition to the data from SUB94, critically assessed data for GaN and InN were used from [Unl03] and [Lei04], respectively.

Table 2-1. Commonly considered species in Ga-In-H-C-Cl-N system from SUB94 database.

Gas Phase	Ga containing species	Ga, Ga ₂ , GaH, GaCl, GaCl ₂ , Ga ₂ Cl ₂ , Ga ₂ Cl ₄ , Ga ₂ Cl ₆ , GaCl ₃
	In containing species	In, In ₂ , InH, InCl, InCl ₂ , In ₂ Cl ₂ , InCl ₃ , In ₂ Cl ₄ , In ₂ Cl ₆
	Cl containing species (excluding III chlorides)	CCl, CHCl, CH ₂ Cl, CH ₃ Cl, CNCl, CCl ₂ , CHCl ₂ , CH ₂ Cl ₂ , CCl ₃ , CHCl ₃ , CCl ₄ , C ₂ Cl, C ₂ HCl, C ₂ H ₃ Cl, C ₂ H ₅ Cl, C ₂ Cl ₂ , C ₂ H ₂ Cl ₂ , C ₂ H ₄ Cl ₂ , C ₂ Cl ₃ , C ₂ HCl ₃ , C ₂ H ₃ Cl ₃ , C ₂ Cl ₄ , C ₂ H ₂ Cl ₄ , C ₂ Cl ₅ , C ₂ HCl ₅ , C ₂ Cl ₆ , C ₆ H ₅ Cl, Cl, HCl, Cl ₂
	Other species	CH, HCN, CH ₂ , CH ₃ , CH ₄ , CN, CN ₂ , C ₂ , C ₂ H, C ₂ NH, C ₂ H ₂ , C ₂ H ₃ , C ₂ H ₄ , C ₂ H ₅ , C ₂ H ₆ , C ₂ N, C ₂ N ₂ , C ₃ , C ₃ H, C ₃ NH, C ₃ H ₄ , C ₃ H ₆ , C ₃ H ₈ , C ₃ N, C ₄ , C ₄ H ₁₀ , C ₄ H ₂ , C ₄ H ₄ , C ₄ H ₆ , C ₄ H ₈ , C ₄ N, C ₄ N ₂ , C ₅ , C ₅ NH, C ₅ H ₈ , C ₅ N, C ₆ H ₆ , C ₆ N, C ₆ N ₂ , C ₇ NH, C ₇ N, C ₈ N, C ₈ N ₂ , C ₉ NH, C ₁₀ N, C ₁₀ N ₂ , C ₁₁ NH, C ₁₁ N, C ₁₂ H ₂₆ , H, NH, N ₃ H, H ₂ , NH ₂ , N ₂ H ₂ , N, N ₂ , N ₃ , NH ₃ , N ₂ H ₄
	Ga containing species	GaCl ₃ (l), Ga(l), GaCl ₃ (s), GaN(s)*, Ga(s)
Condensed Phases	In containing species	InCl(l), InCl ₃ (l), In ₂ Cl ₃ (l), In ₃ Cl ₄ (l), In ₄ Cl ₇ (l), In(l), InCl(s), InCl(s ₂), InCl ₂ (s), InCl ₃ (s), In ₂ Cl ₃ (s), In ₃ Cl ₄ (s), In ₄ Cl ₇ (s), InN(s)**, In(s)
	Cl containing species	CCl ₄ (l), C ₆ H ₅ Cl(l), NH ₄ Cl(l), NH ₄ Cl(s ₁), NH ₄ Cl(s ₂)
	Other species	C(l), C(graphite), Diamond

* GaN(s) thermochemical data was replaced with assessed data in [Unl03]

** InN(s) thermochemical data was replaced with assessed data in [Lei04]

The data for metalorganics (MOs) and adducts were obtained from Przhevalskii *et al.* [Prz98] and listed in Table 2-2. Since some of thermochemical data for MOs and adducts are calculated, it is necessary to validate the data. Values of ΔH°_{298} , S°_{298} , and C_p for all the species used in the calculations plus Al containing species are listed in Appendix A.

Table 2-2. Additionally included gas phase species from [Prz98].

Gas Phase	Ga containing species	Ga(CH ₃) ₃ , GaCH ₃ , Ga(CH ₃) ₃ NH ₃ , GaCH ₃ NH, GaNH ₃ , [Ga(CH ₃) ₂ NH ₂] ₃ , GaCl ₃ NH ₃ , GaH ₂ , GaH ₃ , (GaCH ₃ NH ₃) ₃ , (GaN) ₃ *
	In containing species	In(CH ₃) ₃ , InCH ₃ , InH ₂ , InH ₃

* The gas phase ring-shaped (GaN)₃ species was eliminated due to inconsistency in the results. See section 2.3.1.

2.3 Chemical Equilibrium Calculations

There are two main ways of computationally determining the equilibrium state: stoichiometric and non-stoichiometric algorithms [Smi68]. In the stoichiometric approach, the total Gibbs energy of the system is minimized by solving the set of linear equations produced by introducing the stoichiometric constraints [Mey84]. In the non-stoichiometric approach, the system of nonlinear equations produced for the equilibrium expressions for each reaction in an independent set of reaction is solved.

In this work, Thermo-Calc is used to solve for the equilibrium states. Users need to define atoms and provide initial atomic ratios, temperature, and pressure for equilibrium calculations. The software will generate all possible molecules by combination of defined atoms, as long as they exist in the database. After that, the mole fractions of all the species are calculated and iterated to find the minimum total Gibbs energy of the system. Therefore, it is important to make sure that all the thermochemical data in the database are valid. One way of checking the validity is by computing well-known equilibria.

2.3.1 Thermochemical Data Verification

Starting with established databases, the species list was expanded by review of the literature for the Ga-In-C-H-Cl-N system. To verify the newly included data, well-

known problems were solved to check the consistency. For that purpose, the In-N and Ga-N phase diagrams were generated.

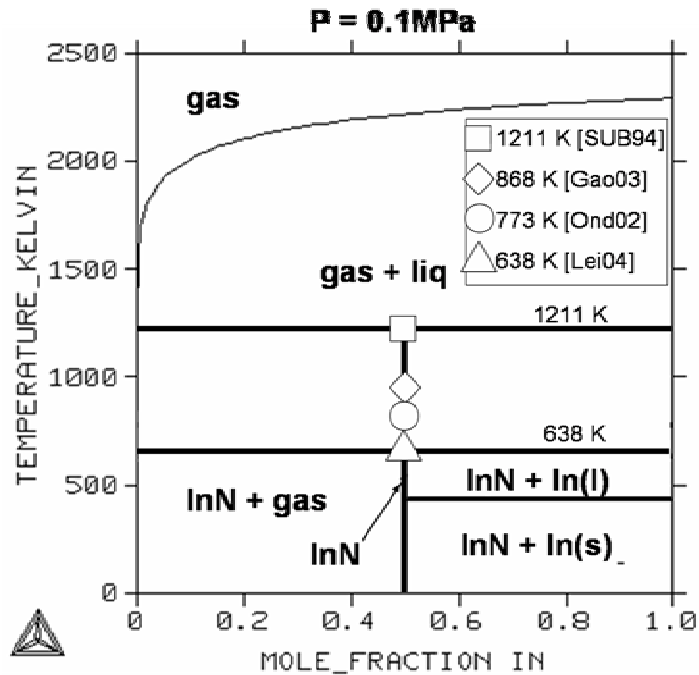


Figure 2-1. Phase diagram of In-N systems at $P = 0.1$ MPa and experimental InN decomposition data.

The decomposition temperatures of InN were measured as 638 K by drop calorimeter [Lei04], 773 K by thermogravimetric analysis (TGA) [Ond02], and 868 K by thermogravimetry-differential scanning calorimetry (TG-DSC) [Gao03]. The calculated decomposition temperature of InN is 1211 K using SUB94 database. In addition, the maximum experimental InN growth temperature is around 973 K (700 °C) according to Chapter 5 and 6 of InN growth study. Therefore, assessment of InN Gibbs energy is required for equilibrium calculations. At this point, the data from [Lei04] is used since it was critically assessed data with experiments. However, it should be noted that the decomposition temperature and growth temperature have a large overlap due to the kinetic barriers. When equilibrium calculation is needed including InN at the growth temperature, the Gibbs energy of InN should be lowered to consider kinetic barrier for

decomposition. In this case, the data from [SUB94] was used as presented in Section 2.3.2.4.

All the newly included species gave results consistent with previously known results for GaN, except for the ring-shaped trimer $(\text{GaN})_3(\text{g})$ species. Figure 2-2 shows the calculated ΔG values for $\text{Ga}(\text{l}) + 1/2 \text{N}_2(\text{g}) = \text{GaN}(\text{s})$ and $\text{Ga}(\text{l}) + 1/2 \text{N}_2(\text{g}) = 1/3(\text{GaN})_3(\text{g})$ reactions. The ΔG value for $(\text{GaN})_3(\text{g})$ formation reaction is significantly lower than GaN(s) formation reaction showing that $(\text{GaN})_3(\text{g})$ is more stable species than GaN(s). However, the existence of $(\text{GaN})_3(\text{g})$ was never confirmed by experiment and the thermochemical data was calculated using estimated parameters [Prz98]. Therefore, it would be reasonable to conclude that a kinetic barrier exists for formation of $(\text{GaN})_3$ or the data for $(\text{GaN})_3$ is incorrect. Ga-N phase diagram was generated excluding $(\text{GaN})_3(\text{g})$, as shown in Figure 2-3.

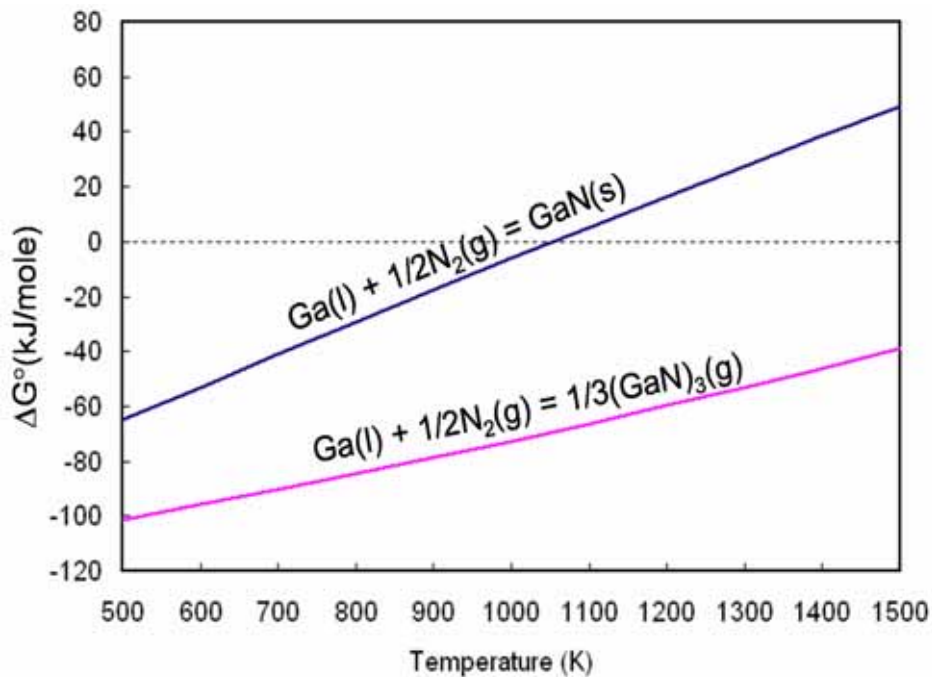


Figure 2-2. Calculated ΔG^{rxn} for GaN(s) and $(\text{GaN})_3(\text{g})$ formation reactions.

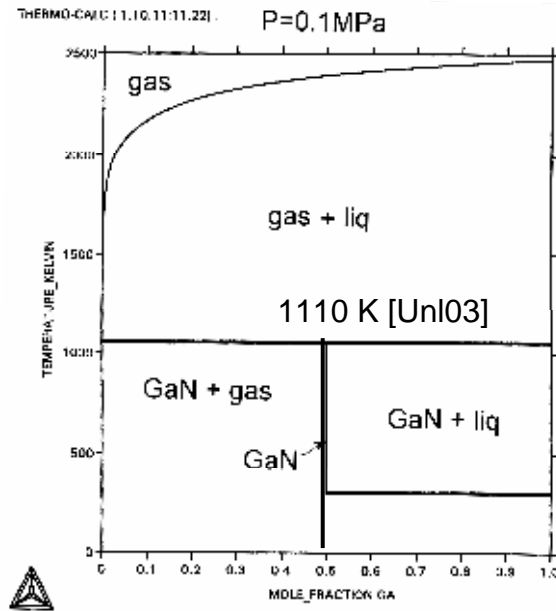


Figure 2-3. Phase diagram of Ga-N systems at $P = 0.1$ MPa. The data for GaN is from [Unl03]

Otherwise, all the new species including MOs and adducts from [Prz98] were added to the database and used for the subsequent equilibrium calculations.

2.3.2 Complex Chemical Equilibrium Calculations

2.3.2.1 Ga-C-H-Cl-Inert System

It will be informative to see the gas phase species after the reaction between TMG and HCl in N_2 carrier gas since no experimental results are available. Hence, the Ga-C-H-Cl-Inert (N_2) system was analyzed first. The schematic of the H-MOVPE inlet is shown in Figure 2-4.

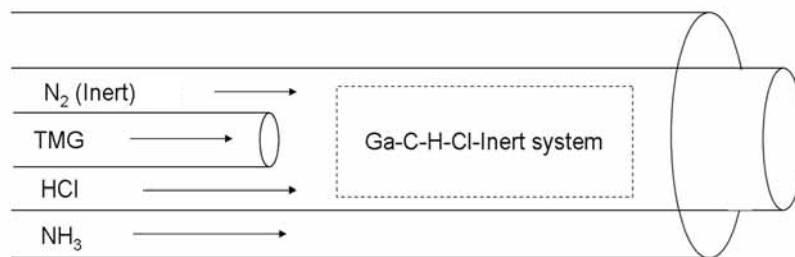


Figure 2-4. Schematic of the inlet of H-MOVPE technique for GaN growth.

TMG, HCl, and N₂ (inert) were mixed to form gas phase species before reacting with NH₃. Although NH₃ is present in the outer tube, it does not interact with TMG and HCl until a certain residence time, since they are separated by the quartz wall. Therefore, only the TMG + HCl + N₂ system will be only considered here.

The base conditions of molar flow rates in the source zone for GaN growth by H-MOVPE are listed in Table 2-3. It should be noted that the atomic ratios are not independent, since TMG is composed of 1 Ga, 3 C, and 9 H atoms; HCl is composed of 1 H and 1 Cl atom. Therefore, $X(C) = 3 \times X(Ga)$ and $X(H) = 9 \times X(Ga) + X(Cl)$ conditions must be satisfied.

Table 2-3. Base inlet conditions for sources for GaN growth and atomic mole fractions for calculation.

Precursors	Flow rate	Flow rate/0.7	Atom	# of Atoms	X(Atom)	Mole fraction
TMG	0.7 sccm	1	Ga	1	X(Ga)	0.00066
HCl	0.7 sccm	1	C	3	X(C)	0.00198
Inert (N ₂)	1050 sccm	1500	H	10	X(H)	0.00660
			Cl	1	X(Cl)	0.00066
			Inert	1500	X(Inert)	0.99010
			Total	1514	Total	1

N₂ as a product of NH₃ decomposition was treated as an active N source, which may react with a Ga species to form GaN in equilibrium calculations. For example, GaN(s) can be formed by Ga(l) and N₂(g) in equilibrium calculation. The source of reactive N is only NH₃ and its intermediate products. The carrier gas, N₂, was thus treated as an inert species, thus all N in the inlet NH₃ was available for reaction; including the product N₂.

Helium (He) was used instead of carrier N₂. The use of different inert gas such as Ne or Ar would give the same results since they are not participating in the reaction. The role of inert gas in equilibrium calculation is related to gas mixture entropy.

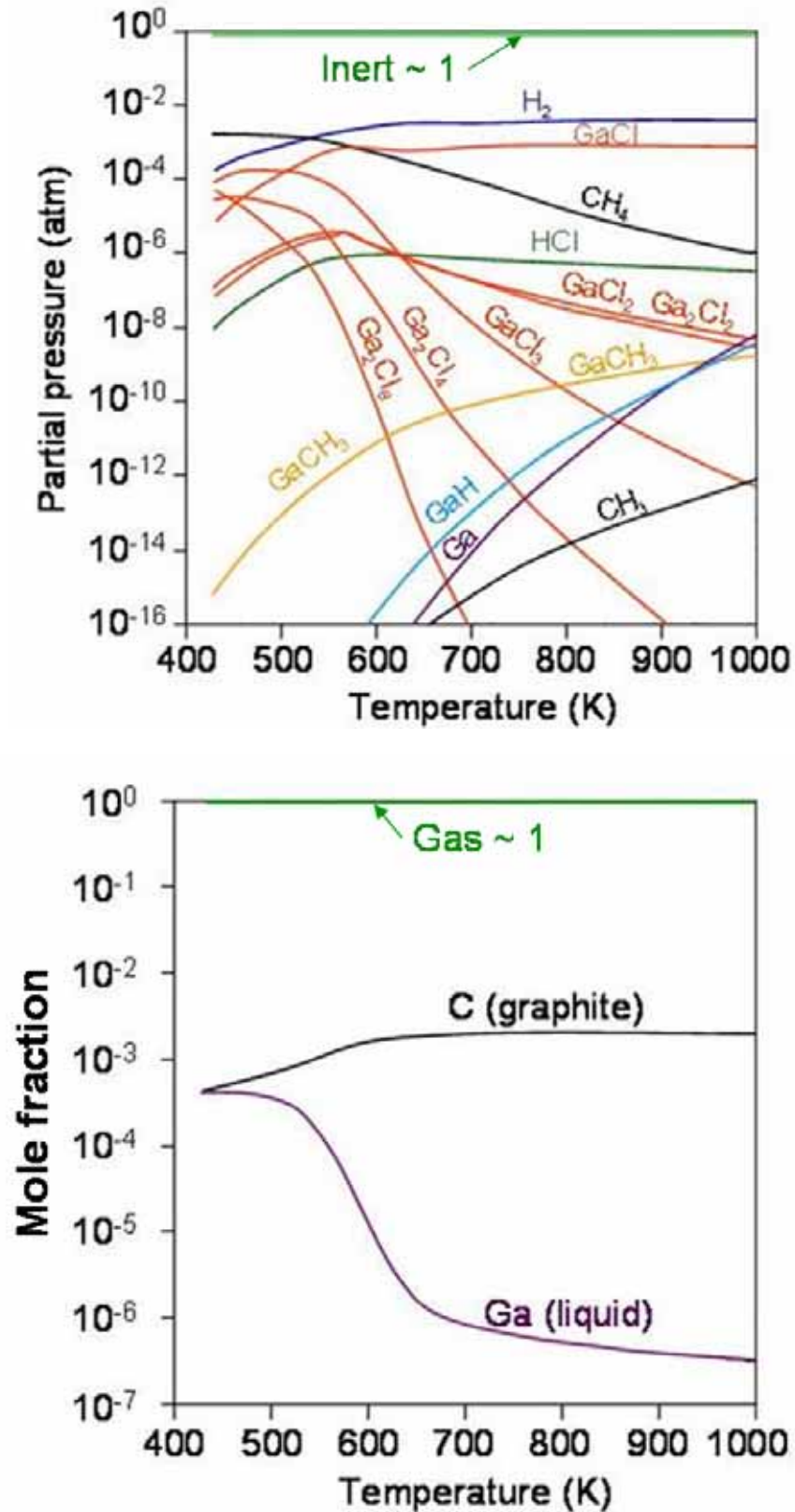


Figure 2-5. Equilibrium partial pressures of gas phase molecules and mole fractions of condensed phases with respect to the temperature in Ga-C-H-Cl-Inert system.

In addition, total pressure and system temperature values $P = 1$ atm and $T = 573$ K were used as the base conditions for calculations of the source zone performance.

Figure 2-5 shows the calculated equilibrium partial pressures of gas phase species in the Ga-C-H-Cl-Inert system, with respect to the temperature. In this figure Cl/Ga was set to 1 and the calculation axis was $T = 430$ to 1000 K.

The most predominant Ga containing gas species was GaCl above 530 K and GaCl₃ below this temperature. The amount of GaCl exceeded the amount of CH₄ at 580 K. The partial pressure of the second dominant species, GaCl₃, decreased at temperatures higher than 500 K. It was also observed that the amount of HCl gas increased up to 600 K and did not change at temperatures higher than 600 K. The partial pressure of monomethylgallium (MMG; GaCH₃), the most dominant organometallic species, increased with temperature. However, the amount of MMG was about 10^{-6} times less than GaCl even at 1000 K. Therefore, the effect of using TMG instead of liquid Ga as the Ga source is negligible, other than adding C to the system.

In this sense it is concluded that the H-MOVPE technique is closer to traditional HVPE rather than the MOCVD technique.

Two condensed phase were present at equilibrium; C (graphite) and Ga(l). Experimental observation of black deposition in H-MOVPE inlet confirmed that the black deposition is composed of C (graphite) hollow tubes filled with Ga [Par05]. To prevent black deposition, a small amount of H₂ should be added to N₂ carrier gas, which is consistent with Park's result [Par05]. Figure 2-6 shows the equilibrium partial pressures and condensed phase mole numbers with respect to $X(H)/\{X(\text{Inert})+X(H)\}$.

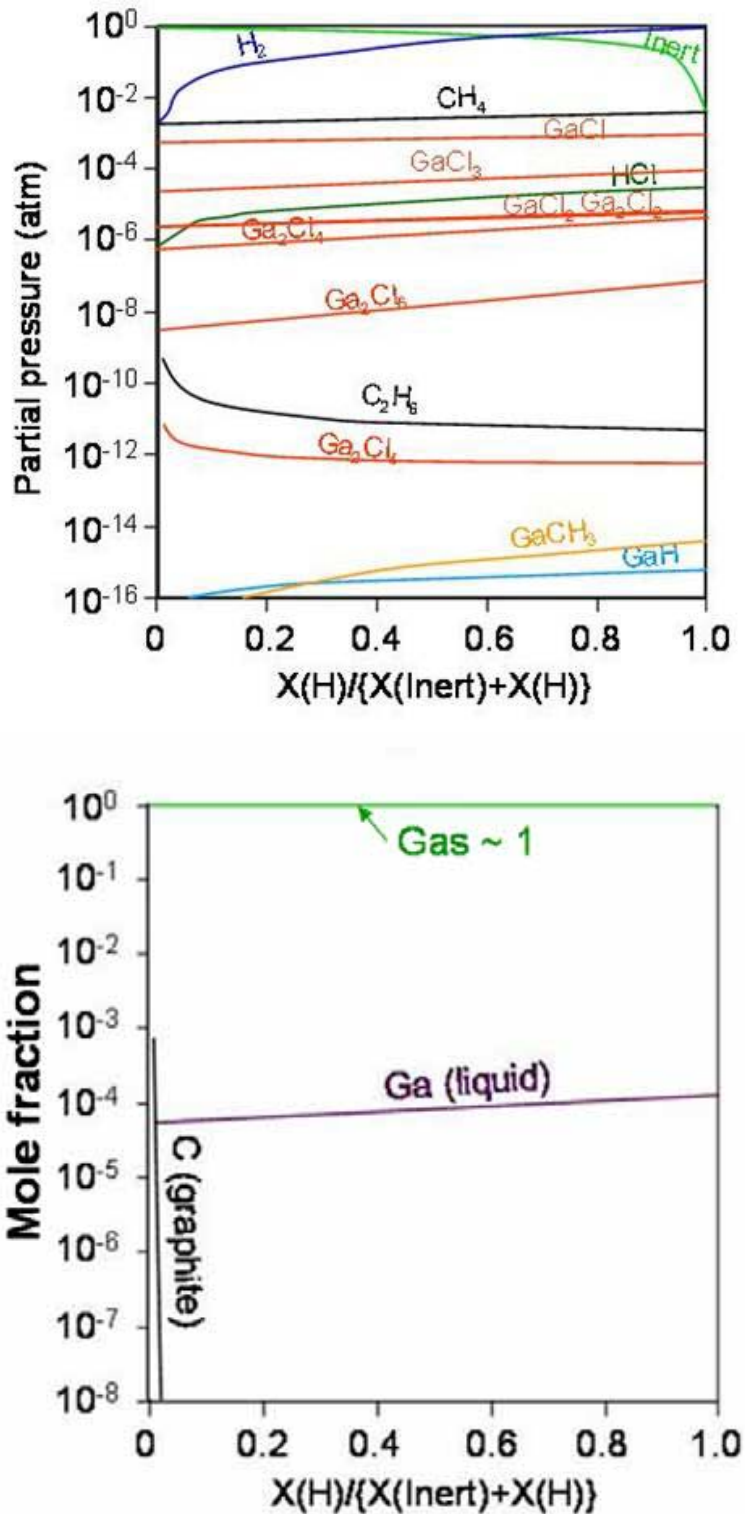


Figure 2-6. Equilibrium partial pressures of gas phase molecules and mole fractions of condensed phases with respect to $X(H)/\{X(\text{Inert}) + X(H)\}$ in Ga-C-H-Cl-Inert system at $P = 1$ atm, $T = 573$ K, $\text{Cl}/\text{Ga} = 1$.

For this calculation, T was set at 573 K and X(H) was varied from 0.0066 to 0.9901 (not 0 to 1) because H and inert gas are always present with NH₃ and HCl (10 % HCl and 90 % N₂ (Inert)). It was noted that the amount of C (graphite) decreased rapidly with increasing H₂, primarily through formation of CH₄. These thermodynamic calculation results agreed well with the experimental results from Park [Par05]. It is also noted that small amount of Ga(l) exists.

With increasing amount of H₂, the partial pressures of the gas phase species did not change significantly. It is also noted that the major species partial pressures showed a gradual increase with increasing H fraction.

It should be noted that the amount of GaCl₃ changed significantly with both temperature and Cl/Ga ratio, but not with H₂ since the partial pressure of GaCl or GaCl₃ exceeded that of HCl, the most dominant Ga or Cl containing species.

The equilibrium partial pressures of the gas phase molecules and condensed phase mole fractions with respect to Cl/Ga ratio are shown in Figure 2-7. The amount of GaCl and GaCl₃ crossed at around Cl/Ga = 2. Furthermore, the amount of HCl prevailed over GaCl₃ at Cl/Ga = 4. The experimental results from Reed [Ree02] showed that the growth rate remained nearly constant from Cl/Ga = 0 to 3, then declined rapidly, falling to zero at near HCl/Ga = 4. This also is reasonably matched with thermodynamic predictions. From the experimental observation of the growth rate, GaCl appeared to be the main precursor to grow GaN rather than GaCl₃. In the condensed phase, the amount of C (graphite) did not change with HCl. In fact, the only C and Cl containing gas phase species is CH₃Cl, which has very low partial pressure at Cl/Ga = 4.

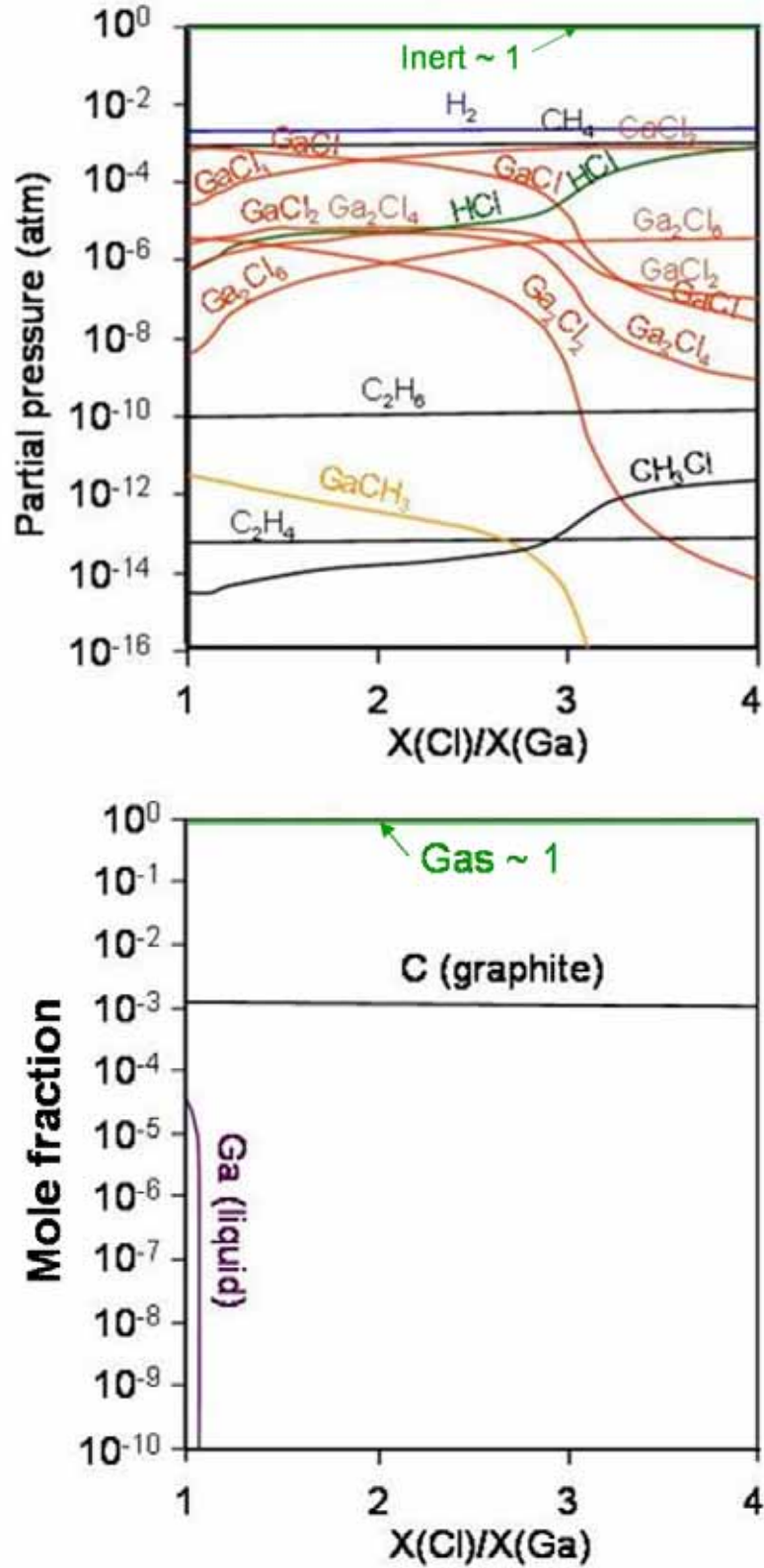


Figure 2-7. Equilibrium partial pressures of gas phase molecules and mole fractions of condensed phases with respect to $X(\text{Cl})/X(\text{Ga})$ ratio 1 to 4 in Ga-C-H-Cl-Inert system at $P = 10^5$ Pa, $T = 573$ K.

Therefore, to prevent C contamination, H_2 carrier gas or, at least, a mixture of H_2 gas is recommended. In addition, the amount of Ga (liquid) rapidly dropped with $Cl/Ga > 1$. According to these calculation results, small amounts of H_2 (~ 4 %) and excess HCl ($Cl/Ga > 1$) are required to grow Ga droplet-free and C-free GaN films.

2.3.2.2 Ga-C-H-Cl-N System

The growth of GaN by H-MOVPE in H_2 carrier gas can be considered as a Ga-C-H-Cl-N system, as shown in Figure 2-8. To calculate the growth conditions of GaN, the Gibbs energy of GaN should be modified, as GaN is thermodynamically unstable at typical growth temperature. For example, the calculated GaN decomposition temperature was 1055 K using the Gibbs energy of GaN recommended by Unland *et al.* [Unl03]. It was found that the decomposition temperature of GaN linearly increases with decreasing the Gibbs energy of GaN by Thermo-Calc calculations. Assuming that the decomposition temperature of GaN is 1500 K, 49 kJ/mole was subtracted from the Gibbs energy of GaN [Unl03].

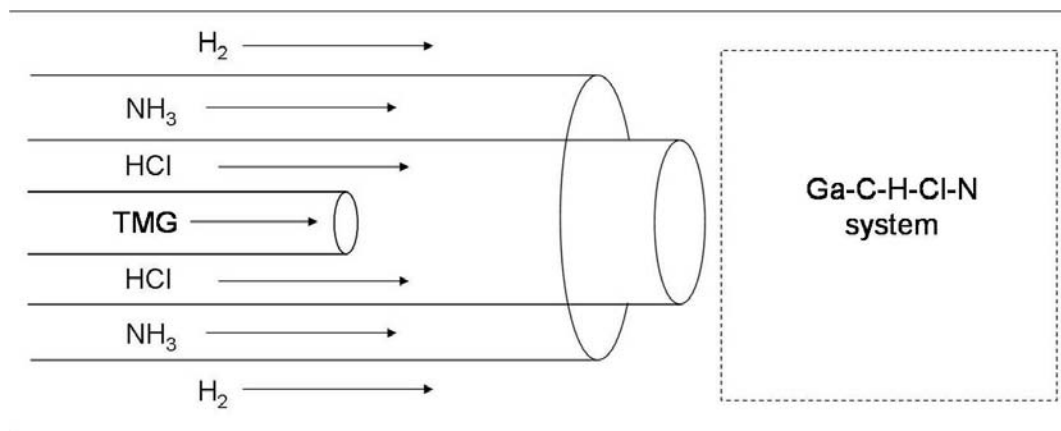


Figure 2-8. Schematic of H-MOVPE for GaN growth: Ga-C-H-Cl-N system. N is present and H_2 is used as a carrier gas in the system compared to Figure 2-4.

The experimental inlet conditions for GaN growth were from [Ree02], including TMG = 2.2 sccm, HCl = 4.4 sccm, NH_3 = 500 sccm, and H_2 = 1600 sccm. Therefore, the

Cl/Ga and N/Ga ratios were 2 and 230, respectively. Given an initial atomic mole fraction of Ga, $X(\text{Ga}) = 4.2 \times 10^{-4} = \text{base}$, the other elements' atomic mole fractions are calculated by $X(\text{C}) = 3 \times X(\text{Ga})$, $X(\text{Cl}) = 2 \times X(\text{Ga})$, $X(\text{N}) = 230 \times X(\text{Ga})$, and $X(\text{H}) = 1 - X(\text{Ga}) - X(\text{C}) - X(\text{Cl}) - X(\text{N})$. The growth-etch transition temperatures were thereafter calculated by changing Cl/Ga ratio from 0 to 10.

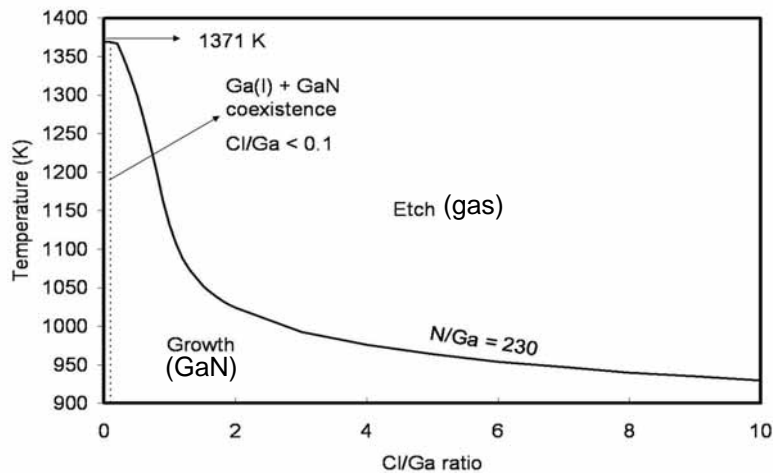


Figure 2-9. Calculated growth-etch transition temperature as a function of Cl/Ga ratio. N/Ga ratio was set at 230.

Figure 2-9 shows the calculated growth-etch transition temperature. It was observed that Ga(l) and GaN coexisted when $\text{Cl/Ga} < 0.1$ and that the upper growth temperature decreased with increasing Cl/Ga ratio. It is also noted that carbon appeared under certain conditions, but is not listed in this figure. The maximum growth-etch transition temperature was 1371 K at $\text{Cl/Ga} = 0$ in case of $\text{N/Ga} = 230$.

Further calculations were carried out to focus on the Ga(l) – GaN coexistence conditions by varying N/Ga ratio (200, 300, 400, 500, and 600) and Cl/Ga ratio (continuously from 0 to 0.5), as seen in Figure 2-10. The decomposition temperature increased from 1371 to 1395 K with increasing N/Ga ratio from 200 to 600, as the N partial pressure increased.

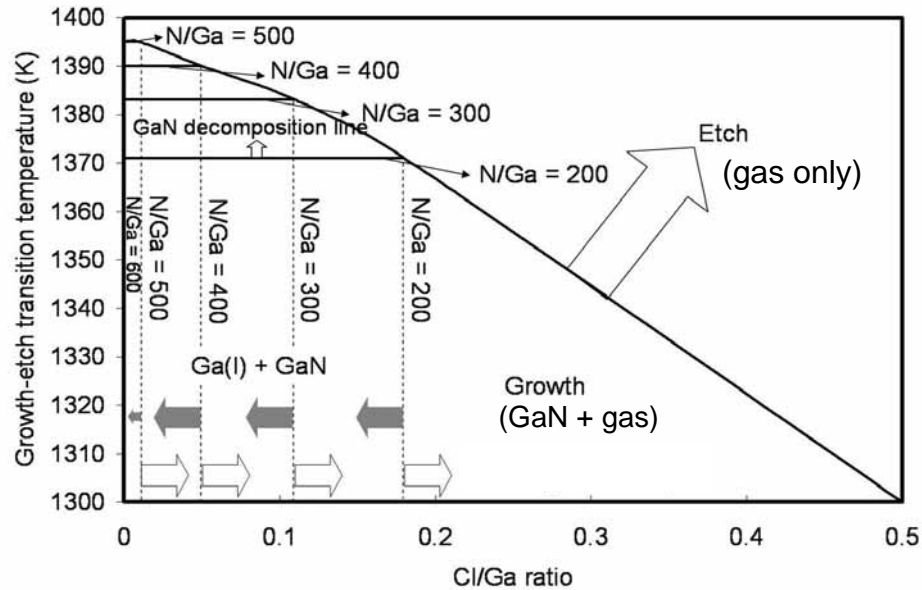


Figure 2-10. Calculated transition of growth-etch and Ga(l) formation as a function of temperature and Cl/Ga ratio. N/Ga ratio was varied from 200 to 600.

This is expected since adding excess N relative to Ga will form the more stable GaN. It was found that the Ga(l) + GaN coexistence regime becomes narrower with increasing N/Ga ratio and completely disappears at N/Ga = ~ 600. This is the N/Ga ratio thermodynamic limit to avoid Ga droplet in MOCVD (Cl/Ga = 0). Since the N/Ga ratio for GaN growth is typically much higher than 600 in MOCVD, Ga(l) was not usually observed. A more or less linearly decreasing trend of growth-etch transition temperature was observed when Cl/Ga was higher than 0.2 regardless of N/Ga ratio. As Cl is added to the system, it primarily appears as GaCl at the elevated temperature, thus making less available for formation of GaN.

2.3.2.3 In-C-H-Cl-Inert System

Similar calculations were performed to analyze the inlet of H-MOVPE for InN growth in inert ambient. Figure 2-11 shows the schematic of the inlet for InN growth. TMI first reacts with HCl in N₂ (inert) carrier gas before reacting with NH₃. Therefore the TMI + HCl + N₂ (inert), or the In-C-H-Cl-Inert (He) system was analyzed to

determine the equilibrium gas and condensed phase species. The base flow rates of TMI, HCl, and N₂ were 0.7 sccm, 0.7 sccm, and 1050 sccm (6.3 sccm with 10% HCl + 200 sccm diluted with HCl + 269 sccm with TMI + 200 sccm diluted with TMI + 375 sccm carrier = 1050 sccm), respectively. Therefore, Cl/In = 1, Inert/In = 1500, P = 1 atm, and T = 573 K were used as the base conditions for calculation. It should be noted that C/In ratio is always 3, because TMI is composed of 1 In, 3 C, and 9 H. The number of H atoms is coupled with 9 TMI and 1 HCl. In other words, the relationship $X(C) = 3 \times X(In)$ and $X(H) = 9 \times X(In) + X(Cl)$ should be always satisfied. The initial atomic mole fractions for In-C-H-Cl-Inert system are tabulated in Table 2-4.

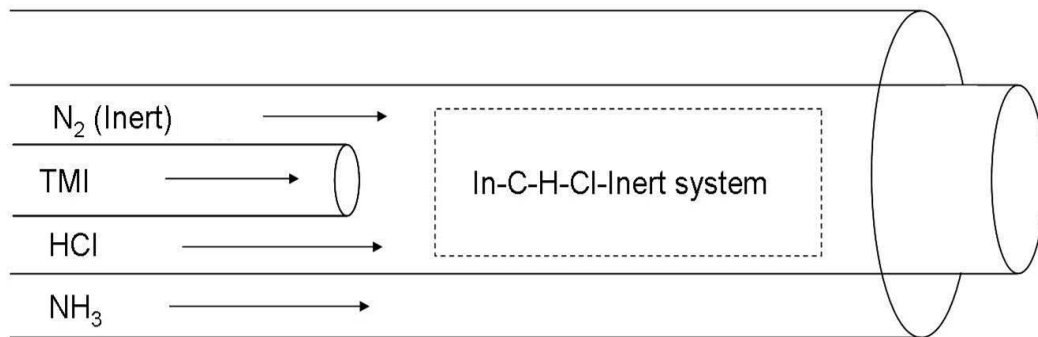


Figure 2-11. Schematic of the inlet of H-MOVPE technique for InN growth.

Table 2-4. Typical growth conditions for InN and atomic mole fractions for calculation.

Precursors	Flow rate	Flow rate/0.7	Atom	# of Atoms	X(Atom)	Mole fraction
TMI	0.7 sccm	1	In	1	X(In)	0.00066
HCl	0.7 sccm	1	C	3	X(C)	0.00198
Inert (N ₂)	1050 sccm	1500	H	10	X(H)	0.00660
			Cl	1	X(Cl)	0.00066
			Inert	1500	X(Inert)	0.99010
			Total	1514	Total	1

Figure 2-12 shows the equilibrium partial pressures and condensed phase mole numbers with respect to temperature at Cl/In = 1. The calculation axis was T = 430 to 1000 K.

The most predominant In containing species was InCl. However, the second dominant In containing species was not InCl₃, as compared to the second most abundant gas species in the Ga based system, GaCl₃. Instead of InCl₃, In₂Cl₂ (the dimer of InCl) had higher partial pressure (10⁵ times higher than InCl₃) at T = 480 to 700 K. The partial pressure of InCl₃ decreased at temperatures higher than 480 K. Although TMI and MMI thermochemical data were included during the calculation, they were not observed in the results. The lowest limit of partial pressure calculation was set as 10⁻¹⁷ atm, thus it can be inferred that TMI and MMI have less than 10⁻¹⁷ atm partial pressure. As a result, it can be concluded that H-MOVPE is closer to HVPE than MOCVD in both InN and GaN growth cases.

For condensed phases, carbon (graphite) and In (liquid) were dominant and the amount of In(l) decreased with temperature. Deposition of a black material in the inlet was occasionally observed during the growth of InN especially when the inlet temperature was too high. Even though a detailed analysis of this black material at the inlet during InN growth was not carried out, it likely consists of C (graphite) and In droplets. To avoid C and In contaminations, similar methods can be used such as addition of H₂ and excess HCl for C and In elimination, respectively.

The effect of H₂ carrier gas was analyzed by increasing the initial atomic H mole fractions. Figure 2-13 shows the equilibrium partial pressures and the amount of condensed phase species with respect to the relative amount of H compared with inert gas, or $X(\text{H})/\{X(\text{H}) + X(\text{inert})\}$. Comparing Figures 2-13 and 2-5 it is noted that the amount of Ga(l) is about an order of magnitude greater than that of In(l) at similar conditions.

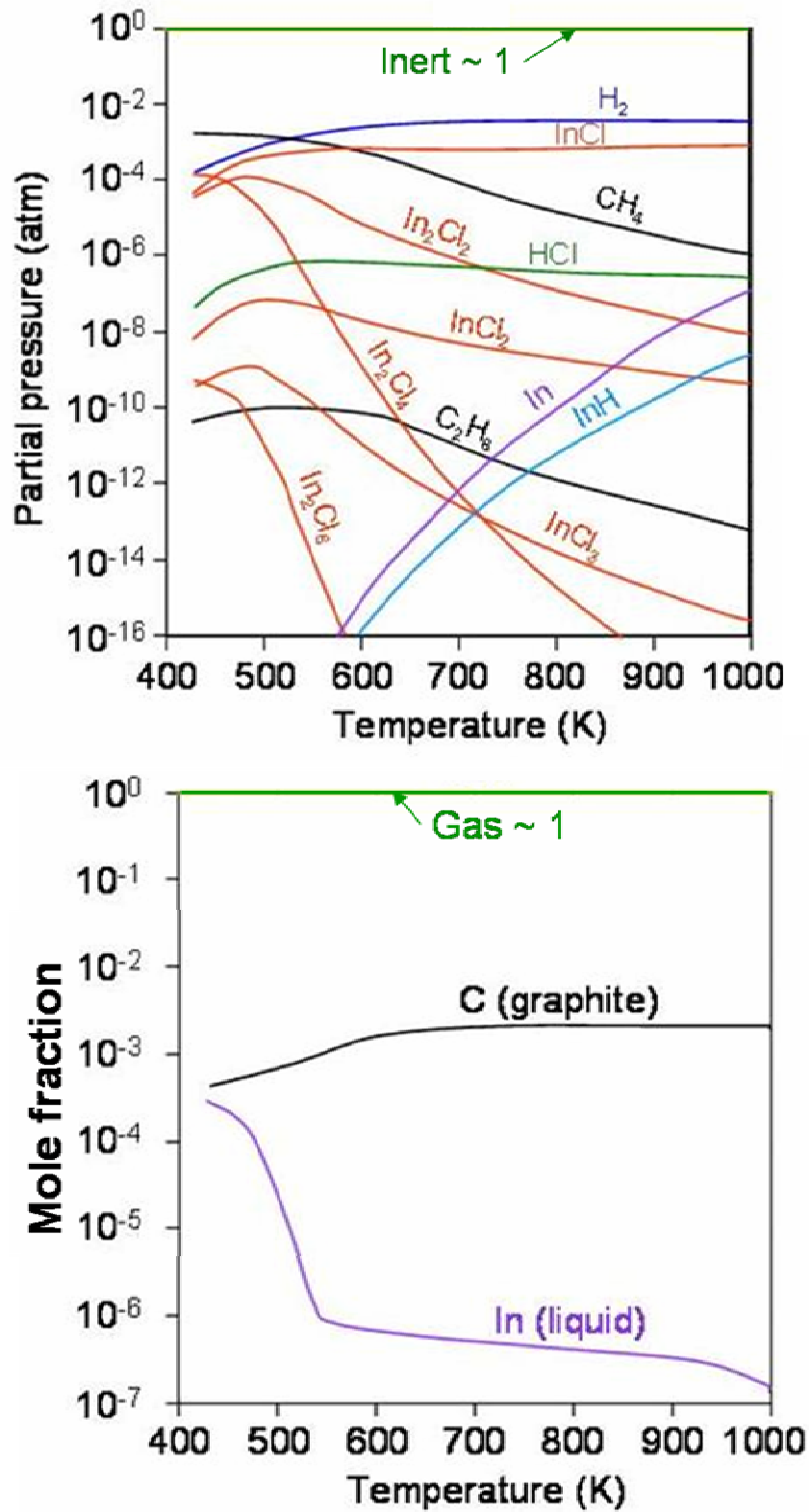


Figure 2-12. Equilibrium partial pressures of gas phase molecules and mole fractions of condensed phases with respect to the temperature in In-C-H-Cl-Inert system.

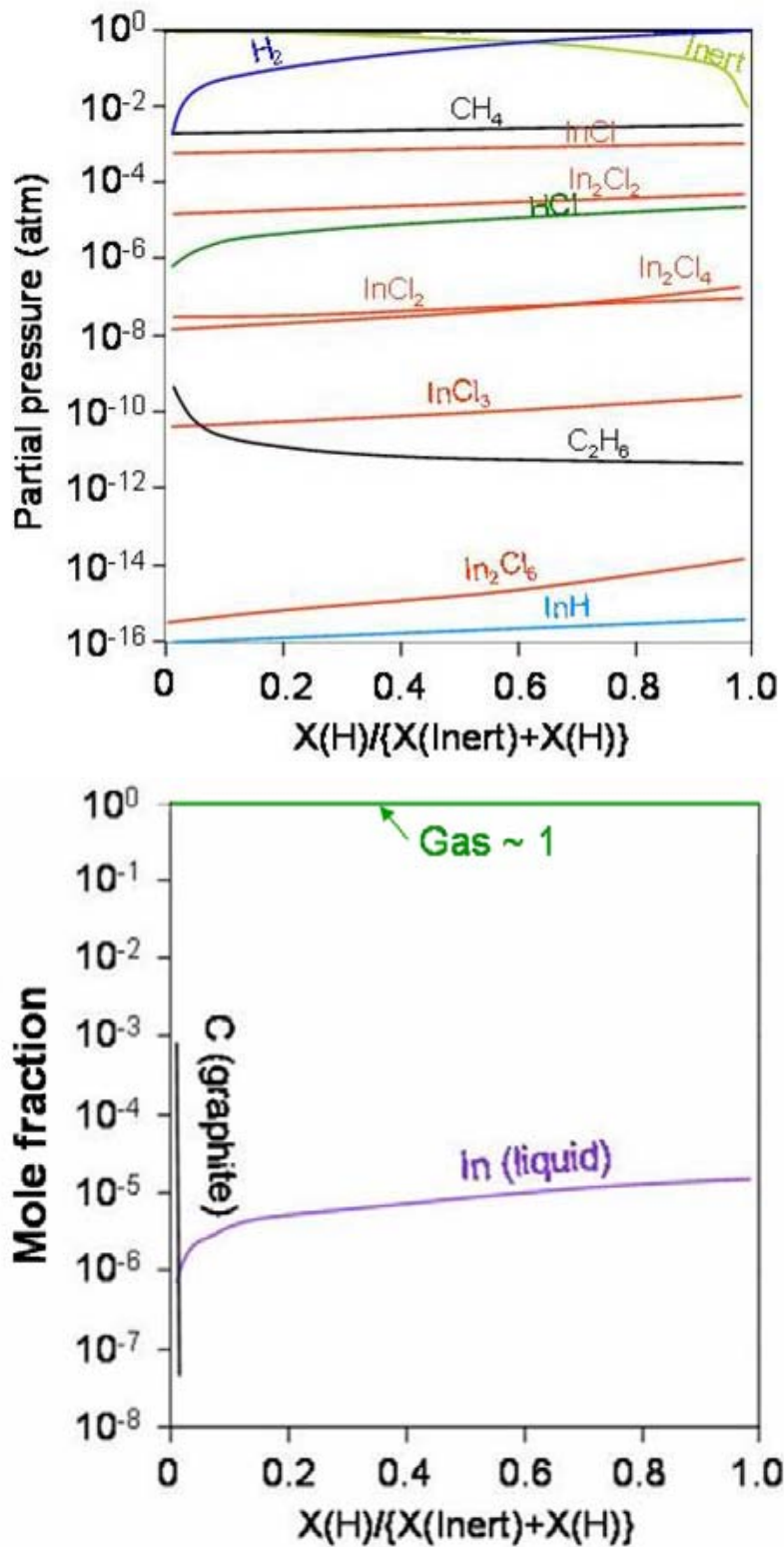


Figure 2-13. Equilibrium partial pressures of gas phase molecules and mole fractions of condensed phases with respect to $X(H)/\{X(\text{Inert}) + X(H)\}$ in In-C-H-Cl-Inert system.

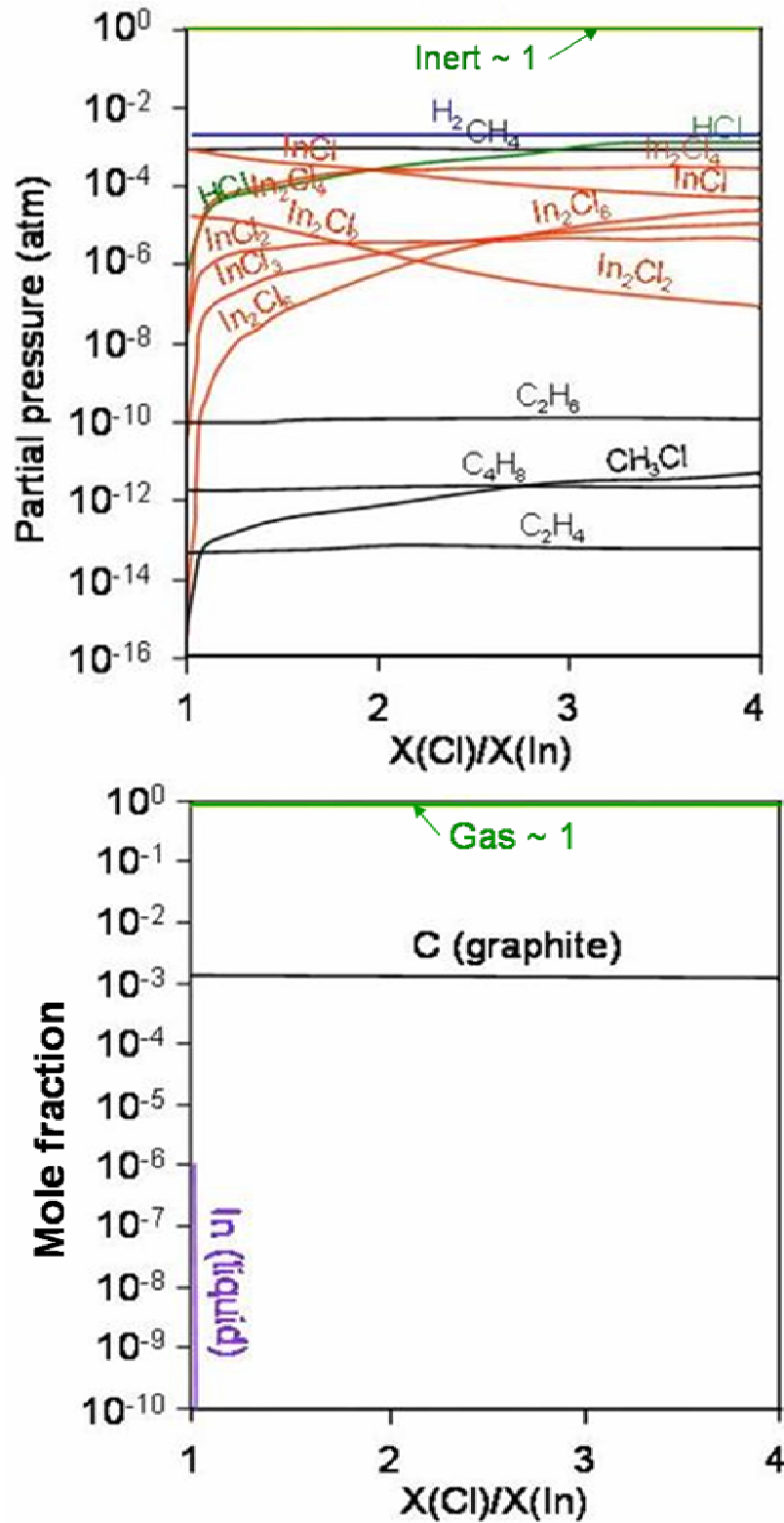


Figure 2-14. Equilibrium partial pressures of gas phase molecules and mole fractions of condensed phases with respect to $X(\text{Cl})/X(\text{In})$ ratio 1 to 4 in In-C-H-Cl-Inert system.

The gas phase species did not change greatly, except for H₂ and other inert gases. An increase of InH was observed; however, the amount of InH was extremely small (10^{-15} atm), thus the role of InH was negligible.

Figure 2-13 shows the equilibrium partial pressures and the amount of condensed phase species with respect to the relative amount of H compared with inert gas, or $X(\text{H})/\{X(\text{H}) + X(\text{inert})\}$. Comparing Figures 2-13 and 2-6 it is noted that the amount of Ga(l) is about an order of magnitude greater than that of In(l) at similar conditions. The gas phase species did not change greatly, except for H₂ and other inert gases. An increase of InH was observed; however, the amount of InH was extremely small (10^{-15} atm), thus the role of InH was negligible.

One of the advantages of H-MOVPE technique is the variation of Cl/In ratio. Therefore, it is interesting to see the effect of Cl/In ratio. The Cl/In ratio was varied from 1 to 4 and the results are shown in Figure 2-14. The predominant In containing species were InCl and In₂Cl₄ (dimer of InCl₂) through Cl/In = 1 to 4 and the amount of HCl, InCl, and In₂Cl₄ reversed at Cl/In > 2. Therefore, an etching effect is expected due to the HCl when Cl/In > 2. The amount of In(l) drops rapidly near Cl/In = 1, and no In(l) exists at Cl/In > 1 and the amount of C (graphite) did not change with Cl/In ratio. To eliminate C contamination, H₂ should be added in the system.

2.3.2.4 In-C-H-Cl-N-Inert System

Thermodynamic calculations were carried out to understand the gas phase and condensed phase species for InN growth by H-MOVPE. Figure 2-15 shows the schematic of the H-MOVPE system using TMI, HCl, NH₃, and N₂ (inert) as precursors. This can be thought as an In-C-H-Cl-N-Inert system. It will be informative to see the

InN growth-etch conditions with change in temperature, Cl/In, and N/In molar ratios since they are the most important growth parameters.

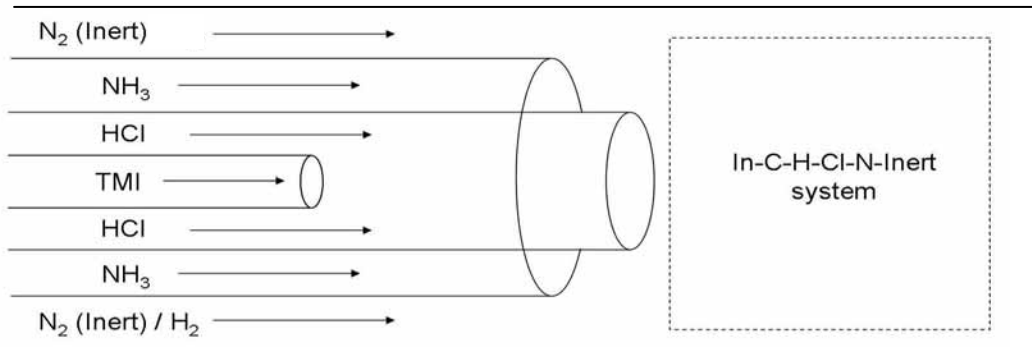


Figure 2-15. Schematic of H-MOVPE inlet with In-C-H-Cl-N-Inert system for thermodynamic calculations. N is present in the system compared to Figure 2-11.

In the equilibrium growth-etch regime calculation, the thermochemical data for solid InN was taken from SUB94 database instead of using the data from [Lei04], since the decomposition temperature of InN (686 K) from [Lei04] is too low for InN. Therefore, InN is thermodynamically more unstable at growth temperature with expressions proposed by [Lei04] as compared to that from the SUB94 database. This is equivalent to lowering the Gibbs energy by about 68.5 kJ/mole.

The initial process parameters for InN growth used in this calculation were $T_{MIn} = 1$ sccm, $HCl = 4$ sccm, $NH_3 = 250$ sccm, and $Inert = 2286$ sccm. Actual process parameters were about 0.7 times less than the given values, for example $T_{MIn} = 0.7$ sccm. However, they were increased by 1/0.7 times for ease of calculation. Therefore, the initial atomic mole fractions were $X(In) = 3.024 \times 10^{-4}$, $X(C) = 3 \times X(In)$, $X(Cl) = 4 \times X(In)$, $X(N) = 250 \times X(In)$, $X(H) = 9 \times X(In) + X(Cl) + 3 \times X(N)$, and $X(Inert) = 1 - X(In) - X(C) - X(Cl) - X(N) - X(H)$. To carry out the calculation Cl/In and N/In ratios were varied and the growth-etch transition temperatures were determined.

As shown in Figure 2-16, the growth-etch transition temperature decreased with increasing Cl/In ratio. When Cl/In ratio > 1 , the added HCl to the system shifts the equilibrium compositions of InCl_x in the vapor phase, and thus it lowered the transition

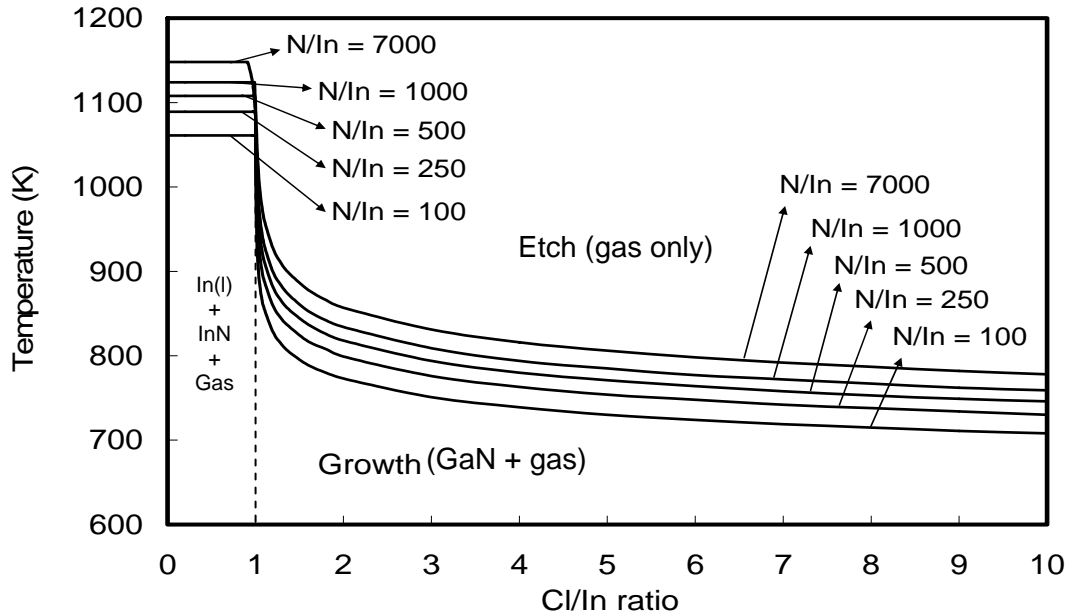


Figure 2-16. Calculated growth and etch regime with respect to temperature and Cl/In ratio. N/In ratio was varied from 100 to 7000.

temperature. As the Cl/In ratio decreases towards unity, the Cl is now not in large excess but approaches the stoichiometry of the dominant vapor phase In species, InCl . Thus a small decrease in the Cl/In ratio frees a relatively higher proportion of the In for participation in growth. For Cl/In ratio less than unity, there is not sufficient Cl to retain the In in the vapor phase and In is now available to form InN . The temperature of the horizontal line for a given N/In ratio is the thermal decomposition temperature, which increases with increasing N/In as expected. In(l) was observed as a product of thermal decomposition reaction below the horizontal lines.

The companion plots of transition temperature vs. N/In atomic ratio are shown in Figure 2-17. The results suggest that the transition temperature increased with increasing

N/In ratio to an asymptotic limit. It is noted that the calculations were only performed for seven HCl/TMIn ratios, each greater than unity. Increasing the N at constant HCl and TMIn input increases the ability of N to compete with Cl for the In. Increasing the N through the addition of NH_3 also increased the H in the system, which also competes with In for the Cl to increase the driving force for InN formation.

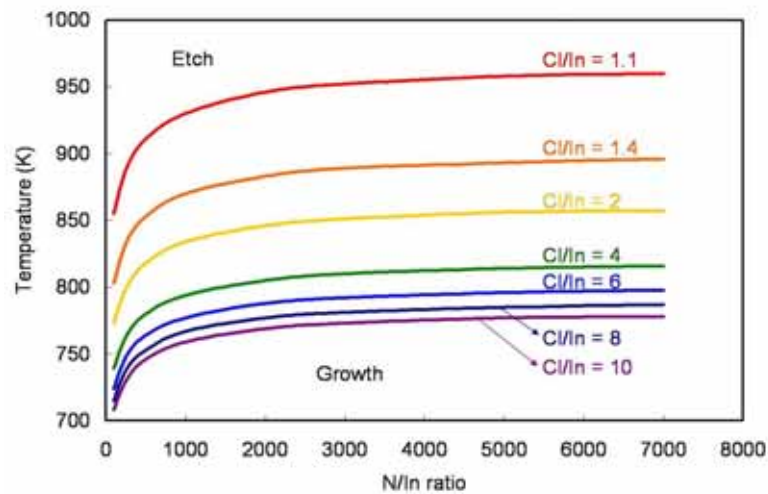


Figure 2-17. Calculated growth and etch regime with respect to temperature and Cl/In ratio. Cl/In ratio was varied from 1.1 to 10.

Figure 2-18 (a) shows the expanded views of the near horizontal lines at high N/In ratios: 4.0×10^4 to 7.0×10^4 . It was observed that both Cl/In and N/In ratios affect In droplet formation significantly. When N/In ratio was 4.0×10^4 , Cl/In ratio should be higher than 0.4 to avoid In droplet formation. When N/In ratio was increased to 5.0×10^4 , the minimum Cl/In ratio to avoid In droplet formation was decreased to 0.3, and so on. Figure 2-18 (b) shows the extended calculation results that include N/In ratio from 100 to 7.8×10^4 and Cl/In ratio from 0 to 1. Higher N/In ratio lowered the minimum Cl/In ratio to avoid In droplet formation, which is consistent with the previous results. It was noted that at N/In ratio $\sim 7.8 \times 10^4$, no In droplet existed, even though no HCl was present (Cl/In ratio 0).

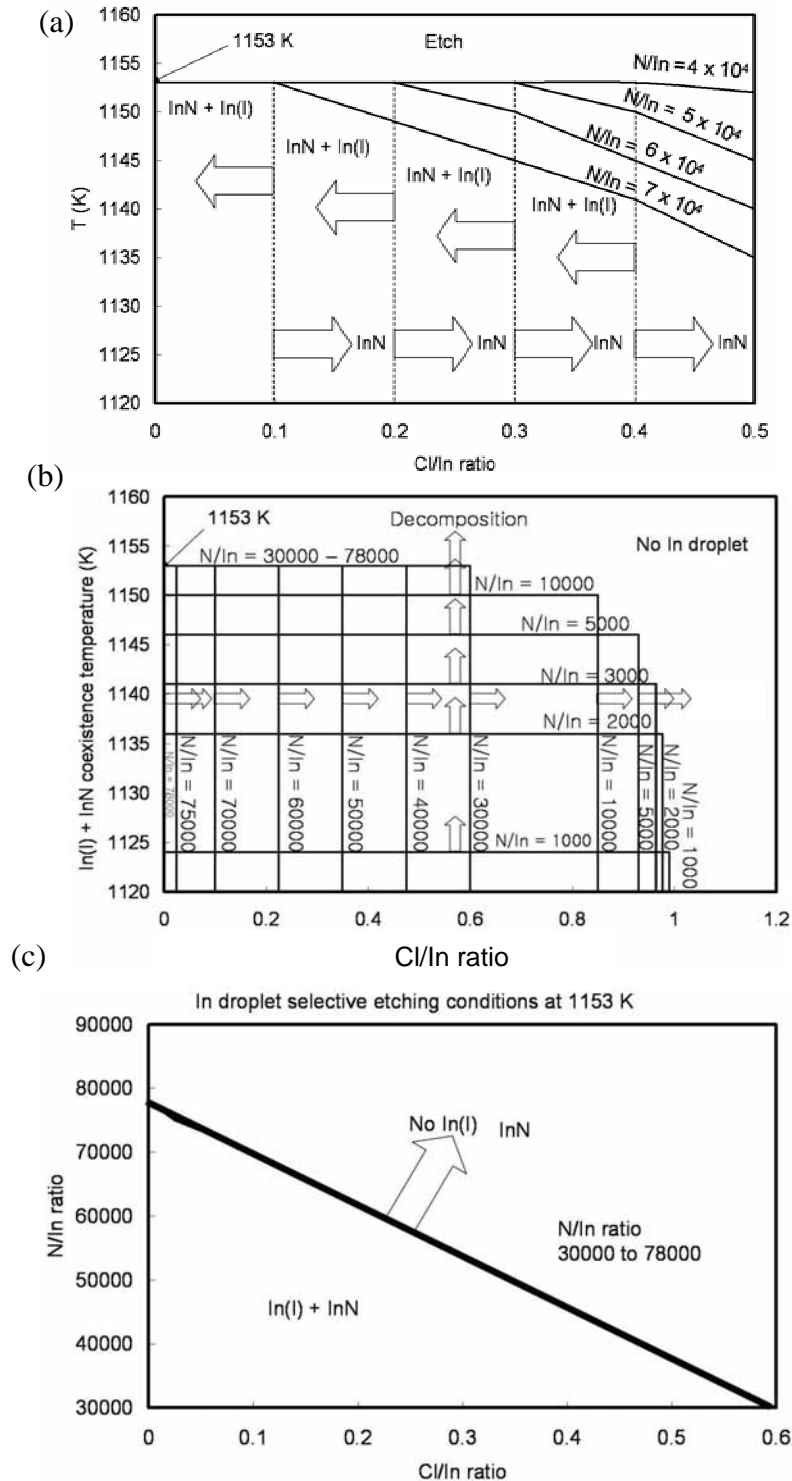


Figure 2-18. Calculated results of the growth, no growth (etch), and In droplet regimes
 (a) $Cl/In = 0$ to 0.5 , $N/In = 4.0 \times 10^4$ to 7.0×10^4 , (b) $Cl/In = 0$ to 1 , $N/In = 1.0 \times 10^3$ to 7.8×10^4 , and (c) In droplet etching conditions at $T = 1153$ K, $P = 10^5$ Pa.

Therefore, In droplet formation can be avoided when the N/In ratio is higher than 7.8×10^4 . Experimental results of InN growth by MOCVD showed that In droplets formed when the NH_3/TMIIn ratio was less than 1.6×10^4 [Mat97].

Although In droplets were not observed when N/In ratio was higher than 1.6×10^4 , the rough surface may be related to In droplet formation. The surface of InN was mirror-like when N/In ratio was higher than 8.0×10^4 , which may represent the complete removal of In droplets during growth [Mat97].

The decomposition temperature of InN did not change while the N/In ratio changed from 3.0×10^4 to 7.8×10^4 ; however, the minimum Cl/In ratio to avoid In droplets decreased at higher N/In ratio. These results are shown in Figure 2-18(c). It is clear that In droplet formation can be avoided by either increasing N/In ratio or increasing Cl/In ratio. Both of these changes provide reactant for In(l) (N to form InN or Cl to form InCl(g)). A key finding is that the determination of the minimum N/In ratio, 7.8×10^4 , to avoid In droplet formation by the MOCVD technique (Cl/In ratio = 0).

In the following, the decomposition temperature change was examined when the N/In ratio was higher than 7.8×10^4 . Figure 2-19 (a) shows the result when the Cl/In ratio was 0. Notice that the N/In ratio axis is a logarithmic scale. The transition temperature decreased with increasing N/In ratio, as long as $\text{N/In} > 7.8 \times 10^4$. The reason for this phenomenon is related to the gas phase species, InH. The partial pressures of InH (P_{InH}), in fact, decreased with increasing N/In ratio. For example, P_{InH} were 7.975×10^{-7} , 9.456×10^{-8} , and 1.125×10^{-8} atm for N/In ratio 10^5 , 10^6 , and 10^7 , respectively. This is expected since the initial atomic mole fraction of In, $X(\text{In})$, was reduced to increase the N/In ratio. The initial $X(\text{In})$ values were 2.486×10^{-6} , 2.499×10^{-7} , and 2.5×10^{-8} for

N/In ratio 10^5 , 10^6 , and 10^7 , respectively. Therefore, the ratios of P_{InH} to $X(\text{In})$ were taken to compare reasonable with the relative effect of InH. $P_{\text{InH}}/X(\text{In})$ ratios were 0.321, 0.378, and 0.450 atm for N/In ratio 10^5 , 10^6 , and 10^7 , respectively. Thus, it can be concluded that the relative amount of InH increased with increasing N/In ratio.

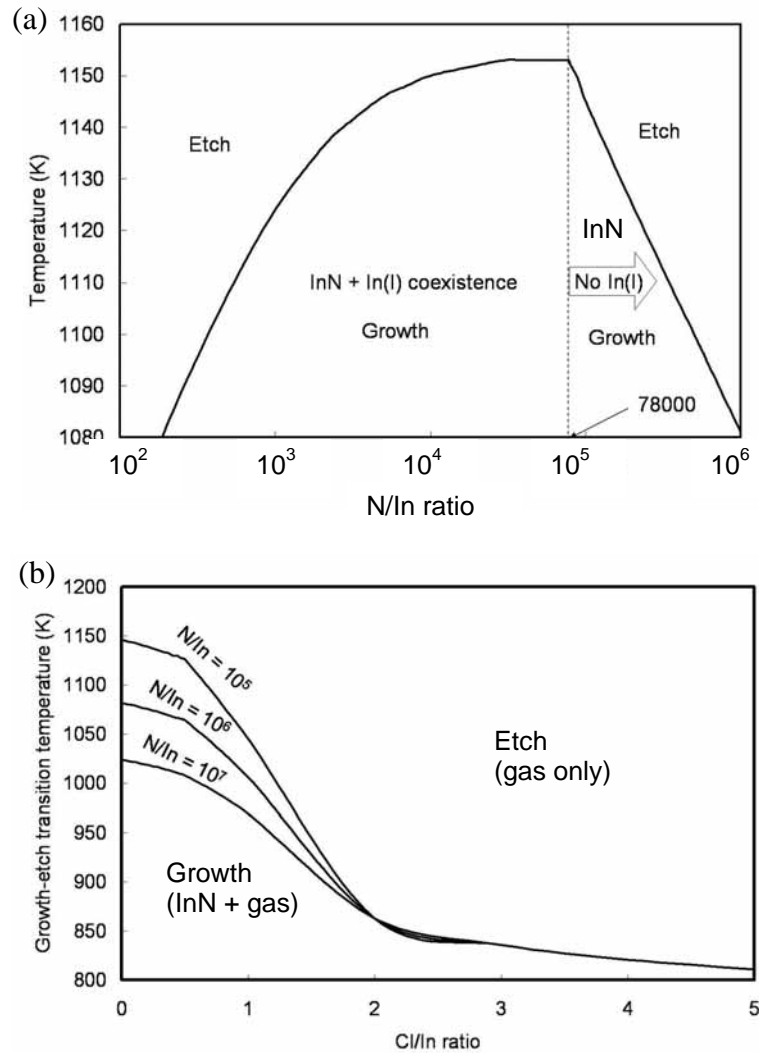


Figure 2-19. Calculated growth-etch transition temperatures (a) In droplet etch conditions when no HCl was present (b) growth-etch transition temperature at high N/In ratios: 10^5 , 10^6 , and 10^7 .

It is also observed from Figure 2-19 (a) that the growth transition temperature lowered with increasing N/In ratio. Thus the maximum growth temperature is lower for very high N/In ratio. It is known that the growth rate of InN decreases with excess NH_3

flow. The results of this calculation may explain the reason of growth rate decrease thermodynamically.

Figure 2-19 (b) shows the calculated growth-etch transition temperatures at three high values of N/In ratio (10^5 , 10^6 , and 10^7). No In droplet was observed in this excessively high N/In ratio due to the InH formation. The transition from growth to etch occurs at a lower temperature; the higher the value of N/In as long as $Cl/In < 2$. For high Cl/In , the excess Cl ties up the In or InCl to minimize the effect of increased N/In.

2.3.2.5 NH_3 Partial Decomposition

Ammonia is the most widely used nitrogen precursor for Group III – Nitride growth. Homogeneous decomposition of NH_3 to N_2 and H_2 is thermodynamically favored and it completes at around 673 K as shown in Figure 2-20.

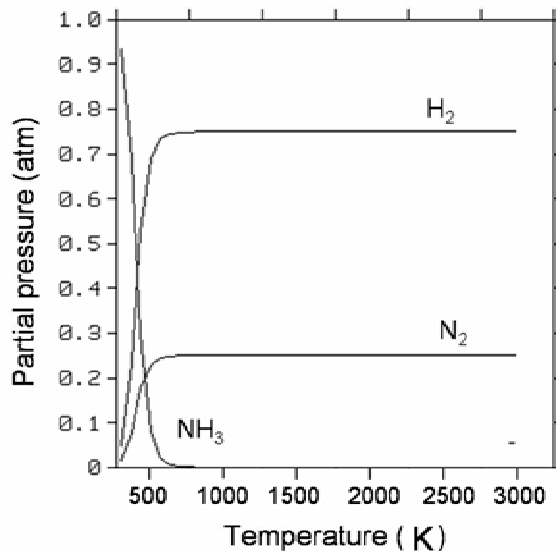
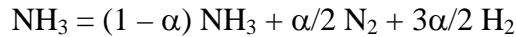


Figure 2-20. Equilibrium partial pressures for decomposition of NH_3 at 1 atm total pressures calculated by Thermo-Calc.

It is known, however, that homogeneous decomposition of NH_3 does not occur easily due to the very high kinetic barrier to break the initial N-H bonds [Seg04, Yum81,

Liu78]. One approach to account this fact in equilibrium calculations is to measure the Gibbs energy of NH_3 to shift the yield curve to high temperatures.

The homogeneous partial decomposition of NH_3 can be written as following.



where α is the degree of completion of NH_3 decomposition reaction.

It was experimentally observed that NH_3 decomposes to an extent $\sim 3\%$ at 950°C as measured by mass spectroscopy [Ban72]. To achieve this conversion at the temperature at 950°C , 170 kJ/mole has to be subtracted from the NH_3 Gibbs energy.

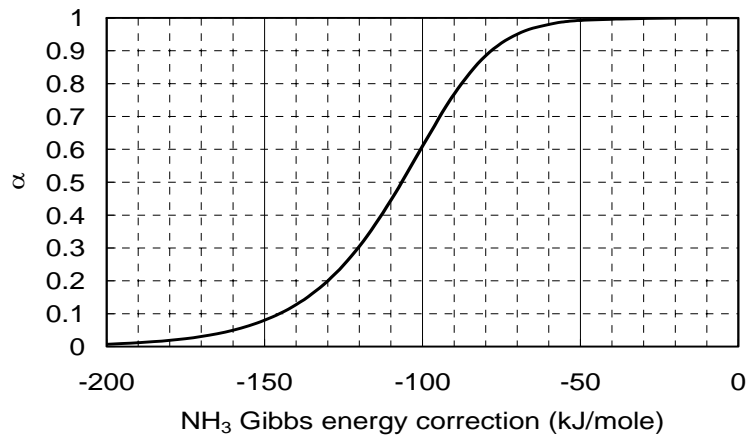


Figure 2-21. Magnitude of the Gibbs energy correction required to achieve a value for partial decomposition (α) at 950°C .

This energy may be considered as the kinetic barrier of NH_3 decomposition to make NH_3 decompose 3% at 950°C . A desired α value at 950°C can be achieved by modifying the Gibbs energy of NH_3 by subtracting various amounts as shown in Figure 2-21. A different value of α at 950°C can be assumed that will give a different value by which to modify the Gibbs energy of NH_3 . The calculated values for the decomposition curves as a function of T are shown in Figure 2-22. The α given in this figure represents the value of the conversion along this curve at 950°C .

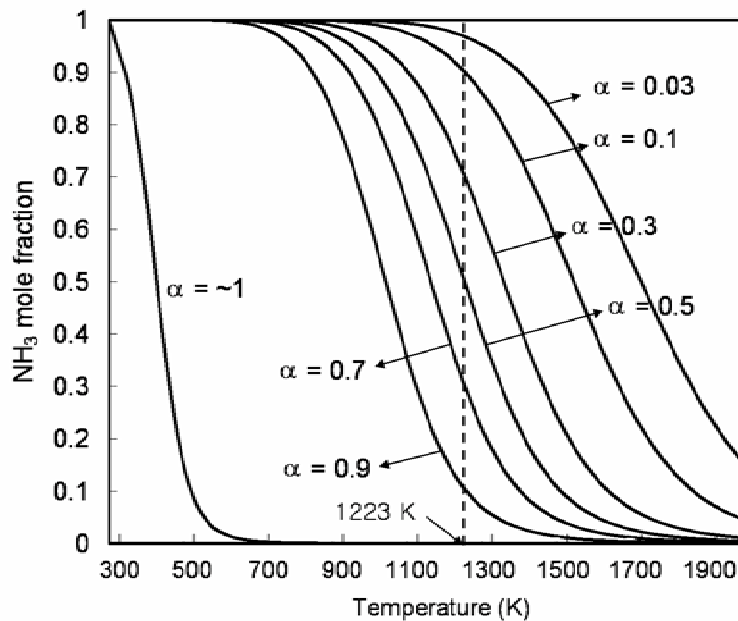


Figure 2-22. NH₃ mole fraction with respect to temperature at different values of α .

2.4 Conclusions

Additional thermochemical data for the Ga-In-H-C-Cl-N system including MOs and adducts were added to the current database [Ree02] and validated. Complex equilibrium calculations were performed and concluded that H-MOVPE is more related to HVPE than MOCVD.

It was concluded that H₂ should be included to eliminate C deposition in the inlet by thermodynamic analysis and experimental observations. In addition, excess HCl (Cl/III > 1) should be present in the system to eliminate Ga or In metal droplets in the inlet.

It was determined that monochlorides (*i.e.*, GaCl and InCl) are predominant species at Cl/III < 2. Excess Cl/III calculations showed that GaCl₃ is predominant when Cl/Ga > 2, whereas HCl prevailed over InCl and In₂Cl₂ at Cl/In > 2 at 573 K. However, monochlorides were always dominant at growth condition for both GaN and InN.

High N/III, low Cl/III, and low temperature generally provide more stable conditions for III nitrides, except for the excessive N/III case. The decomposition temperature of GaN and InN increased with high N/III ratios. Ga(l) + GaN and In(l) + InN coexistence regimes were observed under the low Cl/III ratio conditions. It was determined that for Ga(l) removal in MOCVD ($Cl/Ga = 0$), the N/Ga ratio should exceed 600, whereas for In(l) removal in MOCVD ($Cl/In = 0$), the N/In ratio should be higher than 7.8×10^4 . The results may explain the excessive ammonia flow requirement for InN growth to avoid In droplet formation.

Finally the partial decomposition of NH_3 was considered and the Gibbs energy of NH_3 was reduced to control decomposition efficiency. The kinetic barrier of NH_3 decomposition (170 kJ/mole) was calculated by considering 3 % of NH_3 decomposition at 950 °C.

CHAPTER 3
STRESS DETERMINATION STUDIES OF GALLIUM NITRIDE FILM ON
SAPPHIRE

3.1 Introduction

Due to the lack of bulk single crystals, GaN films are usually grown on foreign substrates, such as sapphire or SiC. Stress and dislocations are inevitable because of lattice and thermal expansion mismatches between GaN and foreign substrates. Excess stress may cause cracks and bows of the GaN films and dislocations may act as carrier traps resulting in low-mobility materials. Hence, a stress and dislocation study is important to improve device performance.

The most widely used substrate for GaN growth is sapphire, due to its thermal and chemical stability, AlO_xN_y compliant layer formation at the surface after nitridation, and relatively low cost. SiC is a substrate that provides better lattice and thermal expansion match and thermal and chemical stability, in addition, but the cost of SiC is still very high, restricting commercial use. Therefore, focusing on studying the stress of GaN film on sapphire is helpful as it is more cost-effective than SiC and will lead to improvement in GaN/sapphire-based device reliability.

The stress state of a film can be measured by several techniques. Lattice parameter changes (*i.e.*, strain), curvature, or vibrational frequency changes are some of the properties that can be readily measured to ascertain the stress of the film. Those parameters are usually obtained by XRD reciprocal space mapping, optical or stylus profilometry, laser reflectance, Raman spectroscopy, and photoluminescence.

XRD is a non-destructive and direct method to measure the lattice parameters of the film. XRD θ - 2θ scan (also known as powder XRD, XRD 2θ - ω scan, or low resolution XRD) can determine d-spacing parallel to the surface of the films; however, the lattice parameters obtained in this way cannot be used for stress measurement because the 2θ value can shift depending on the sample height and the tilt on the sample mount during the XRD measurement. In addition, when a single crystal is used, there are only peaks from the lattice spacing parallel to the surface. For example, if a single GaN crystal was measured by LR-XRD, there will be only GaN (002) and GaN (004) peaks, which can only be used to calculate out-of-plane lattice parameters, while in-plane lattice parameters cannot be obtained. Therefore, XRD reciprocal space mappings should be carried out to measure lattice parameters precisely to calculate the strain of the film. It is time-consuming to measure the lattice parameters of the samples by XRD reciprocal space mapping due to the alignments steps. In addition, the lattice parameters obtained by XRD-SM may not represent the surface properties because of the X-ray penetration depth. The stress measured by XRD should be considered as the average value from the X-ray interaction volume. X-ray penetration depth depends not only on the material, but also X-ray incidence angle (ω). As a result, precise determination of X-ray penetration depth is not simple.

Curvature of the film can be measured by optical profilometer, stylus profilometer (also known as alpha step), laser reflectance, or other techniques, such as XRD rocking curves with displacing the sample position. The disadvantage of optical profilometer and laser reflectance is their sensitivity towards surface roughness. Since both techniques

utilize the reflected light from the surface, if the surface is rough or has structures on it, it is difficult to measure the curvature of the film.

Curvature can also be measured by stylus profilometer. It requires direct contacts between the tip and the surface. While the surface roughness is not a significant obstacle to using this technique, direct contact may damage the surface. In addition, if the film has fabricated structures on it, it is not possible to use stylus profilometer for curvature measurement. Nevertheless, stylus profilometer may be the quickest and easiest way to measure the curvature and the roughness of the film, though it is not recommended for samples that will be damaged by direct contact.

XRD rocking curves with displacing the sample position is a non-destructive and surface roughness-independent technique that measures the curvature of the crystallographic planes, rather than the surface. Although it is time-consuming to measure the curvature of the film due to the alignment steps, this may be the only way to non-destructively measure the curvature of rough samples.

The general disadvantage of curvature measurements is that they cannot measure small stresses in flat films. In other words, the stress must be large enough to create curvatures within the film. Therefore, small stresses in films without curvature should be measured by more sensitive techniques, such as Raman spectroscopy.

Raman spectroscopy is well-established as a non-destructive and relatively rapid method to measure the average value of film stress. Raman spectroscopy operating in confocal mode can show the peak shifts along the thickness. The results can be used to deduce the stress variation along the depth of the sample.

Another way of studying stress of the film is through modeling. According to the critical thickness theory, the lattice parameter of the overgrown film will turn into its unstrained value once dislocations are formed. The lattice parameter variation along the thickness, however, was experimentally observed, even well above the critical thickness. The result cannot be predicted if the traditional concept of critical thickness or Frank-van der Merwe's semi-infinite model is used. Shen-Dann's layer-by-layer growth model allows for continuous changes in lattice parameters along the thickness, as well as dislocation density reduction as the film becomes thicker.

This chapter will explore how the stress of the film was measured by vibration frequency changes (Raman E_2 phonon peak shifts), lattice parameter change (XRD space map), and curvature (profilometer, XRD rocking curves). Extensive characterizations such as XRD rocking curves, XRD pole-figure, AES, and SIMS were carried out to determine the crystal structure and chemical compositions. For lattice strain modeling, Shen-Dann's layer-by-layer growth model was adopted and compared with experimental data. Although the model used only lattice parameters and elastic constants of the film and substrate, the results matched well with experimental data.

3.2 Effects of Lattice and Thermal Expansion Mismatches

Before examining the stress measurements and modeling of GaN films, it would be instructive to explore the main sources of film stress, which are lattice and thermal expansion mismatches. The effects of these sources of film stress were studied as follows.

3.2.1 Lattice Mismatch at Growth Temperature

To calculate the stress due to the lattice mismatch during the growth, it is important to consider the lattice parameters at the growth temperature, rather than at room

temperature. The lattice parameters of GaN, sapphire, Si, and SiC at high temperature would be larger than the parameters at room temperature due to the thermal expansion. For convenience, calculations were performed assuming the growth temperature is 1300 K and room temperature is 300 K. Although the growth experiments of this study were mostly performed at 1123 K, the calculation results would give some idea of lattice parameters change at high temperature.

The definition of linear thermal expansion coefficient is given as equation (1):

$$\alpha\Delta T = \frac{\Delta L}{L_0} \quad (1)$$

where α is the linear thermal expansion coefficient, ΔT is the temperature difference, ΔL is the linear variation of the lattice parameter, and L_0 is the lattice parameter at room temperature. The definition of misfit, f , is given as equation (2):

$$f = \frac{a_s - a_f}{a_s} \quad (2)$$

where a_s and a_f stand for the lattice parameters of substrate and film.

The lattice parameters of GaN and widely-used substrates such as c-Al₂O₃, Si(111), and 6H-SiC at 300 K and 1300 K are tabulated in Table 3-1.

Table 3-1. Lattice parameters of GaN and widely used substrates at 300 and 1300 K.

	Structure	a_{300K} (Å)	TEC α_a (x 10 ⁻⁶ /K)	a_{1300K} (Å)	Misfit (%) at 300 K	Misfit (%) at 1300 K
GaN	Wurtzite	3.189	5.6	3.207	0	0
c-Al ₂ O ₃	Rhombohedral	4.758 *(2.747)	7.5	4.794 *(2.768)	- 16.09	- 15.86
Si (111)	Diamond	5.431 *(3.841)	2.7	5.445 *(3.851)	+ 16.97	+ 16.72
6H-SiC	Wurtzite	3.086	4.2	3.093	- 3.34	- 3.69

* 30° rotation was considered.

The results show that the lattice misfits calculated at room temperature and at the growth temperature are not particularly different.

To see the critical thickness at the growth temperature (1300 K, in this case), the GaN/6H-SiC system was considered. The critical thickness can be approximately expressed by equation (3).

$$h_c = \frac{b}{8\pi(1+\nu)f} \left[\ln\left(\frac{h_c}{b}\right) + 1 \right] \quad (3)$$

where b is Burger's vector, ν is Poisson's ratio, and f is the misfit. Plugging in the typical values such as b (Burger's vector) $\approx a_f = 3.2 \text{ \AA}$, $\nu = 0.2$, and $f = 0.03$ (in the case of SiC), gives $h_c = 2.2 \text{ \AA}$, which is less than one mono-layer. In this case, dislocations will form at the interface. The other substrates such as Si and sapphire will have even smaller critical thickness. Therefore, critical thickness does not have much meaning in the case of heteroepitaxy of GaN on any currently widely used substrates. In fact, a critical thickness may only exist when the lattice misfit is smaller than 0.8 % and the thickness is less than 10 monolayer scales ($< 5 \text{ nm}$).

3.2.2 Thermal Expansion Mismatch

Most materials compress during the cooling process, except for some rare negative thermal expansion coefficient materials (*i.e.*, see section 8.4). Hence, both GaN and substrates compress during cooling at different ratios due to differences in their thermal expansion coefficients. Calculated thermal strains during cooling ranging from 1300 to 300 K are listed in Table 3-2 for GaN as well as c-Al₂O₃, Si(111) and 6H-SiC. 30 ° rotated lattice parameters for c-Al₂O₃ and Si(111) were used for practical comparison with GaN basal plane and denoted in parentheses.

Table 3-2. Lattice constants at 1300 and 300 K and thermal strain ($\Delta T = 1000$ K) of GaN and widely used substrates.

	Structure	$a_{1300\text{K}}$ (Å)	$a_{300\text{K}}$ (Å)	Compressive strain during cooling	Difference with GaN
GaN	Wurtzite	3.207	3.189	0.56 %	0
c-Al ₂ O ₃	Rhombohedral	4.794 *(2.768)	4.758 *(2.747)	0.76 %	- 0.20 %
Si (111)	Diamond	5.445 *(3.851)	5.431 *(3.841)	0.29 %	+ 0.27 %
6H-SiC	Wurtzite	3.093	3.086	0.42 %	+ 0.14 %

* 30° rotation was considered.

3.2.3 Combination of Lattice and Thermal Expansion Mismatches

Figure 3-1 summarizes the stress caused by thermal expansion and lattice mismatches assuming $\Delta T = 1000$ K. It should be noted that all the lattice parameters that were from different crystal structures were modified (*i.e.*, 30 rotation) for better comparison with GaN since GaN often showed 30 ° rotation with respect to sapphire.

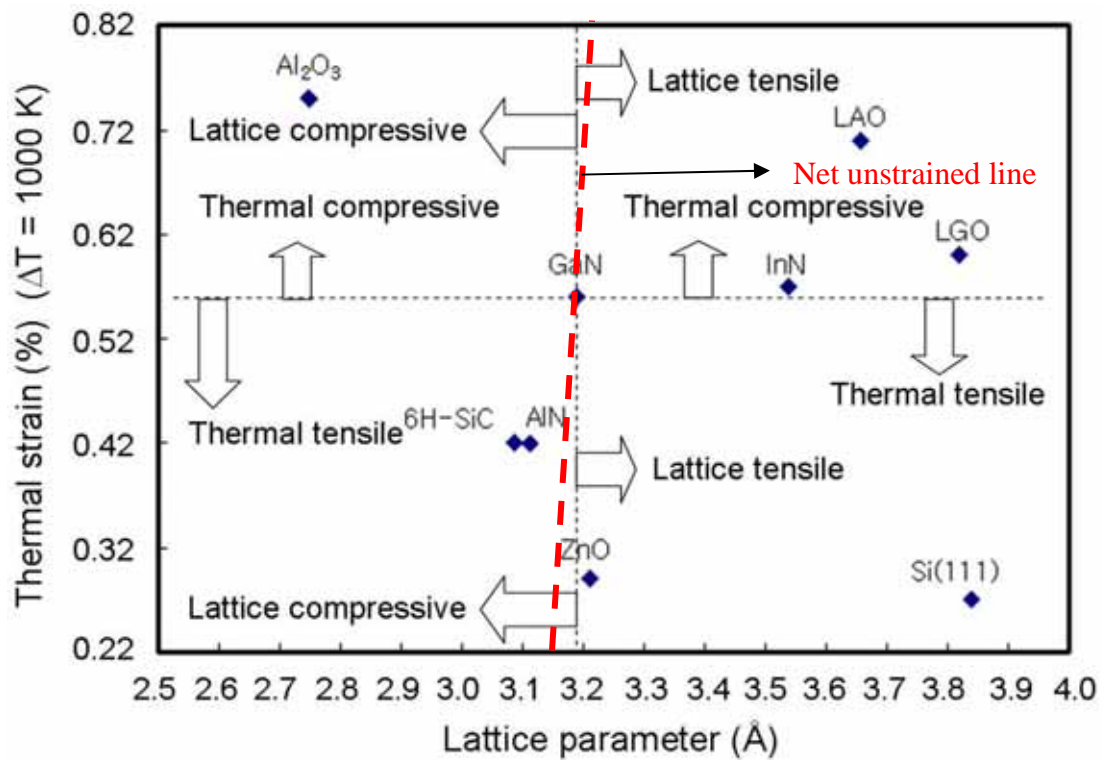


Figure 3-1. Substrates for GaN plotted with thermal strain versus lattice parameters at room temperature.

It is predicted that c-Al₂O₃ compressed more than GaN during cooling. As a result, GaN films grown on c-Al₂O₃ substrates usually show compressive stress due to both thermal and lattice stress. In contrast, GaN films grown on Si substrates show tensile stress because they compress less than GaN film during cooling, in addition to tensile stress caused by lattice mismatch at growth temperature. This figure suggests that both 6H-SiC and AlN are good substrates for GaN, due not only to close lattice parameters, but also the closest thermal expansion coefficients. In addition, the compensation of thermal tensile stress and lattice compressive stress will be beneficial to grow stress-free GaN material. A net unstrained line in the figure represents complete compensation of stress by equivalent contributions of lattice and thermal strain.

It should be noted that thermal expansion and lattice mismatches are not the only parameters that dominate tensile and compressive stress in the film. Use of buffer layers or nitridation will change the surface properties considerably. If the surface properties change, the growth mode may change. Tensile stress at the grain boundaries during islands coalescence mode would be significant, especially if the proper buffer layer is not used. For example, GaN grown on Al₂O₃ shows cracks due to the excessive tensile stress, though compressive stress was present due to the lattice and thermal expansion mismatch [Etz01].

3.3 Stress Measurements of GaN Films on Sapphire

The stress was measured in two samples grown by Mastro during comparison study of HVPE and MOCVD films. (p 64 in [Mas01]). One sample was a 3 μm thick GaN film grown on sapphire by H-MOVPE and the other was a 1 μm thick GaN film grown on sapphire by MOCVD. It should be noted that the term “MOCVD” here refers to hot wall H-MOVPE without HCl flow at atmospheric pressure, and should not be considered as

typical MOCVD, which often uses cold walls at lower pressure. In other words, both samples were grown by H-MOVPE technique with and without HCl inclusion on sapphire substrate without buffer layer growth. Table 3-3 lists the growth conditions of both samples in this study.

Table 3-3. The growth conditions of the two samples for stress measurements.

Samples	Growth T (°C)	Cl/Ga	NH ₃ flow rate (sccm)	Buffer layer
H-MOVPE GaN	950	2	500	Not used
MOCVD GaN	950	0	500	Not used

[Mas01]

3.3.1 GaN Structural and Compositional Studies

To validate the structural quality of the film and ensure the film was grown epitaxially; the typical approach uses HR-XRD rocking curves and XRD pole figures.

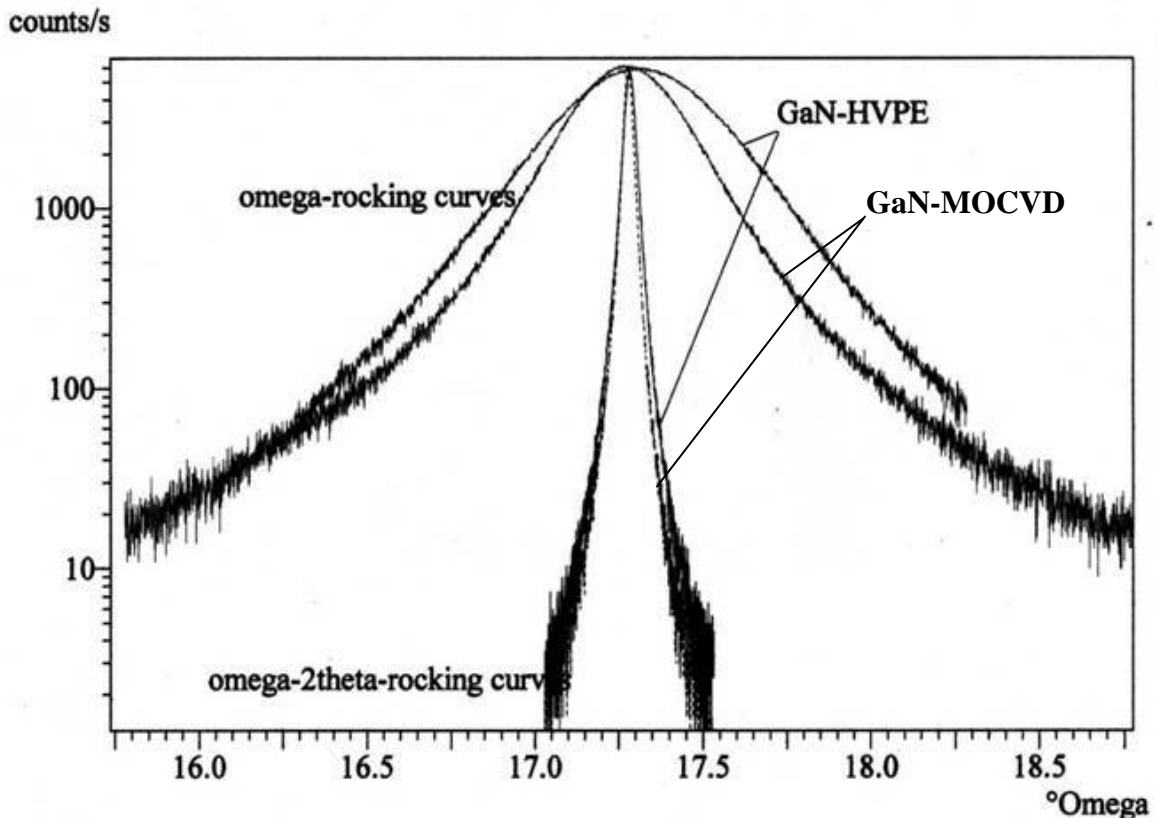


Figure 3-2. XRD ω and θ -2 θ rocking curve of MOCVD and H-MOVPE grown GaN on sapphire, XRD FWHM; ω -rocking curve (MOCVD: 1261 arcsec, H-MOVPE: 1790 arcsec); θ -2 θ rocking curve (MOCVD: 92 arcsec, H-MOVPE: 122 arcsec).

Figure 3-2 shows XRD ω and θ - 2θ rocking curves of both the MOCVD and H-MOVPE grown samples. The FWHM of ω -rocking curves of MOCVD and H-MOVPE grown samples were 1261 and 1790 arcsec, respectively. The homogeneity of lattice spacing in the crystal is measured by XRD θ - 2θ rocking curve and the homogeneity of the normal axis of the lattice planes are measured by ω -rocking curve. Typically it is more likely to have uniform lattice spacing than uniform direction of lattice planes. Therefore, the FWHM of θ - 2θ rocking curves are usually smaller than that of ω -rocking curve. The FWHM values of 122 and 92 arcsec were obtained from MOCVD and H-MOVPE grown samples, respectively.

There is no clear criterion of crystallinity by only the rocking curve method, though higher crystal quality results in smaller FWHM. XRD pole figure is often used to check if the film is grown epitaxially. Figure 3-3 shows XRD pole figures of the (116) sapphire and MOCVD growth GaN (112). A 30° rotation of GaN film with respect to sapphire substrate was clearly seen because the lattice mismatch can be reduced significantly from 49 % to 14 % in this way. The results confirmed that the GaN films were indeed grown epitaxially.

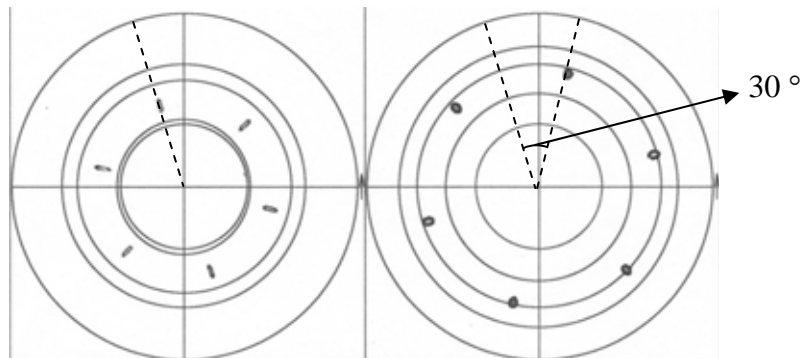


Figure 3-3. Pole figures for the (116) sapphire substrate ($2\theta = 57.490^\circ$) and (112) GaN by MOCVD ($2\theta = 69.185^\circ$). The GaN in-plane axis is rotated by 30° with respect to the sapphire axis.

Similar results were found with the GaN grown by H-MOVPE (Figure 3-4). A 30° rotation with respect to sapphire and clear epitaxial growth were confirmed. It is noted that the shapes of the peaks from sapphire and GaN are different. The peaks from sapphire substrate are much sharper in shape compared to the peaks from GaN, because the crystal quality of sapphire is superior to GaN.

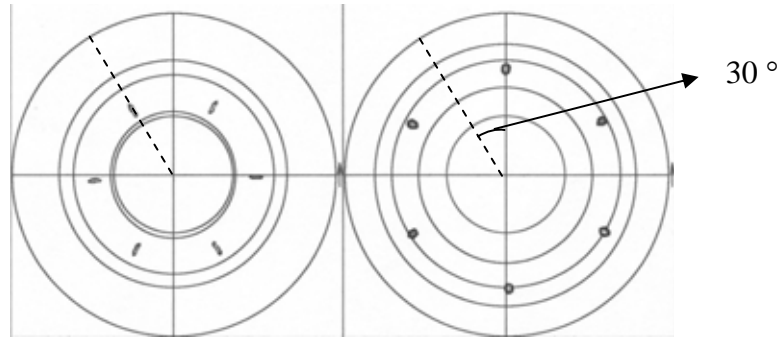


Figure 3-4. Pole figures for the (116) sapphire substrate ($2\theta = 57.490^\circ$) and (112) GaN by H-MOVPE ($2\theta = 69.185^\circ$). The GaN in-plane axis is rotated by 30° with respect to the sapphire axis.

Auger Electron Spectroscopy (AES) was used for chemical composition analysis. Figure 3-5 shows the AES surface scan and depth profile of GaN on sapphire grown by MOCVD. Ga (52.8 %), N (30.1 %), C (10.7 %), and O (6.3 %) were detected on the surface. Surface C and O quickly disappeared within 1 min of sputtering. Since the thickness of the GaN was reasonably thick ($\sim 1\ \mu\text{m}$), the typical sputtering rate ($\sim 100\ \text{\AA}/\text{min}$) would require 100 min of sputtering time to fully profile. To reduce sputtering time, the raster size was decreased by a factor of 5, so the sputtering rate increased fivefold. In addition, the detection sequence was reduced to decrease sampling time. The results show that the GaN films were mainly composed of only Ga and N from the surface to the interface. Adsorbed C and O on the surface were apparently from air exposure.

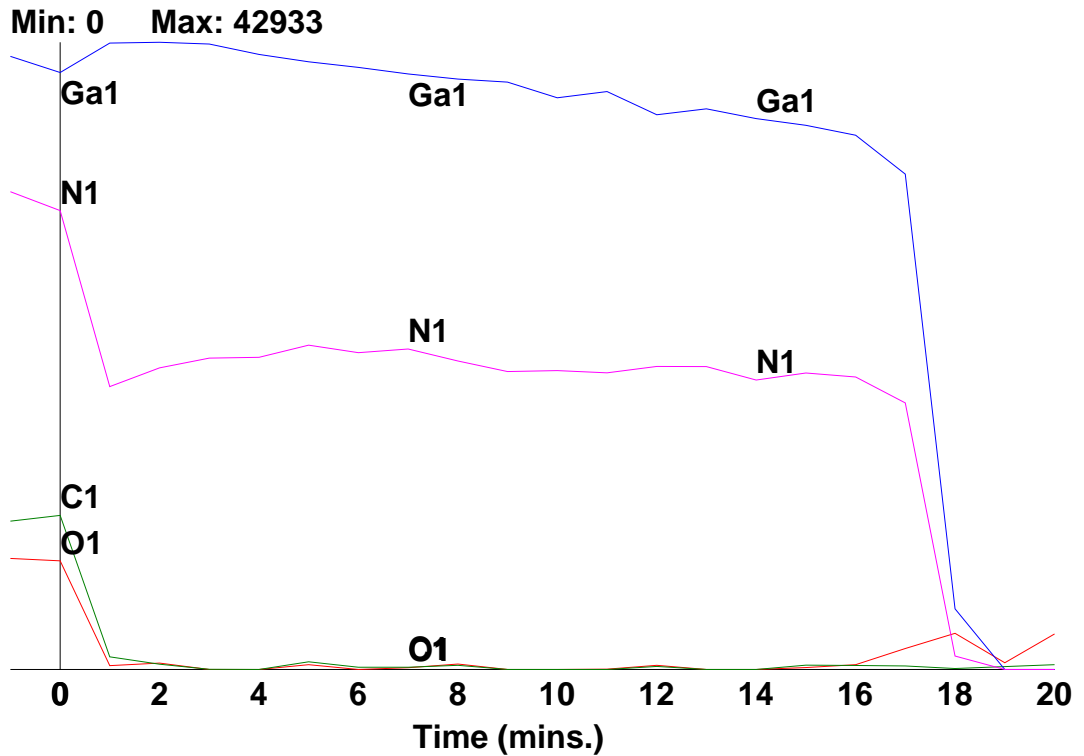
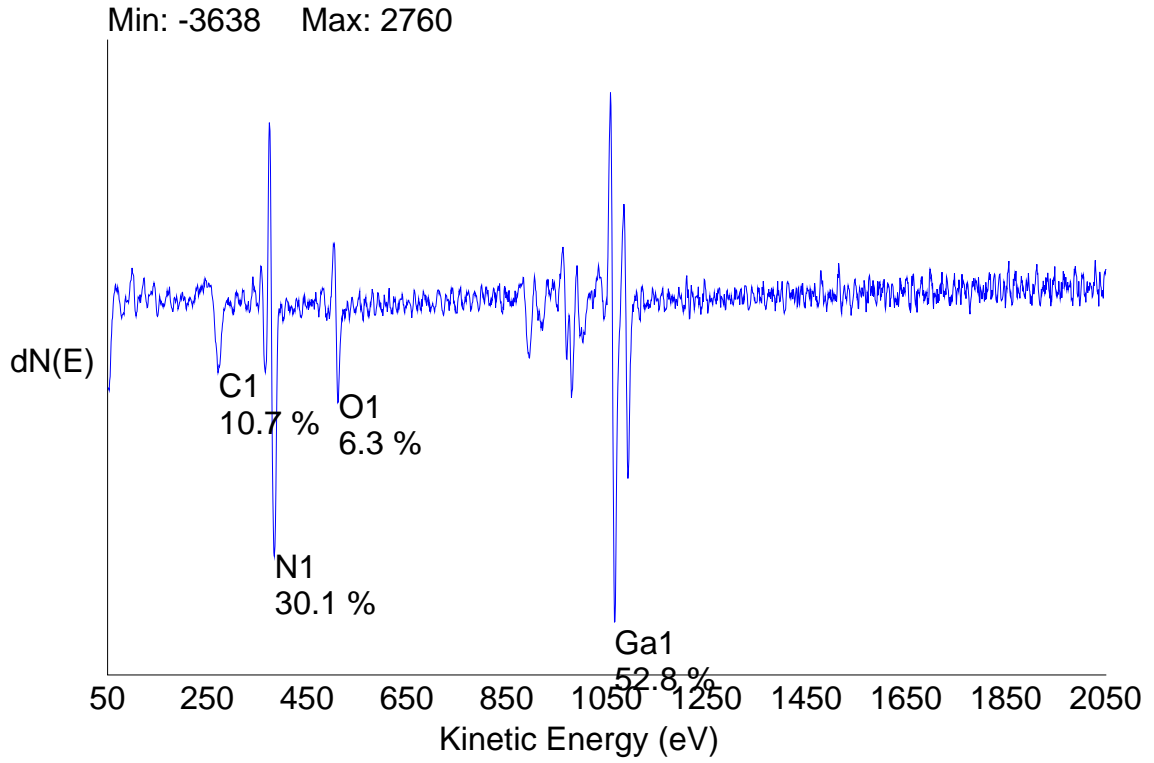


Figure 3-5. AES surface scan and depth profile of GaN on sapphire grown by MOCVD

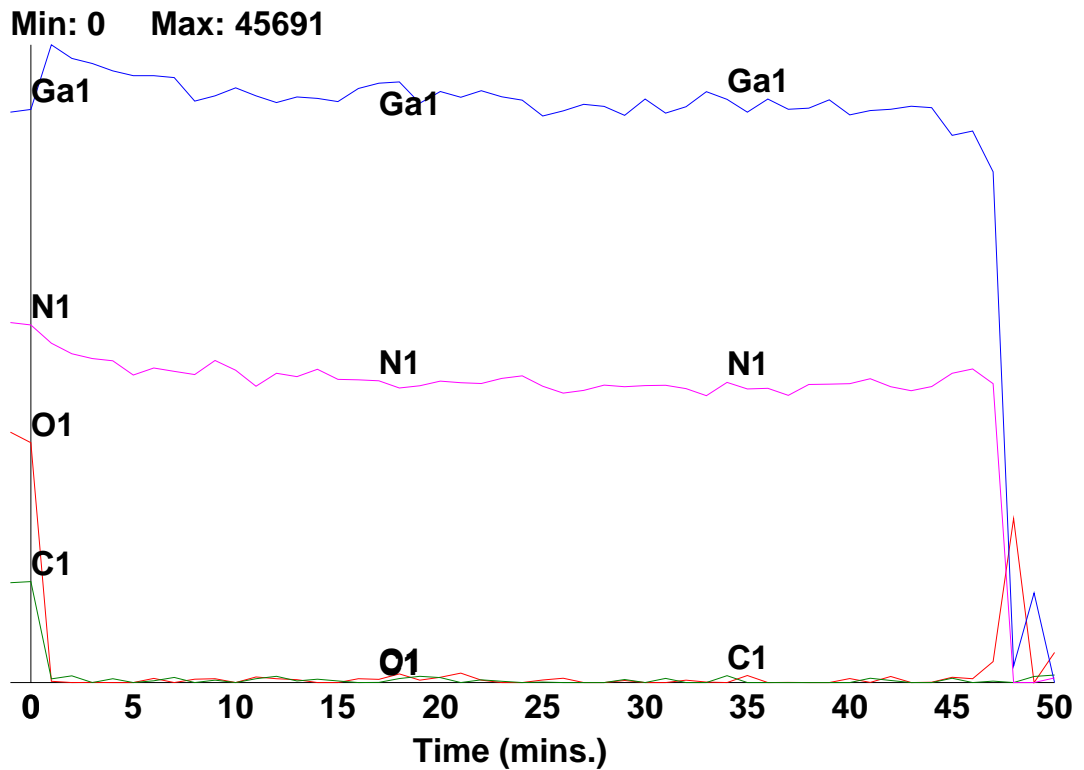
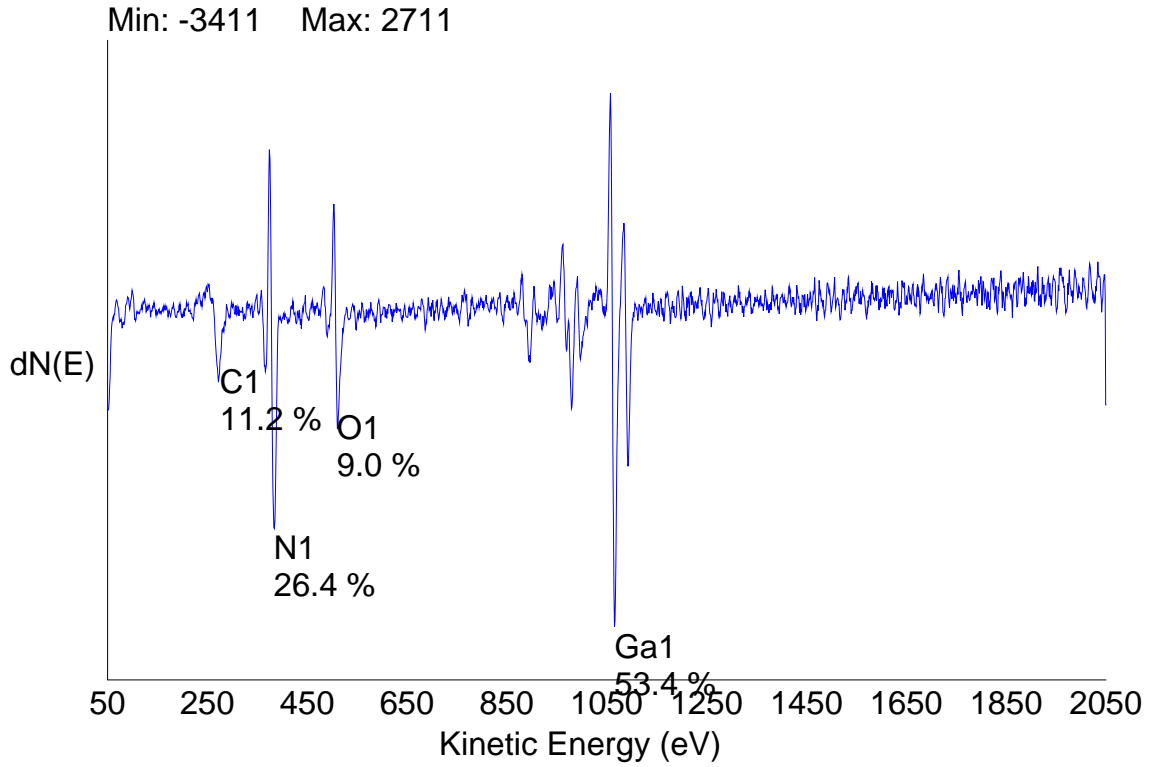


Figure 3-6. AES surface scan and depth profile of GaN on sapphire grown by H-MOVPE.

Similar AES surface scanning followed by depth profile was done on H-MOVPE GaN on sapphire as shown in Figure 3-6. The surface chemical compositions were Ga (53.4 %), N (26.4 %), C (11.2 %), and O (9.0 %). The thickness of GaN was 3 μm . Therefore, the fivefold increased sputtering rate was again used by reducing raster size. Uniform Ga and N profiles were obtained from the surface to the interface once more. It is noteworthy that the sputtering rate was indeed $\sim 500 \text{ \AA}/\text{min}$. Only adsorbed surface C and O existed just as in the previous case.

3.3.2 Stress Measurements by Raman Spectroscopy

The Raman shifts of the stress sensitive GaN E_2 mode have been reported by several researchers, and the reported values cover the large range, from 565 to 572 cm^{-1} [Mel97, Tab96], showing the differences of the residual stress in the epitaxial film. It would be helpful to have the freestanding GaN E_2 mode as a standard since there would be no substrate effect. The reported shifts of the E_2 mode for freestanding GaN samples, however, show a relatively wide range from 565 to 570 cm^{-1} [Mel97, Tab96, Dav97, Age97]. Freestanding GaN films grown by HVPE technique may contain high impurity levels (mainly oxygen), resulting in hydrostatic stress. The E_2 mode of stress-free GaN is known as 568 cm^{-1} at room temperature that was measured from a thick (50 – 70 μm) GaN film grown by chloride-hydride vapor phase epitaxy (CHVPE) [Dav98]. More discussion about Raman E_2 peak position is presented in Table 1-2 in Chapter 1. The residual stress in both epitaxial films was measured by Raman spectroscopy.

The depth-dependent Raman measurements of MOCVD and H-MOVPE deposited GaN films were carried out by a collaborator (Seok-Ki Yeo in Dr. Chinho Park's group, Yeung Nam University, Korea) using a Renishaw System-2000 (located in Miryang

National University, Korea) in confocal mode. The laser output power was set at 20 mW with an excitation wavelength of 514.5 nm. The focused beam size was approximately 2 μm , accumulation time was 10 sec, and a CCD detector was employed. By controlling the slit width and CCD pixel size, signals from different depths could be resolved.

Figure 3-7 shows the measured Raman shifts of GaN E_2 mode of (a) MOCVD GaN surface, (b) H-MOVPE GaN surface, and (c) the depths profiles.

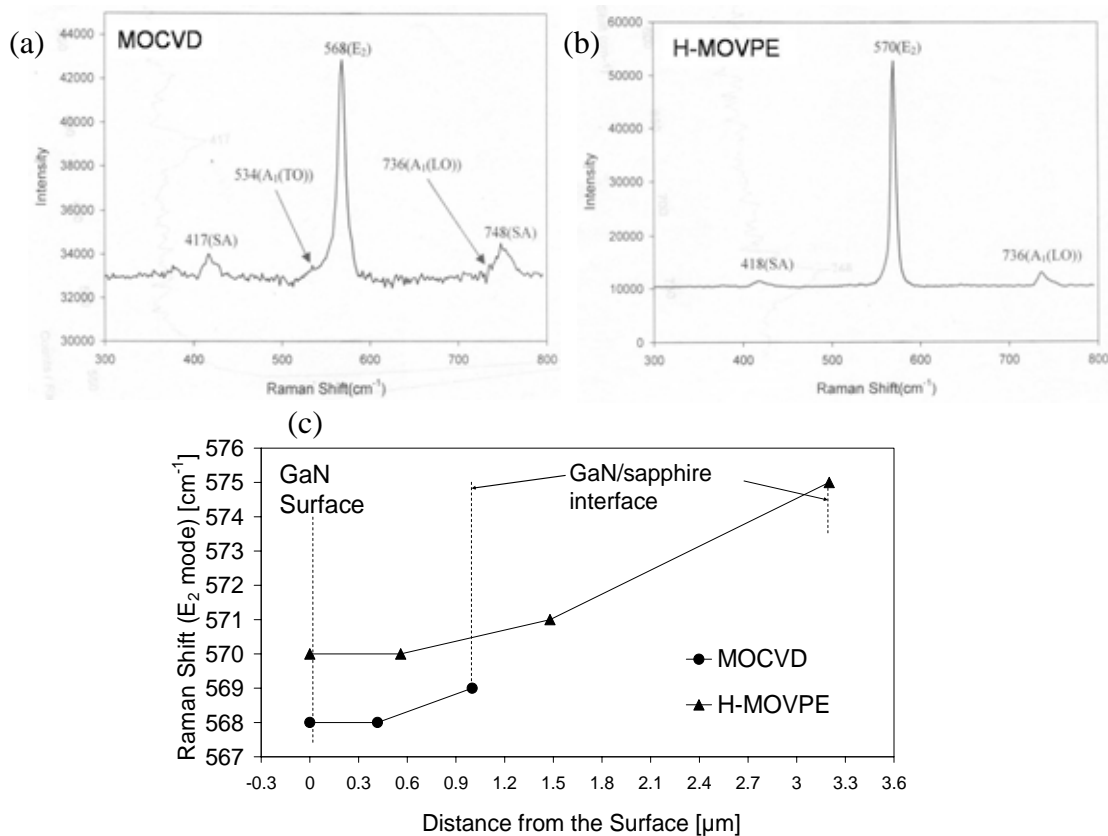


Figure 3-7. Raman E_2 peak shifts at the surface (a) MOCVD, (b) H-MOVPE, and (c) depth profile.

In the case of the MOCVD grown film, the E_2 peak varied from 568 cm^{-1} (GaN surface) to 569 cm^{-1} (GaN/sapphire interface). In the case of the H-MOVPE grown sample, however, the E_2 peak varied from 570 cm^{-1} (GaN surface) to 575 cm^{-1} (GaN/sapphire interface). This indicates that the H-MOVPE film was in a state that was more compressive than that of the MOCVD sample. It is commonly assumed that HVPE

grown epitaxial film may have higher oxygen content because the growth takes place at atmospheric pressure, whereas MOCVD grown film usually contains less oxygen due to reduced pressure. However, “MOCVD” in this case is referring H-MOVPE without HCl. No difference in oxygen content was expected since the same reactor was used at the same pressure. The AES results agreed with this assumption.

It is reported that a biaxial (c and a axes) stress of 1 GPa shifts the E_2 Raman mode by $2.7 \pm 0.3 \text{ cm}^{-1}$ [Dav97] and a hydrostatic stress of 1 GPa shifts it by 4.17 cm^{-1} [Per92], and these values were used to calculate the stress of the epitaxial film. The MOCVD grown GaN was considered as stress-free due to the Raman E_2 position appearing at 568 cm^{-1} . The H-MOVPE grown sample, however, may contain compressive stress judged by high frequency shift ($568 \rightarrow 570 \text{ cm}^{-1}$) of E_2 peak. If the 2 cm^{-1} of shift was purely due to the biaxial stress, the stress in the GaN film would be 0.74 GPa. Likewise if the 2 cm^{-1} of shift was caused by only hydrostatic stress, the stress in the GaN would be 0.48 GPa. Therefore, other stress measurements should be carried out to compare the values and find the origin of stress.

The curvature and the lattice parameters of the epitaxial film were measured to cross-check the stress values obtained by the other techniques. Stoney’s equation [Sto09] was used to calculate the curvature of the substrates, and Shen’s formula [She02] was used to estimate lattice parameters after obtaining the stress value from Raman spectroscopy.

3.3.2.1 Curvature Calculations

From the Raman spectroscopy results, the curvature of the film was calculated and compared to the other measurements. It was shown that the stress of the $3 \mu\text{m}$ H-MOVPE GaN film on sapphire substrate is substantial and thus substrate bowing was

expected. The relation between the film stress and substrate curvature (κ) is given by Stoney's equation, $\kappa = 6\sigma_f h_f / (M_s h_s^2)$ [Sto09]. In this expression, σ_f is the biaxial stress in the film, h_f , h_s are the thicknesses of the film (3 μm : H-MOVPE, 1 μm : MOCVD) and substrate (300 μm : sapphire), respectively. M_s is the substrate biaxial modulus, which is 602 GPa for sapphire [Hel92]. The radius of curvature was calculated as 4.1 m by using 0.74 GPa (biaxial stress). Similarly, the radius of curvature was calculated as 6.3 m by assuming 0.48 GPa (hydrostatic stress).

3.3.2.2 Lattice Parameter Calculations

From the stress measured by Raman spectroscopy, the lattice parameters were calculated with proper assumptions. Shen *et al.* [She02] organized equations for hexagonal GaN epitaxial thin films assuming isotropic strain in the epitaxial film. These equations predict the changes in the stress of the film with respect to the growth plane when both the growth plane and the underlying substrate are hexagonal. Substituting and rearranging the original equation gives:

$$a(\text{\AA}) = a_0 - a_0 \{(s_{11} + s_{12})E_s\}^{0.5} \quad (7)$$

The range in the reported values for the elastic compliances in equation (7) are $s_{11} = 0.00297$ to 0.00502 and $s_{12} = -0.00066$ to -0.00121 GPa^{-1} [Dav98, Tal96, Pol96, Sav78]. The range-centered values $s_{11} = 0.003995$ and $s_{12} = -0.000935$ were used in the calculation. The values of a_0 are the unstrained GaN lattice parameters (3.189 \AA for MOCVD and 3.067 \AA for H-MOVPE films assuming hydrostatic strain) and a is the lattice parameter of the strained GaN epitaxial films that is a function of stress (E_s). The lattice parameter value of strained GaN assuming biaxial stress will be much smaller than 3.067 \AA .

Now that we have calculated curvature and lattice parameters by stress data from Raman spectroscopy, these values will be compared with other techniques.

3.3.3 Lattice Parameter Measurements by XRD Reciprocal Space Mapping

The most straightforward method to measure the strain of the films is measuring the lattice parameters of the film. XRD reciprocal space mapping is an effective tool to measure the lattice parameters. In XRD reciprocal space mapping, a series of θ - 2θ scans are collected with changing sample tilt offsets (ω). Any strain of epitaxial layer would be shown as an asymmetrical shape of contour lines.

The crystallographic plane spacing, d , of a hexagonal structure is given by equation (4).

$$\frac{1}{d^2} = \frac{4}{3} \left(\frac{h^2 + hk + k^2}{a^2} \right) + \frac{l^2}{c^2} \quad (4)$$

where d is the lattice spacing, h , k , and l are the Miller indices ($h k l$), a and c are the in-plane and out-of-plane lattice parameters, respectively. To measure the lattice parameters of the film accurately, at least two non-parallel crystallographic planes should be chosen and space maps taken. The Philips X'Pert MRD instrument was used to measure the reciprocal space mapping by using the triple axis monochromator for exclusive use of Cu $K_{\alpha 1}$ spectrum.

Bragg's law is given as equation (5).

$$\lambda = 2d \sin \theta \quad (5)$$

where λ is the wavelength of the X-ray excitation source (Cu $K_{\alpha 1}$ at 1.54056 Å), d is the lattice spacing that is given as equation (4), and θ is the Bragg angle that is to be measured by XRD space map. Figure 3-8 shows XRD reciprocal space maps of

symmetry peak (002) and asymmetry peak (114) from the GaN film grown by H-MOVPE. The measured 2θ values of (002) and (114) peaks were 34.56460° and 99.97260° , respectively. Plugging in the values to the above equations gave lattice parameters $a = 3.187 \text{ \AA}$ and $c = 5.186 \text{ \AA}$, which are similar to literature values.

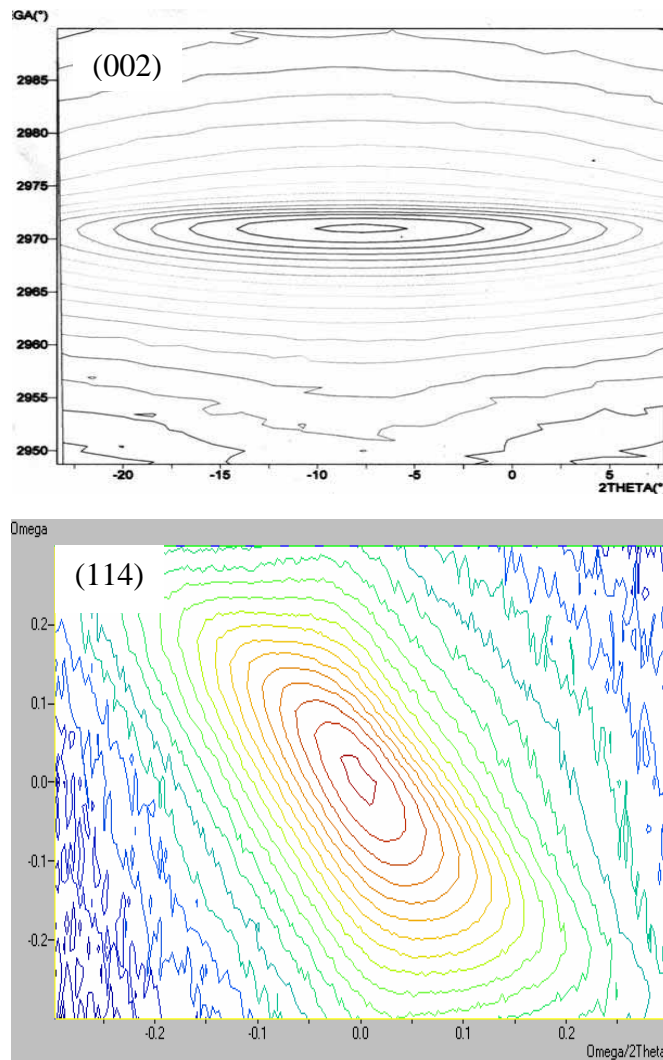


Figure 3-8. XRD reciprocal space mapping of H-MOVPE grown GaN (002) and (114) peaks.

Similar measurements were performed on the MOCVD grown GaN sample as shown in Figure 3-9. The values of $2\theta = 34.55500^\circ$ and 99.941870° were obtained for

(002) and (114) peaks, respectively to give lattice parameters $a = 3.188 \text{ \AA}$ and $c = 5.187 \text{ \AA}$.

It should be noted that the lattice parameters obtained by reciprocal space mapping are average values of the film from the X-ray interaction volume *i.e.*, the reciprocal space mapping cannot measure the depth profile. An XRD reciprocal space mapping, however, can give qualitative information on variations of the lattice parameters with depth.

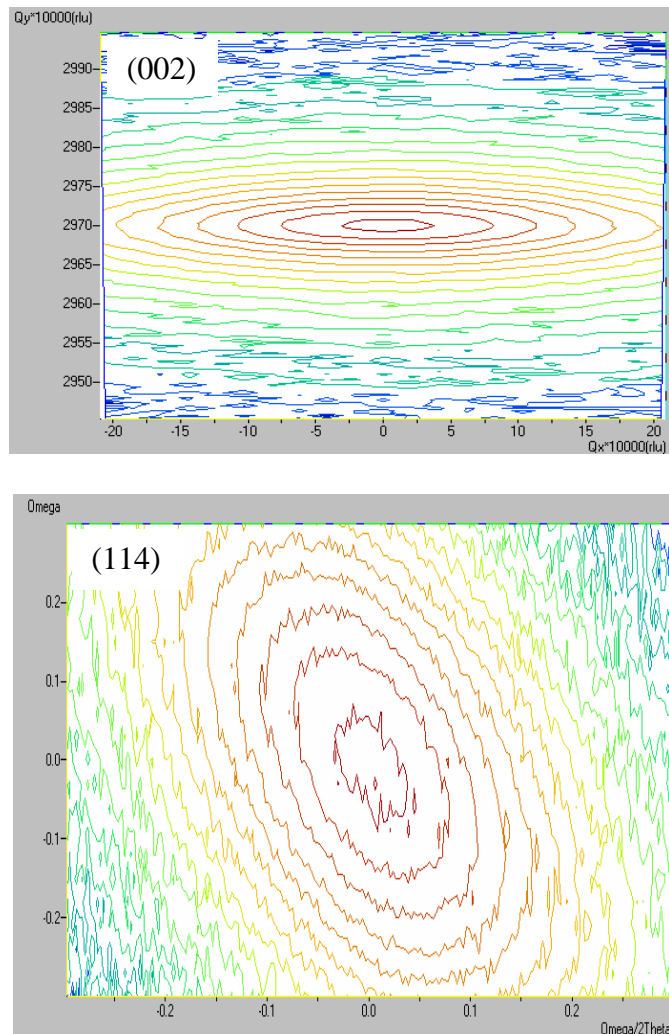


Figure 3-9. XRD reciprocal space mapping of MOCVD grown GaN(002) and (114) peaks.

Thus the c -axis, the upper line spacing is smaller and lower line spacing is wider. The results suggest that the c -axis lattice parameter had various values. The vertical cross

section of the reciprocal space mapping can be thought as a ω - 2θ rocking curve. Because it is shifted to a higher ω value, it can be concluded that the distribution of the lattice parameters will be on the smaller side (*i.e.*, under compressive stress).

Table 3-4 presents selected reported lattice parameters of GaN [Mel97]. The values obtained by XRD-SM showed $a = 3.187 \text{ \AA}$ and $c = 5.186 \text{ \AA}$ for H-MOVPE GaN and $a = 3.188 \text{ \AA}$ and $c = 5.187 \text{ \AA}$ for MOCVD GaN. These values are similar to bulk GaN crystal values. Therefore, it was concluded that the GaN film grown by H-MOVPE is almost strain free but under slight compressive strain (not enough to measure the lattice strain quantitatively), whereas the film grown by MOCVD is strain free.

Table 3-4. GaN a and c lattice parameters measured at 300 K (\AA).

Samples description	a (\AA)	c (\AA)
Thin ($<1.5 \mu\text{m}$) GaN layers grown by HVPE on SiC [Mel97]	3.1937-3.1969	5.1786 -5.1811
Bulk GaN crystal grown by HVPE [Mel97]	3.1893 (Ga face) 3.1879 (N face)	5.18560 (Ga face) 5.18534 (N face)
Annealed bulk GaN crystal grown by HVPE [Mel97]	3.1890	5.18500
Thick GaN layers grown by HVPE on sapphire [Det92]	3.1892 ± 0.0009	5.1850 ± 0.0005
Bulk GaN crystals grown at high pressure [Les96]	3.1890 ± 0.0003 (Ga face) 3.1881-3.1890 (N face)	5.1864 ± 0.0002 (Ga face) 5.1856-5.1864 (N face)

[Mel97]

3.3.4 Curvature Measurements by XRD Rocking Curve

The most widely used method for measuring residual stress of the film is curvature measurement. *In situ* curvature measurements are usually carried out using laser reflectance. In addition, there are a number of *ex situ* curvature measurements, which include optical and stylus profilometer (alpha step), laser reflectance, and XRD rocking curve. Curvature measurement by reading an XRD rocking curve is useful regardless of

the surface roughness. Since the surface of HVPE and H-MOVPE grown films are often rough, measuring the XRD rocking curve is the preferred choice.

The curvature measurement procedure is illustrated in Figure 3-10. The XRD rocking curve was initially obtained with the normal alignment procedure. After the alignment of the rocking curve, the sample position was changed precisely. If there was curvature in the sample, the rocking curve was then realigned, and the value of $\Delta\omega$ was obtained. The different ω values can be used to calculate the curvature of the sample.

The radius of curvature can be calculated by equation (6).

$$R = \frac{\Delta x}{\Delta\omega} \quad (6)$$

where R is the radius of curvature, Δx is the displacement of the sample, and $\Delta\omega$ (radians) is the difference of omega values upon displacement of the sample.

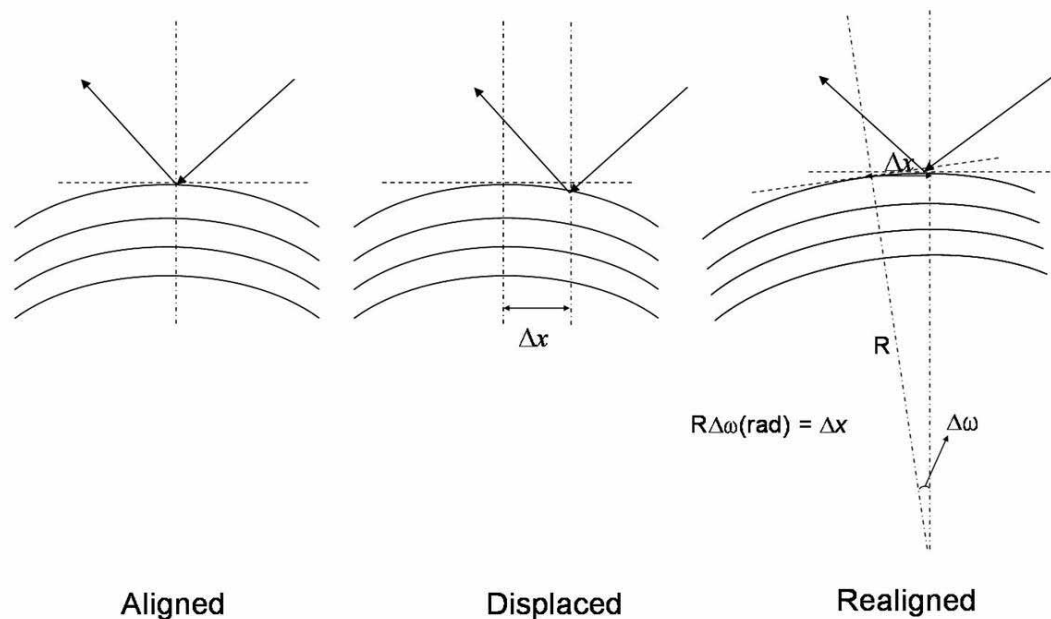


Figure 3-10. The procedure of determining curvature by measurements of XRD rocking curves.

The XRD rocking curve measurement method was used to determine the curvature of the 3 μm thick GaN grown by H-MOVPE. By displacing the sample position precisely by 5 mm in the x-direction, the ω value changed from 17.26163 to 17.28132, as shown in Figure 3-11. Using the given equation, the calculated radius of curvature of 14.5 m was obtained, which is practically a flat surface. The results agreed well with the measurements by XRD reciprocal space mapping in that there is not significant strain in the H-MOVPE grown GaN film.

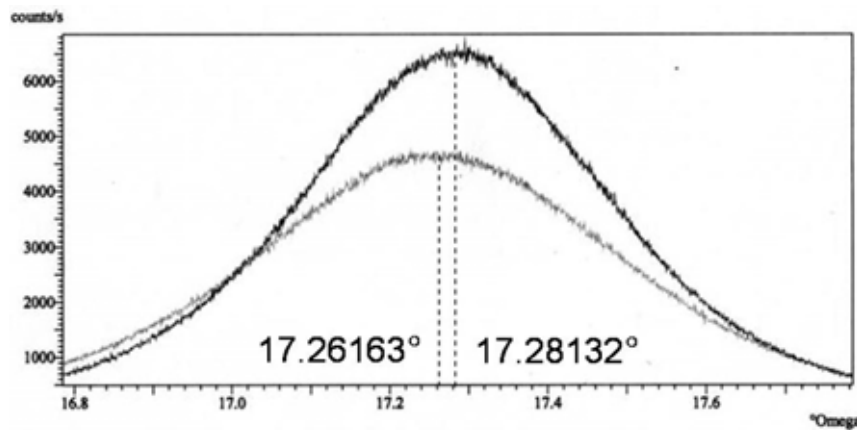


Figure 3-11. Curvature measurements by XRD rocking curve by displacing the H-MOVPE grown GaN/c-Al₂O₃ sample in x-direction by 5 mm.

Table 3-5. Stress, lattice parameter, and curvature of the H-MOVPE GaN with depth.

Distance from the surface [μm]	Stress [GPa] by Raman factor	Radius of Curvature by Raman	Radius of Curvature by XRD RC	Lattice parameter by Raman	Lattice parameter by SM
0 (surface) and 0.6 (bulk): two points showed identical E ₂ shift	0.74 (biaxial) 0.48 (hydrostatic)	4.1 m (biaxial) 6.3 m (hydrostatic)	14.5 m	3.067 Å	3.187 Å

The radius of curvature calculated from Raman spectroscopy showed 4.1 to 6.3 m. It was also measured by XRD rocking curve (14.5 m) and stylus profilometer (15 m).

Considering these results, it appears that the curvature of the film is ~ 15 m and thus is practically flat. However, the lattice parameters deduced from the stress measurement by Raman spectroscopy and the ones directly from XRD reciprocal space mapping exhibited inconsistent results. Therefore, the stress of the film measured by Raman spectroscopy may not be from lattice strain (*i.e.*, a change in lattice parameter). To elucidate the reason for the existence of compressive stress measured by Raman spectroscopy without changing lattice parameters, the chemical compositions were examined.

No significant difference between the MOCVD and H-MOVPE samples was observed by both XRD and AES analysis as in Section 3.3.1. Therefore, secondary ion mass spectroscopy (SIMS) was used to measure the chemical compositions since AES is not as sensitive as SIMS if impurities compose less than 1% of the matrix. SIMS depth profiles were acquired with a Perkin-Elmer PHI 6600 SIMS system using a 5 keV Cs primary ion beam and negative secondary acquisition. The current intensity was set at 158 or 90 nA and the raster size was $350 \times 350 \mu\text{m}^2$. Several profiles for each sample were obtained from various sampling spots. Quantification of impurities by SIMS requires using standards with known concentrations of the species in the same matrix as the samples of interest, because SIMS is a very matrix dependent technique. In other words, when using SIMS, the sensitivity of the same element varies with matrix composition. When standards are not available, it is possible to compare the intensity levels between samples by measuring the relative intensity of the impurity and a matrix ion. Therefore, to compare the oxygen level between samples, the ratios of O intensity to the GaN intensity were calculated for each sample.

Figure 3-12 shows SIMS oxygen depth profiles of MOCVD and H-MOVPE grown GaN films. It is clear that the O concentration of MOCVD film is higher than in the H-MOVPE film. Regardless of the higher oxygen content, the MOCVD GaN samples showed no stress by Raman spectroscopy and XRD. On the other hand, the H-MOVPE GaN samples with lower oxygen content showed significant compressive stress measure by Raman spectroscopy, but no stress by XRD. It is known that Raman E_2 peak shift is mainly related to the biaxial stress or hydrostatic stress in the film that may be related to the oxygen concentration. It appears that, however, the Raman E_2 peak shift may not be related to biaxial stress or oxygen concentration in this case, because the lattice parameters measured by XRD did not change.

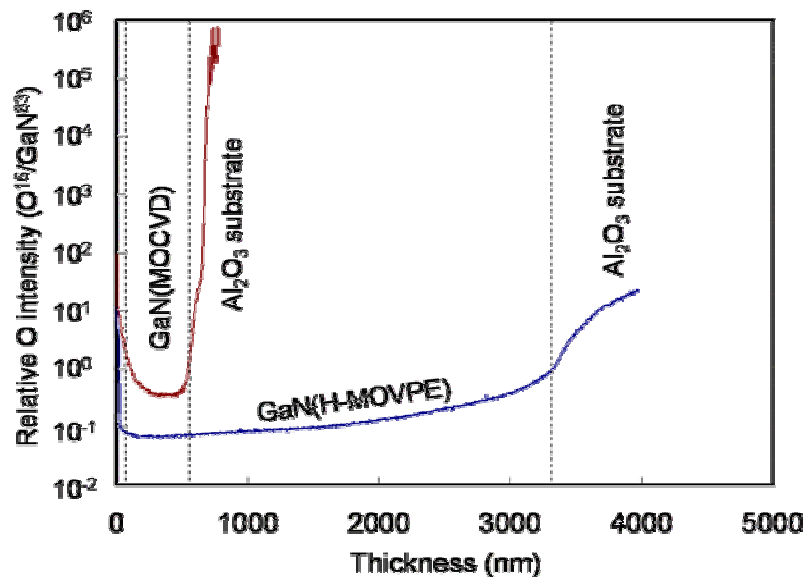


Figure 3-12. SIMS oxygen depth profiles of MOCVD and H-MOVPE grown GaN films.

The stress-free Raman E_2 peak positions are still in question, whether it is 570 (H-MOVPE) or 568 cm^{-1} (MOCVD). It was expected that the MOCVD GaN would have less oxygen as it showed an E_2 phonon peak at 568 cm^{-1} , and was thus assumed to be stress-free GaN. However, H-MOVPE GaN showed a much lower oxygen concentration

with a Raman E_2 phonon peak at 570 cm^{-1} , which is supposed to indicate significant compressive stress. Another approach is to consider 570 cm^{-1} as the stress-free E_2 mode and that 568 cm^{-1} indicates tensile stress that is related to the growth mode. It should be noted that the term “MOCVD” here is not the same as typical MOCVD, which produces superior quality materials, but H-MOVPE without HCl, utilizing a hot wall in atmospheric pressure. The MOCVD grown GaN may be growing by island coalescence growth mode although there is no evidence of island growth and structural quality confirmed it is epitaxially grown film. It is known that significant tensile stress generates at the grain boundaries of islands. If H-MOVPE GaN was stress-free and MOCVD GaN film is under tensile stress, this may make sense. However, the reason for this discrepancy is not clear yet. It should be noted that these measurements were performed on almost 6 years old samples. Therefore some oxidation/degradation may have taken place and this may caused the inconsistent results.

3.4 Stress Modeling of GaN on Sapphire

After measuring stress in GaN film on sapphire, it is useful to calculate the stress in GaN film using traditional and modified stress modeling. By comparing the calculated results with experiments, the most important factors to induce stress in film can be identified. Fran-van der Merwe’s semi-infinite model and Shen-Dann’s Layer-by-layer growth model were applied in this study and compared with experiments.

3.4.1 Frank-van der Merwe’s Semi-infinite Model

Misfit dislocation density was calculated using the Frank-van der Merwe’s semi-infinite overgrowth model, as represented in Figure 3-13. In this model, the strain will be completely relaxed by dislocation formation after $p/2$ thickness, and the film has no effect

on the substrate beyond this thickness. Here p , the Vernier period of misfit dislocation, is defined as equation (8).

$$p = \left| \frac{a_s a_f}{a_s - a_f} \right| \quad (8)$$

where a_s and a_f are the lattice parameters of film and substrate, respectively.

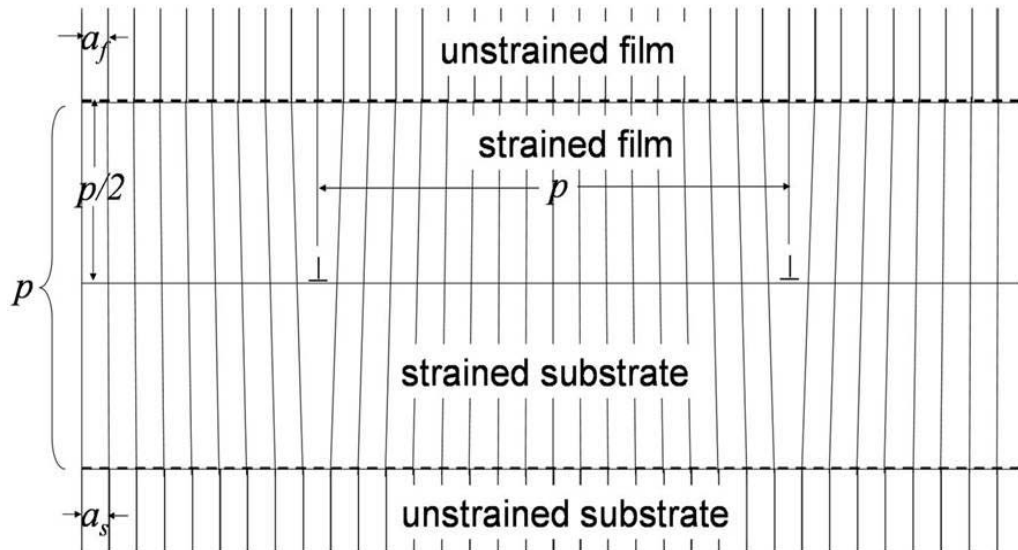


Figure 3-13. Frank-van der Merwe's semi-infinite overgrowth model.

In this model, only pure edge dislocations were considered and only form if sufficient strain energy is available to provide the formation energy. The value of $p/2$ is ~ 9.3 nm for GaN on 6H-SiC. The $p/2$ value of the other substrates such as sapphire and Si will be even smaller than this.

Table 3-6. Calculated misfit dislocation density of GaN on widely used substrates with Vernier period.

	p (Å)	Misfit dislocation density (cm^{-2})
GaN	∞	0
c-Al ₂ O ₃	20.221	2.4×10^{13}
Si (111)	19.177	2.7×10^{13}
6H-SiC	87.011	1.3×10^{12}

Table 3-6 shows calculated Vernier periods with misfit dislocation density of GaN on c-Al₂O₃, Si (111), and 6H-SiC. The Vernier period can be thought as 1-D misfit

dislocation density. Therefore 2-D misfit dislocation density was calculated from the square of the Vernier period by assuming uniform distribution of misfit.

It should be noted that this simple model agreed fairly well with experiments for the case of a Ge deposit on Si(001) [Mar03]. However, the variation of in-plane lattice parameters of GaN grown on AlN/Al₂O₃ was experimentally observed by XRD up to 1 μm thickness [Kim99]. Therefore, Frank-van der Merwe's semi-infinite model could not be applied to the GaN/Al₂O₃ system at device-relevant thicknesses.

3.4.2 Layer-by-Layer Growth Model

A better model that describes gradual changes in lattice parameters and gradual creation of misfit dislocation was developed by Shen and Dann [She06] and illustrated in Figure 3-14.

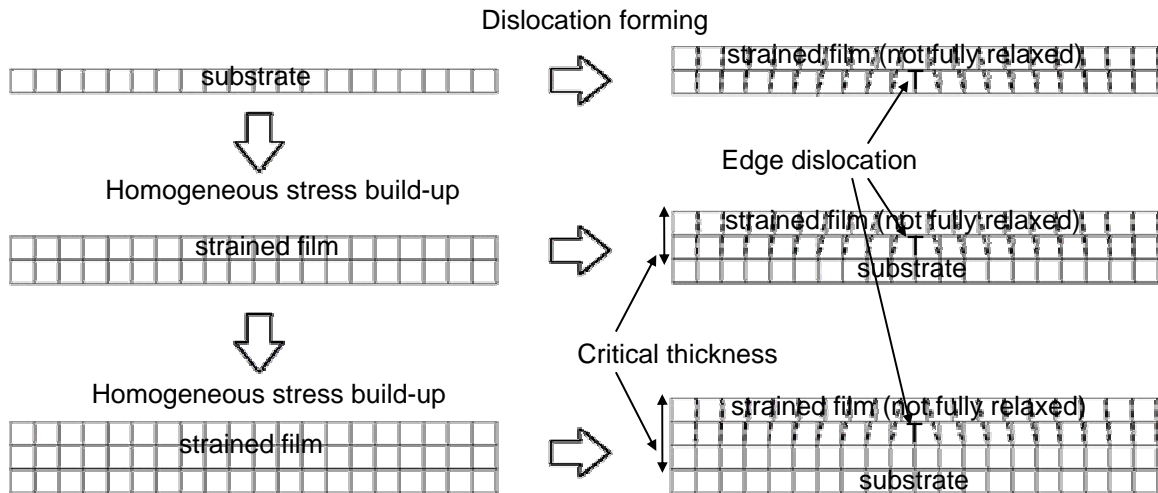


Figure 3-14. Shen-Dann's layer-by-layer model.

When overgrowth material is deposited on a foreign substrate, it will experience homogeneous stress without forming dislocation as long as the thickness is smaller than the critical thickness. This stress will proportionally increase with increasing numbers of layers until finally the material will form dislocations to relax the stress when the

thickness reaches a critical thickness. Dislocations will form periodically, but the in-plane lattice parameters do not necessarily become their unstrained values, unlike Frank-van der Merwe's semi-infinite model. An underlying assumption is that the bonds at the interface are much weaker than the bonds in the overgrown films and the substrates. After it reaches a critical thickness, the lattice constant will be closer to the bulk (unstrained) material. The consequent growth after the critical thickness will be a similar process. Here it was treated that the dislocation formed layer as a new substrate. The new substrate will match the lattice of the overgrowth film better than the original substrate. Therefore, the critical thickness will be thicker. Nevertheless, it will experience the same stress relaxation mechanism by forming dislocations again, until it reaches the second critical thickness through the accumulation of stress.

Stress (homogeneous strain energy) proportionally increases with increasing numbers of layers, while the dislocation (periodic strain energy) number accumulates. The sum of these two energies will have a minimum at certain point as the number of layers is increased. Finding this minimum energy with respect to the sum of strain and dislocation energy will give gradual lattice parameter changes.

3.4.2.1 Strain Energy (Homogeneous Stress) Calculations

The procedure to obtain the strain energy of overgrowth GaN on sapphire and LGO has been calculated by Shen *et al.* [She02]. Using the lattice parameters provided in Table 3-7 and elastic constants in Table 3-8 [Tak96], the strain energy calculations of a GaN film grown on AlN/Al₂O₃ were performed.

Since both film and substrate are hexagonal and the basal plane of each material is used in epitaxial growth, the strain in x and y directions are symmetrical and can be simply written as equation (9).

$$\varepsilon_x = \varepsilon_y = \frac{a - a_0}{a_0} \quad (9)$$

where a and a_0 are the lattice parameters of the growth layer and the substrate in the basal plane, respectively. Following Shen's work [She02], the strain energy per unit volume is expressed as equation (10).

$$U = \frac{1}{s_{11} + s_{12}} \left(\frac{a - a_0}{a_0} \right)^2 = \frac{\varepsilon_x^2}{s_{11} + s_{12}} \quad (10)$$

Table 3-7. Lattice constants (\AA) of GaN, AlN, and Al_2O_3 .

Material	a	c
GaN (wurtzite)	3.189	5.185
AlN (wurtzite)	3.112	4.980
Al_2O_3 (wurtzite)	4.758	12.991

Table 3-8. Elastic stiffness coefficients c_{ij} (GPa) and compliances s_{ij} (1/GPa) of GaN, AlN, and Al_2O_3 .

	c_{11}	c_{12}	c_{13}	c_{33}	c_{44}	s_{11}	s_{12}	s_{44}
GaN	374	106	70	379	101	0.00297	-0.00077	0.0099
AlN	424	103	71.3	455	138	0.00255	-0.00057	0.0072
Al_2O_3	495	160	115	497	146	0.00232	-0.00066	0.0068

[Tak96]

To compare the calculated results with experimental results, AlN buffer layer on Al_2O_3 substrate was considered as the substrate, because AlN buffer layers are widely used between GaN and Al_2O_3 substrate. Kim *et al.* [Kim99] employed X-ray diffraction to investigate the strain relaxation of GaN/AlN on sapphire. A thin 32 \AA layer of AlN was grown on a sapphire substrate followed by a subsequent GaN layer. $a_0 = 3.084 \text{ \AA}$ in-plane lattice constant of the 32 \AA film of AlN on sapphire was measured as their experimental data. This lattice constant of AlN on Al_2O_3 was considered as the starting value for a_0 in the strain energy calculation.

3.4.2.2 Dislocation Energy (Periodic Strain Energy) Calculation

Van der Merwe [Mer63] has derived the dislocation energy per unit area and Jesser [Jes67] reorganized the result as equation (11). Since the dislocation energy per unit area is assumed to be symmetrical, one dimensional dislocation was defined as ${}_x E_d$ with unit of J/m. This value is multiplied by the specific area (area per mole) to have energy per mole unit.

$${}_x E_d = \frac{G_1 b_x}{4\pi^2} \{1 + \beta_x - (1 + \beta_x^2)^{1/2} - \beta_x \ln[2\beta_x(1 + \beta_x^2)^{1/2} - 2\beta_x^2]\},$$

$$\text{where } \beta_x = \frac{2\pi G_1 b_x}{P(1 - \nu_1) \left(1 + \frac{G_1}{G_2}\right) G} \quad (11)$$

G_1 indicates the shear modulus of AlN and G_2 denotes that of Al_2O_3 . G without a subscript represents the shear modulus of GaN, ν is Poisson's ratio and b_x (Burger's vector) is given as equation (12):

$$b_x = \frac{2a_1 a_2}{a_2 + a_1} \quad (12)$$

Finally, P is the Vernier periodicity of dislocations and denoted by equation (13):

$$P = \frac{a_1 a_2}{a_2 - a_1} \quad (13)$$

The required elastic properties for the calculations are listed in Table 3-9.

Table 3-9. Shear moduli, Poisson's ratios, and lattice parameters of GaN, AlN, and Al_2O_3 .

	G	ν	a (Å)
GaN	1.01×10^{11}	0.2578	3.189
AlN	1.38×10^{11}	0.2224	3.112
Al_2O_3	1.46×10^{11}	0.2848	4.758

[Tak96]

3.4.2.3. Total Strain Energy Calculations

The total strain energy is defined as the sum of homogeneous strain energy, periodic strain (dislocation) energy, and interface energy as equation (14).

$$E_{\text{total}} = E_{\text{strain}} + E_{\text{disloc}} + E_{\text{interface}} \quad (14)$$

The strain energy per unit area and the dislocation energy were calculated by equations (10) and (11), respectively. The interfacial energy was neglected because the area between the layers was assumed to be negligible compared with total strain and dislocation energies. As the number of layers increases, the strain energy proportionally increases as in equation (15):

$$E_{\text{strain}} = n \times 6,230 \text{ kJ/mol} \times \varepsilon^2 \quad (15)$$

where n = the number of layers and $1/(s_{11}+s_{12})_{\text{GaN}} = 454.1 \text{ GPa}$, or $6,230 \text{ kJ/mol}$ was used in the calculation. It should be noted that ε is only a function of the lattice parameter of GaN for a given substrate. Hence, strain energy is only a function of lattice parameter change.

The dislocation energy of GaN on AlN/Al₂O₃ was calculated by equation (11) and the sum of strain energy and the dislocation energy was taken as total energy (stress in the GaN/AlN/Al₂O₃ system).

As the number of layers increases, the total energy decreases. At certain point, the total energy will be minimized by the adequate contribution of strain and dislocation energy as shown Figure 3-15.

From this calculation, the lattice constant that results in a minimum of the total energy could be found and is often turned the critical thickness. The calculated lattice constant was used as a new substrate's lattice constant and the same steps were repeated

until it reached the unstrained GaN lattice constant, 3.189 Å. The lattice constants and the minimum total energy with the number of layers are listed in Table 3-10. The term critical thickness in Table 3-10 represents the thickness of GaN film from the substrate/film interface.

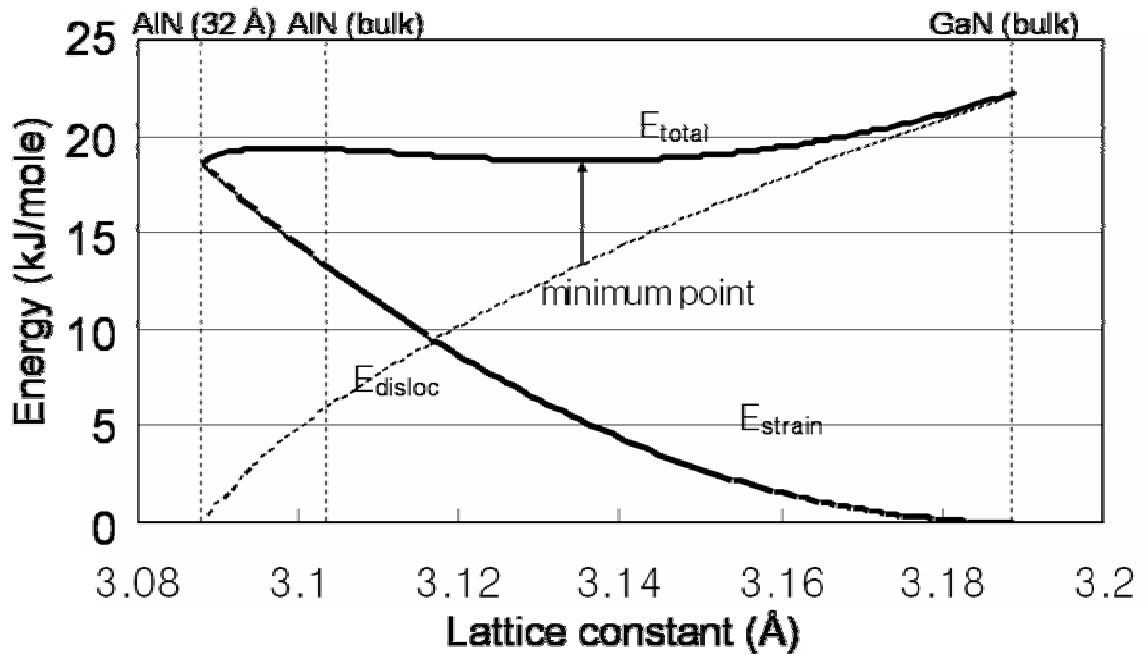


Figure 3-15. Minimum energy calculation of stress + dislocation energy.

Table 3-10. Calculated lattice constants and total energy.

Number of layers	Lattice constant (Å)	Critical Thickness (Å)	E_{total} (J/mol)
1 – 3	3.135	10.45474	18740
4 – 10	3.157	15.62296	12425
11 – 23	3.167	36.38896	8328
24 – 44	3.174	67.52497	6299
45 – 77	3.178	109.0171	4624
78 – 125	3.18	171.2573	3608
126 – 186	3.182	249.0612	3603
187 – 269	3.184	316.4641	2509
270 – 399	3.186	430.5291	1961
400 – 703	3.188	674.2136	1436

The in-plane lattice constant versus the thickness of GaN layer are compared with experimental data [Kim99] in Figure 3-16. In their study, sets of GaN films were grown on Al_2O_3 substrates using AlN buffer layer by MBE. The lattice parameters of thin AlN

and GaN films were determined by *ex situ* X-ray reciprocal space mapping. Poisson's ratio for GaN was applied to calculate the out-of-plane lattice constants affected by lateral deformation. As in-plane lattice constants increase, the out-of-plane lattice parameters decrease.

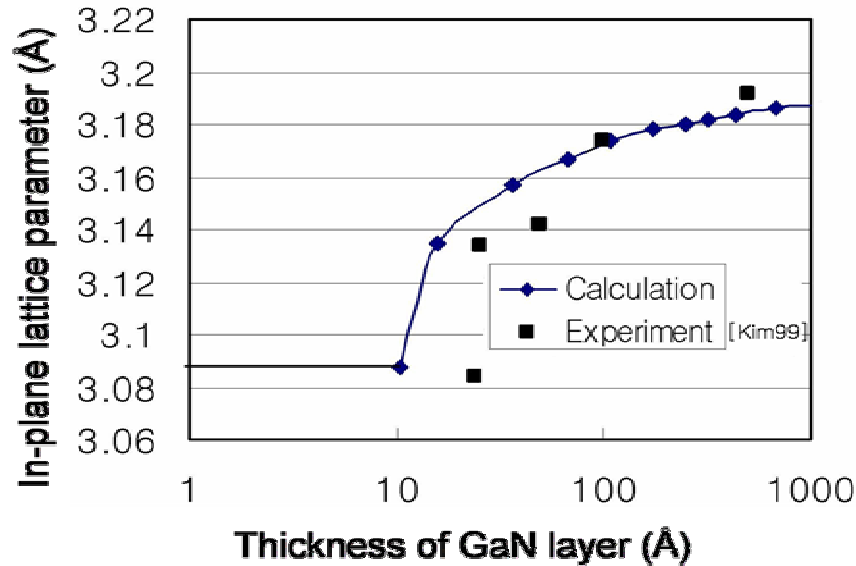


Figure 3-16. In-plane lattice constants of GaN on AlN/sapphire.

The calculated total strain energy at the interface was added to the Gibbs energy of GaN and the decomposition temperature of GaN was lowered by 44 K from 1110 K to 1066 K by Thermo-Calc. The unstrained GaN thermodynamic data were taken from [Unl03]. By adding the strain energy to the Gibbs energy of GaN, the decomposition temperature of strained thin GaN film on various substrates can be predicted.

3.5 Conclusions

The effect of lattice mismatch was calculated at growth temperature and showed that critical thickness is only important when smaller lattice mismatch system is considered. Critical thickness calculation does not have much meaning when GaN film

on any widely used substrates such as SiC, Al₂O₃, and Si were concerned since misfit dislocations forms at the interface.

Effects of thermal expansion mismatch and lattice mismatch at growth temperature were considered and it was found that various substrates would induce compressive and/or tensile stresses on GaN, due to the combination of lattice and thermal expansion mismatches.

Several stress measurements were carried out on two GaN samples grown on sapphire substrate by H-MOVPE and MOCVD. Although Raman spectroscopy is known to be a good technique to measure the stress of the materials, considerable stress difference between the two samples showed that Raman spectroscopy in this case may not be an adequate technique to measure the stress of the film due to the inconsistent results with other techniques. Lattice parameters of GaN were precisely measured by HR-XRD reciprocal space mapping and no significant difference between the two films were confirmed. Further curvature measurement by XRD and stylus profilometer confirmed the samples were almost completely flat. The crystal structure and chemical compositions of the samples were characterized by XRD rocking curves, XRD pole figures, and AES, but no significant difference was observed. Only SIMS showed varying oxygen concentrations between the two samples. The peak position of Raman E₂ mode may be related to not only the strain of the film, but also oxygen concentration although the results showed obvious contradiction. It is not clear at this point whether Raman peak shifts were mainly related to the oxygen concentration or other factors such as growth mode difference, which may cause tensile stress at the grain boundaries. Most of all, analyzing almost 6 year old sample was not a good approach since the samples

may be partially experienced degradation and oxidation. Similar procedures with fresh samples will provide fair comparison of various stress measurement techniques.

Frank-van der Merwe's semi-infinite model was used and it was found that the model is not applicable to the GaN/Al₂O₃ system at device-relevant thicknesses. Strain and dislocation energy modeling was carried out using Shen-Dann's layer-by-layer growth model, based on total energy minimization, which agreed well with the experimental data. The decomposition temperature of strained GaN was decreased by 44 K due to the inclusion of the total strain energy.

CHAPTER 4 GROWTH OF GALLIUM NITRIDE ON SILICON BY H-MOVPE

4.1 Introduction

The growth of GaN films on a Si single crystal wafer has been pursued for over 30 years (*i.e.*, [Mor73]). Although the quality of GaN on Si was not good in the early attempts, there was motivation to grow GaN on Si since Si is the highest quality and lowest cost substrate material available. Large size, high quality, both *p* and *n*-type doping, and low cost are some of the advantages of Si substrates. The availability of Si substrates in large size (maximum 12 inch diameter) is especially attractive when mass production of high-volume, low cost GaN/Si-based devices such as LEDs are considered. The two main goals of growing GaN on Si are: (i) growth of thin (4 to 5 μm) crack-free GaN film on Si. and (ii) growth of freestanding ($> 100 \mu\text{m}$) GaN using Si wafers as a foundation. The former is needed for GaN/Si based devices such as LEDs. The large diameter of Si will reduce device fabrication costs compared to sapphire substrates. Moreover, the heat generated from the LEDs would drain more easily through Si because it has a much higher thermal conductivity (145 W/mK) than Al_2O_3 (5.43 W/mK). The growth of GaN on sapphire has been limited to 2" diameter wafers. Although large diameters of sapphire are available, the wafer bow on large diameter wafers produced by the mismatch prevents device processing. Furthermore, sapphire is not electrically conducting so top-side contacts are needed. Larger diameter growth of thick GaN on Si or sapphire has been impeded due to the significant cracking problems. If freestanding

GaN could be grown on 12 inch Si wafer without cracking and bowing, it will be an important breakthrough for GaN-based device development.

A GaN film on Si is under tensile stress during growth and under additional tensile stress during the cooling due to the lattice and thermal expansion differences. “Tear-like” cracks can form to accommodate excess tensile stress. Therefore, the growth of crack-free GaN film on Si substrate is a challenge. The reported maximum thickness of crack-free GaN grown on Si with multiple AlN interlayers was 7 μm , as measured by *in situ* curvature measurement. [Kro03].

In this chapter, the H-MOVPE technique will be introduced first. Chemical reactions and a reactor schematic will be shown to give insight into the H-MOVPE technique. For GaN film growth on Si, bare Si substrates and GaN/AlGaN/AlN/Si templates were used. The templates were grown by MOCVD techniques and provided by Nitronex. The goal of the present study is to grow both thin and thick GaN films on Si substrates by H-MOVPE. By utilizing a relatively low growth temperature (850 °C) rather than MOVPE growth temperature (typically 1050 °C), thermal stress can be reduced by ~ 20 %. For crack-free, thick GaN growth, InN was used as a buffer material since InN is known to be a softer material than GaN and Si. To study structural effects, InN columnar films, nanorods ($d = 250 \text{ nm}$), thick nanorods ($d = 500 \text{ nm}$), and microrods were tested as buffer materials to give a compliant layer between GaN and Si.

4.2 H-MOVPE Growth Technique

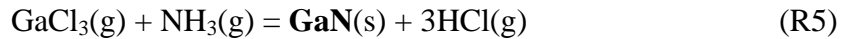
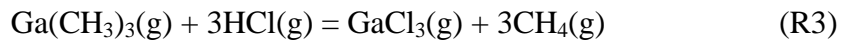
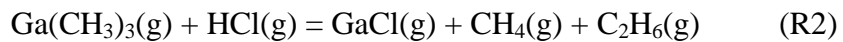
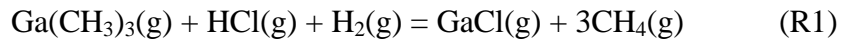
4.2.1 Chemical Reactions of H-MOVPE Technique

Hydride Metalorganic Vapor Phase Epitaxy (H-MOVPE) has proven to be a promising technique to grow GaN films on LiGaO_2 , LiAlO_2 , and Si utilizing the high

growth rate and easy precursor switching afforded by this process [Ree02, Mas01, Kry99]. Trimethylgallium (TMG), ammonia (NH₃), and 10 % HCl (balance 90 % N₂) were used as the precursors. N₂, H₂, or 4% H₂ (balance 96 % N₂) were typically used as carrier gases.

A thermodynamic analysis was carried out to better understand the expected gas phase species and condensed phases in the Ga-C-H-Cl-N-Inert and In-C-H-Cl-N-Inert systems. The results are presented in Chapter 2.

The overall reactions for GaN growth by H-MOVPE technique are:



TMG reacts with HCl in a H₂ ambient and produces presumably GaCl and CH₄ (R1). When H₂ is not present, GaCl can still form with CH₄ and C₂H₆ as by-products (R2). TMG can react with excess HCl (Cl/Ga ≥ 3) and form GaCl₃ (R3) especially at low temperature (< 500 K) as shown in thermodynamic analysis (Figure 2-5). Both GaCl and GaCl₃ can react with NH₃ and form GaN with HCl and/or H₂ as by-products (R4, R5). It is also known, however, that it is difficult to thermally decompose NH₃ at low temperature because of slow kinetics.

4.2.2 H-MOVPE Reactor Schematics

The H-MOVPE reactor schematic is shown in Figure 4-1. There are six individually controllable furnace zones, as shown in Figure 4-1 (a). The furnace elements

have a capability of heating to 1300 °C, but the practical growth zone temperature limit was 1000 °C because quartz may soften over 1000 °C. The typical growth temperature for GaN was 850 °C for high temperature growth and 560 °C for low temperature growth, as these were the optimized growth temperatures suggested by Reed [Ree02].

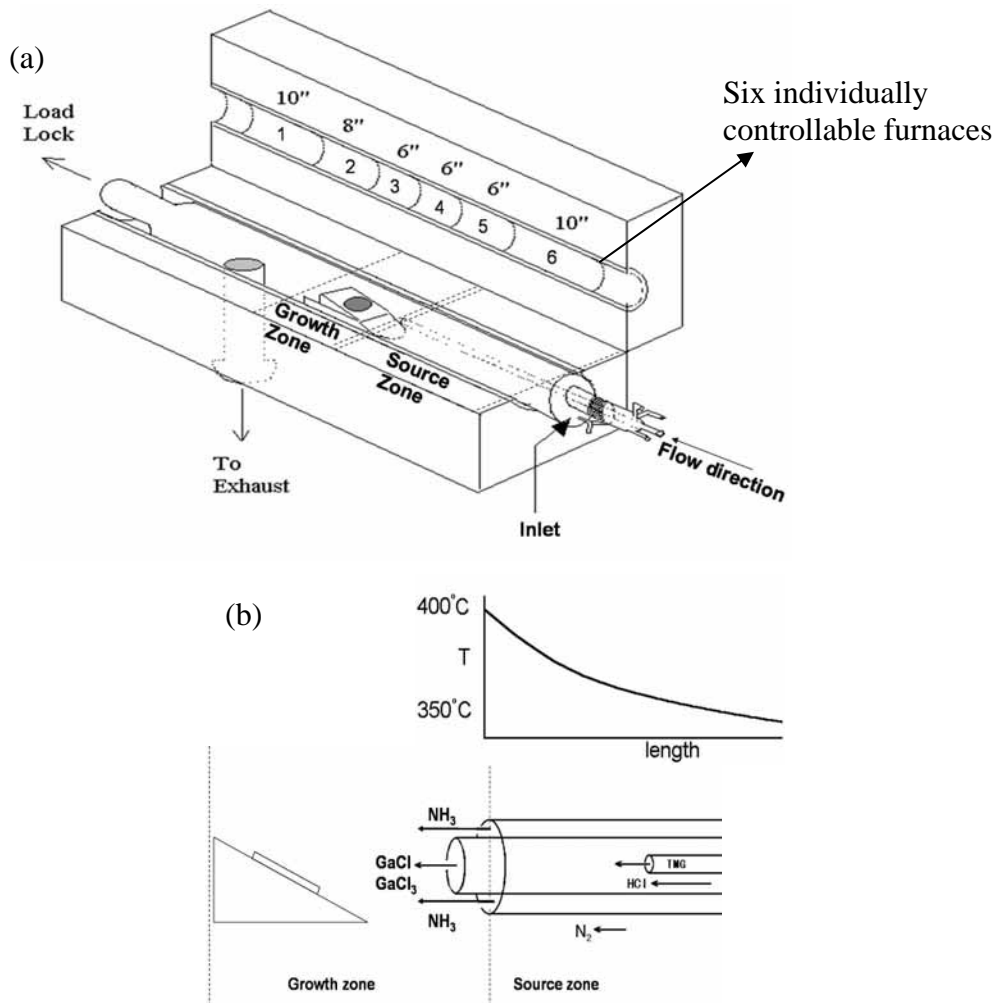


Figure 4-1. Schematics of H-MOVPE (a) bird eye view of the entire reactor, (b) the source and growth zones with temperature profile in the source zone [Ree02].

To prevent TMG decomposition before it reacts with HCl, the maximum inlet temperature is maintained below 400 °C, as shown in Figure 4-1 (b). The source zone consists of tri-concentric quartz tubes. The input gases do not meet each other until a certain residence time passes. Ideally, the reaction products of the source zone, *i.e.*, GaCl

or GaCl_3 , will react with the NH_3 on the surface of the substrate. In the less ideal case, GaN is formed in the gas phase and GaN particles will drop on the substrate surface, which then act as 3-dimensional nuclei. Therefore, it is very important to control the source zone conditions (*i.e.*, inlet gas ratios, concentric inlet tilting, the distance from the inlet to the substrate) to give optimal and reproducible epitaxial growth conditions.

Figure 4-2 shows the Process Flow Diagram (PFD) of the H-MOVPE system located in the Microfabritech, research area at the University of Florida. Its capabilities include 3 bubblers, 3 toxic/corrosive gas cylinders, H_2 , N_2 , and an additional carrier gas such as He or Ar. House N_2 is always provided by liquid N_2 boil-off to prevent lines from clogging and to keep the reactor free of moisture.

There are a number of advantages to H-MOVPE. Quick switching of the input sources is essential for multiquantum well (MQW) structure or atomic layer deposition (ALD). In traditional HVPE, although HCl flow is turned off to stop GaCl supply, a thin GaCl_x layer on the liquid Ga can still provides GaCl to the growth zone. As a result, rapid switching of the group III source is restricted. The high growth rate (50 $\mu\text{m/hr}$ maximum) is also an advantage when thick film growth is desired. The large surface area of the hot quartz wall also helps NH_3 cracking because NH_3 is known to crack more easily on the surface. But N radical recombination will produce inert N_2 , and thus must be minimized before reaching the substrate. The freedom to control six individual temperature zones is advantageous to adjust the gas phase reactions.

H-MOVPE has some disadvantages as well. The costs of metalorganics are much higher than pure metal sources and the growth rate (< 50 $\mu\text{m/hr}$) is not as high as traditional HVPE (> 100 $\mu\text{m/hr}$).

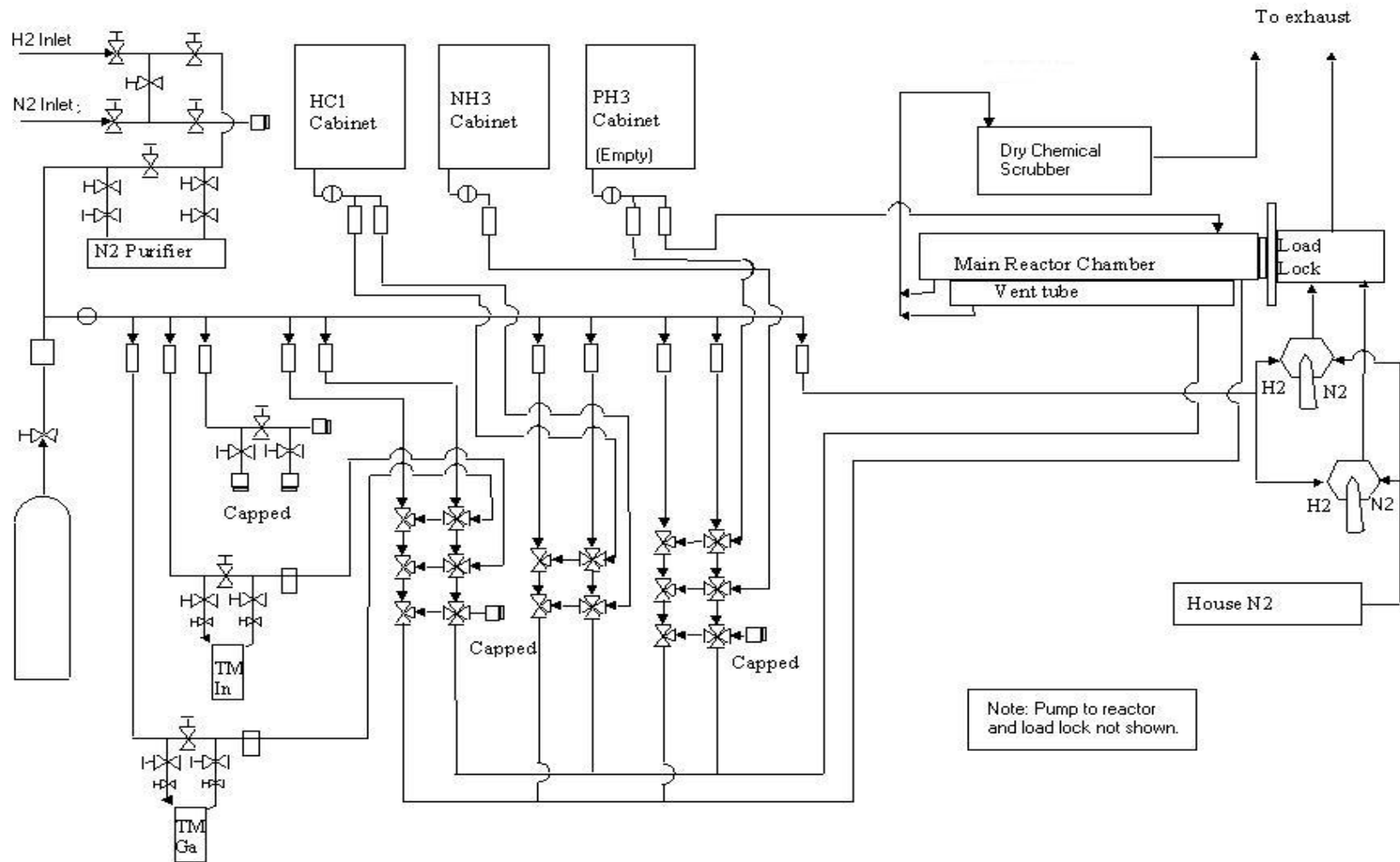


Figure 4-2. Process Flow Diagram (PFD) of H-MOVPE system [Ree02].

The surface of an H-MOVPE-grown sample is usually rough compare to a MOCVD surface because of the high growth rate and the tendency to grow N-terminated GaN, although this surface can be smoothed by chemical-mechanical polishing (CMP) or subsequent growth of Ga-terminated GaN by MOCVD.

4.3 Thick GaN Growth on Al₂O₃

Before starting the growth of GaN on Si substrates, thick GaN films were grown on Al₂O₃ and GaN/Al₂O₃ substrates to produce reference materials to compare with GaN films grown on Si substrate.

The GaN/Al₂O₃ template was grown by MOCVD and provided by Uniroyal optoelectronics. The thickness of the MOCVD-grown GaN film was 5 μm as measured by cross-sectional SEM. The thick GaN growth was performed at atmospheric pressure in a H₂ ambient. Before the growth, HCl was applied in the reactor for 10 sec to clean the substrate surface *in situ*. The TMG flow rate was maintained at 3.2 sccm, HCl (10 % HCl, 90 % N₂) flow rate was 4.8 sccm (Cl/Ga = 1.5), NH₃ flow rate was 2000 sccm (N/GA =570), and H₂ carrier flow rate was 1600 sccm. During the cooling process, NH₃ was provided to prevent GaN decomposition until the substrate temperature was below 300 °C.

The crystal quality of the Uniroyal starting GaN/sapphire materials was assessed by an XRD θ -2 θ scan and HR-XRD ω -rocking curve. Figure 4-3 shows the XRD results of the templates. It is noteworthy that the GaN (002) peak shows a secondary peak at around $2\theta = 31.1^\circ$ due to the Cu K β radiation. This secondary peak appears only when the film quality is excellent and should not be confused with GaN (100) that appears at $2\theta = 32.4^\circ$. The intense GaN (002) peak from the near-perfect lattice spacing is the

reason for this artifact. XRD also showed weak Al_2O_3 substrate peaks because the GaN film thickness was almost the same as the X-ray penetration depth ($\sim 5 \mu\text{m}$ for GaN [Pas01]).

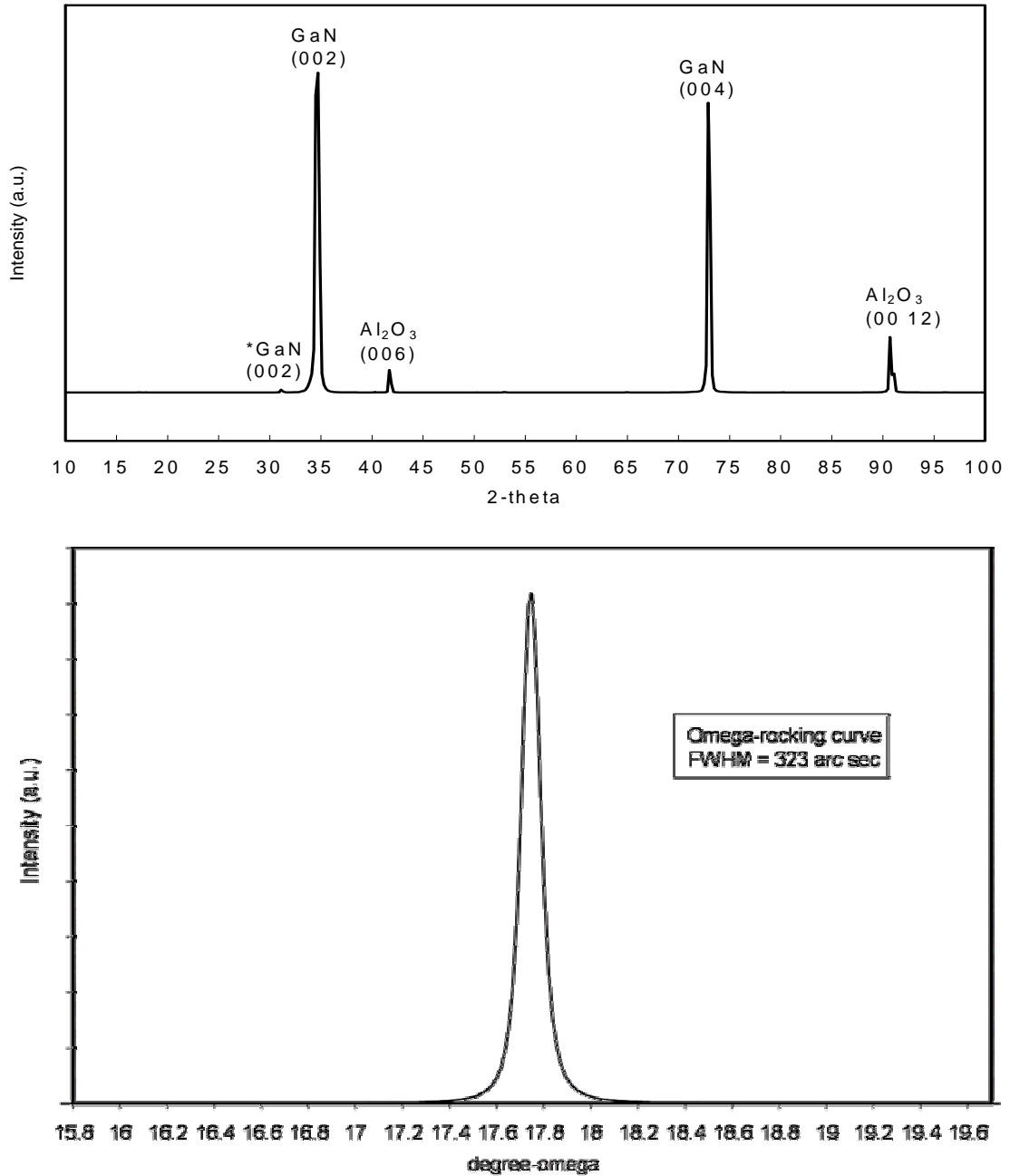


Figure 4-3. XRD θ - 2θ scan and ω -rocking curve of as received GaN/ Al_2O_3 template from Uniroyal Optoelectronics. * denotes the secondary peak due to $\text{Cu K}\beta$ radiation.

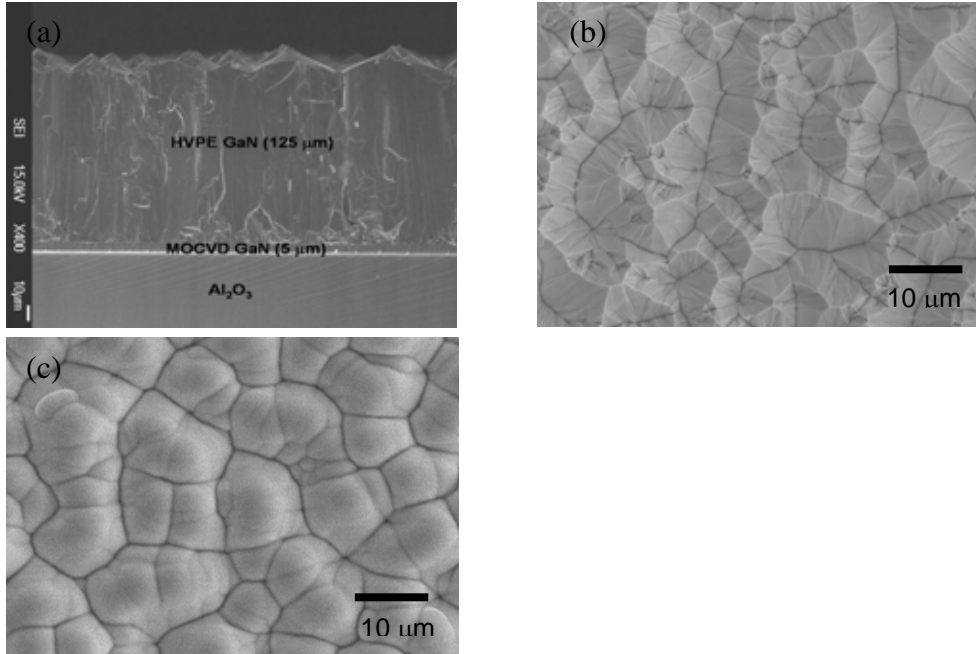


Figure 4-4. SEM images of GaN film (a) Cross-sectional SEM of 125 μm thick H-MOVPE GaN film on GaN/ Al_2O_3 template, (b) SEM plan-view of the same sample. (c) Plan-view of LT-HVPE smoothing layer.

A maximum thickness of 125 μm was obtained during the 10 hr growth. The film showed no cracks, although the surface was very rough, as shown in Figure 4-4 (a) and (b). The rough surface is due to the high growth rate and N-terminated surface of GaN observed in HT-HVPE growth. Therefore LT-HVPE GaN was grown at 560 $^{\circ}\text{C}$ to smooth the extremely rough surface as seen in Figure 4-4 (c). Although the structural quality of LT-GaN may be lower than GaN grown at higher temperature, the surface became smoother as observed by SEM. The surface of LT-GaN, however, is still not smooth enough to be measured by AFM to obtain RMS roughness. Subsequent growth of high quality MOCVD layer on LT-HVPE layer should be a good approach to smooth the surface and produce freestanding GaN substrate that can be used for epitaxial growth. Another approach to improve the surface roughness without sacrificing the crystal quality

is chemical mechanical polishing (CMP). These steps, however, were not carried out in this work.

The bowing of the film was measured by profilometer. The calculated radius of curvature was about 10 m, which is practically flat. (see Chapter 3 for discuss on method)

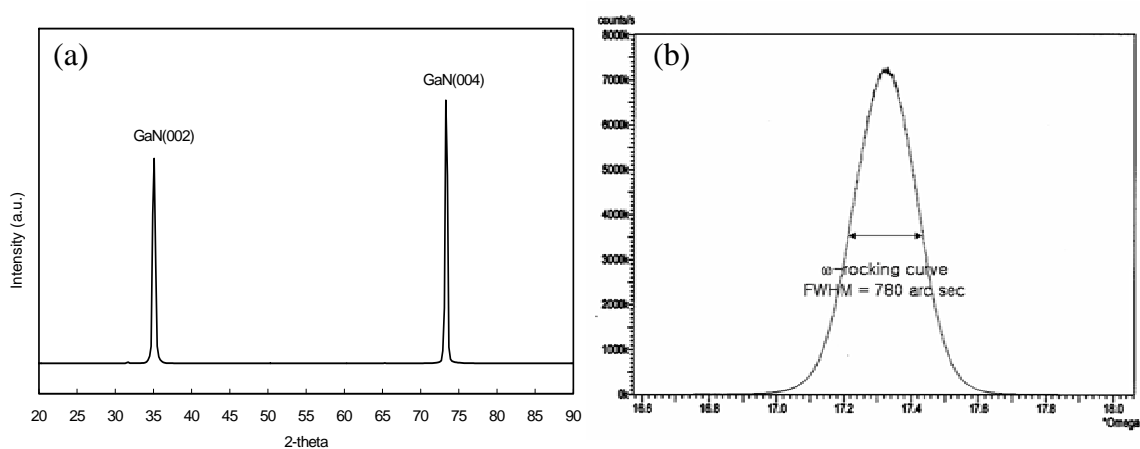


Figure 4-5. XRD of GaN film (a) XRD θ - 2θ scan of thick ($45\ \mu\text{m}$) GaN on GaN/ Al_2O_3 , (b) XRD ω -rocking curve of GaN (002) peak; FWHM = 780 arcsec.

Figure 4-5 (a) shows XRD θ - 2θ scan of a $45\ \mu\text{m}$ thick GaN on GaN/ Al_2O_3 template. Only the intense GaN (002) and GaN (004) peaks were observed consistent with a single crystal orientation. Figure 4-5 (b) shows typical XRD ω -rocking curve of GaN (002) peak. The 780 arcsec FWHM indicates that the grown GaN film has high structural quality.

AES analysis was performed to determine the chemical composition of the GaN film (Figure 4-6). The surface of the as grown GaN film showed oxygen and carbon peaks due to the surface adsorbed molecules during air exposure. The concentrations of C and O dropped significantly during the sputtering. Sputtering was carried out with 3 keV Ar^+ ion beam. Assuming a typical 10 nm/min sputtering rate, the thickness of C contained layer was $\sim 10\ \text{nm}$. After sputtering, Ga, N, and O were the main components of the GaN film.

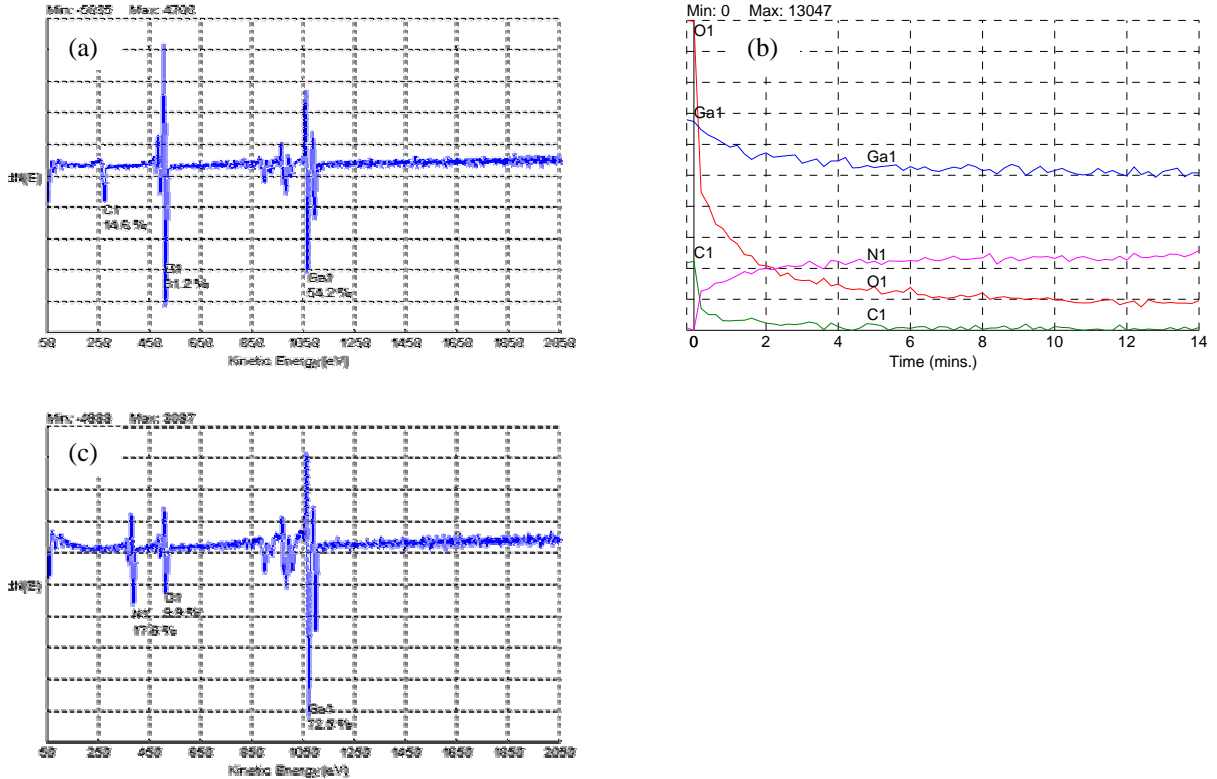


Figure 4-6. Auger Electron Spectroscopy of 45 μm thick GaN film (a) surface scan (b) sputtering depth profile (c) surface scan after sputtering.

The concentration of O (9.9 %) in the film was uniform as judged by AES sputtering depth profile after 4 min sputtering. Since a standard material that contains known value of oxygen in GaN is absent, the quantitative analysis by AES is not reliable. The extreme roughness ($\sim 0.8 \mu\text{m}$) of the film may be responsible for the high oxygen concentration because sputtering only removes part of the film when the film is very rough [Wan03]. In addition, the sputtered surface oxygen can re-adsorb due to the slow sputtering rate. The surface oxygen can be completely removed using higher sputtering rate as shown in Figure 3-6. Otherwise, GaN film had a uniform composition as judged by the AES depth profile.

Table 4-1 lists the electrical properties of 45 μm thick GaN film grown on Uniroyal GaN/ Al_2O_3 template by Hall measurement. It showed intrinsic n-type material with a

carrier concentration of $2.6 \times 10^{20} \text{ cm}^{-3}$ and Hall mobility ($45.9 \text{ cm}^2/\text{Vs}$). The electrical property measurements show that the H-MOVPE GaN films have very high background carrier concentration due to the O contamination or N-vacancy.

Table 4-1. Electrical properties of GaN film grown on GaN/Al₂O₃ template.

Sheet Resistance [Ω/square]	Sheet Hall Coefficient [cm^2/C]	Type	Thickness [μm]	Carrier concentration [$1/\text{cm}^3$]	Hall Mobility [cm^2/Vs]
0.11727	5.3823	n	45	2.6×10^{20}	45.9

Four-point probe was used to measure the sheet resistance of the as received GaN/Al₂O₃ template and the GaN films grown for 3 hrs on GaN/Al₂O₃. The results are shown in Table 4-2.

Table 4-2. Sheet resistance and resistivity measured by four-point probe.

Sample name	Sheet Resistance(Ω/sq)	Thickness (μm)	Resistivity ($\Omega \text{ cm}$)
3 hr growth on GaN/Uniroyal	3.3	30.3	0.01
GaN/Uniroyal as received	20.0	5	0.01

Sheet resistance is a property that depends on the thickness of the material, while resistivity is a material property that does not depend on the thickness. Both films showed $0.01 \Omega \text{ cm}$ resistivity. This fairly low resistivity shows that the GaN film was fairly conducting.

4.4 GaN Growth on Si

4.4.1 Growth of Thin and Thick GaN on Si

4.4.1.1 Nitronex GaN/Si template

The growth of high-quality thin (3 to 4 μm) GaN on Si is important for GaN/Si-based device applications. Utilizing this relatively low ($850 \text{ }^\circ\text{C}$) growth temperature, GaN could be grown with a device relevant thickness (3 to 4 μm), and crack-free GaN on the GaN/AlGaN/AlN/Si template provided by Nitronex. In part, the lower growth

temperature reduced the thermal expansion effects by ~ 20 % over that of a high temperature (1050 °C) growth.

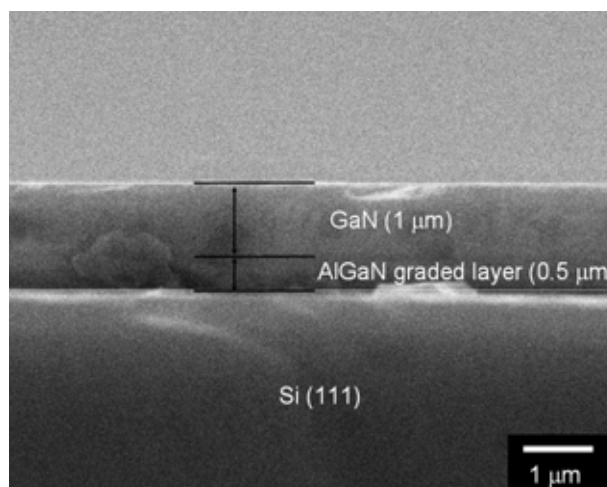


Figure 4-7. X-SEM image of GaN on Si using AlGaN graded layer (provided by Nitronex).

Although ~ 7 μm thick crack-free GaN on Si has been reported [Kro03] incorporating multiple AlN interlayers, the maximum thickness of a commercially available crack-free GaN layer on Si is about 1 μm [We03]. In this case [We03], graded AlGaN interlayers were used between GaN and Si. Trimethylaluminum (TMA) and ammonia (NH₃) were used to grow the AlN buffer layer, and trimethylgallium (TMG) was added into the system to grow compositionally graded AlGaN layer. Finally, the GaN layer was grown on the AlGaN graded layer at 1050 °C. The thickness of the GaN film was 1 μm and that of AlGaN graded layer was about 0.5 μm as shown in Figure 4-7.

XRD θ -2 θ scan (Figure 4-8 (a)) shows several AlGaN graded layer peaks with a strong substrate peak. The sharp and multiple AlGaN peaks indicate that the Ga/Al ratio in the graded AlGaN layer was not continuously changing but had discrete values. The GaN (002) peak of the received film, determined by FWHM of the XRD ω -rocking curve, shows high crystal quality (800 arcsec), as shown in Figure 4-8 (b), but not as high

quality as the GaN film grown on Al_2O_3 . This material was used as a substrate for thick GaN growth.

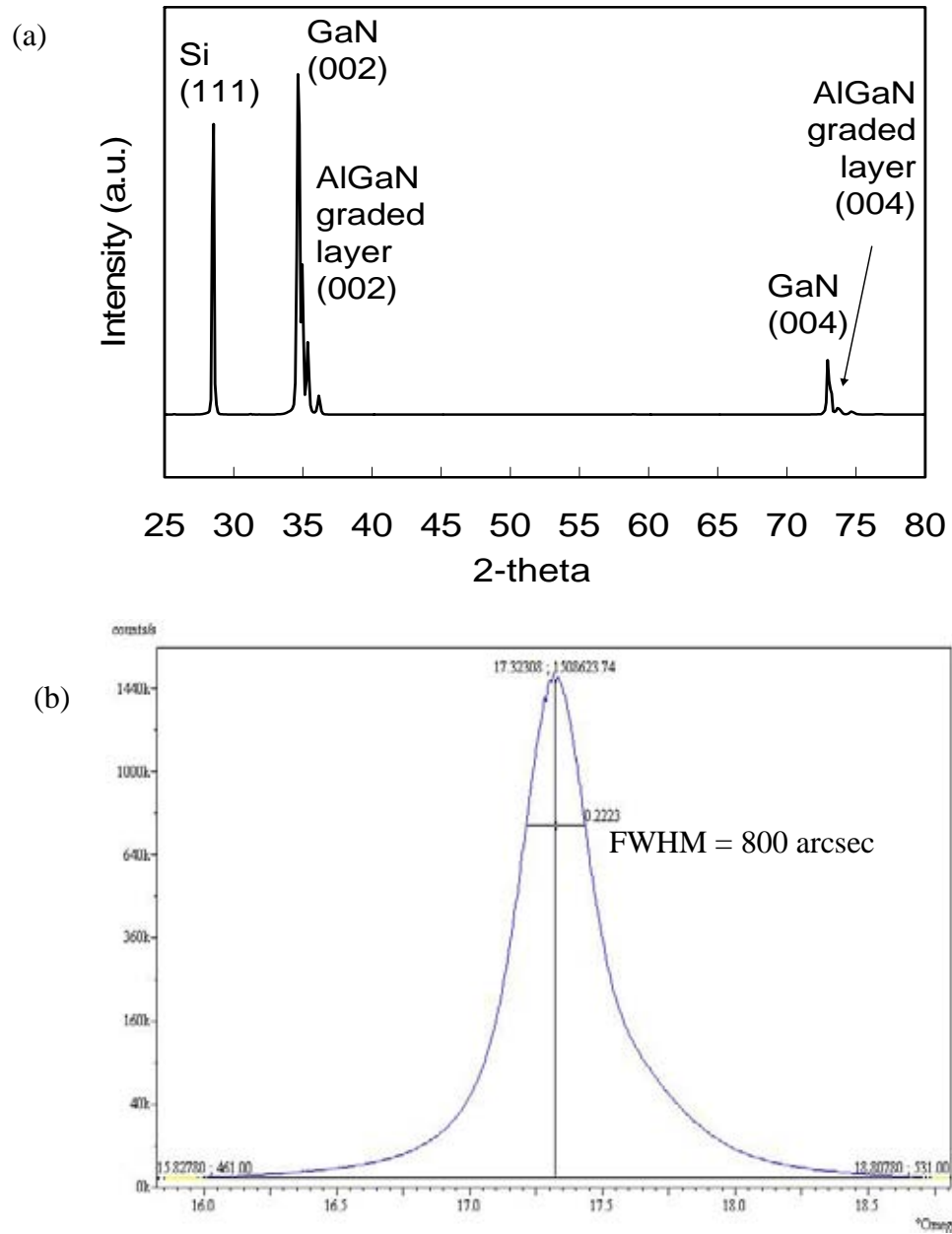


Figure 4-8. XRD θ - 2θ scan and HR-XRD ω -rocking curve of as received GaN/Si from Nitronex, FWHM = 0.222° (800 arcsec).

4.4.1.2 Growth of Thin GaN Using Nitronex Template

Under the selected growth conditions ($\text{Cl}/\text{Ga} = 1.5$, $\text{N}/\text{Ga} = 570$, $T = 850^\circ\text{C}$), a 10 to 15 $\mu\text{m}/\text{hr}$ growth rate is observed. Film thicknesses were measured by cross sectional SEM from cleaved samples. To achieve device relevant 3 to 4 μm thick GaN, 15 min growth time was performed. Figure 4-9 shows the plan and cross-sectional views of crack-free, 2 μm thick GaN grown on GaN/Si (111).

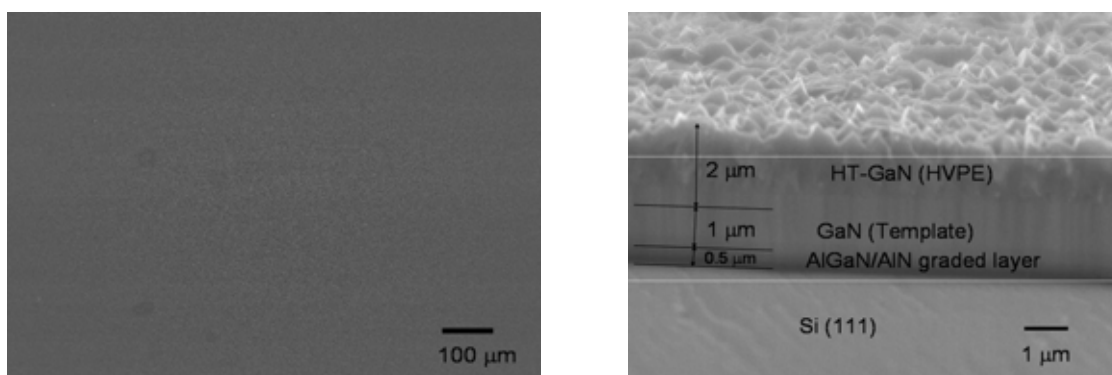


Figure 4-9. SEM plan and cross sectional views of 2 μm H-MOVPE + 1 μm MOVPE crack-free GaN grown on AlGaN/Si graded layer.

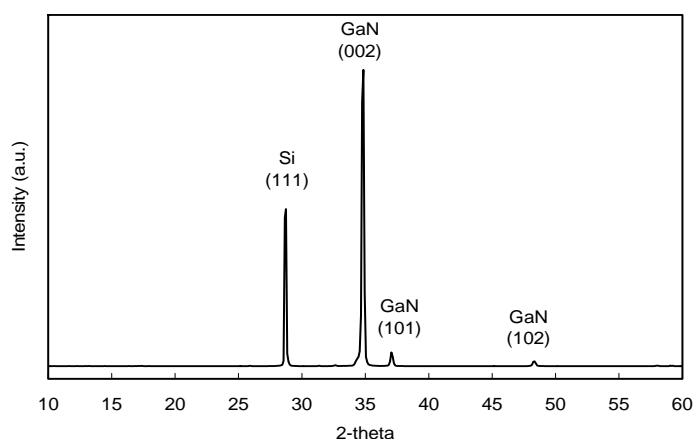


Figure 4-10. XRD θ - 2θ scan of 2 μm H-MOVPE + 1 μm MOVPE crack-free GaN grown on AlGaN/Si graded layer.

No cracks were observed in the 1 cm x 1 cm sample presumably due to the relatively low (850°C) growth temperature. The rough surface is a typical feature of H-MOVPE. An average roughness of 830 nm was measured by profilometry (Dektak II).

Figure 4-10 shows XRD θ - 2θ scan of 3 μm thick GaN film (2 μm HVPE + 1 μm GaN template) on AlGaIn/Si substrate. Intense GaN (002), small (101), (102) peaks, and Si (111) substrate peaks show that the GaN film was highly textured along the [002] axis.

4.4.1.3 Growth of Thick GaN Using the Nitronex Template

Thick ($> 20 \mu\text{m}$) GaN growth was carried out using the same procedure but with a longer growth time of 30 min to 4 hrs. Most samples grown in H-MOVPE and thicker than 7 μm on bare Si substrates and GaN/Si templates showed cracks regardless of cooling rate or annealing process, as exemplified seen in Figure 4-11.

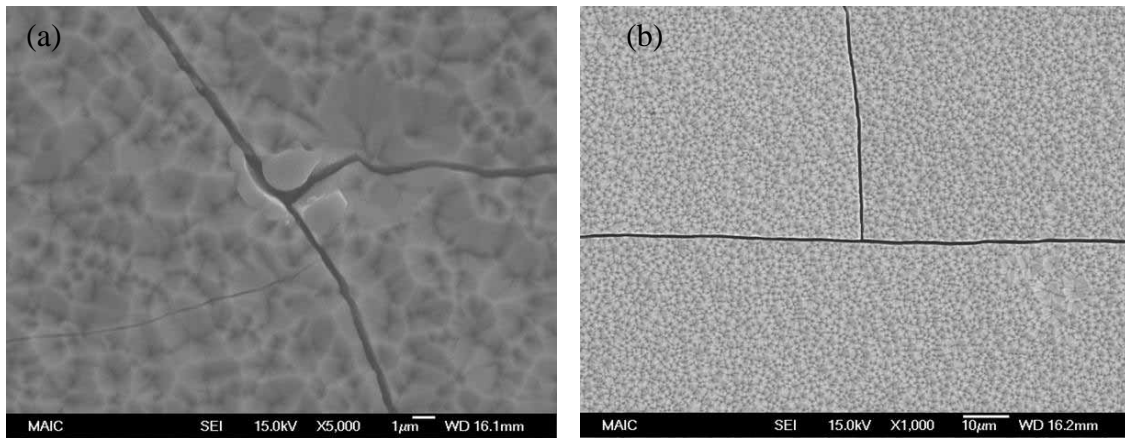


Figure 4-11. SEM plan-views of thick (55 μm) GaN films grown on GaN/Si templates (4 hr) with (a) fast cooling and (b) slow cooling. Note two micrographs are at different magnification.

Cracks can be generated during growth or cooling due to the excess tensile stress caused by large lattice and thermal expansion differences.

It was observed that the cracks penetrated through the Si substrate and separation occurred inside the Si, as shown in Figure 4-12.

Similar phenomena often occur during the growth of GaN on GaN/AlGaIn/AlN/Si template. Examining the cracked pieces showed that the strong cohesion between GaN and Si (or AlN and Si in GaN/AlGaIn/AlN/Si template case), as well as the brittleness of

Si, were responsible for cracking to take place in pre interior of the Si wafer. The nano-indentation hardness of the GaN, AlN, and Si are 20 [Now99], 18 [Yon02] and 14 GPa [Suz96], respectively. This brittleness of Si added with the large tensile stress (chapter 3) created by the lattice mismatch and thermal expansion differences makes the growth of crack-free GaN on Si even more challenging.

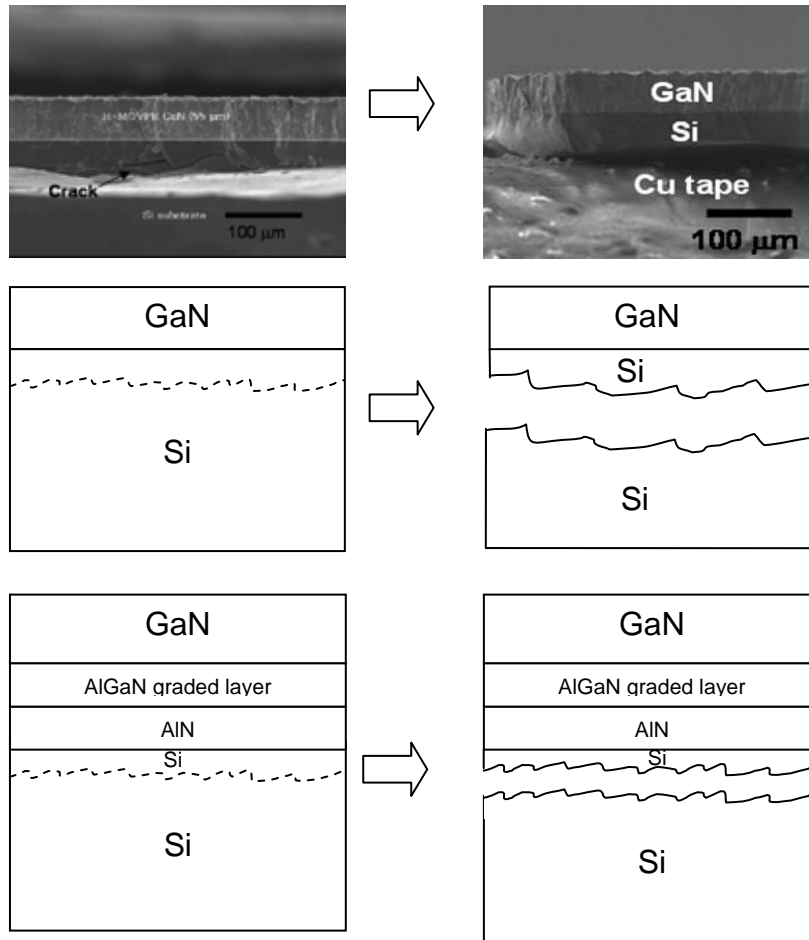


Figure 4-12. Schematic of crack generation of GaN on Si and GaN on Nitronex template. Cracking penetration to Si were observed in both cases.

To determine the crystal quality, XRD θ - 2θ scan was performed using a Philips APD 3720. The resulting intense GaN(002) and GaN(004) peaks are shown in Figure 4-13.

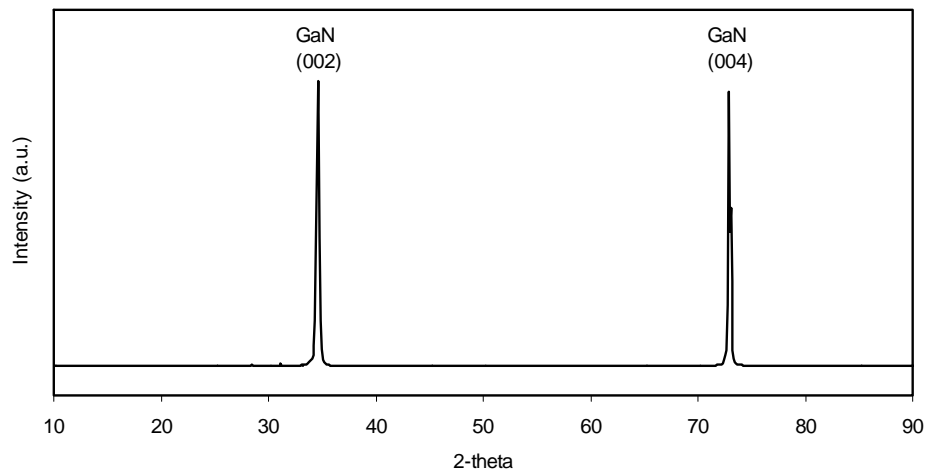


Figure 4-13. XRD θ - 2θ scan of thick (55 μm) GaN film on GaN/Si template for 4 hr.

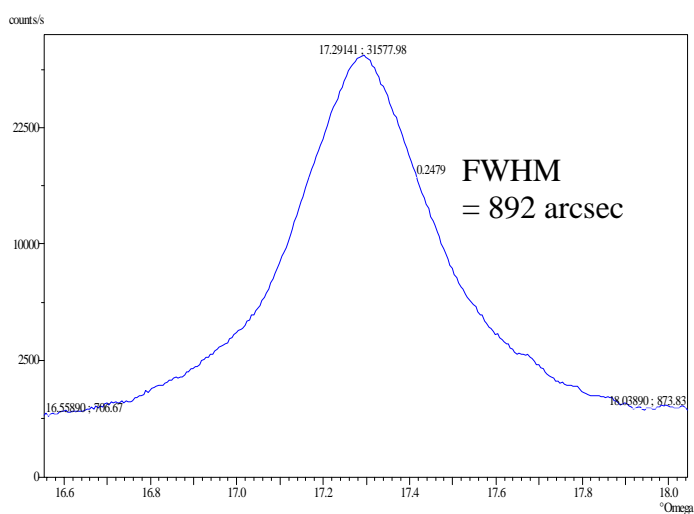


Figure 4-14. XRD ω -rocking curve of GaN (002) peak of 55 μm thick GaN. FWHM = 0.248° (892 arcsec).

The result implies that the d-spacings of (002) and (004) planes are uniform. The ω -rocking curve result is shown in Figure 4-14. The FWHM of the ω -rocking curve of the GaN (002) peak is 0.248° (892 arcsec). These two results, XRD θ - 2θ scan and ω -rocking curve, confirm that the grown GaN film is a high quality crystal (similar to the received GaN/Si template), although the film was cracked.

4.4.2 Growth of Thick GaN on Si Using InN Interlayers

Thick GaN films grown on Si demonstrate significant cracking problems due to the excess tensile stress produced by large lattice and TEC mismatch between the GaN film and Si substrates. To overcome cracking problems, different techniques have been tried, including multiple AlN interlayers [Sch06, Mas06, Yu06, Jam05, Zha05, Rei03, Lia01, Ven05], AlGaN graded layers [Mar01, We03, Abl05, Wan05], patterned Si [Zam01], and *in situ* SiN masking (non-uniform deposition) [Dad03]. All the methods showed some decrease of bowing and cracking, but no method successfully produced crack-free thick (> 20 μm) films because there still remains excessive tensile stress, as well as strong cohesion between GaN (or AlN buffer layer) and Si. This investigator is not aware of any report of using InN as a buffer layer.

To avoid cracks, InN was used as a buffer material to provide a weak bond between Si and the interfacial layer, since InN is known to be a softer material than GaN and Si (Nano indentation hardness: 11 [Edg97], 20 [Now99], and 14 GPa [Suz96] for InN, GaN, and Si, respectively). Also the bond strength of In-N (7.7 eV) is similar to that of Si-Si (7 eV) and less than the Ga-N (8.9 eV) or Al-N (11.5 eV) and Si-N (10.5 eV). The bond strength of Si-Si is the weakest. Therefore, the cracking penetration to Si substrate is expected and was observed as shown in Figure 4-12.

Taking advantage of the low decomposition temperature and softness of InN, indirect/weak contacts between GaN film and Si substrate could be established via the InN interlayer. InN buffer materials and GaN films were all grown by H-MOVPE technique. Easy switching of precursors made it possible to grow a variety of InN structures and GaN films without transferring to another reactor. InN was grown on Si,

followed by a thin low temperature (LT)-GaN to prevent decomposition of the InN, and finally high temperature (HT)-GaN. The growth schematic to obtain crack-free thick GaN on Si is illustrated in Figure 4-15.

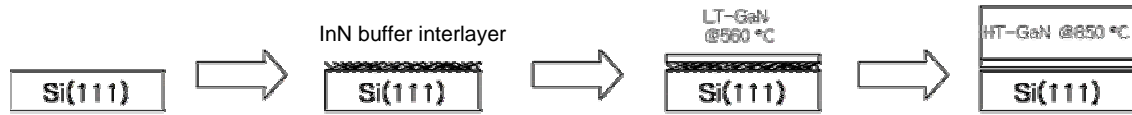


Figure 4-15. The schematic to obtain thick GaN on Si(111) using InN buffer materials.

After InN growth at 560 to 600 °C, the temperature was reset to 560 °C and a low temperature (LT)-GaN was deposited at 560 °C for 10 to 30 min to cover the InN before starting growth of the thick HT-GaN film. After LT-GaN deposition, the temperature was increased to 850 °C and the HT-GaN was grown. During the heating and cooling processes N_2 was always provided. After growth, the reactor was cooled in N_2 ambient. The cooling rate was approximately 15 °C/min.

4.4.2.1 InN Growth on Si(111)

InN columnar film, small nanorods ($d = 250$ nm), large nanorods ($d = 500$ nm), and microrods were grown on Si substrates for comparison.

Table 4-3. Growth conditions for InN buffer interlayer on Si.

Growth T (°C)	Cl/In	N/In	Time	Feature
560	1	2500	1 hr	(a) Columnar Film
600	4	250	20 min	(b) Nanorods ($d = 250$ nm)
600	4	250	1 hr	(c) Nanorods ($d = 500$ nm)
650	5	250	1 hr	(d) Microrods

The growth conditions for the various samples are tabulated in Table 4-3.

Figure 4-16 shows the plan-view of the SEM images of each of the buffer interlayers evaluated. All InN material showed well-faceted hexagonal structures and single crystallinity as confirmed by TEM-Diffraction Pattern (DP) spot patterns as

presented in Chapter 5. At low growth temperature (560 °C), low Cl/In (1), and high N/In ratios (2500), InN columnar polycrystalline films were grown. By changing the growth time and the conditions as indicated in Table 4-3, the other microstructures were grown. The morphology evolution depending upon the growth parameters are presented in details in Chapter 5.

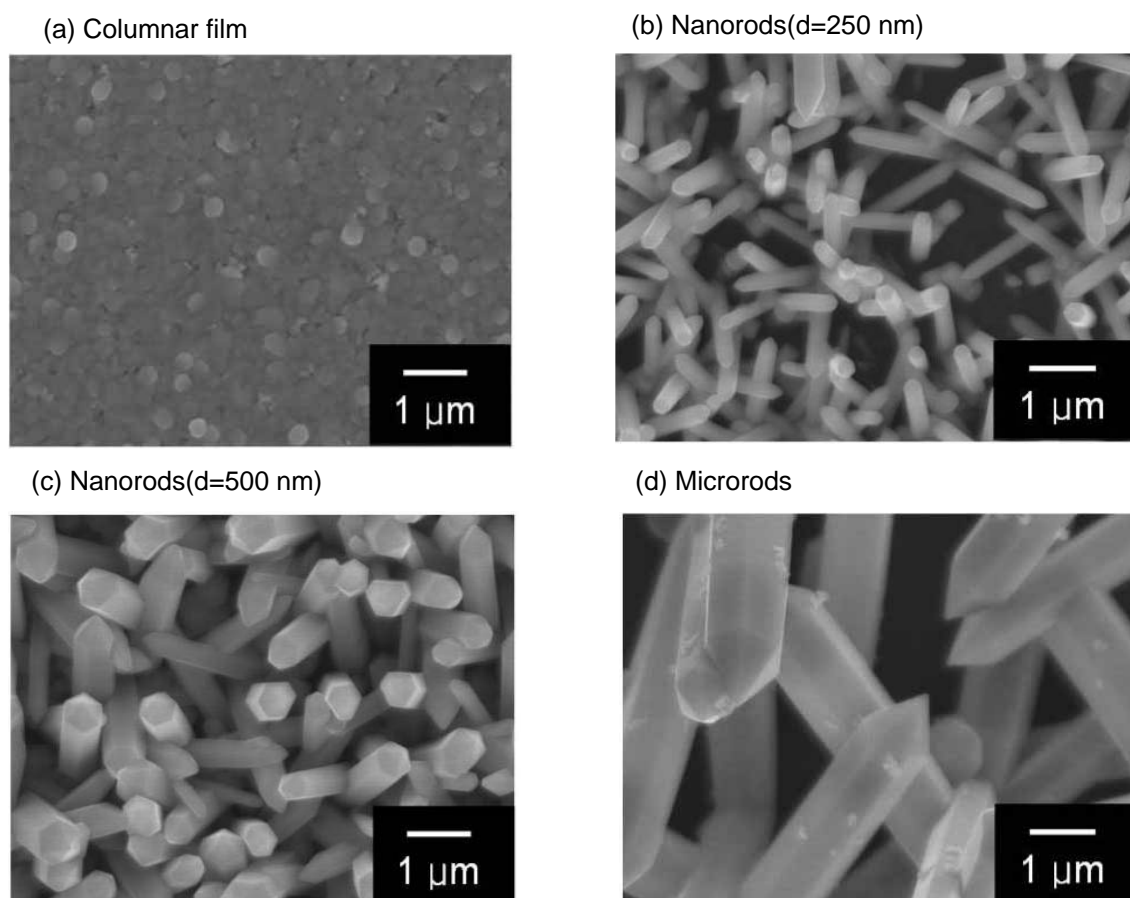


Figure 4-16. SEM plan-view of InN columnar film, small nanorods ($d = 250$ nm), large nanorods ($d = 500$ nm), and microrods grown on Si(111).

4.4.2.2 LT-GaN Growth on InN Buffer Materials/Si(111)

The 4 different templates which are shown in Figure 4-16 were used as templates for subsequent GaN growth. LT (560 °C)-GaN was grown on the 4 different templates for comparison of the structural effects of InN buffer material. Figure 4-17 shows the

SEM images of the LT-GaN grown on various InN crystals for 10, 20, and 30 min. The growth conditions for LT-GaN were set as $T = 560\text{ }^{\circ}\text{C}$, $\text{Cl/In} = 1.5$, and $\text{N/In} = 570$.

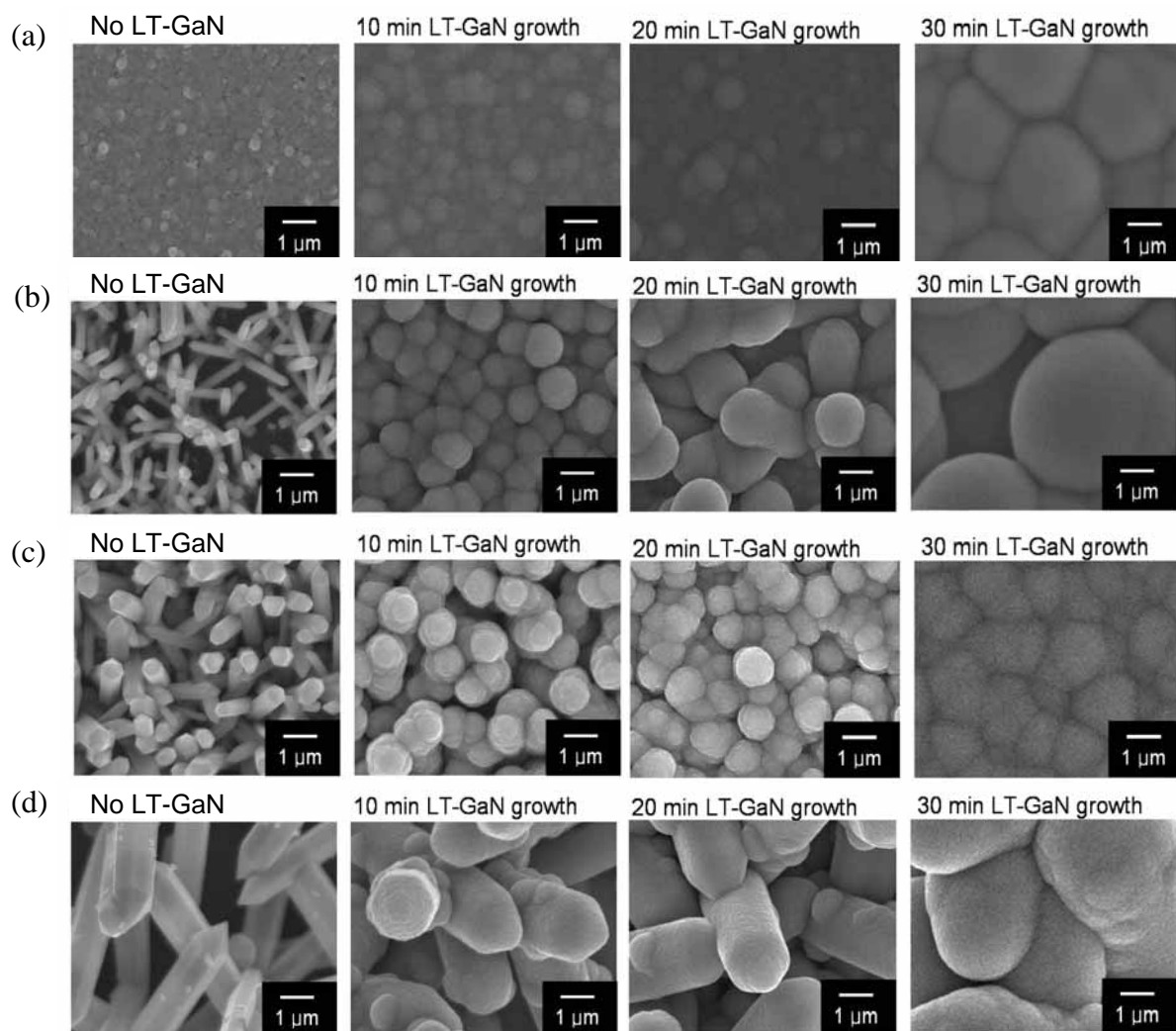


Figure 4-17. SEM plan-view of 10, 20, and 30 min LT-GaN grown on (a) InN columnar film, (b) smaller nanorods ($d = 250\text{ nm}$), (c) larger nanorods ($d = 500\text{ nm}$), and (d) microrods.

Significant changes in the morphology were observed as the growth time increased from 10 to 30 min. Only InN columnar films and larger nanorods ($d = 500\text{ nm}$) provided uniform coverage of LT-GaN (Figure 4-17 (a) and (c)), while the smaller nanorods ($d = 250\text{ nm}$) and microrods demonstrated non-uniform coverage of LT-GaN (Figure 4-17 (b)

and (d)). From the observation of non-uniform and small InN samples it was found that GaN deposition occurred mainly on the InN surface rather than on the Si substrate.

Figure 4-18 (a) shows a wider area SEM plan-view of 30 min LT-GaN grown on InN nanorods. LT-GaN started to coalesce after 30 min, and an interesting embossed pattern could be seen. The cross-sectional view (Figure 4-18 (b)) shows that the thickness of the LT-GaN was $\sim 4 \mu\text{m}$ and that voids were formed at the interface. XRD θ - 2θ scan (Figure 4-18 (c)) showed GaN (002), InN (002), and InN (101) peaks, as well as the Si (111) substrate peak. This data shows that InN nanorods still exist after 30 min LT-GaN growth. This is expected since $560 \text{ }^\circ\text{C}$ is well below the decomposition temperature of InN. No In metal was detected by XRD.

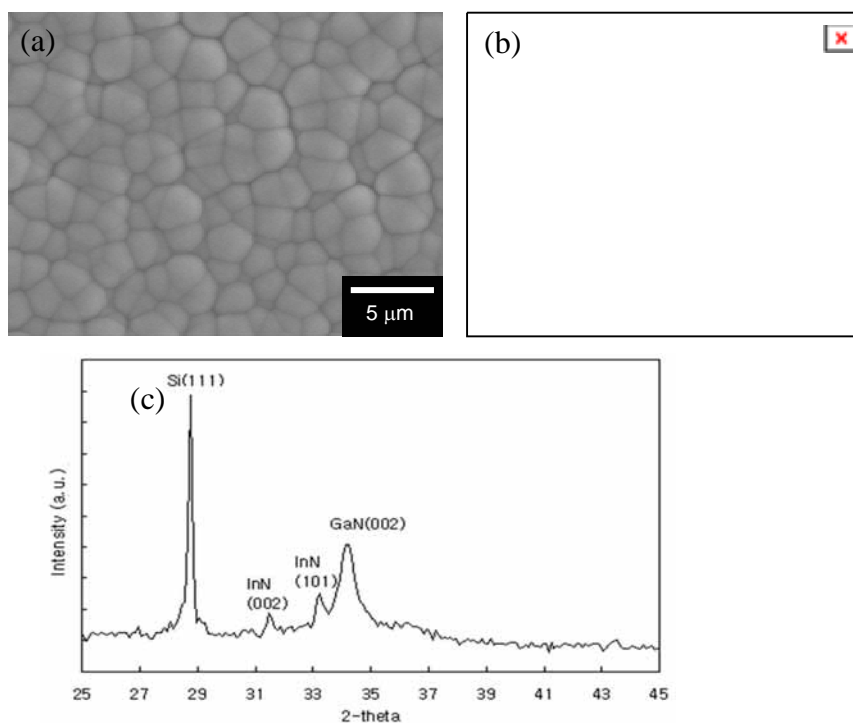


Figure 4-18. LT-GaN deposited on InN nanorods ($d = 500 \text{ nm}$) on Si(111) for 30 min ($\sim 4 \mu\text{m}$) (a) plan-view of LT-GaN on InN nanorods, (b) cross-sectional view (c) XRD θ - 2θ scan

4.4.2.3 Thick HT-GaN Growth on LT-GaN/InN/Si(111)

Thick GaN films were next grown at 850 °C for 2 hr after 30 min LT-GaN growth on InN crystals. The growth condition for HT-GaN was the same as the base growth conditions used for growth of GaN on sapphire (Cl/Ga = 1.5, N/Ga = 570, and T = 850 °C). N₂ was used as the carrier gas due to the instability of InN in H₂.

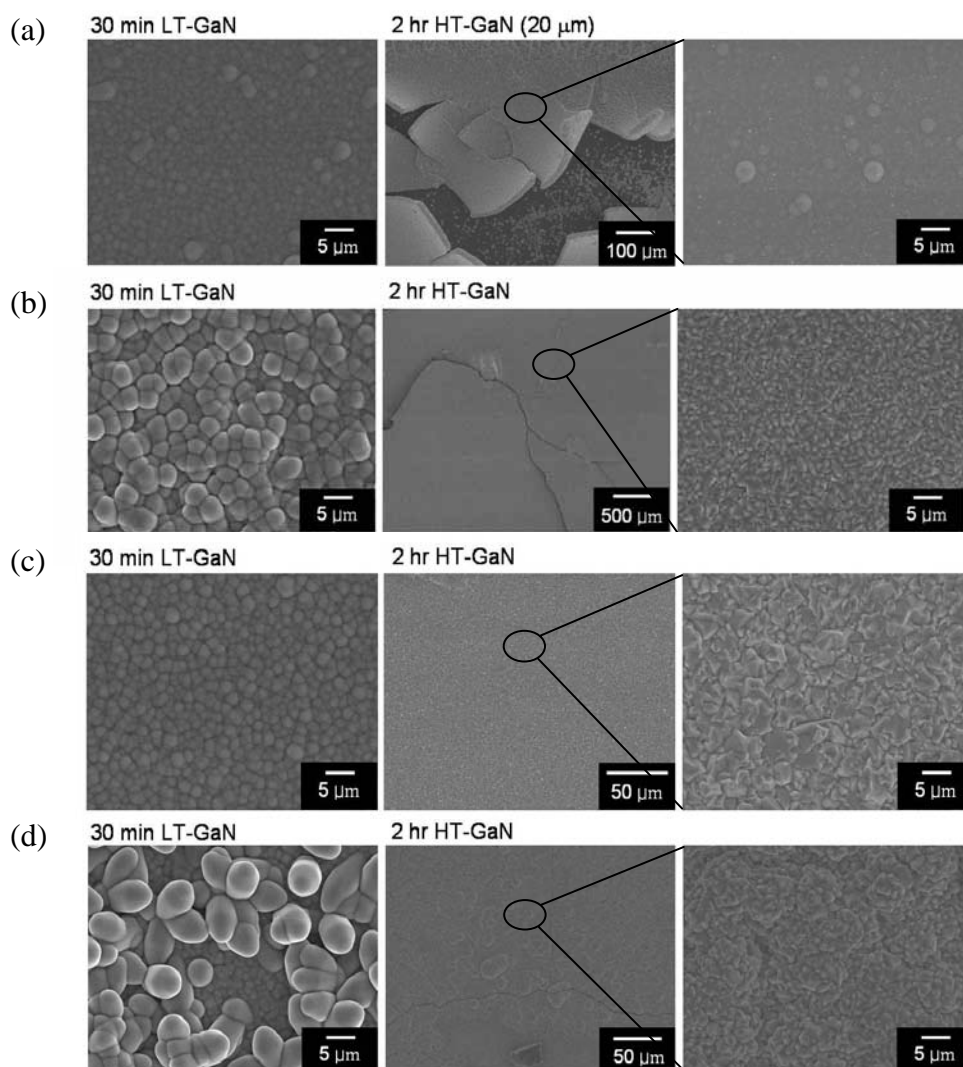


Figure 4-19. HT-GaN/LT-GaN growth on various InN structures (a) InN columnar film, (b) small nanorods ($d = 250$ nm), (c) large nanorods ($d = 500$ nm), and (d) microrods. The right figures show expanded views of the surface of HT-GaN films.

Figure 4-19 shows the morphology of thick ($\sim 20 \mu\text{m}$) GaN films grown on LT-GaN for each of the 4 different InN interlayer microstructure. Figure 4-19 (a) shows thick GaN grown on the InN columnar film/Si. Significant peeling of the GaN film is evident. From observation of GaN deposition on the surface exposed by the cracking process, it was confirmed that the cracking and peeling occurred during the growth and not during the cooling. Figure 4-19 (b) shows the thick GaN grown on smaller InN nanorods ($d = 250 \text{ nm}$) over Si(111). Cracks were observed due to the non-uniform deposition of InN nanorods and LT-GaN. Figure 4-19 (c) shows the best result of crack-free thick GaN, which was grown on the large InN nanorod ($d = 500 \text{ nm}$) interlayer. Although the surface is still rough, it is clear that dense and uniform InN nanorods are a good candidate structure for thick, crack-free GaN growth on Si(111). Figure 4-19 (d) shows cracking of thick GaN film on InN microrods on Si. Again, the observation of cracks correlated with the films exhibiting more pronounced surface roughness.

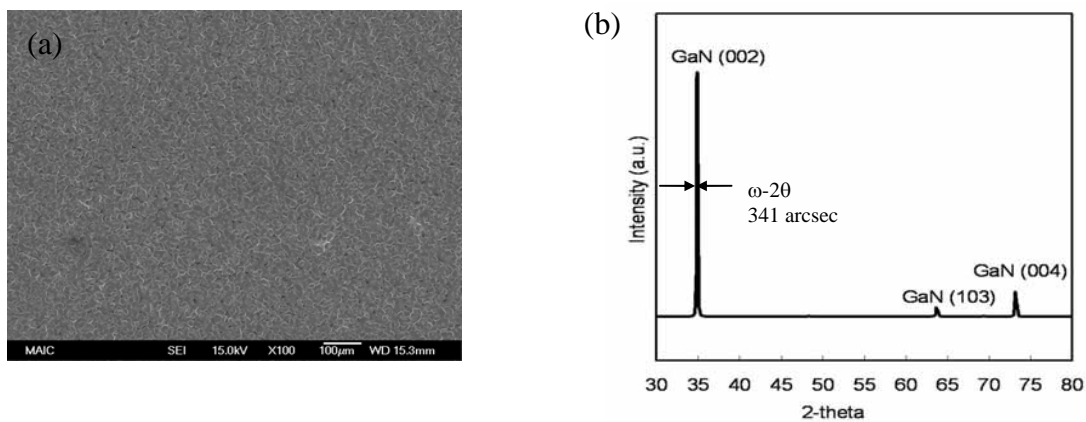


Figure 4-20. Thick ($28 \mu\text{m}$) and freestanding (self-separated) GaN grown on InN nanorods/Si (a) SEM plan-view of the GaN film, (b) XRD θ - 2θ scan.

The GaN film occasionally self-separated from the Si substrates without effort. SEM and XRD results of freestanding and crack-free GaN film ($28 \mu\text{m}$ thick) grown on InN nanorods ($d = 500 \text{ nm}$)/Si (111) substrates are shown in Figure 4-20.

No cracks were observed by SEM over the wide range of the film, as seen in Figure 4-20 (a). Low resolution XRD (Figure 4-20 (b)) shows GaN (002), (004), and (103) peaks. No InN was detected presumably because at the growth temperature (850 °C), the InN dissolved into the $\text{In}_x\text{Ga}_{1-x}\text{N}$. The film was polycrystalline, but highly textured along the [002] axis with an FWHM of 341 arcsec.

Figure 4-21 shows a cross-sectional view of crack-free thick (40 μm) GaN grown on Si substrate using dense and large ($d = 500 \text{ nm}$) InN nanorods. In this case, self-separation did not occur. InN nanorods at the interface were not visible after HT-GaN. InN likely dissolved into GaN to form $\text{In}_x\text{Ga}_{1-x}\text{N}$ alloy at the interface. Another possibility is that the InN thermal decomposed to give a high N_2 pressure. This could provide a force for new crack propagation, similar to splitting Si with large H in implants. Therefore, the occasional self-separations may be related to the two preferential paths: InN decomposition leading self-separation and $\text{In}_x\text{Ga}_{1-x}\text{N}$ alloy formation for adhesive growth.

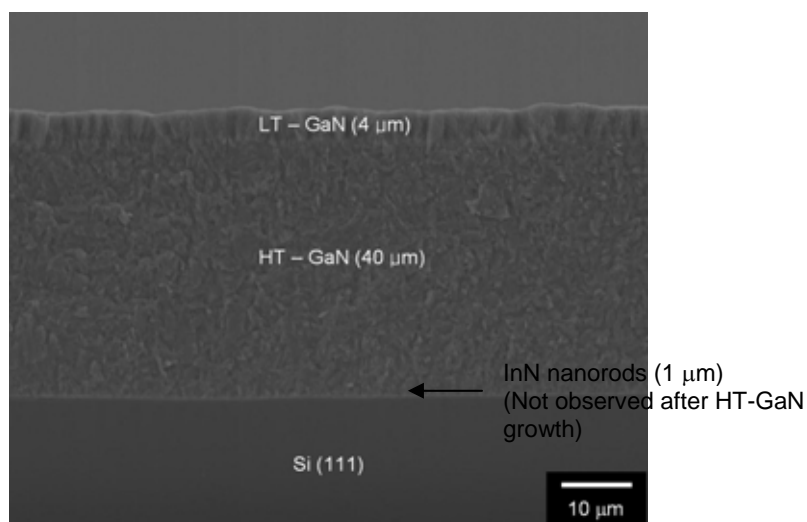


Figure 4-21. Cross-sectional view of thick GaN grown on InN nanorods/Si(111). The surface was covered by LT-HVPE layer grown after thick HT-HVPE.

Figure 4-22 compares an HT-GaN grown rough surface with a LT-GaN capped surface. The rough surface was covered by growing a LT-GaN (4 μm) layer after the thick film growth to smooth the surface. It is noted that the capping layer surface resembles the LT-GaN grown on InN nanorods. The surface of LT-GaN, however, is not smooth for direct device fabrication. In fact, the electrical properties and crystal quality of the LT-GaN are inferior. Since one goal was to grow thick GaN substrate using Si, high quality MOCVD GaN should be grown on this thick GaN substrate. Before MOCVD growth, CMP should be carried out to smooth the surface of HT-GaN.

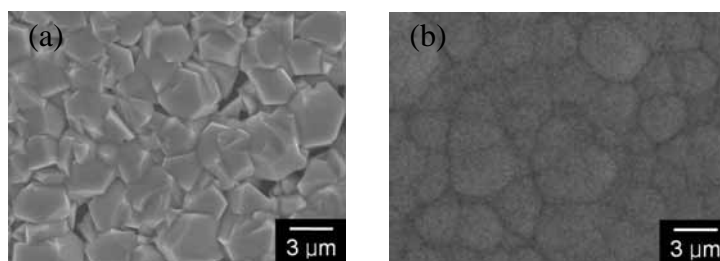


Figure 4-22. SEM plan-view of thick GaN grown on InN nanorods ($d=500\text{ nm}$)/Si(111). (a) as grown HT-GaN surface, (b) covered LT-GaN surface.

4.5 Conclusions

Crack-free and thin (3 μm) GaN was successfully grown on GaN/AlGaIn/Si templates utilizing a relatively low (850 $^{\circ}\text{C}$) growth temperature.

Attempts to grow thicker films resulted in cracking. Cracks were observed in thick (> 7 μm) GaN films that were grown either directly on Si(111) or grown on multiple AlGaIn graded layers/Si templates. It was observed that the cracks penetrated to the Si substrate. Strong cohesion between GaN and Si, as well as the brittleness of Si, were responsible for the cracking.

To avoid cracks, InN columnar film, nanorods with different diameters ($d = 250\text{ nm}$ and $d = 500\text{ nm}$), and microrods were grown as a buffer material on Si(111). Low

temperature (560 °C) GaN was deposited thereafter to prevent InN from decomposing at the higher growth temperature used to grow thick GaN. LT-GaN uniformly covered only InN columnar films and nanorods ($d = 500$ nm), while nanorods ($d = 250$ nm) and microrods demonstrated non-uniform coverage of LT-GaN.

It was found that the structure of the InN interlayer was critical to growing crack-free GaN film. Thick GaN grown on InN columnar film as well as smaller nanorods ($d = 250$ nm) and microrods exhibited cracks. Crack-free thick GaN film, however, was grown on the dense InN nanorods ($d = 500$ nm) interlayered on Si(111). Voids at the interface were found to be beneficial to growing crack-free GaN. The crack-free GaN film grown on InN nanorods/Si showed strong texturing in the [0002] axis (FWHM of $\omega-2\theta$ rocking curve: 341 arcsec), although it was polycrystalline. Crack-free (crack-free area: 10 mm x 5 mm), 40 μm thick GaN was successfully grown on Si substrates using mats of dense nanorods interlayer. GaN occasionally self-separated from the Si substrate without effort, due to the low decomposition temperature of InN. The results show that using InN dense nanorods ($d = 500$ nm) over Si is a promising technique to grow crack-free thick GaN on Si substrates.

CHAPTER 5 GROWTH OF INDIUM NITRIDE NANORODS BY H-MOVPE

5.1 Introduction

The group III nitrides are receiving considerable attention as host semiconductors for optoelectronic and high-power, high-temperature electronic device applications. Among the nitrides, InN has the smallest effective mass and highest electron drift velocity, making it a particularly attractive material for high-speed electronic devices. The growth of one-dimensional (1D) semiconductors, such as nanowires and nanorods, holds the promise of improved crystal quality, as well as the ability to use quantum size effects to adjust the material properties. Therefore, coupling the excellent transport properties of InN with the advantages of nanostructured materials may offer superior electronic device fabrication.

GaN [Kuy04, Han97, Deb05] and InN 1D structures [Lia02, Lan04, Tan04] have been demonstrated using an Au catalyst to promote growth by a vapor-liquid-solid (VLS) mechanism. Closed-spaced vapor transport using pure indium metal or In_2O_3 and ammonia has been used to grow InN nanostructures without an external catalyst [Zha02, Joh04a, Vad05, Luo05]. It is possible that the liquid In precursor structures self-seed the growth to provide a VLS mechanism.

It would be helpful for device fabrications to use chemical vapor deposition (CVD) to produce InN nanostructures in a controlled manner. The effect of input NH_3/TMIIn molar ratio on the growth of InN films has been studied [Joh04j, Dra06, Sin04]. Its influence on InN 1D structures, however, has not been reported since most studies

[Zha02, Joh04a, Vad05, Luo05] used closed spaced vapor transport, in which it is difficult to control the molar ratio. There are a limited number of reports of synthesis of InN nanostructures by CVD [Par01, Sar05], HVPE [Ond02], and MBE [Dim04, Oli03, Sto06], which can independently control the inlet molar ratios. Nevertheless, no morphological study by changing process parameters such as N/In, Cl/In ratios, and growth temperature has been reported.

In the present work, InN films and nanorods were grown by H-MOVPE. An advantage of H-MOVPE is that the added HCl can prevent formation of In droplets [Kan04], reducing the need for excess NH_3 and allowing growth of InN at a reasonable rate. It was also hoped that the surface morphology would improve given that the deposition reaction is reversible. The promise of improved structural quality in InN nanorods is that, once nucleated, the ratio of the contact area to free surface area is much less than in the case of film, reducing substrate effects. This difference, in addition to the potential for dislocations terminating at the sidewalls, should significantly improve the structural quality of the material. Furthermore, a hot-walled reactor increases the extent of NH_3 cracking.

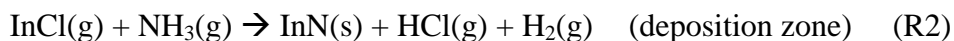
The surface morphology evolution was observed with the effects of the growth temperature, HCl/TMIn and NH_3 /TMIn molar ratios to determine optimal growth conditions for InN nanorods.

The boundaries between InN growth and etch regimes were calculated based on chemical equilibrium and the results were compared with experimental data. Extensive characterizations focusing on InN nanorods were carried out and the structural, chemical, optical, and electrical properties of InN nanorods were measured.

As an application, the high surface to volume ratio of nanorods renders them potential candidates for sensing applications. Therefore, InN nanorods were fabricated with Pt nanoparticle deposition to function as an H₂ sensor and promising results were obtained.

5.2 Chemical Reactions for InN Growth by H-MOVPE

H-MOVPE is a versatile technique because it can independently control N/In, Cl/In molar ratios, and growth temperature. InN crystals were grown by the H-MOVPE technique. The indium and nitrogen sources were TMIIn (TMI solution, Epichem) and NH₃ (Anhydrous Grade 5, Matheson-Trigas), respectively and HCl (10 % HCl, 90 % N₂, Air Products) was used to *in situ* form InCl precursor. The overall reactions of InN growth are as following:



TMIIn reacts with HCl and forms InCl and by-products such as CH₄ and C₂H₆ (R1). The reactions in H₂ ambient were not considered since InN is generally grown in inert environment. InCl₃ and other chlorides formation reactions are negligible because InCl is dominant species in the wide range of temperatures (T > 450 K) as shown in Figure 2-12. InCl reacts with NH₃ and forms InN and produces HCl and H₂ as by-products (R2).

5.3 InN Nanorods Growth Optimization

During the exploratory study of the InN film growth as presented in Chapter 6, possible conditions for InN nanorod growth were determined. The base conditions for InN nanorod growth are listed in Table 5-1. The substrates used in this study were c-Al₂O₃, GaN/c-Al₂O₃, and Si(111) although occasionally a-, r-Al₂O₃ and Si(100) were used.

Table 5-1. Base conditions of InN nanorods growth.

Growth T	TMI flow rate	HCl flow rate	NH ₃ flow rate	N ₂ flow rate
600 °C	0.7 sccm	2.8 sccm (Cl/In = 4)	175 sccm (N/In = 250)	1600 sccm

The growth parameters were varied to study morphological evolution of InN to determine optimal growth conditions for InN nanorod formation.

5.3.1 Experimental Procedure

To grow InN, c-Al₂O₃, GaN/c-Al₂O₃, and Si(111) wafers were normally used as the substrates. Si(111) and c-Al₂O₃ substrates were cleaned by wet cleaning process such as dipping in the warm trichloroethylene, acetone, and methanol for 5 min each followed by DI water rinse and nitrogen gun dry, whereas GaN/c-Al₂O₃ substrate was only cleaned by nitrogen gun with static eliminator. The substrates were loaded together and InN was grown simultaneously to avoid run-to-run variation.

The TMI flow rate was maintained at 0.7 sccm, 10 % HCl flow rate was 0 to 4.2 sccm (Cl/In ratio from 0 to 6), NH₃ flow rate was 70 to 5000 sccm (N/In ratio from 100 to 7000), and N₂ carrier flow rate was constant at 1600 sccm. After growth, the reactor was cooled to room temperature at a rate of -15 °C/min. During the cooling process NH₃ was provided to prevent InN decomposition up to 300 °C. The reactor pressure was maintained at ~ 1 atm.

5.3.2 Results

5.3.2.1 Effects of Growth Temperature and HCl/TMI Molar Ratio

When the temperature was lower than 400 °C or higher than 750 °C, no InN growth occurred. The extent of NH₃ cracking was extremely low at T < 400 °C and InN decomposed rapidly around 750 °C. The decomposition is somewhat altered depending

on etching effect of H_2 from NH_3 decomposition. As a result, it is not surprising that no growth occurred below 400 and above 750 °C.

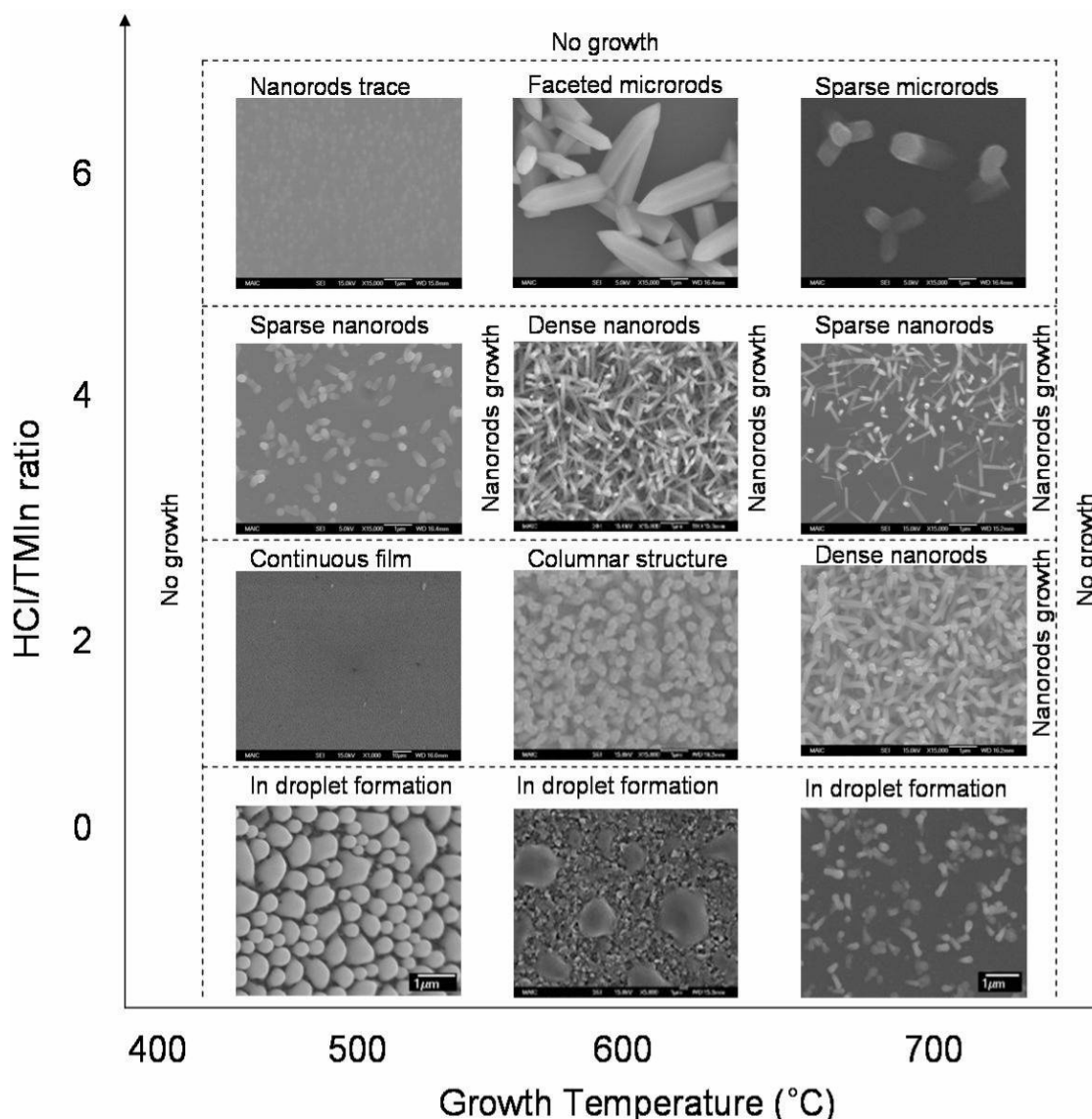


Figure 5-1. The growth map of InN at different HCl/TMI ratio with growth temperature; N/In = 250; Growth time = 1 hr; Substrate = c-Al₂O₃.

The first column of Figure 5-1 shows the results in the case where the growth temperature was around 500 °C. When HCl/TMI = 0, In droplet formation was observed. When HCl/TMI ratio was 1 to 2, continuous InN films were grown without indium droplets formation. The unreacted indium after InN formation perhaps is retained in the vapor phase as volatile InCl_x species. As a result, no In droplets were observed.

At higher HCl/TMIn ratios (> 3) at the same temperature ($500\text{ }^{\circ}\text{C}$), for example HCl/TMIn = 4 and $500\text{ }^{\circ}\text{C}$, nucleation was difficult because there was not sufficient active nitrogen at the low temperature and excess HCl leading towards etching. At these conditions sparse nanorods could be formed. The sizes of nanorods in both lengths and diameters and the number density were small because the growth rate was low at low temperature with excess HCl conditions.

Interesting morphological evolution was observed at a growth temperature around $600\text{ }^{\circ}\text{C}$ (second column). When no HCl was provided, InN film was again grown with In droplets. At HCl/TMIn = 1 to 2, columnar structures developed leading to the polycrystalline InN films. When HCl/TMIn = 3 to 5, long and dense nanorods were grown. Sparse and well faceted microrods were observed at HCl/TMIn = 6. Although the growth rate was higher at $600\text{ }^{\circ}\text{C}$, the nucleation of InN was difficult at high HCl/TMIn ratios. Once nucleated, the crystals tended to grow larger rather than creating new nucleation sites. The third column shows the results at high growth temperature ($T = 700\text{ }^{\circ}\text{C}$). In droplets formed again when HCl was not provided. At HCl/TMIn = 1 to 2 dense nanorods were formed rather than 2-D films. It is noteworthy that the effects of HCl/TMIn ratio and growth temperature are similar because they are related to InN etching and decomposition, respectively. As a result, dense nanorods were grown at high HCl/TMIn (~ 4) and intermediate growth T ($\sim 600\text{ }^{\circ}\text{C}$), or intermediate HCl/TMIn (~ 1) and high growth T ($\sim 700\text{ }^{\circ}\text{C}$). At HCl/TMIn = 4 and $T = 700\text{ }^{\circ}\text{C}$, sparse and long nanorods were grown. The high temperature ($\sim 700\text{ }^{\circ}\text{C}$) made the nucleation of nanorods difficult due to the decomposition effect. Once nucleated, the nanorods tended to grow along the most favorable directions rather than forming other nucleation sites. Finally, at

HCl/TMIn = 6, the nucleation of InN was difficult, so low density microrods growth was anticipated for the reason similar to the above.

5.3.2.2 Effects of NH_3/TMIn Molar Ratio and Substrate Material

The effect of NH_3/TMIn ratio, another important growth parameter, was investigated with different substrates: c- Al_2O_3 , GaN/c- Al_2O_3 , and Si. For comparison, those substrates were loaded together. In previous experiments, it was found that long and dense nanorods were grown when the NH_3/TMIn ratio was around 250 in a temperature range 600 to 650 °C and the HCl/TMIn ratio was around 3 to 5.

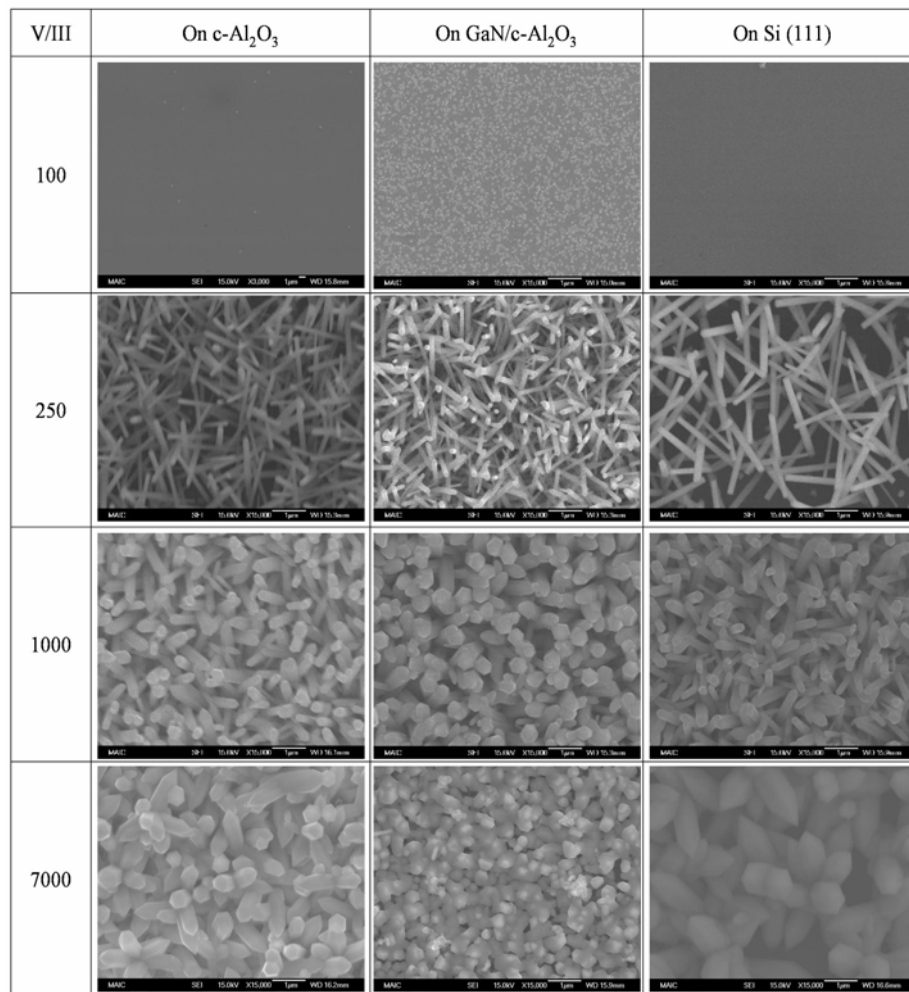


Figure 5-2. Scanning electron micrographs of InN film and nanorods. NH_3/TMIn were varied from 100 to 7000; Other growth conditions are HCl/TMIn = 4, T = 600 °C; Growth time = 1 hr.

It was found that the length of the nanorods after 1 hr of growth was typically ~ 1 μm , with a diameter in the range 50 to 380 nm, depending on the value of the NH_3/TMIIn ratio. While changing the NH_3/TMIIn ratio (Figure 5-2), it was found that nanorods were only grown when NH_3/TMIIn ratio was 250. At NH_3/TMIIn ratio greater than 10^3 , the diameters of the rods became larger. At very high ($\text{N/In} = 7 \times 10^3$) NH_3/TMIIn conditions, microrods with sharp edges or even continuous polycrystalline films were grown with granular surface morphology as shown in Figure 5-2.

The results can be explained by the amount of active nitrogen from NH_3 decomposition. When hardly any NH_3 was provided ($\text{N/In} = 100$), there was not enough active nitrogen to form InN, so that the growth of both InN films and nanorods was limited. When intermediate amounts of NH_3 were provided ($\text{N/In} = 250$), the growth occurred in a selective way. In other words, the growth occurred in the most stable direction (in this case along c-axis). When abundant NH_3 was supplied, there was enough active nitrogen in the system, so that growth could occur isotropically. This prevents the directional growth and rather large diameter microrods were grown (*i.e.*, $\text{N/In} = 1000$). If excessive NH_3 was provided, the etching effect from H_2 cannot be ignored and the growth rate decreased (*i.e.*, $\text{N/In} = 7000$).

Due to the similarity of the crystal structure, it is easier to form InN nuclei on GaN. Therefore the films and nanorods on GaN/c- Al_2O_3 substrates tend to be denser than the ones on c- Al_2O_3 and Si(111) substrates.

5.3.2.3 Equilibrium Analysis

To better understand the growth conditions of InN nanorods, a complex chemical equilibrium analysis of the In-N-Cl-H-C-Inert system was performed. Details about the thermochemical data collection, calculation procedures, and detailed studies along with

the equilibrium predictions are presented in Chapter 2. For comparison, experimental observations were plotted in Figure 5-3 along with the equilibrium predictions. The outcome from the multiple growth runs are shown on this figure, indicating whether film growth, nanorod growth, or no growth occurred. These data span a range of conditions (HCl/TMIn ratio 1 to 7; NH_3 /TMIn ratio 100 to 7000, and growth temperature 400 to 750 °C).

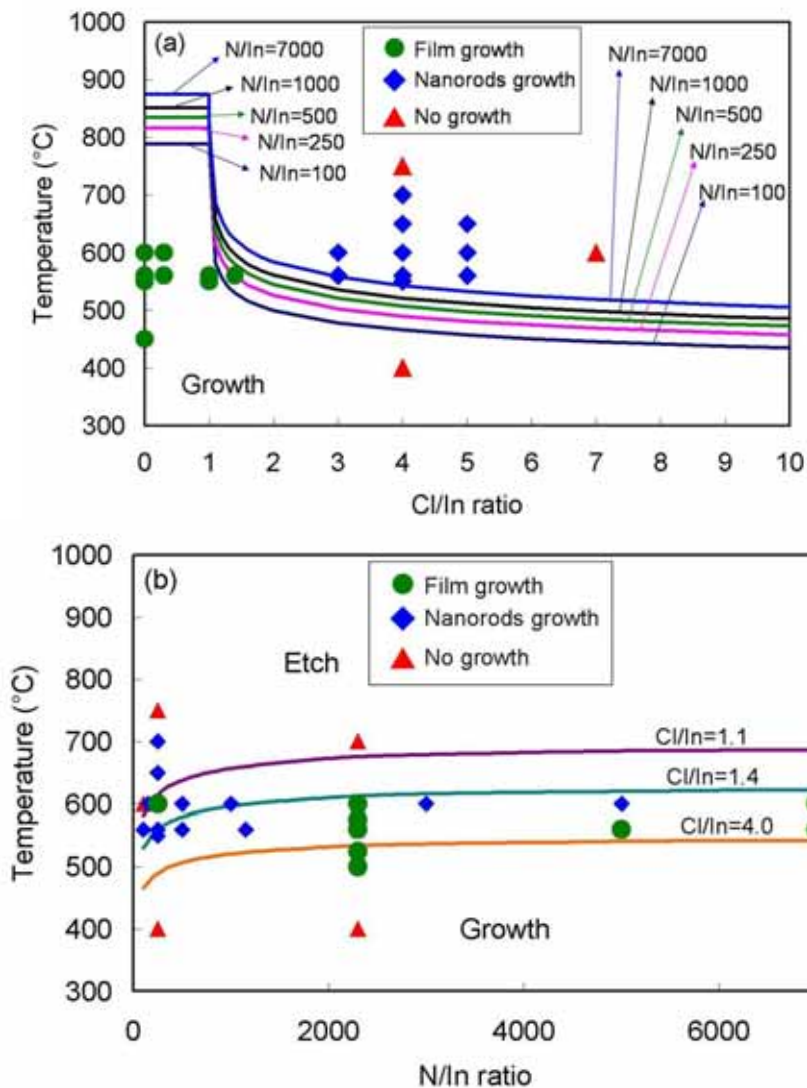


Figure 5-3. The calculated boundary of the growth and etch regimes and experimental observations. (a) deposition temperature vs. HCl/TMIn ratio for selected N/In atom ratios; (b) deposition temperature vs. N/In atomic ratio for selected HCl/TMIn ratios.

The general trend is consistent with the equilibrium predictions particularly the results with variable Cl/In ratio. Although kinetic limitations likely exist for both growth and etching, particularly at low temperature, the transition point occurs when etching and deposition reactions are in balance and thus might be expected to be better predicted by equilibrium calculations. There is one outlier at an HCl/TMIn ratio of 4, for which no growth is observed at conditions well into the growth region. This particular run was at the lowest temperature (400 °C), and the thermal cracking of NH₃ is very difficult so that no N is available for growth [Ban72].

The conditions of several experiments and their outcome are provided in this figure. The general trend is consistent with the experimental observations, although two outliers at low temperatures are noted. The general agreement between experimental observations and conditions predicted to yield no net growth or etching suggests that operating near this transition allows for fine control of the nucleation process, and thus the opportunity to control the density and dimensions of the nanostructures. Of course, kinetic limitations will be present and influence the actual process. It is unclear what mechanism initiates nanorod growth; it is also unclear by what mechanism the 'bulk' nanorods grow. The cooperation of In liquid is improbable since In liquid was not observed by SEM study. In addition, the existence of In liquid is unlikely in HCl ambient since InCl_x formation is dominant reaction in chlorinating environment at high temperature. Once stable nuclei form on the substrate surface, epitaxial growth is expected for conditions of moderate lattice mismatch because epitaxy will generate a minimum energy. Therefore, InN nanorods showed very high structural quality as judged by TEM-DP (Figure 5-12).

5.4 Properties of InN Nanorods

The grown InN nanorods were characterized by various techniques to examine the morphology, crystallinity, chemical compositions, optical, and electrical properties.

5.4.1 Morphology

Field Emission Scanning Electron Microscopy (FE-SEM) was used to observe the surface morphology after growth. Figure 5-4 shows selected images of InN nanorods at given conditions. Well faceted hexagonal pillar structures are clearly seen. The diameters ranged 100 to 300 nm and the lengths were $\sim 1 \mu\text{m}$ for 1 hr growth.

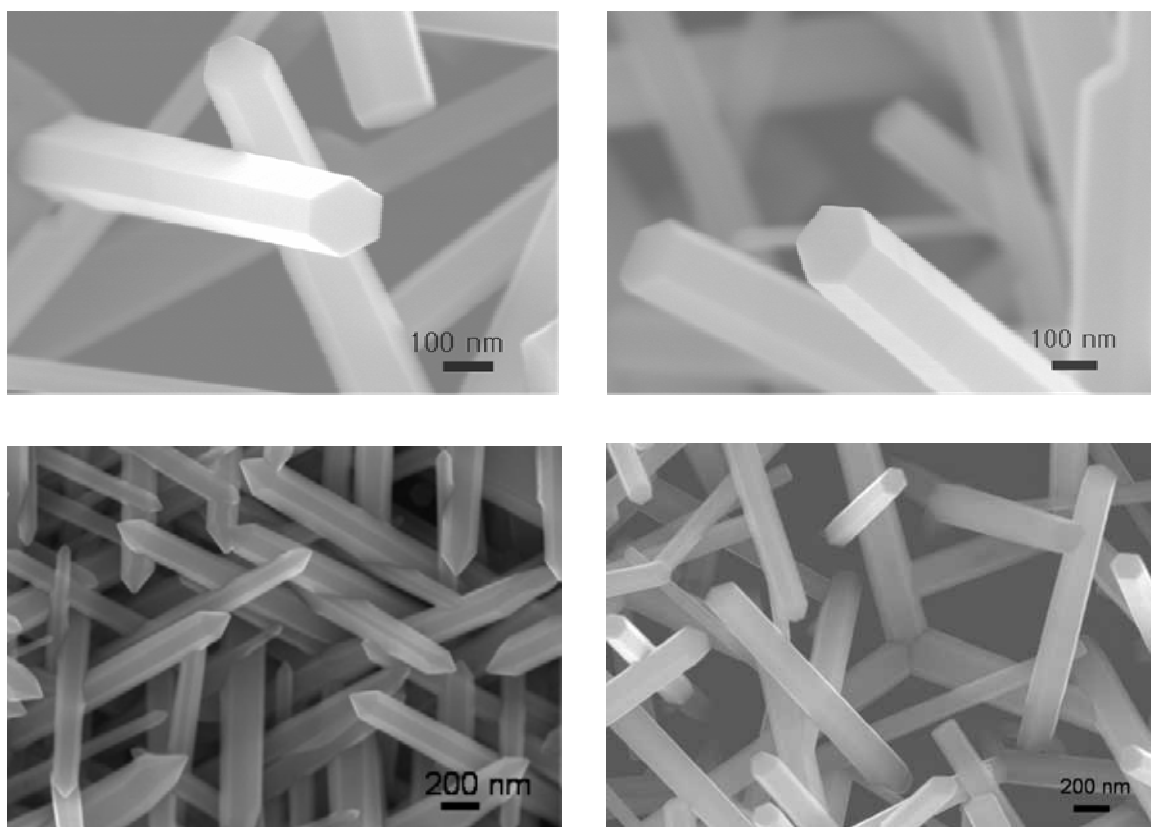


Figure 5-4. Scanning electron micrographs of InN nanorods grown at optimal conditions; Cl/In = 4, N/In = 250, T = 600 °C, for 1 hr growth on Si(111).

5.4.2 Crystallinity

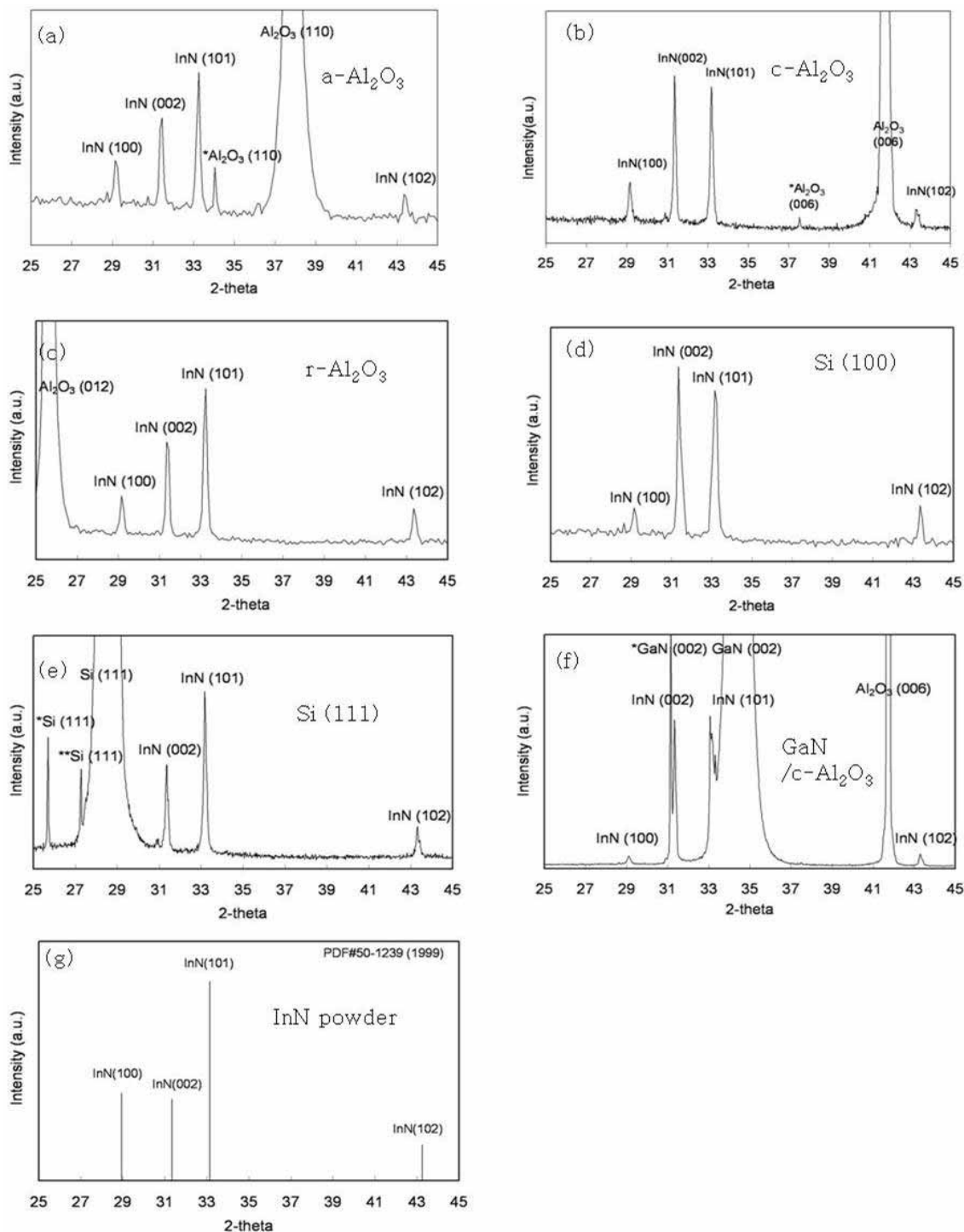


Figure 5-5. XRD θ - 2θ scan of InN nanorods grown on various substrates (a) $a\text{-Al}_2\text{O}_3$, (b) $c\text{-Al}_2\text{O}_3$, (c) $r\text{-Al}_2\text{O}_3$, (d) Si(100), (e) Si(111), (f) GaN/ $c\text{-Al}_2\text{O}_3$, and (g) PDF#50-1239 (powder diffraction file).

XRD θ - 2θ scans of nanorods grown on a, c, r-sapphire, Si(100), Si(111), and GaN/c-Al₂O₃ substrates was performed using a Phillips APD-3720 diffractometer. It is known that cubic phase GaN could be grown on Si(100) and non-polar GaN could be grown on a- or r- sapphire [Cra02, Pas04]. The hope was that different substrate may provide nanorods that have different phases or polarity.

The patterns show only diffracted peaks attributed to hexagonal InN (Figure 5-5.).

Furthermore, the XRD results show that within the detection limits, neither crystalline indium oxide (In₂O₃), nor metallic indium was present.

Although individual nanorods were single crystalline (confirmed by TEM-Diffraction Pattern), the patterns showed only peaks related to InN. If they were randomly oriented the pattern should match the powder pattern. It was found, however, that the nanorods were not randomly oriented as compared to the powder pattern shown in Table 5-2 and Figure 5-5 (g).

Table 5-2. Intensity ratio comparison with XRD powder pattern with different substrates.

Substrate/PDF#	Intensity ratio (%) (100)/(101)	Intensity ratio (%) (002)/(101)	Intensity ratio (%) (101)/(101)	Intensity ratio (%) (102)/(101)
InN nano on a-Al ₂ O ₃	49	74	100	29
InN nano on c-Al ₂ O ₃	39	107	100	22
InN nano on r-Al ₂ O ₃	37	69	100	30
InN nano on Si (100)	32	114	100	33
InN nano on Si (111)	N/A	59	100	24
InN nano on GaN/c-Al ₂ O ₃	9 (lowest)	130 (highest)	100	11(lowest)
PDF#50-1239	44	41	100	18

Comparing the powder pattern (PDF#50-1239) to the nanorods, it was concluded that the intensity of the InN (002) peak was consistently higher than the InN powder pattern, regardless of the substrate type. InN nanorods grown on GaN substrates showed the highest intensity of InN (002) peak, whereas the intensities of (100) and (102) were the lowest compared to the nanorods grown on the other substrates. This is a definite feature of texturing in the [002] direction because the intensity of the (002) peak from randomly oriented crystals (*i.e.*, powder) should be less than half compared with the (101) peak. The results suggest that a GaN substrate may be a good substrate for growth of aligned nanorods.

5.4.3 Self-alignment

Controlled growth of uniformly-aligned InN nanorods would have certain advantages for advanced InN-based devices such as LEDs, laser diodes, and sensors. Aligned nanorods, however, have only been observed on GaN/c-Al₂O₃ substrate.

The range of conditions for the growth of aligned nanorods is still under investigation. A possible growth mechanism may be In_xGa_{1-x}N formation at the interface since it is epitaxially grown but the evidence is not conclusive at this point.

Figure 5-6 shows SEM images of aligned InN nanorods grown on GaN/c-Al₂O₃ substrate without an external catalyst or template. Nanorods can be aligned in both dense and sparse manners as shown in Figure 5-6 (a) and (b). The edge shapes of the nanorods are either sharp (a), (b) or flat (c). The substrates were all GaN/c-Al₂O₃ and no alignment was observed on the other substrates, such as Al₂O₃ and Si.

XRD θ -2 θ scan was carried out to characterize the d-spacing perpendicular to the surface. Only InN (0002) and (0004) peaks were detected with the substrate GaN (0002)

and (0004) peaks seen in Figure 5-7. The results showed that the aligned nanorods were epitaxially grown along the [0002] direction, perpendicular to the GaN surface.

To see the alignment degree of nanorods with respect to the growth direction, XRD ω -rocking curve was obtained with FWHM = 1.29° , as shown in Figure 5-8. Although the FWHM is much wider than in the case of a film, it is noteworthy that the nanorods are indeed aligned in the [0001] direction and that the growth definitely occurred along the [0001] axis.

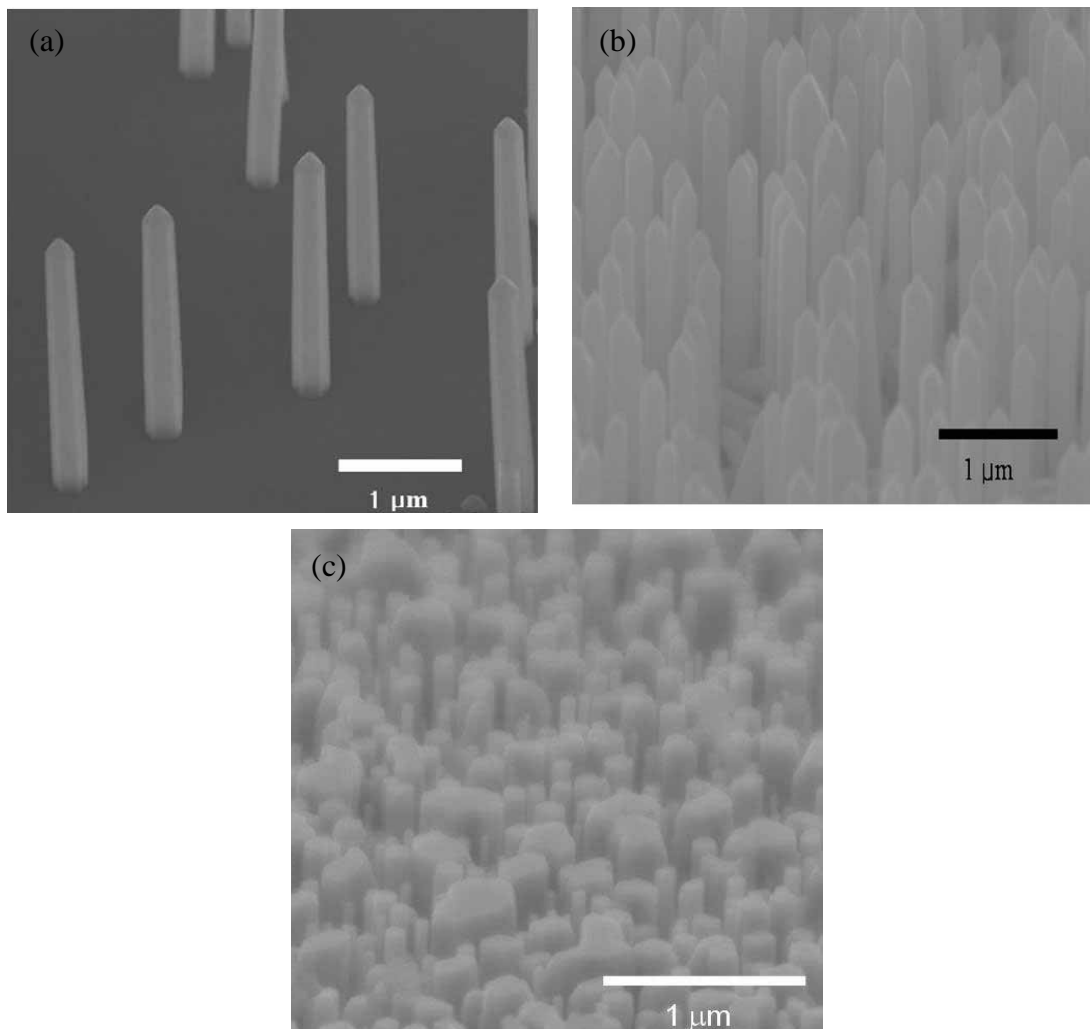


Figure 5-6. Scanning Electron Micrographs of aligned InN nanorods grown on GaN/ Al_2O_3 substrates. (a) sparse nanorods with sharp tips (b) dense nanorods with sharp tips (c) dense nanorods with flat tips.

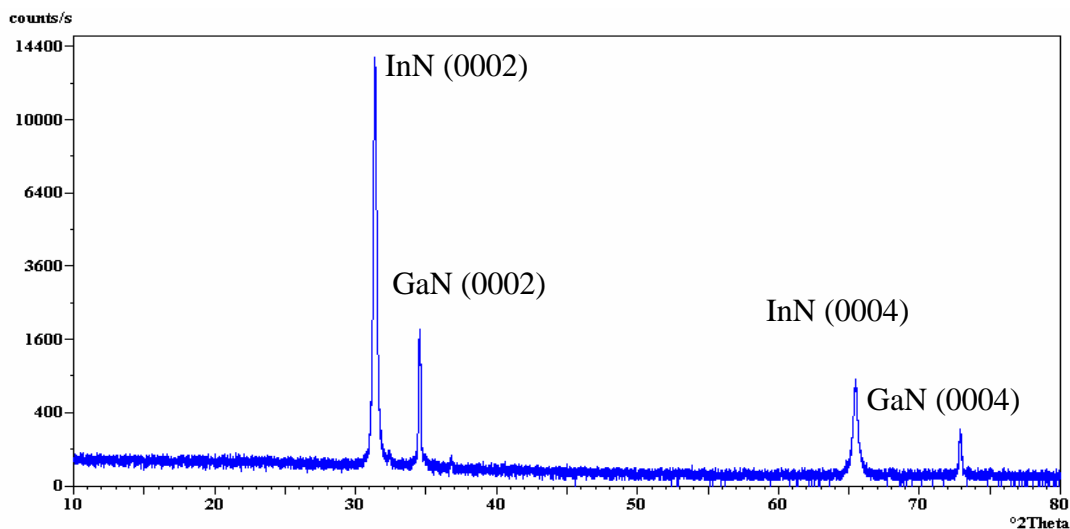


Figure 5-7. XRD scan of aligned InN nanorods on GaN/c-Al₂O₃ substrates.

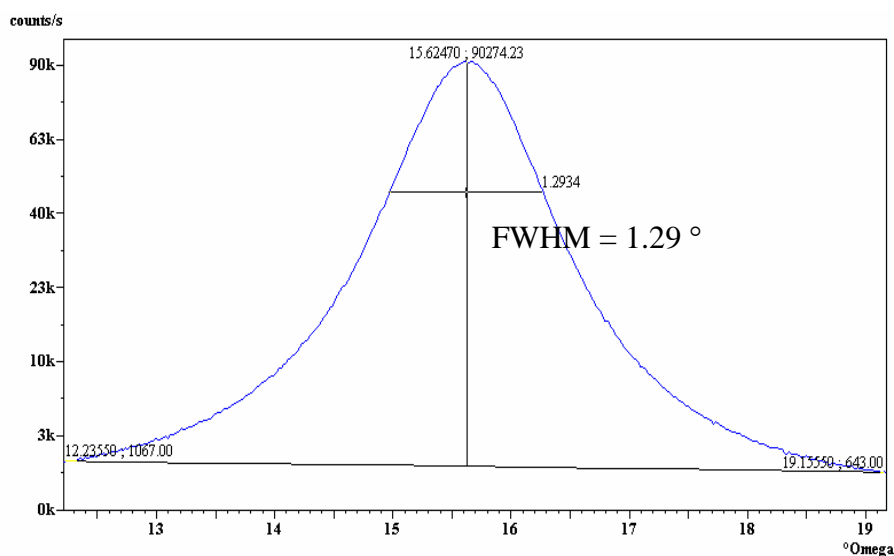


Figure 5-8. XRD ω -rocking curve of aligned InN nanorods on GaN/Al₂O₃.

To see rotational alignment with respect to the substrates, XRD pole figures were taken. Figure 5-9 shows XRD pole figures of self-aligned InN nanorods on GaN/c-Al₂O₃ substrate. XRD pole figures were obtained by using a Philips MRD X'Pert System. As seen in the figure, the InN (103) plane was selected to demonstrate the pole figures. The X-ray detector angle (2θ) and the incidence X-ray beam angle (ω) were set at 57.012 and 28.506°, respectively. For pole figure measurement, Ψ -tilt was changed from 0 to 90° while rotating the sample 360° around the ϕ -axis. Coincidentally, the c-Al₂O₃ (116)

plane has similar d-spacing (1.602 \AA) as the InN (103) plane (1.614 \AA). Although the Al_2O_3 (116) plane has similar d-spacing, it was not parallel to the InN (103) plane.

Therefore, both peaks were observed at different ψ in the pole figures.

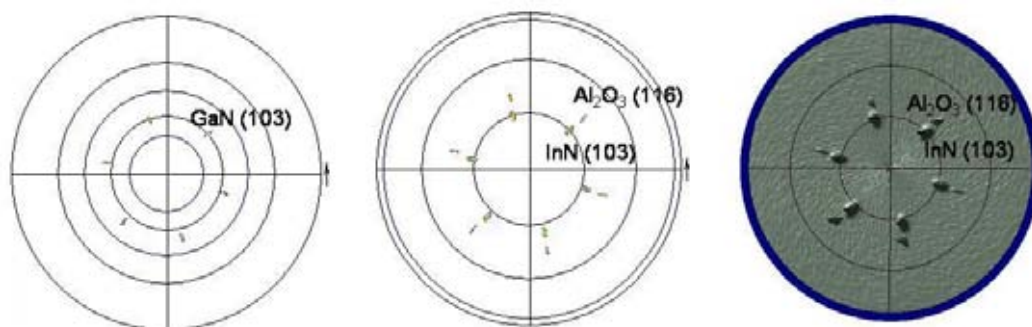


Figure 5-9. XRD pole figure of self-aligned InN nanorods (Substrate: GaN/c- Al_2O_3).

It was observed that the GaN (103) peak appeared at the same ϕ as InN (103) in the first figure. Moreover, the previous pole figure results on GaN/ Al_2O_3 (Figures 3-8 and 3-9) showed that the GaN (112) plane was rotated 30° with respect to Al_2O_3 (116) plane. This confirms that InN nanorods were grown on GaN without rotation, but that both InN and GaN have rotated 30° with respect to the Al_2O_3 substrate. This is the evidence that InN nanorods are aligned not only vertically but also in-plane; that is epitaxially. The schematic of the (103) plane with respect to rotation axis is illustrated in Figure 5-10.

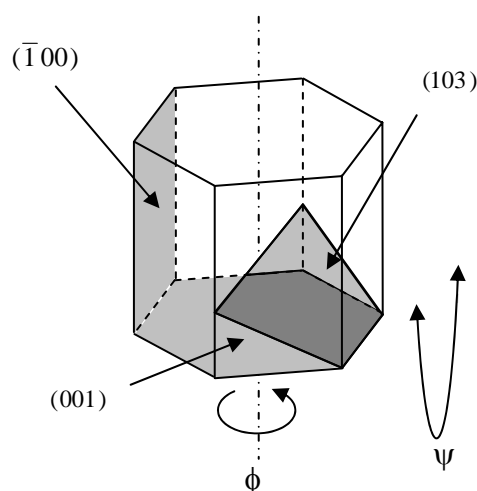


Figure 5-10. InN (103) plane and ϕ -axis for pole figure measurement.

Self-alignment only occurred when GaN substrates were used. Therefore it is suggested that the possible growth mechanism may be InGaN formation at the interface. The nucleation started from InN nano-crystallines formed on a GaN substrate. InGaN may form at the interface by inter-diffusion of In and Ga. Those InGaN nuclei will be epitaxial, so that the growth will replicate the same crystal structure of the substrate. The concentration of In will gradually increase during the InN growth with c-axis and graded InGaN nanorods would serve as the base. Therefore the growth axis would be the c-axis and vertically and rotationally self-aligned InN nanorods could be grown.

5.4.4 Growth Axis and Structural Properties

The structural properties of InN nanorods (grown in optimal conditions) were analyzed by TEM. The insert in Figure 5-11 (a) shows the splitting of the reflections in the $[10\bar{1}0]$ and $[11\bar{2}0]$ selected area electron diffraction patterns (SADP). The schematic illustrates that the splitting results from the intersection of the Ewald sphere with the streaks of diffracting intensity extending through each reflection. The three streaks in reciprocal space, which originate from the well-defined hexagonal shape of the nanorod, are perpendicular to the NR facets. Depending on the zone axis orientation, the Ewald sphere intersects either two or three streaks, thus enabling determination of the facet plane. A bright field (BF) image of the NR is presented at the bottom of Figure 5-11 (a). Electron diffraction patterns confirmed that the nanorods are single crystalline with a $[0001]$ growth axis and $(10\bar{1}0)$ facet planes. It is interesting to note that this type of faceting appears to be different from faceting in wurtzite ZnO nanorods, where facets were found to predominantly reside on the $(11\bar{2}0)$ planes [Din04, Dav99]. TEM also showed that the shape of nanorod tips is affected by growth conditions: nanorods exhibited either flat top or pyramid-truncated shape (Figure 5-4), *i.e.*, Figure 5-11 (a),

with side facets residing on the $(10\bar{1}1)$ planes. Dark- and bright-field images Figure 5-11 (b) revealed that nanorods are threading dislocation-free with sparse planar defects.

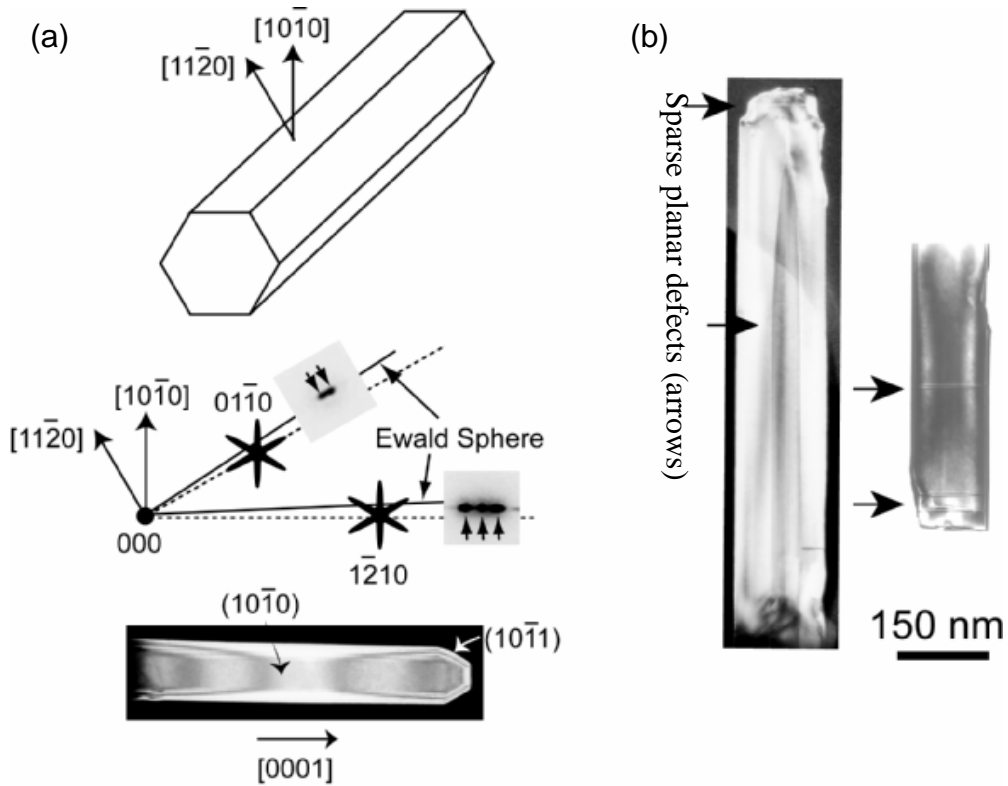


Figure 5-11. Transmission electron micrographs of an InN nanorod (a) splitting of reflections and (BF) bright field image at the bottom, (b) sparse planar defects by dark- and bright-field image.

These defects extended across individual nanorods and can be attributed to the stacking faults residing on the (0001) planes.

The distance of crystallographic planes can be precisely analyzed by measuring the distances between the transmitted spot and diffracted spots of TEM-DP as described by the following relation.

$$Rd_{hkl} = \lambda L$$

where R is the measured distance between transmitted spot and diffracted spot [cm], d_{hkl} is the spacing of the crystallographic planes ($h k l$) [\AA], λ is the wavelength of the electron beam [\AA], and L is the camera distance [cm]. The wavelength of the electron beam depends on the acceleration voltage that is typically 100 to 200 kV in TEM. For instance, the wavelength of electron beam is 0.037 \AA at 100 kV and 0.024 \AA at 200 kV.

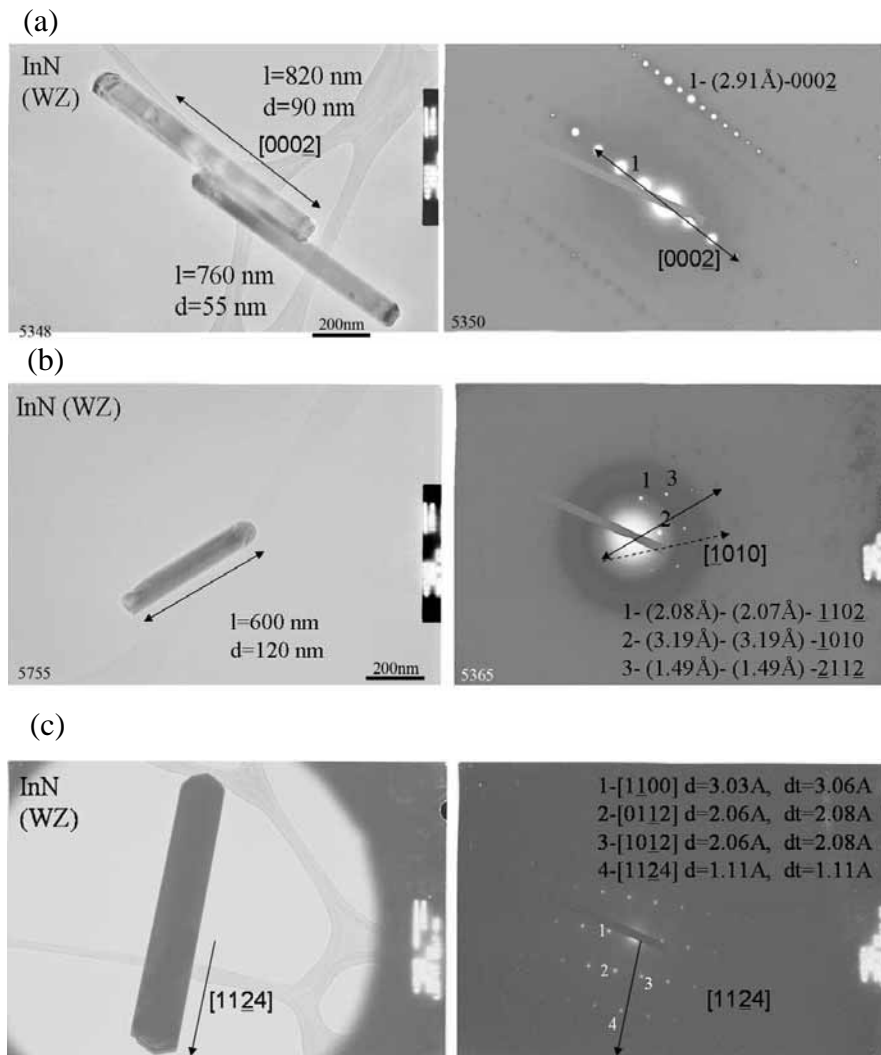


Figure 5-12. TEM and SAD of InN nanorods (WZ) with growth axes (a) $[0002]$, (b) $[1010]$, and (c) $[1124]$.

Rather than separately using electron beam wavelength (λ) and camera distance (L), a camera constant (λL) is used to calculate the distance of the crystallographic planes in

practice. Since λL [\AA cm] is constant, d_{hkl} [\AA] can be directly obtained by measuring R [cm].

Figure 5-12 shows transmission electron micrographs with selected area diffraction (SAD), in other words, TEM diffraction pattern (DP). The distances between transmitted spots and diffracted spots were measured and converted to the distance between the crystallographic planes. The results clearly showed that an individual InN nanorod was a single crystalline with wurtzite structure and a growth axis mainly along $[000\bar{2}]$, as shown in Figure 5-12 (a). Although a majority of the nanorods were wurtzite with a $[000\bar{2}]$ growth axis, some exceptions were found. A few wurtzite InN nanorods samples showed 20° off $[\bar{1}010]$ (Figure 5-12 (b)) and $[11\bar{2}4]$ (Figure 5-12 (c)) growth axes other than $[000\bar{2}]$.

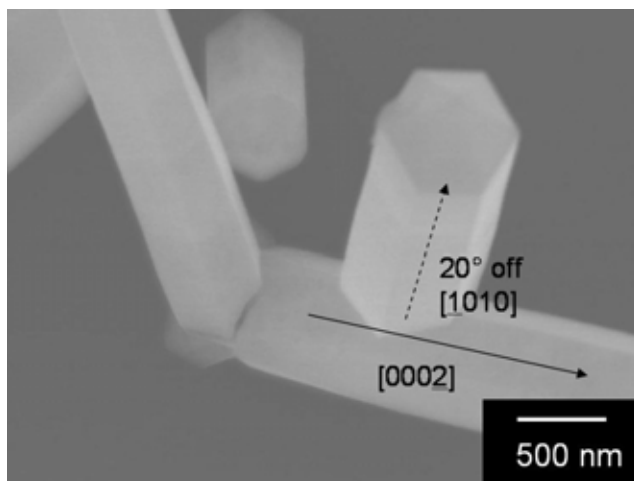


Figure 5-13. SEM image of wurtzite InN nanorod grown on the side wall of a nanorod.

A similar occurrence was observed by SEM, as shown in Figure 5-13. The InN nanorods nucleated on the side wall of the nanorods and elongated tilted in the $[\bar{1}010]$ direction. Therefore, growth along the c-axis is not the only mechanism to explain the elongation of nanorods, although it was found that $[000\bar{2}]$ was the main growth axis, as confirmed by both TEM and XRD.

Interestingly, zincblende InN nanorods a few degrees off the $[220]$ growth axis and body-centered cubic In_2O_3 with a $[402]$ growth axis were found, as shown in Figure 5-14. The zincblende InN phase was usually observed in a mixture with the wurtzite phase in thin films [Spe06, Tsu05, And05, Yam98jcg]. Therefore, the existence of pure InN zincblende without wurtzite phase inclusion is a unique result.

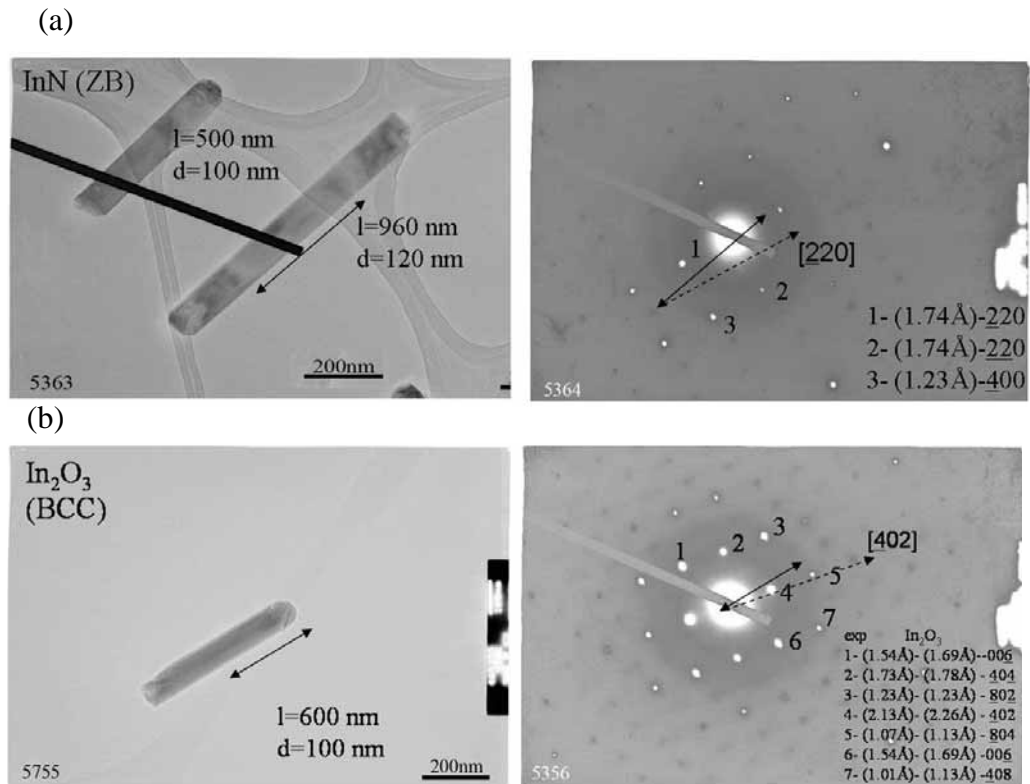


Figure 5-14. TEM and SAD of InN and In_2O_3 nanorods (a) InN (ZB) growth axis = a few degrees off $[220]$ (b) In_2O_3 (BCC) growth axis = $[402]$.

Few In_2O_3 (BCC) nanorods were rarely observed during the TEM analysis.

Although the source of the oxygen is unclear, the high crystal quality of In_2O_3 suggested that the oxygen existed during the growth. It also showed that the oxygen would not incorporate in the InN crystals by replacing N, but rather by forming In_2O_3 crystals. This is expected since the crystal structures of InN and In_2O_3 are intrinsically different.

Oxygen may incorporate in InN through the interstitial sites; however the maximum amount of oxygen concentration in InN is known to be ~ 0.3 % [Yos03].

5.4.5 Polarity

Wurtzite group III nitrides usually have spontaneous polarization effects, since most of time they are grown along the polarized axis. These polarization effects are beneficial in some cases and should be avoided in other cases. For example, 2 dimensional electron gas (2DEG) formations at the AlGa_N/Ga_N interface enhance the mobility of high electron mobility transistors (HEMT) significantly [Smo01]. On the other hand, it may change the wavelength of LEDs (red shift), or decrease the intensity of LEDs due to the charge separation induced by polarization effect [Im98]. Another benefit of polarity study is that it may illuminate the growth mechanism. It is known that the Ga_N films grown by MOCVD and HVPE techniques have different polarity because the growth mechanism is different. For example, the Ga_N films grown by MOCVD have Ga polarity with a smooth surface, and vice versa. The growth mechanism of InN nanorods is not understood yet. The study of InN nanorods polarity may help to clarify the growth mechanism of InN nanorods.

Convergent beam electron diffraction (CBED) is a very good tool to determine crystal structure and polarity. Unlike conventional selected area diffraction (SAD) that uses a parallel incident beam, CBED uses a convergent beam of electrons and generates diffraction discs instead of spots. The discs contains valuable information and can be used to determine thickness, lattice parameters, phase change, point and space group, Burger's vector, etc. Therefore, CBED was carried out during HR-TEM analysis to determine the polarity of an InN nanorod.

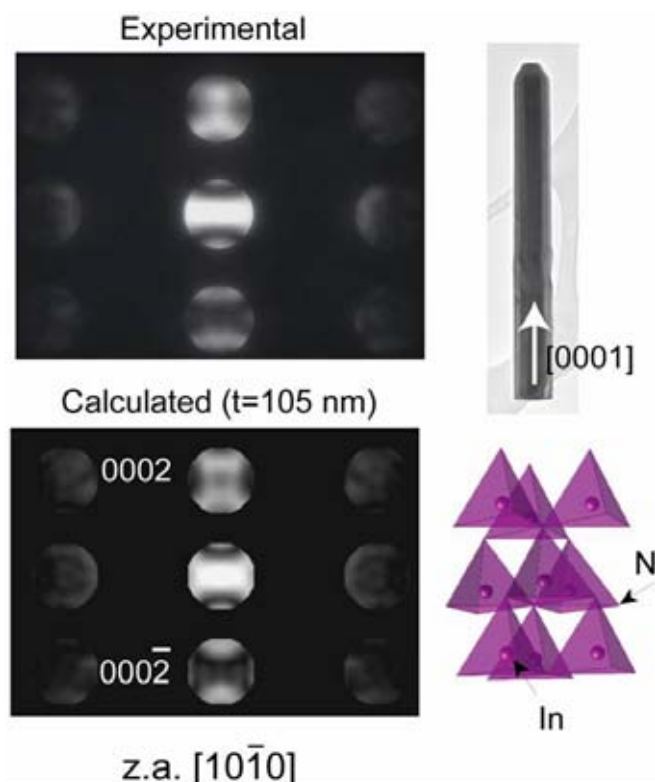


Figure 5-15. CBED of the InN nanorod.

As in Figure 5-15, it was determined that InN nanorods grow in the c -axis and have N-polarity, just as films grown by H-MOVPE. This was expected since there is always excess HCl in the system. HCl preferably reacts with In and forms InCl. As a result, N always remains on top.

5.4.6 Chemical Composition

The surface of InN nanorods were mainly composed of indium and nitrogen without chlorine, as confirmed by AES (Figure 5-16) spectrum, (detection limit $\sim 1\%$). The carbon in the AES spectrum was assumed to be from the surface adsorption during air exposure. For sputtering, 30 sec of 3 keV Ar⁺ beam with a 30° sputtering angle was used. Significant Ar⁺ ion beam damage occurred on the surface of InN nanorods.

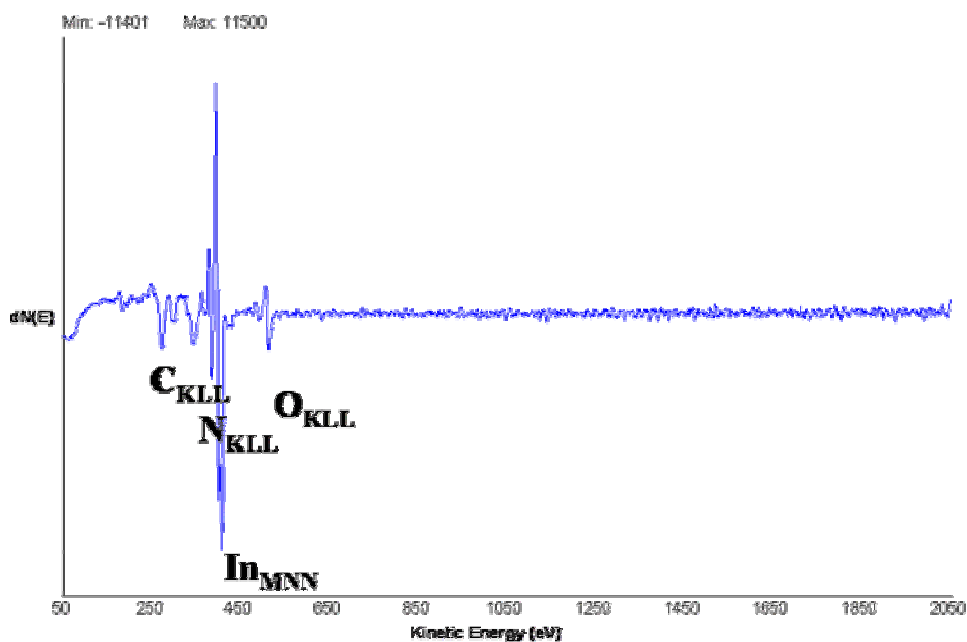


Figure 5-16. AES spectrum of surface scan of as grown InN nanorods at $T = 600\text{ }^{\circ}\text{C}$, $\text{HCl/TMIn} = 4$, $\text{NH}_3/\text{TMIn} = 250$, 1 hr growth on c-sapphire.

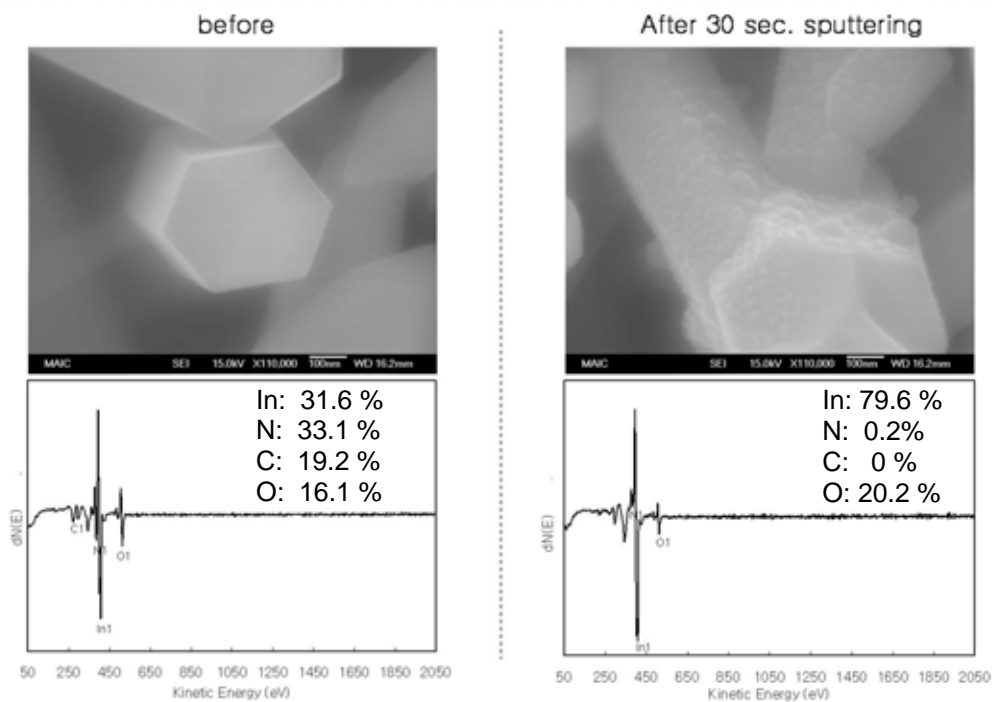


Figure 5-17. Scanning electron micrographs with AES of InN nanorods before and after AES sputtering damage.

Consequently, In droplets formation was observed as shown in Figure 5-17. It is noted that the concentration of In increased from 31.6 % to 79.6 % after sputtering. Nitrogen is no longer detected by AES only In and O. The results are consistent with literature [Kos04] because the Ar⁺ ion beam damages the InN surface at a sputtering angle lower than 60°. The ion beam incidence angle should be adjusted for InN sputtering. The suggested sputtering angle was > 80°; however that will only reduce the sputtering rate and the inherent problem will still exist.

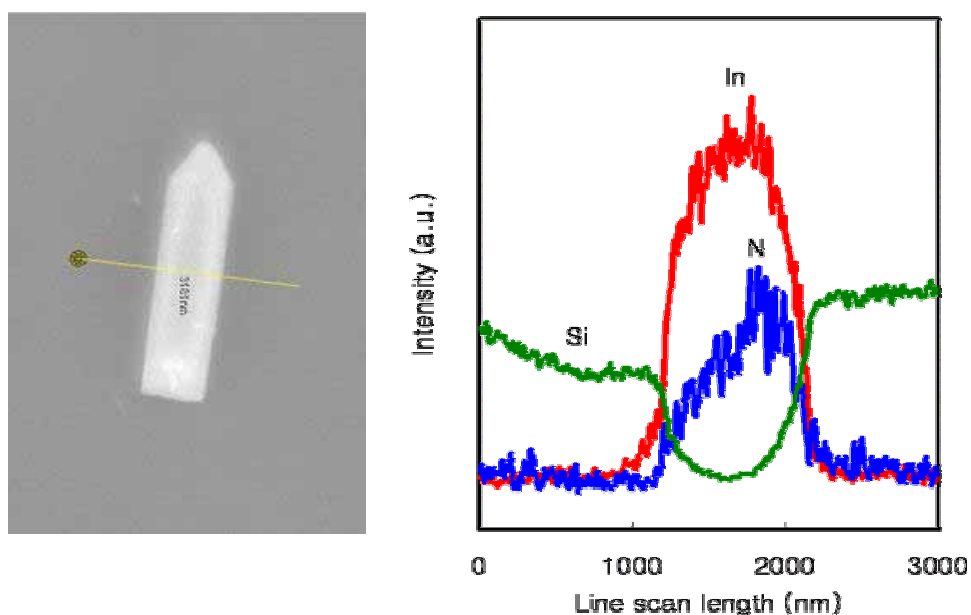


Figure 5-18. EDS line-scan of an InN nanorod grown on Si substrate.

The chemical composition of an InN nanorod on Si substrate was analyzed by EDS line-scan as shown in Figure 5-18. The nanorods are clearly composed of In and N. No oxygen or carbon was detected by EDS.

5.4.7 Photoluminescence

The bandgap energies of InN films and nanorods were measured by room temperature PL. As shown in Figure 5-19, maximum PL emissions were obtained around 1.08 eV with a significant left shoulder.

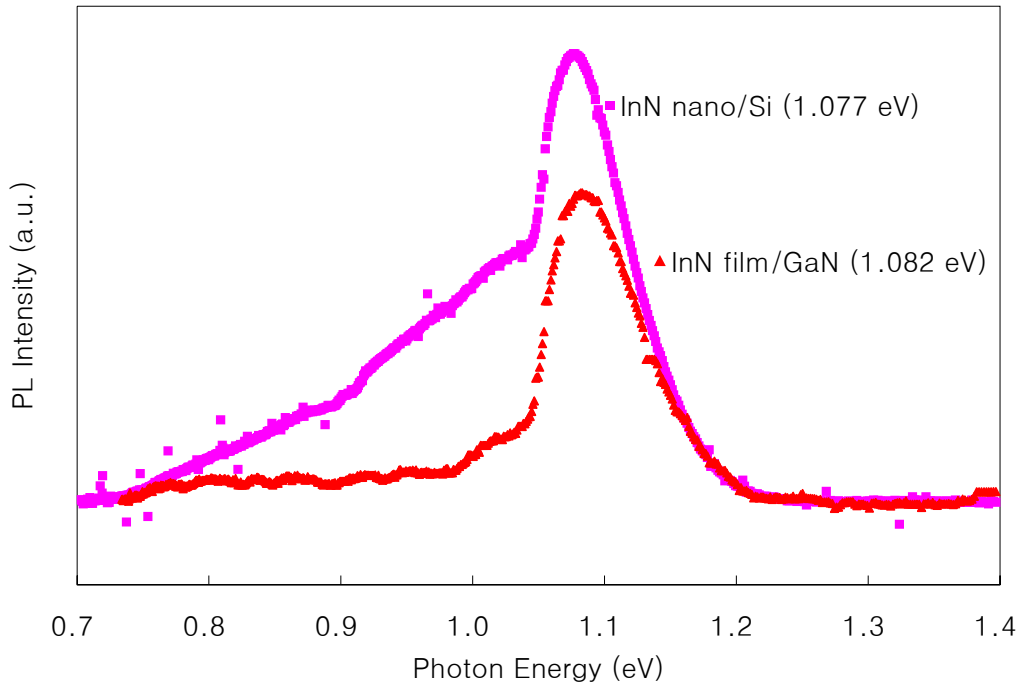


Figure 5-19. Room temperature (300 K) PL of InN nanorods grown on Si substrate and InN film on GaN substrate, maximum intensity observed around 1.08 eV.

This value matches well with the value of MBE grown sample, 1.1 eV [Inu01], where they estimated the bandgap energy by absorption coefficient squared plots. Although their characterization technique and the growth method were different from this work, their value for bandgap energy is similar. A 1.1 eV bandgap was also theoretically suggested based on density-functional theory (DFT) calculations [Dav02]. This value could be considered as a possible InN bandgap, although further research is required.

The differences in optical properties between the film and the nanorods were not substantial, because the diameters of nanorods were too large to exhibit a quantum size effects. The left shoulder of PL from nanorods showed that there are lots of continuous peaks from 0.7 to 1.0 eV that may represent mixture of lower bandgap InN (pure) and higher bandgap InN (containing oxygen).

Low temperature PL was performed to observe optical property changes with respect to temperature (Figure 5-20).

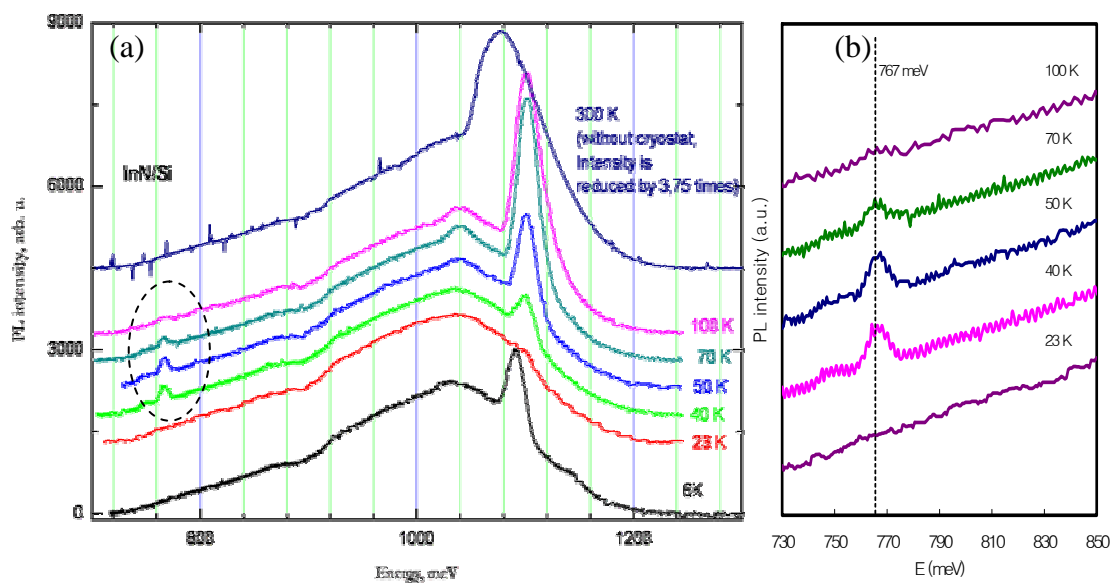


Figure 5-20. Low Temperature (6 K to 300 K) PL of InN nanorods on Si substrate (a) whole detection range, (b) magnified range between 730 to 850 meV from 23 to 100 K region.

It is known that at a low temperature the PL spectrum gives more detailed information about the near-band-edge region, donor-acceptor region, and the defect-band region. The near-band-edge region includes free excitons (X), donor bound excitons (DX) and acceptor bound excitons (AX). The PL spectrum on a Si substrate shows that all the "classic" lines are present (free exciton, bound, exciton, exciton droplet). These lines disappear as the temperature increases, as they should. The bandgap of these lines is around 1.1 eV, which is the bandgap of Si.

At low temperature (6 K), it is seen that the PL emitting from the Si substrate. It nearly disappears by 23 K, but reappears upon increasing the temperature, it was seen that this line reappears. This is very unusual and its value (1.1 eV) suggests that this is Si, but

that the temperature behavior is completely different. So it is either InN, or InN somehow affects Si in a way that it begins to emit light.

It is noteworthy that from 40 to 100 K an obvious peak appeared and disappeared at 767 meV. This result is consistent with Lan et al's report [Lan04].

5.4.8 Cathodoluminescence

The bandgap energy of InN nanorods grown on sapphire was also measured by CL at 7 K, as shown in Figure 5-21.

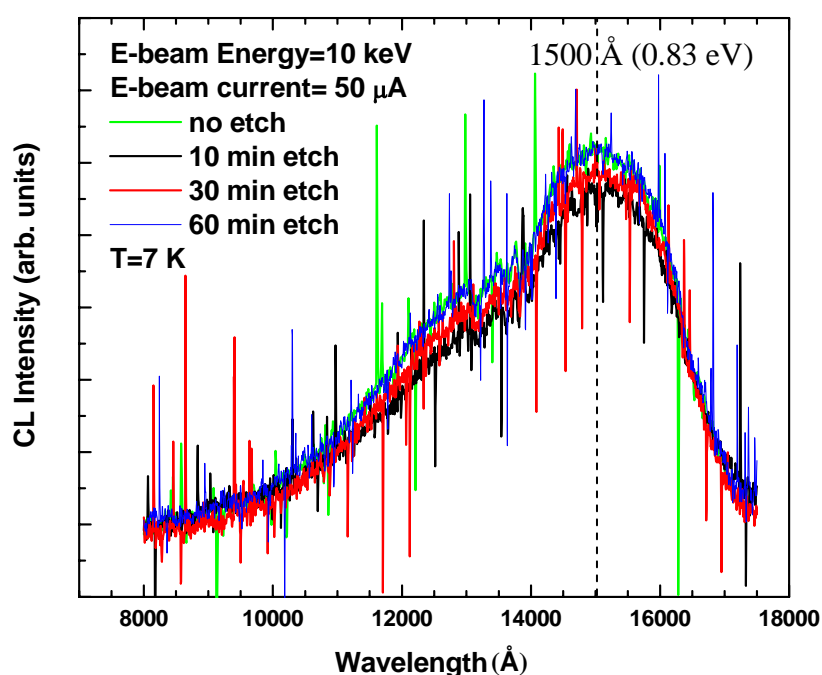


Figure 5-21. CL spectra of InN nanorods grown on sapphire.

The e-beam energy and current were set at 10 keV and 50 μA , respectively. To remove the surface oxides and possible In metal or In_2O_3 contaminations, the samples were wet etched in 1 % aqueous HCl solution for 10, 30, and 60 min each. Slight improvements in the intensity were observed with longer etch time, but the effect was not significant. A bandgap of 0.83 eV was detected by CL. Note that e-beam was 10 keV – much higher than Ar^+ in AES. Therefore, there may be very similar effect happening –

damage and In formation – or simply InN decomposition during these characterizations. The wet etching before CL was not a good approach since there is no In for as grown InN nanorods. The wet etching should have been tried after CL or AES measurement to remove In droplets on the surface.

5.4.9 Raman Spectroscopy

Raman spectroscopy is a well-established non-destructive technique to study vibrational phenomena in solids. Since inelastic light scattering in crystals is susceptible to selection rules, this technique can be conveniently used to identify crystalline structures and evaluate material quality and composition. Similar to AlN and GaN, InN crystal with a 2H (wurtzite) structure belongs to the space group C_{6v}^4 and has two molecules per unit cell. Group theory predicts eight zone-center optical phonons, namely $1A_1$ [transversal optical (TO)], $1A_1$ [longitudinal optical (LO)], $2B_1$ (optically inactive or “silent”), $1E_1$ (TO), $1E_1$ (LO), and $2E_2$.

The first order Raman spectrum of InN NRs deposited directly on Si substrate is shown in the bottom spectrum of Figure 5-22. Three phonon lines were clearly observed, despite the noise, at 451 cm^{-1} , 496 cm^{-1} , and 596 cm^{-1} , which can be assigned to A_1 (TO), E_2^2 , and E_1 (LO), respectively. The line at 522 cm^{-1} is the first order phonon of the Si substrate. The measured phonon energy values are between 3 cm^{-1} and 8 cm^{-1} larger than the values reported in the literature [Dav99, Che05]. These shifts may result from stress and/or heat reduction, due to the sample morphology and experimental conditions, respectively. It was observed that measurements performed with small laser spots and higher laser power resulted in damage to the sample. It was also observed that the E_2^2 phonon is more susceptible to stress, consistent with the larger energy difference reported in the present work [Kim05]. The different relative intensities of the observed phonon

lines, as compared with reported data, do not result from breaking of the selection rules, but mostly from the near random orientation of the nanorods. A typical Raman spectrum of the InN NRs deposited on GaN/Si substrate is represented in the top spectrum of Figure 5-22. Note the similarity of both spectra, with the exception of the additional lines at 531 cm^{-1} and 561 cm^{-1} , which are assigned to the GaN phonons $A_1(\text{TO})$ and $E_1(\text{TO})$, respectively. The sharpness of the InN lines is consistent with good crystalline quality of the nanorods.

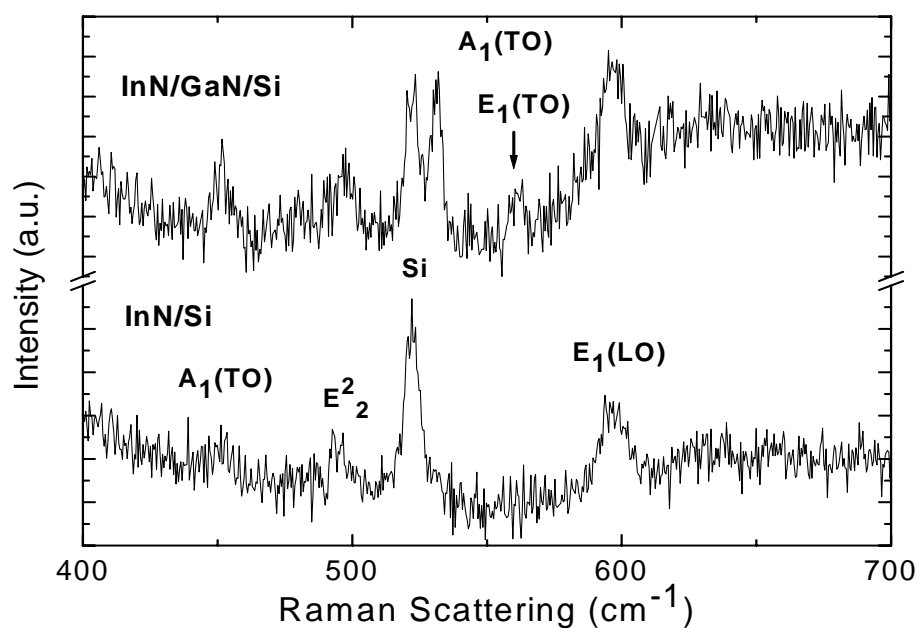


Figure 5-22. Room-temperature Raman scattering of InN nanorods deposited on Si and GaN/Si substrates.

5.4.10 Electrical Properties

It is essential to measure the electrical properties of InN nanorods because one of the ultimate goals will be fabricating devices. Carrier concentration is one of the most commonly measured electrical properties, determined by Hall measurement.

Hall measurements were carried out on InN films and nanorods grown on $c\text{-Al}_2\text{O}_3$ substrates after CL measurement. Since Hall measurement is known to damage the

surface of the sample during metal contact preparation, it is customary to do Hall measurement as the last step. Indium contacts were made to the surface of InN films and InN nanorods. Since the numerical density of the nanorods was very high, the nanorods were treated as a thin film.

Table 5-3. Electrical properties of InN films and nanorods.

Sample	Sheet Resistivity [Ω/sq]	Sheet Hall Coefficient [cm ² /C]	Type	Carrier concentration [1/cm ³]	Hall Mobility [cm ² /Vs]
InN film/Al ₂ O ₃	9.2582	4.6047x10 ²	n	1.35x10 ²⁰	49.7
InN nanorods/Al ₂ O ₃	7.0065	2.1749x10 ²	n	2.87x10 ²⁰	31.1

Table 5-3 shows some electrical properties of the InN films and nanorods. Both film and nanorods were unintentionally n-type doped. The carrier concentration measured by Hall is $1.35 \times 10^{20} \text{ cm}^{-3}$ for film and $2.87 \times 10^{20} \text{ cm}^{-3}$ for nanorods. Considering the structures between pillar structured films and a bed of nanorods, similar Hall measurement results were expected. The rather high carrier concentration indicates that the grown InN films and nanorods may have oxygen incorporation during the CL measurement. It appears that InN is very sensitive to electron beam, intense light sources, or just air exposure and forms In metal or In₂O₃ on the surface. This should prevent the correct measurements of properties of InN.

It would be interesting to measure the electrical properties of a single nanorod. This, however, was not carried out since the length of nanorods is still too short ($\sim 1 \mu\text{m}$) for electrical measurement.

5.4.11 Field Emission Properties

A sharp edge is beneficial for field emission applications. It was occasionally observed that the edges of InN micro/nanorods are very sharp, as shown in Figure 5-23.

Therefore, it is interesting to measure the field emission properties of these micro/nanorods.

To determine if InN could be used as field emitters, InN nanorods on Si were used as a cathode and placed under high voltage to measure the threshold field. During the measurement, the pressure was kept at 4×10^{-9} Torr, anode-cathode spacing (d) = $65 \mu\text{m}$ with circular anode 1.25 mm in diameter. 10 I-Vs were taken during ramp up and down each time and very reproducible results were obtained. However, a threshold field of $32 \text{ V}/\mu\text{m}$ was found at 1 nA. The typical value of the threshold field is $\sim 5 \text{ V}/\mu\text{m}$ for single-wall carbon nanotube (SWNT), $\sim 4 \text{ V}/\mu\text{m}$ for multi-walled carbon nanotube (MWNT), $> 8 \text{ V}/\mu\text{m}$ for diamond, and $> 25 \text{ V}/\mu\text{m}$ for amorphous carbon [Bon98]. The threshold field of InN nanorods ($32 \text{ V}/\mu\text{m}$) is higher than that of carbon nanotubes. Therefore, InN nanorods do not look promising for field emission applications because it will require higher voltages to produce field emissions.

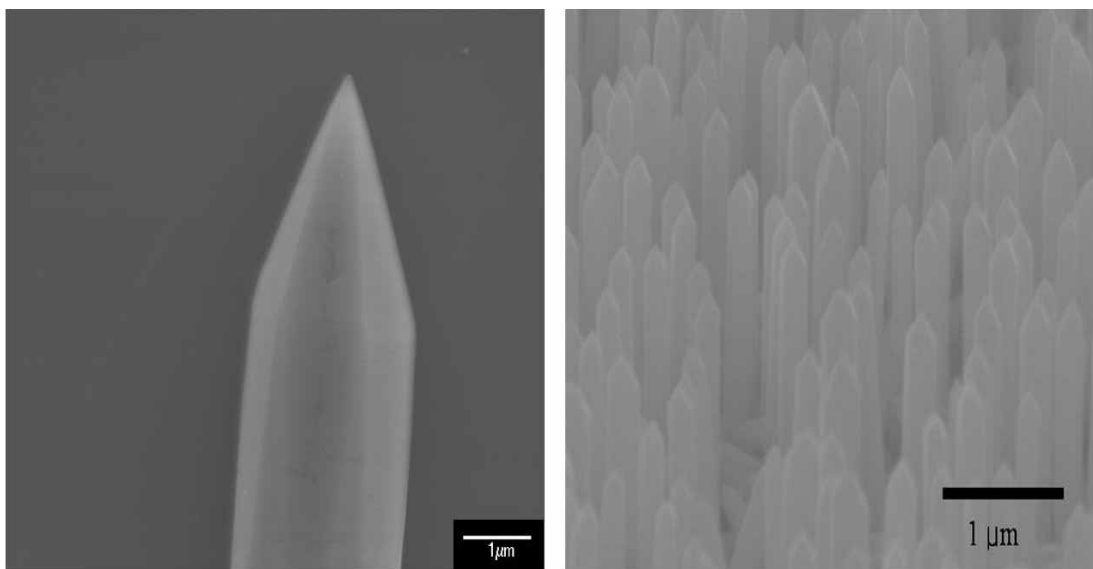


Figure 5-23. Scanning Electron Micrograph of sharp edge InN nanorods grown on Si (single NR on the left) and on GaN/Al₂O₃ substrates.

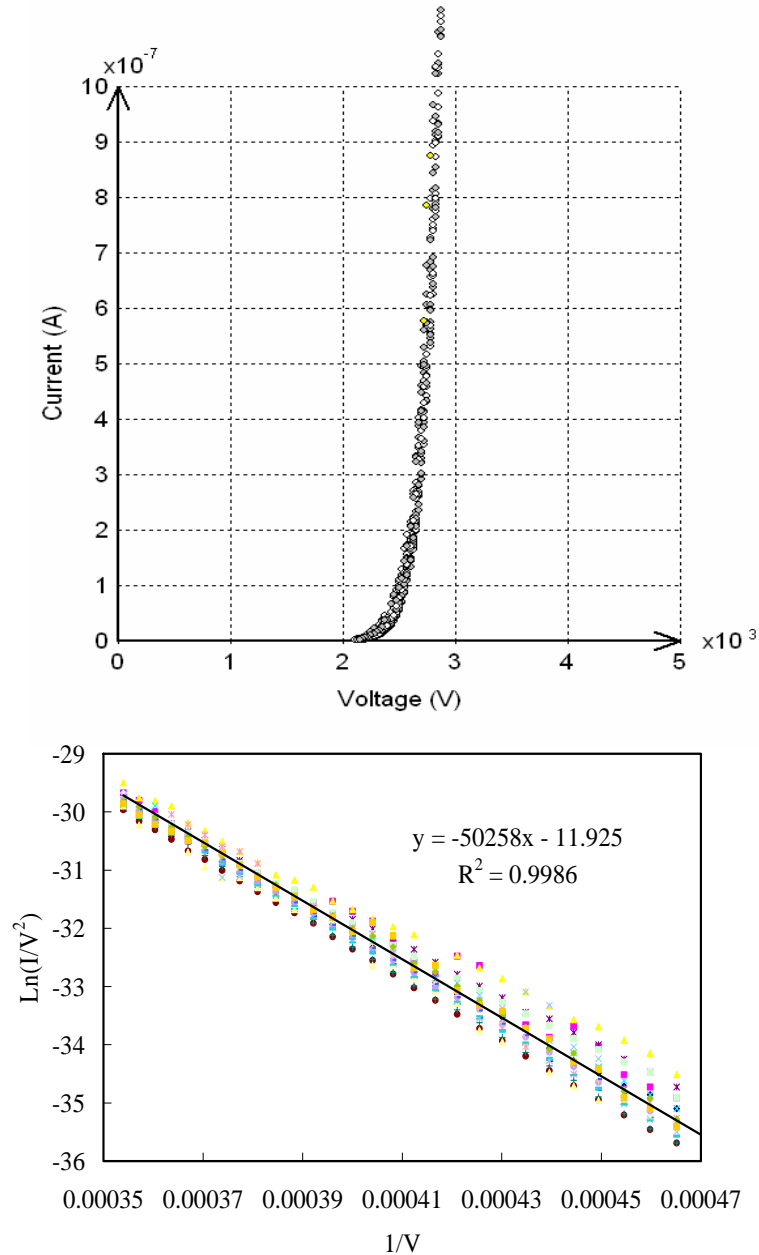


Figure 5-24. I-V curves and Fowler-Nordheim plots of InN nanorods on Si.

Figure 5-24 shows Fowler-Nordheim (F-N) plots measuring the I-V curve with schematic of F-N tunneling. The current created by quantum mechanical tunneling was derived in 1928 by Fowler and Nordheim. There are variable expressions of F-N relations and one simple expression can be written as following after WKB (Wigner, Kramers, Brillouin) approximation [Bon98].

$$I = A(\beta^2 E^2 / \phi) \exp(-B\phi^{3/2} / \beta E) \quad (1)$$

$$E = V/d \quad (2)$$

where A is a constant, $B = 6.83 \times 10^9$ [V eV^{-3/2} m⁻¹], ϕ is the work function, E is the macroscopic electric field, β is the field enhancement factor (geometrical factor), V is the applied potential, and d is the distance between the anode and cathode.

By assuming that free electron theory applies, $A = 6.2 \times 10^6 (\mu/\phi)^{1/2} / (\mu + \phi)$ [A/cm²]. By rearranging equations (1) and (2),

$$I\phi d^2 / (A\beta^2 V^2) = \exp(-B\phi^{3/2} d / \beta V) \quad (3)$$

$$\text{Ln}(CI/V^2) = D/V \quad (4)$$

$$\text{Ln}(I/V^2) = D/V - \text{Ln}(C) \quad (5)$$

where $C = \phi d^2 / A\beta^2$ and $D = -dB\phi^{3/2} / \beta$ which are constants.

The most important feature of F-N relations is that the current generated by field emissions is proportional to the exponential of 3/2 power of work function of the material which was derived starting from the time-independent Schrödinger equation.

The straight-line relation deduced by equation (5) shows the generated current is due to the field emission effect, also called Fowler-Nordheim tunneling. Since V is usually much larger than I in field emission case, the $\text{Ln}(I/V^2)$ term is negative. In addition, B and C are all positive constants, so that D has a negative value. Therefore, the y intercept and slope all have negative values. The slope (D) of the Fowler-Nordheim plot is related to anode-cathode spacing, the work function of the material, and the geometrical factor. The geometrical factor for SWNT ranges from 2500 to 10000 and for MWNT ranges from 1000 to 3000 [Bon98]. The work function of InN is unknown to date. Assuming the work function of InN is ~ 4 eV (since the work function of GaN and

AlN are 4.3 and 3.7 eV, respectively [He06]), the geometrical factor was calculated to be 78, which is very low compared to CNTs. The results, however, are in good agreement with the F-N relation. Although InN nanorods did not show promising electrical properties for field emitter, the high surface to volume ratio of dense InN nanorods may be used as sensor applications since the exposed surface area is much larger than thin film.

5.5 Pt-dispersed InN Nanorods for Selective Detection of Hydrogen at Room Temperature

Utilizing the high surface to volume ratio of InN nanorods, very sensitive sensors could be fabricated. In this study, a mat of InN nanorods was used for selective detection of hydrogen at room temperature using Pt coatings to promote H_2 dissociation.

5.5.1 Experimental Procedure

InN nanorods were grown on c- Al_2O_3 substrates by H-MOVPE. In selected samples, the nanorods were coated with Pt nanoparticles deposited by sputtering.

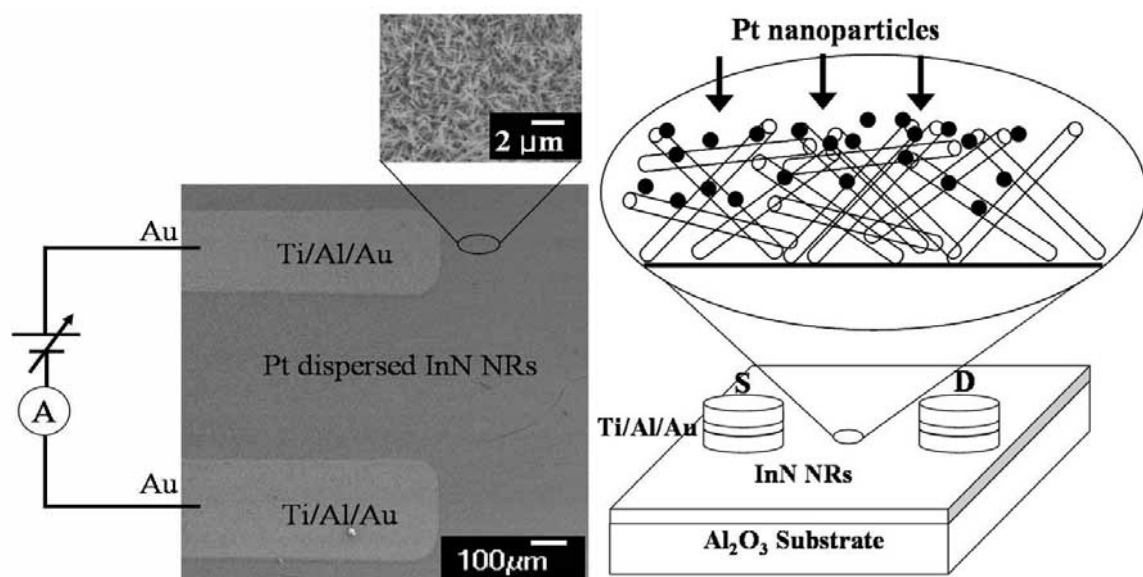


Figure 5-25. SEM images and schematic of hydrogen gas sensor made of Pt nanoparticle dispersed InN nanorods.

A shadow mask was used to pattern sputtered Ti/Al/Au electrodes contacting both ends of multiple nanorods on the c-Al₂O₃ substrates. The separation of the electrodes was ~ 500 μ m. Au wires were bonded to the contact pad for current-voltage (I-V) measurements performed at 25 °C in a range of ambient (N₂, O₂, N₂O, ND₃ or 10 to 250 ppm H₂ in N₂). Note that no underlying thin film of InN was observed at the growth conditions of these tested nanorods. The schematic of this device is shown in Figure 5-25.

5.5.2 Results

The I-V characteristics from the uncoated multiple nanorods were linear with typical currents of < 0.6 mA at an applied bias of 0.5 V as shown in Figure 5-26.

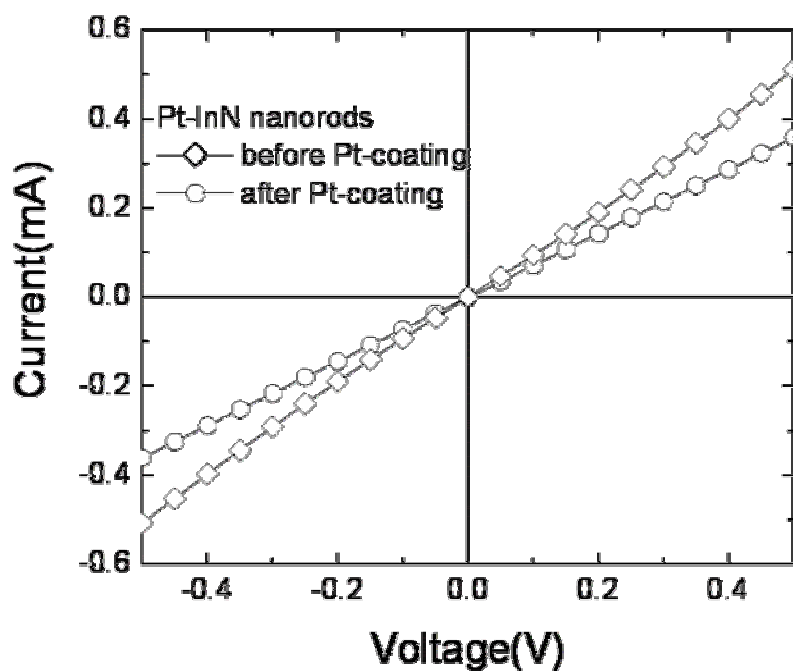


Figure 5-26. I-V characteristics from uncoated and Pt-coated InN nanorods.

After Pt coatings, the resistance of the nanorods was slightly higher. This may be due to the introduction of sputter damage that decreased the conductivity of the nanorods. The

current for the uncoated nanorods was not affected by the measurement ambient, *i.e.*, they showed no response to hydrogen.

Figure 5-27 shows the time dependence of current (top) or relative resistance change (bottom) of the Pt-dispersed multiple InN nanorods as the gas ambient is switched from N₂ to various concentrations of H₂ in air (10 to 250 ppm) and then back to air as time proceeds.

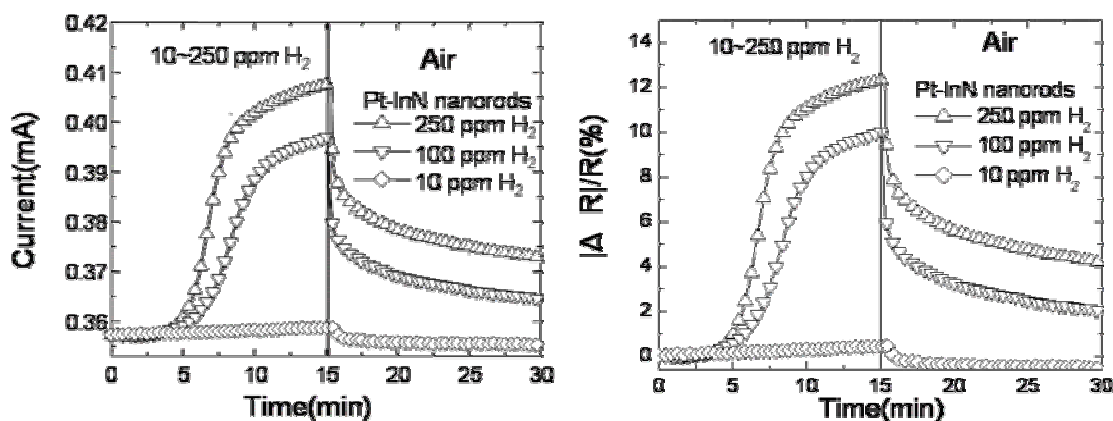


Figure 5-27. I-Time plot of 10 to 250 ppm H₂ test by Pt-InN nanorods (left) and $|\Delta R|/R(\%)$ -Time plot of 10 to 250 ppm H₂ test by Pt-InN nanorods (right).

There are several aspects of the data. Note that the addition of the Pt coating on the nanorods now produces a strong response to the presence of hydrogen. The addition of the Pt appears to be effective in catalytic dissociation of the H₂ to atomic hydrogen. There was no response of either type of nanorod to the presence of O₂ in the ambient at room temperature. The nanorod resistance still changes at least 15 min after the introduction or removal of the hydrogen. The change in resistance during exposure to hydrogen was slower in the beginning and the rate resistance change reached a maximum at ~ 15 min of exposure time. This could be due to some of the Pt becoming covered with native oxides, which is removed by exposure to hydrogen. Since the available surface Pt for catalytic chemical absorption of hydrogen increased after the removal of

the oxide, the rate of resistance change increased. However, the Pt surface gradually became saturated with hydrogen and the rate of resistance change decreased. The reversible chemisorption of reactive gases at the surface of nitrides and oxides can produce a large and reversible variation in the conductance of the material [Mit03]. The relative response of the Pt-coated nanorods was a strong function of H_2 concentration in N_2 . The Pt-coated InN nanorods detected hydrogen down to 10 ppm, with relative responses of $\sim 10\%$ at 100 ppm and 12% at 250 ppm H_2 in N_2 after 15 min exposure. The gas sensing mechanisms suggested in the past for semiconductors include the desorption of adsorbed surface hydrogen and grain boundaries in polycrystalline materials [Mit98], exchange of charges between adsorbed gas species and the surface leading to changes in depletion depth [Har95] and changes in surface or grain boundary conduction by gas adsorption/desorption [Cha94]. The detection mechanism is still not firmly established in these devices and needs further study. In addition, hydrogen introduces a shallow donor state in InN and this change in near-surface conductivity may also play a role [Dav03].

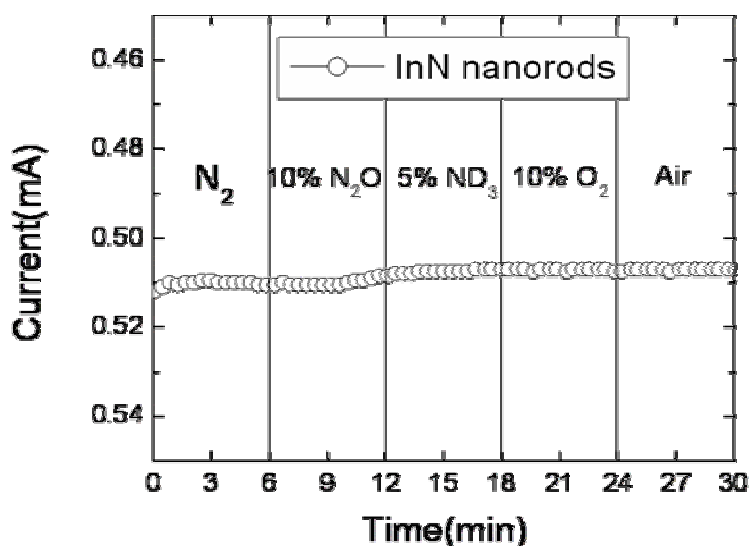


Figure 5-28. N_2 , N_2O , ND_3 , and O_2 test for InN nanorods.

Figure 5-28 shows the time dependence of resistance changes in the Pt-coated InN nanorods as the gas ambient is switched from vacuum to N₂, oxygen, nitrous oxide or ammonia (using the deuterated version), and then back to air. This data confirms the absence of sensitivity to O₂. The rate of resistance change for the nanorods exposed to the 250 ppm H₂ in N₂ was measured at different temperatures. An activation energy of ~ 12 kJ/mole was calculated from the slope of the Arrhenius plot. This value is larger than that of a typical diffusion processes. Therefore, the dominant mechanism for this sensing process is more likely to be the chemisorption of hydrogen on the Pt surface.

Moreover, the data was recorded at a power level of ~ 0.3 mW, which is low even in comparison with CNTs [Say05, Lu04]. This is attractive for long-term hydrogen sensing applications.

5.6 Conclusions

InN nanorods were successfully grown by H-MOVPE by adjusting HCl/TMIn, NH₃/TMIn ratios, and growth temperature. The optimal growth conditions were found to be HCl/TMIn = 4, NH₃/TMIn = 250, and T = 600 °C. This study showed that H-MOVPE is a promising technique to grow not only thick/thin films, but also nanostructured materials.

It was found that the majority of nanorods were single crystalline with wurtzite structure and that the growth axis was mainly c-axis [000 $\bar{2}$] with N-polarity. InN nanorods grown along different axes, and zincblende InN and bcc In₂O₃ were rarely observed. It, however, suggests that at least 4 growth axes are possible for InN nanorods growth. For example, InN wurtzite nanorods growth axes can be [000 $\bar{2}$], [$\bar{1}$ 010], [11 $\bar{2}$ 4],

and InN zincblende nanorods growth axis [220]. The growth axis for In₂O₃ growth was [402].

The main chemical components of InN nanorods were In and N, and no O, C, and Cl was detected by EDS. AES was found not to be a suitable technique for InN because InN is vulnerable to sputtering damage.

Following the growth study, vertically aligned nanorods were grown on GaN/c-Al₂O₃. InGaN formation at the interface was suggested for the self-aligned growth mechanism.

Room temperature PL showed that the bandgap of InN films and nanorods are around 1.1 eV, although undecided peaks were observed at 0.767 eV at low temperature.

The key finding of these studies is that the growth transitioned from a continuous film to micro-structured to nano-structured surfaces as the thermodynamic driving force transitioned through the growth to etching conditions. Thermodynamic equilibrium analysis demonstrated InN etching/growth regimes. It also showed that the nanorods' growth took place during the etch regime, whereas InN films were grown mainly during the growth regime. This suggests that the most stable atomic bonds persisted through the harsh growth conditions and nanorods could still grow along the most favorable c-axis direction.

Finally, Pt-coated InN nanorods based sensor was fabricated and ppm level of H₂ sensing was achieved at room temperature at very low power by utilizing a large surface area to volume ratio. InN nanorods may potentially be placed on cheap transparent substrates such as glass, making them attractive for low-cost sensing applications under very low power conditions.

CHAPTER 6
EXPLORATORY STUDY OF INDIUM NITRIDE FILMS GROWTH BY H-MOVPE

6.1 Experimental Procedure

The growth of InN films by H-MOVPE was studied by varying the growth parameters HCl/TMIn and NH₃/TMIn molar ratios and the growth temperature. A detailed description of the H-MOVPE technique is presented in Chapter 4. The indium, nitrogen, and chlorine sources were trimethylindium (TMI solution, Epichem), NH₃ (Anhydrous Grade 5, Matheson-Trigas), and HCl gas (10 % HCl in 90 % N₂, Air Products), respectively.

GaN/c-Al₂O₃ substrates were typically used in this study. The thickness of the GaN film (grown by MOVPE in Uniroyal optoelectronics) on c-Al₂O₃ was 5 μm measured by cross-sectional SEM. Substrates were cleaned by high pressure nitrogen gun with a static eliminator to remove potential particles on the surface before loading.

After loading the substrates, the temperature of the reactor was increased at a rate of 15 °C/min until the desired growth temperature was reached. HCl gas was applied *in situ* for 10 sec to clean the surface just prior to growth. N₂ was used as the carrier gas since H₂ is known to inhibit InN growth [Dra04].

Table 6-1. Base conditions of InN film growth.

Growth T	TMI flow rate	HCl flow rate	NH ₃ flow rate	N ₂ flow rate
560 °C	0.7 sccm	0.7 sccm (Cl/In = 1)	1750 sccm (N/In = 2500)	1600 sccm

Table 6-1 shows the base conditions of this growth study, which was adopted from InN film growth in a chlorinating environment [Kan04]. It is very important to choose

the right base conditions to reduce the number of experiments, especially when there are several growth parameters, as in this case. The HCl/TMIn ratio was changed from 0 to 6 by changing HCl flow rate from 0 to 4.2 sccm while keeping TMIn and NH₃ flows and growth temperature constant at 0.7 sccm, 1750 sccm, and 560 °C, respectively.

6.2 Results

6.2.1 Effect of HCl/TMIn Molar Ratio

Figure 6-1 shows SEM images of InN crystals grown for 1 hr at HCl/TMIn = 0, 0.3, 1, and 4, while keeping the other parameters constant (NH₃/TMIn = 2500, T = 560 °C). Indium metal droplets were observed when HCl was not provided (HCl/TMIn = 0).

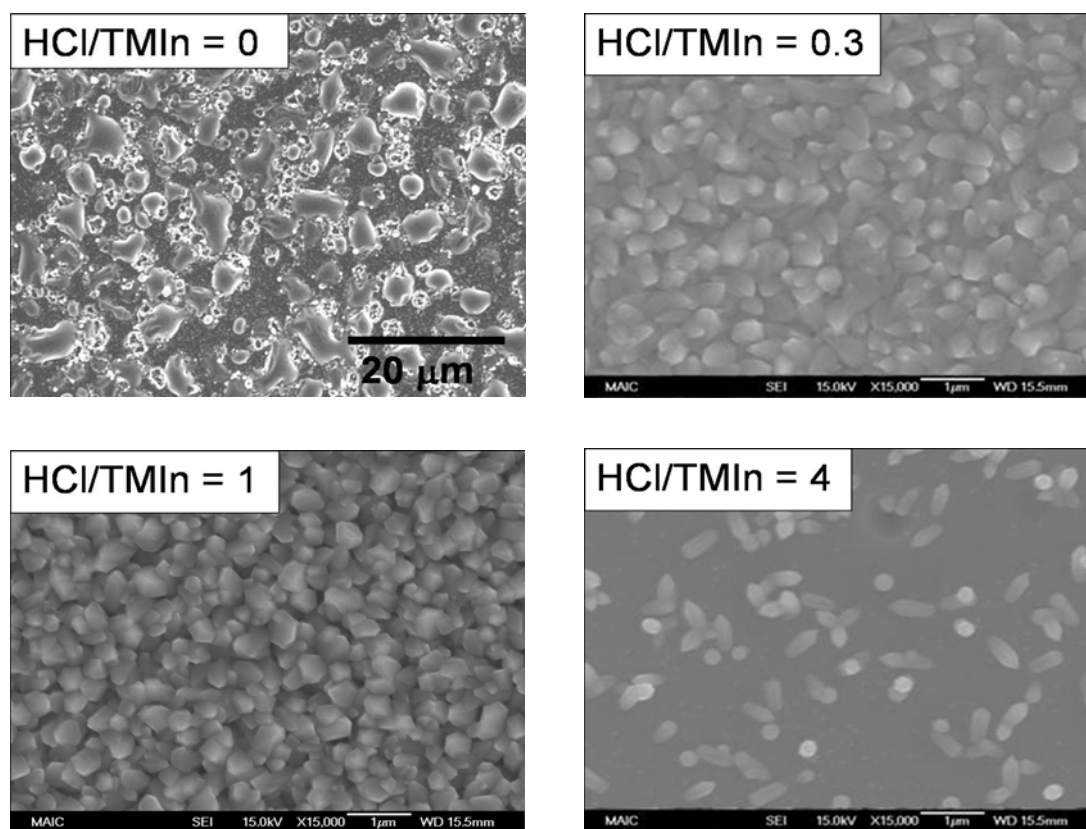


Figure 6-1. Scanning electron micrographs of InN films (a) HCl/TMIn = 0, (b) HCl/TMIn = 0.3, (c) HCl/TMIn = 1, and (d) HCl/TMIn = 4. Other growth conditions: T = 560 °C; P = 760 Torr; N/In ratio=2500; substrate: GaN/Al₂O₃; growth time = 1 hr.

When the HCl/TMIn is greater than 0.3, crystal grains ranging from 300 to 500 nm were viewed by SEM. The faceting was more clearly seen in cases with higher HCl/TMIn ratio. By looking at the crystal shapes and XRD results, the InN films grown were confirmed to be polycrystalline. At HCl/TMIn = 4, nanostructured materials were observed with a well-faceted surface.

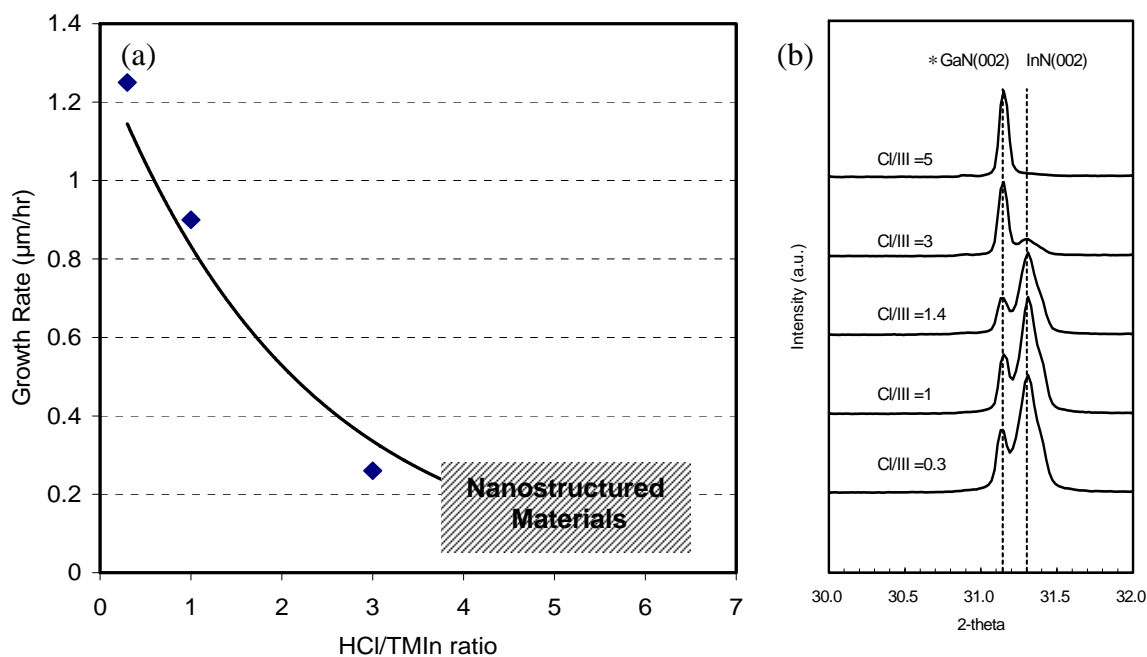


Figure 6-2. Growth rate and XRD of InN (a) InN growth rate and (b) XRD scan with respect to HCl/TMIn ratio; $T = 560\text{ }^{\circ}\text{C}$, $N/\text{In} = 2500$, substrate = GaN/ Al_2O_3 ; growth time = 1 hr.

Figure 6-2 shows the variation in the growth rate with respect to HCl/TMIn molar ratio along with XRD results. All the thicknesses were measured by cross sectional SEM. The thickness of rough film, however, is difficult to define. Therefore the growth rate determination should contain some error. A significant decrease in the growth rate was observed with increasing HCl/TMIn ratio. As HCl/TMIn ratio increased, the extra Cl shifted In from solid InN to the vapor phase as InCl_x species. Highly textured InN in the [002] direction was detected by XRD when HCl/TMIn were varied from 0.3 to 3. Interface InGaN formation possibly caused the strong texturing in the [002] direction.

Since GaN/Al₂O₃ substrates were used, the 2 θ range was truncated at 33.0 because of the intense GaN (002) substrate peak at 34.6°. It is noted, however, that the full diffraction pattern showed the film was polycrystalline and textured. The GaN (002) peak around 31.1° was from the Cu K β emission (X-ray source) denoted by an asterisk (*), which only appeared when the GaN film was of excellent quality.

6.2.2 Effect of Growth Temperature

Figure 6-3 shows the plan-view of SEM images of InN grown at 500, 525, 560, and 600 °C for 1 hr. Non-uniform films were grown at low temperature (500 °C). The films look more uniform at moderate temperature, between 525 and 560 °C. The film exhibited 300 to 500 nm grain sizes. The surface of the InN looked more faceted at a higher temperature (T = 600 °C).

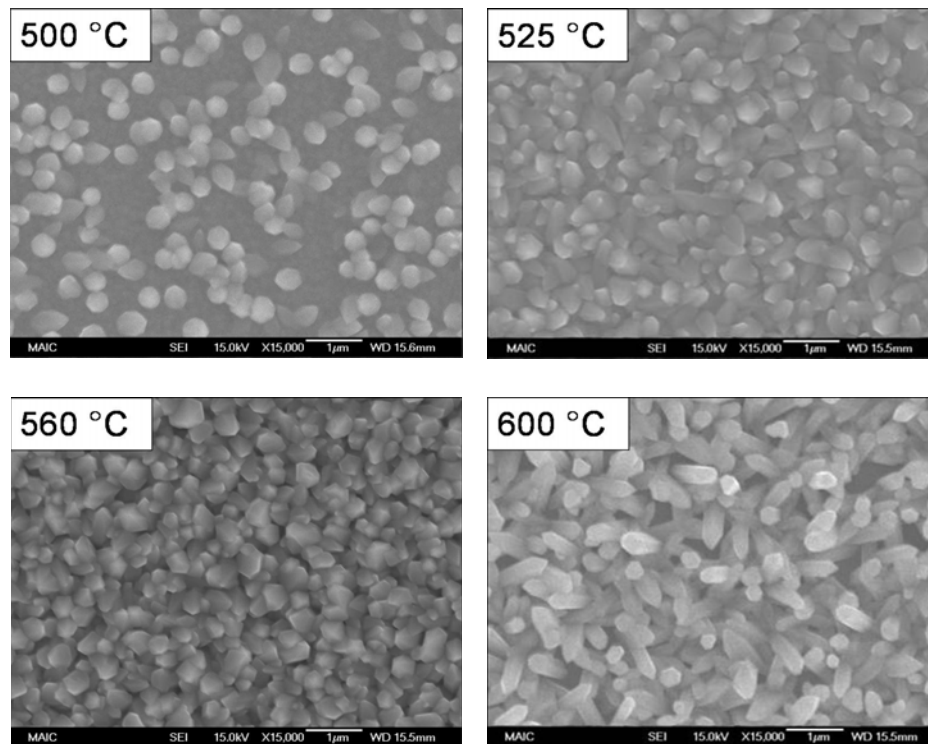


Figure 6-3. SEM plan-views of InN films grown at different temperatures (a) 500, (b) 525, (c) 560, and (d) 600 °C; Other growth conditions Cl/In ratio = 1; P = 760 Torr; N/In ratio = 2500; Substrate = GaN/c-Al₂O₃; growth time = 1 hr.

It is difficult to judge the crystal quality by the shapes of the grains, but more faceted crystals tend to have better crystal quality from the crystal grower's experience. A number of hexagonal shapes were observed. This may indicate that the InN grown at 600 °C was of high crystal quality although further clarification as TEM-DP is required to confirm high crystal quality.

The growth temperature was changed from 300 to 700 °C and the resultant growth rate changes and XRD results are shown in Figure 6-4. The growth rate increased as the growth temperature increased in a kinetically limited regime, while it stayed constant in a diffusion limited regime. Unsurprisingly, the growth rate decreased as the growth temperature was near the decomposition temperature of InN.

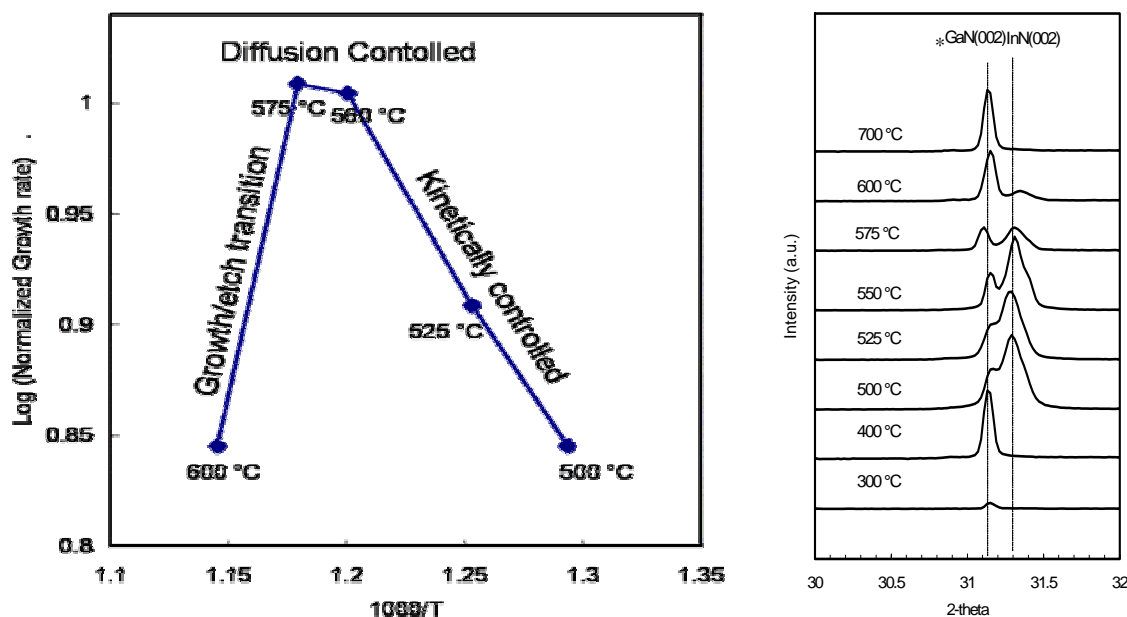


Figure 6-4. Growth rate and XRD scans with respect to the growth temperature (a) Log_e (Normalized growth rate) vs $1000/T$ (K), (b) XRD scans in 2 theta ranges from 30° to 32°; growth temperature 300 to 700 °C; growth time = 1 hr.

The slope of the kinetically controlled regimes (Arrhenius plot) shown in Figure 6-4 (a) was used to calculate the activation energy by the following equation:

$$G = Ae^{-E_a/RT}, \text{ or } \ln G = -\left(\frac{E_a}{R}\right)\frac{1}{T} + \ln A \quad (1)$$

where G is the normalized growth rate (unit less), A is a constant (also called pre-exponential factor), E_a is the activation energy, R is the gas constant, and T is absolute temperature. The activation energy obtained from the slope of Arrhenius plot was 14.3 kJ/mole (0.15 eV), which was considerably lower than typical metalorganic precursors. The typical activation energy for CVD growth in the kinetic regime ranges from 0.5 to 1 eV [Raa93]. The result suggested that *in situ* formed InCl (as a product of TMIIn and HCl reaction) may be a good precursor as it has lower activation energy than typical MO precursors. It could be argued, however, that the obtained activation energy may not be accurate since only three experimental points were used in this calculation.

The growth rate began to decrease when the temperature was higher than the decomposition temperature of InN, as seen in Figure 6-4. No InN peak was observed by XRD at < 400 °C as well as > 700 °C. A highly textured InN (002) peak was detected from 500 to 600 °C. Therefore, it can be concluded that the possible InN growth temperature range is 400 °C $< T < 700$ °C, which is consistent with Kim's result [Kim06].

6.2.3 Effect of NH₃/TMIIn Molar Ratio

SEM plan-view micrographs of InN grown at different N/In ratio (namely NH₃/TMIIn, or N/In molar ratio) are shown in Figure 6-5. It should be noted that there was no InN XRD peak at N/In =100 because the InN non-uniformly deposited under this condition. Hexagonal shapes, however, were clearly seen in the low N/In case by SEM. The grain sizes became smaller as the N/In ratio increased and film-like morphology was observed at N/In = 10000.

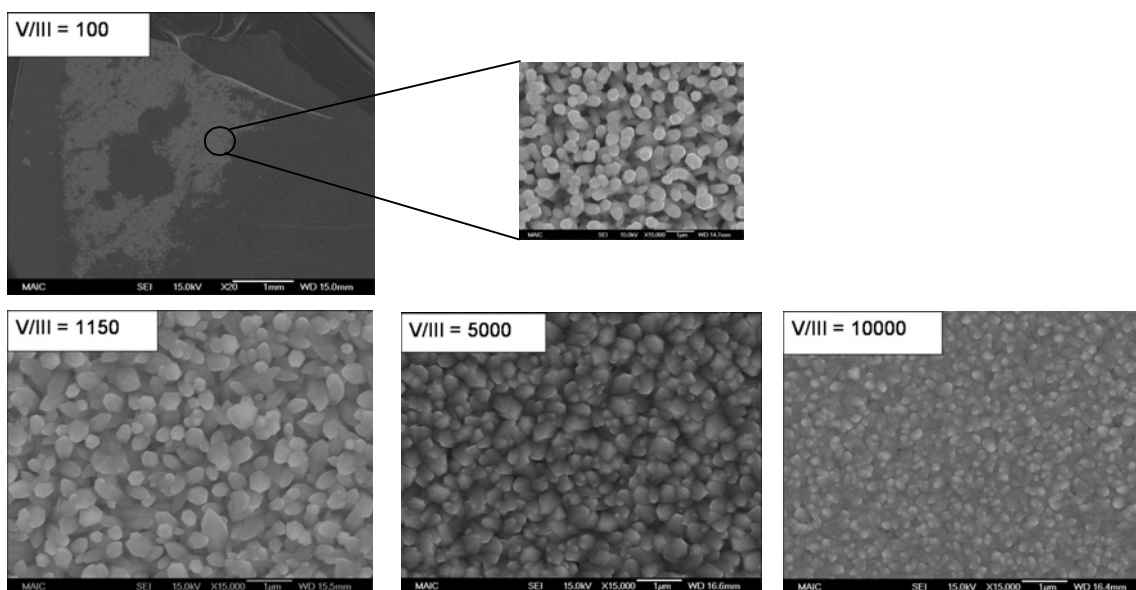


Figure 6-5. Scanning electron micrographs of InN films grown in different NH_3/TMIn ratios; other growth parameters Cl/In ratio = 1; P = 760 Torr; Growth T = 560 °C; growth time = 1 hr.

It was known that the growth rate of GaN did not change considerably with NH_3/TMGa molar ratio [Ree02]. On the contrary, the growth rate of InN significantly changed with NH_3/TMIn ratio, as shown in Figure 6-6.

The NH_3/TMIn molar ratio was changed from 100 to 50000. A maximum growth rate of 1.6 $\mu\text{m/hr}$ was achieved at the lowest NH_3/TMIn ratio (0.3) and it significantly decreased with increasing NH_3/TMIn ratio as shown in Figure 6-6 (a). It should be noted that not only the thickness of the film but also the morphology (grain size) of the film is changing. The comparison of growth rates with different morphology films may not be appropriate. Nonetheless, comparing with the maximum growth rate in conventional MOCVD system, it is about an order of magnitude higher. The reason of this high growth rate may be due to the higher reactivity of InCl than TMIn, a decrease in the H_2 from low NH_3/TMIn ratio, and/or the hot reactor wall, which facilitated NH_3 decomposition. An InN (002) peak was always observed from 250 to 10000 by XRD, although the highly textured (002) peak was only detected in the N/In range 500 to 5000,

as shown in Figure 6-6 (b). The intensity of the InN (002) peak was too low to be seen because of the decrease in the thickness at high NH_3/TMIIn ratios. Therefore, the intensity of XRD data was multiplied by 10 or 30 times to see the peaks more clearly, as seen in Figure 6-6 (c).

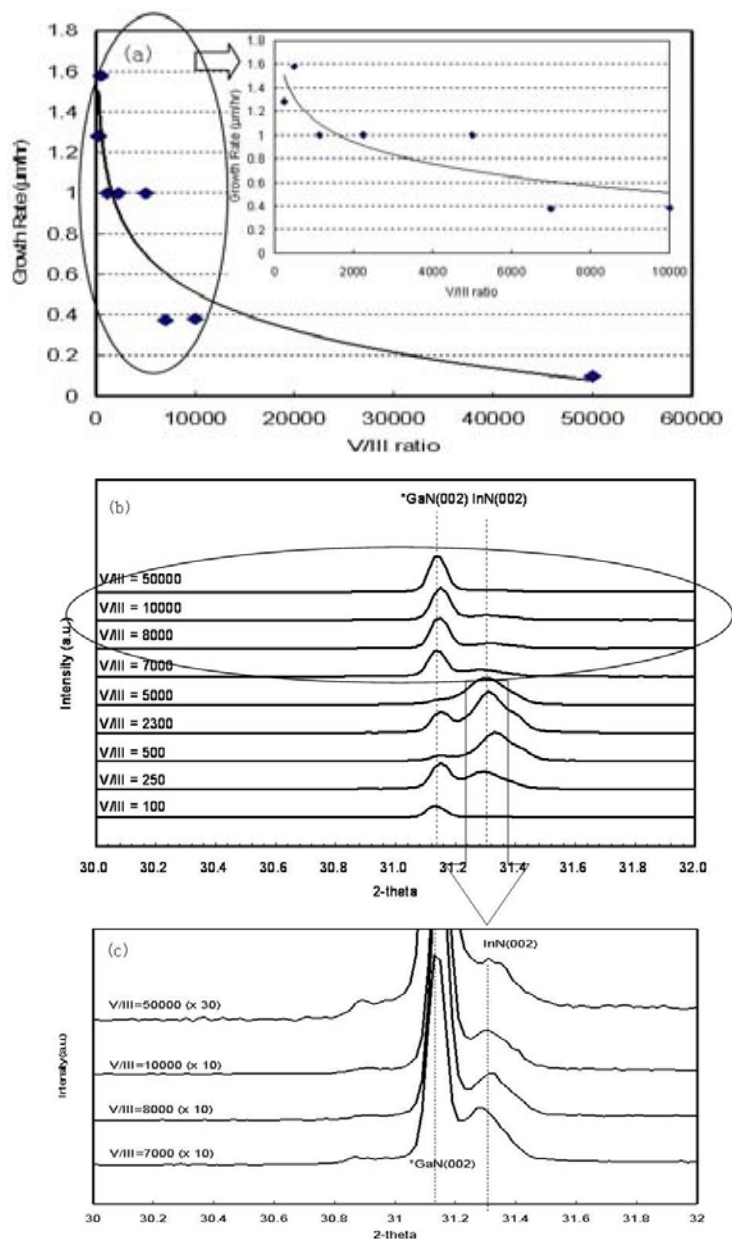


Figure 6-6. Growth rate and XRD scans with respect to NH_3/TMIIn ratio (a) Growth rate vs. N/In (NH_3/TMIIn) ratio, (b) XRD scans of 2 theta range from 30 to 32° when N/In was 100 to 50000 , (c) enlarged view of XRD for N/In range 7000 to 50000 ; Cl/In ratio = 1 ; $P = 760$ Torr; growth $T = 560^\circ\text{C}$; growth time = 1 hr

6.2.4 Effect of Buffer Layer

6.2.4.1 Surface Morphology of InN Films without Buffer Layer

The surface morphology of the polycrystalline InN films was characterized by AFM, with an example shown in Figure 6-7. (1 μm x 1 μm scanned area). The growth conditions were $\text{NH}_3/\text{TMI} = 10000$, $\text{HCl}/\text{TMI} = 1$, $T = 560^\circ\text{C}$, and the growth time = 1 hr without a buffer layer. The substrate was GaN/c- Al_2O_3 . The observed grain size was in the range of 100 to 250 nm with a rough surface. The RMS roughness by AFM was 34 nm, suggesting that more optimization is required to obtain a smoother surface.

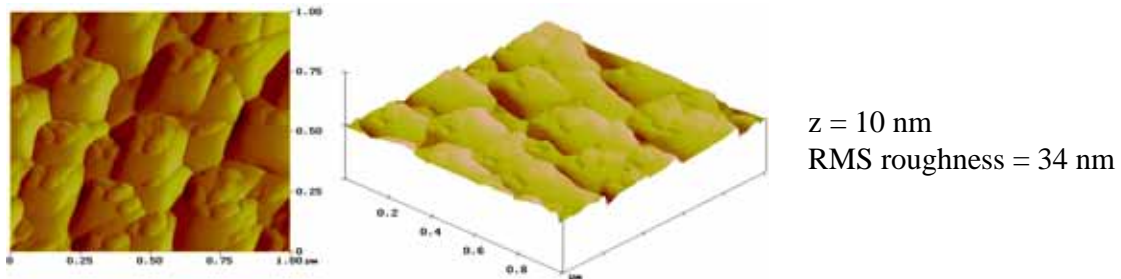


Figure 6-7. AFM images of the InN films. $\text{NH}_3/\text{TMI} = 10000$, $\text{HCl}/\text{TMI} = 0.3$, $T=560^\circ\text{C}$; Substrate = GaN/c- Al_2O_3 ; growth time = 1 hr

6.2.4.2 Growth of InN Films with Low Temperature Buffer Layer

Optimal buffer layer growth conditions were adopted from Kim's buffer layer study [Kim06]. The buffer layer was grown at $T = 450^\circ\text{C}$ for 30 min followed by HT-InN growth at $T = 560^\circ\text{C}$, $\text{NH}_3/\text{TMI} = 5000$, and $\text{HCl}/\text{TMI} = 1$ for 1 hr.

The substrate used in this study was GaN/ Al_2O_3 . About 0.89 μm thick HT-InN film was grown. The surface morphology and thickness are shown in Figure 6-8.

To determine the crystal quality of the InN film with a buffer layer, XRD θ -2 θ scan and XRD ω -rocking curves were obtained. Figure 6-9 shows the InN film highly textured along the [002] axis.

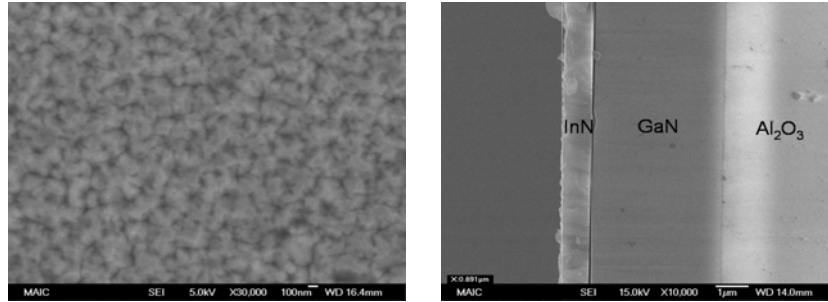


Figure 6-8. SEM plan-view and cross-sectional of InN films on GaN/Al₂O₃ substrate; N/In = 5000, Cl/In = 1, T = 560 °C, and growth time = 1 hr with 450 °C buffer layer growth for 30 min.

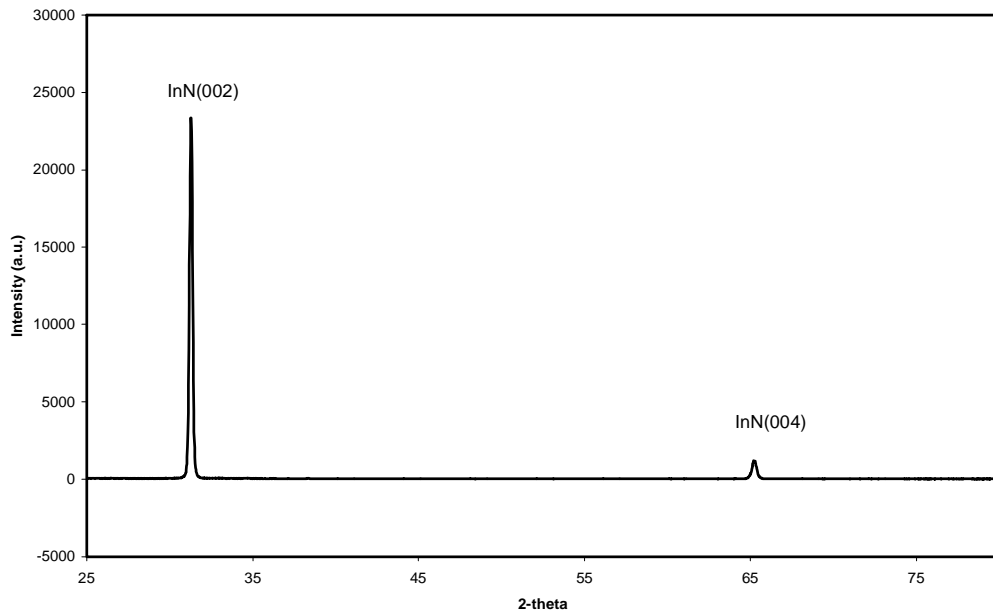


Figure 6-9. XRD θ - 2θ scan of InN grown on GaN/Al₂O₃ substrate; N/In = 5000, Cl/In = 1, T = 560 °C, and growth time = 1 hr with 450 °C buffer layer growth for 30 min.

Although the thickness of InN film was 0.89 μm , the substrate peaks related to GaN (002) and Al₂O₃ (006) were not observed. The absence of substrate peaks suggest that the films were grown along a tilted axis with respect to the c-axis of GaN/Al₂O₃. XRD ω -rocking curve (Figure 6-10) shows that the grown InN film is high crystal quality. The crystal quality of InN, however, was not as good as that of GaN. For example, the FWHM of the ω -rocking curve of H-MOVPE grown InN film was 2.55 ° (9180 arcsec),

while the typical FWHM of the XRD ω -rocking curve of GaN grown by H-MOVPE was about 780 arcsec, as presented in Figure 4-5.

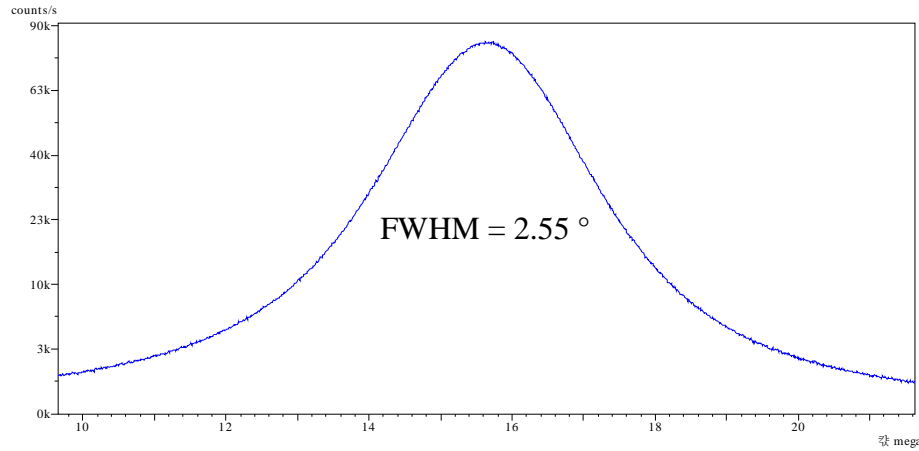


Figure 6-10. XRD ω -rocking curve of InN grown on GaN/Al₂O₃ substrate; N/In = 5000, Cl/In = 1, T = 560 °C, and growth time = 1 hr with 450 °C buffer layer growth for 30 min.

6.2.5 Growth of InN Films on Al₂O₃ and Si

InN films were grown on Al₂O₃ and Si substrates using the same LT-buffer layer described in the previous section. Sapphire is the most frequently used substrate for III – nitride growth due to its thermal and chemical stability and the formation of AlN or AlO_xN_y at the surface with nitridation process is also beneficial.

The advantages of a Si wafer as a substrate material for InN are numerous. Not to mention the advantages of integration with already well-developed Si technology, another interesting possibility is the fabrication of tandem solar cell using InN/Si structure. Growth on Si substrate is known to be more difficult than growth on Al₂O₃, due to the dissimilarity of the surface atomic structures and the thermal expansion mismatch. The lattice mismatch of InN on Si (8 %) is less than that of InN on Al₂O₃ (-26 %), but the thermal expansion coefficient mismatch of InN on Si (52 %) is more than that of InN on Al₂O₃ (-34 %).

Figure 6-11 shows the XRD θ - 2θ scan of InN film grown on c- Al_2O_3 substrate.

The peak from InN is only from the (002) plane showing that the film is highly textured in the [002] direction.

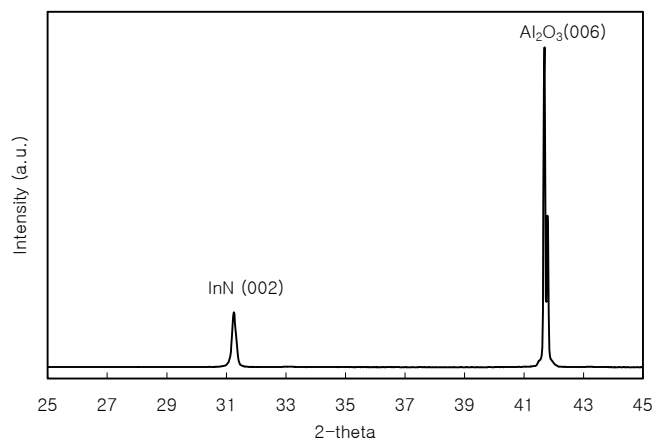


Figure 6-11. XRD θ - 2θ scan of InN film grown on c- Al_2O_3 substrate; N/In = 5000, Cl/In = 1, T = 560 °C, and growth time = 1 hr with 450 °C buffer layer growth for 30 min.

Figure 6-12 shows the θ - 2θ scan of InN film grown on Si(111) substrate for 2 hr at the same growth conditions with a 30 min LT-buffer layer. Here it was observed that a very intense InN (002) peak with a small Si (111) peak, suggesting that the film is thick (about X-ray penetration depth of $\sim 5 \mu\text{m}$).

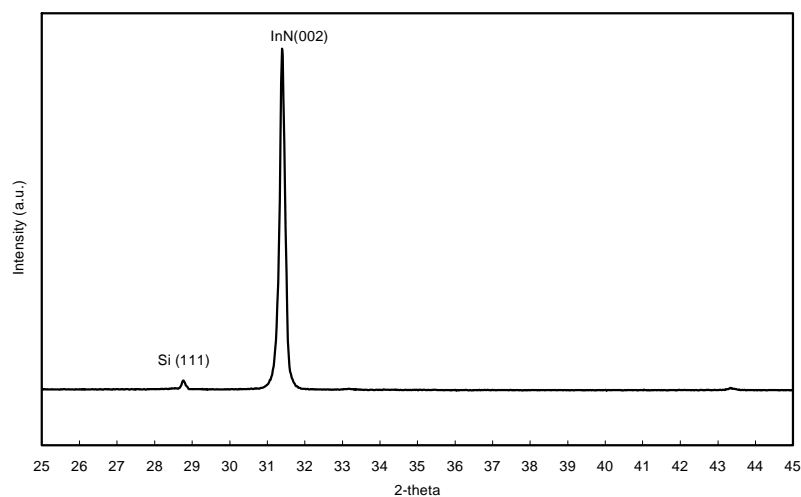


Figure 6-12. XRD θ - 2θ scan of InN film grown on Si(111) substrate. N/In = 5000, Cl/In = 1, T = 560 °C, and growth time = 2 hr with 450 °C buffer layer growth for 30 min.

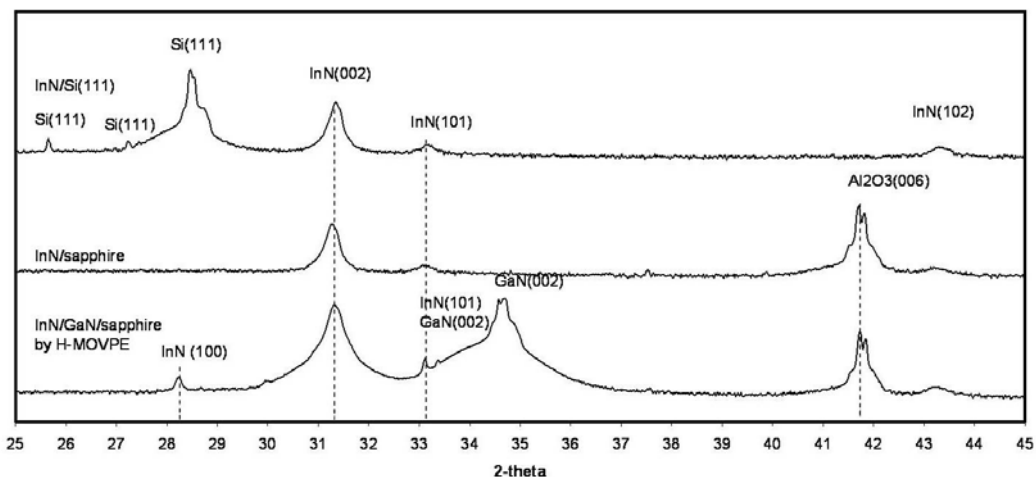


Figure 6-13. XRD θ - 2θ scan comparison of InN film grown on different substrates: N/In = 5000, Cl/In = 1, T = 560 °C, and growth time = 1 hr with 450 °C buffer layer growth for 30 min.

To compare the substrate effects, the XRD results were organized in logarithmic scales as shown in Figure 6-13. InN films grown on Si(111), c-Al₂O₃, and GaN/Al₂O₃ substrates were compared. The data suggests that the InN film is highly textured in the [002] axis, regardless of the substrate used. All samples, however, showed InN(100), InN(101), and InN(102) peaks, which suggested that the InN films were polycrystalline.

6.3 Conclusions

The morphology evolution of InN was studied by changing the growth parameters HCl/TMIn, NH₃/TMIn molar ratios, and growth temperature. The growth rate decreased with increasing HCl/TMIn and NH₃/TMIn molar ratios due to the etching effect of HCl and H₂. The growth rate increased in a kinetically controlled regime, stayed constant in a diffusion controlled regime, and decreased in a growth/etch transition regime with increasing growth temperature. The possible InN growth temperature range of 400 °C < T < 700 °C was determined as a result. The optimal growth condition for single crystalline InN film by H-MOVPE is still under study. More optimization, especially

with the various buffer layers, should be performed to get high-quality single crystal films with a smooth surface.

CHAPTER 7
EXPLORATORY STUDY OF GALLIUM NITRIDE NANORODS GROWTH BY H-MOVPE

InN nanorods were successfully grown, as presented in Chapter 5. Following the growth of InN nanorods, the growth of GaN nanorods was attempted, since GaN has a number of potential attractive applications. For example, UVLED, high power and high temperature devices can be fabricated utilizing the wide energy bandgap and thermal stability of GaN.

7.1 Experimental Procedure

The base conditions for GaN nanorod growth are listed in Table 7-1. Growth was carried out with or without a nitridation process. As a nitridation process, only 800 sccm of NH₃ was provided with N₂ for 15 min after growth zone temperature was increased to 850 °C; c-Al₂O₃, GaN/c-Al₂O₃, and Si(111) were used as the substrates. Both N₂ and H₂ carrier gases were tested. The Cl/Ga molar ratio was changed in the range 2 to 19, while N/Ga ratio and growth temperature were set at 250 and 850 °C, respectively.

Table 7-1. Base conditions for GaN micro/nanorods growth.

Growth T	TMGa flow rate	HCl flow rate	NH ₃ flow rate	N ₂ flow rate
850 °C	3.2 sccm	6.4 sccm (Cl/Ga = 2)	800 sccm (N/Ga = 250)	1600 sccm

7.2 Results

It is observed from viewing SEM micrograph that a GaN film was grown on the GaN/c-Al₂O₃ substrate, while GaN microrods were grown on the c-Al₂O₃ and Si (111) substrates at the base conditions (T = 850 °C, Cl/Ga = 2, N/Ga = 250) without nitridation in N₂ carrier gas, as shown in the first row of micrographs in Figure 7-1. Scattered

growth of GaN is expected on Si with nitridation since GaN is difficult to nucleate on Si_3N_4 . An increase of the Cl/Ga ratio from 2 to 3 made the nucleation of GaN less favorable, as seen in the second row of micrographs. Thus, there is no GaN deposition on c- Al_2O_3 or Si(111) at Cl/Ga = 3. An interesting worm-shaped streamline is observed on the GaN/c- Al_2O_3 substrates. This result suggests that nucleation of GaN is more favorable on GaN substrates rather than Al_2O_3 and Si substrates when nitridation was not used to prepare the after surfaces

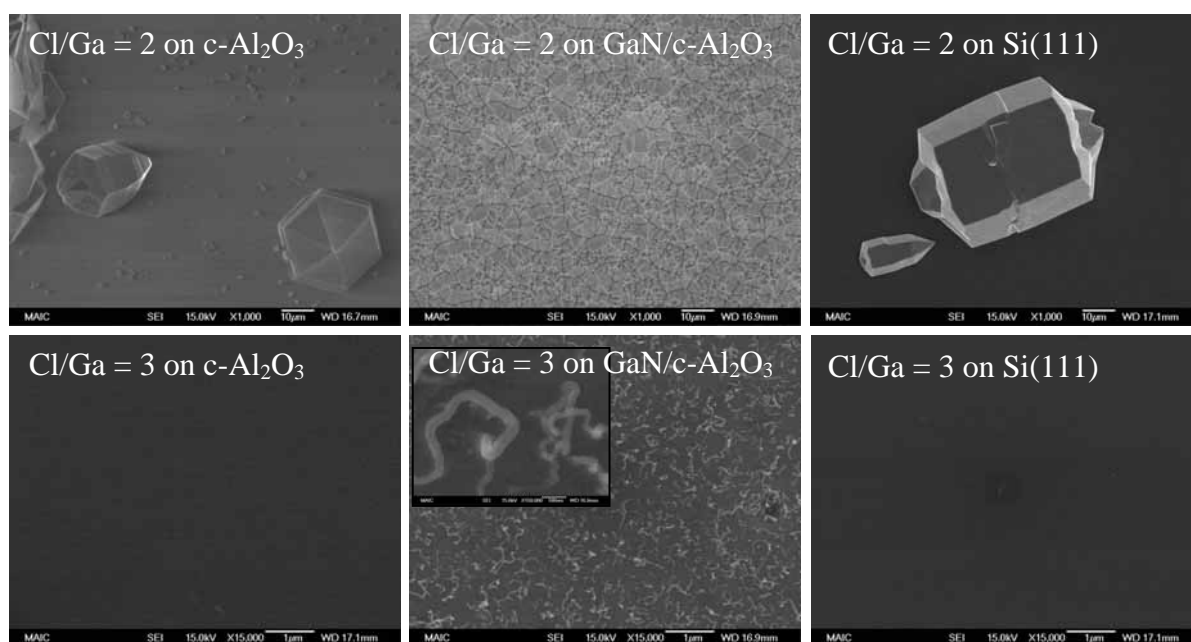


Figure 7-1. SEM plan-view micrographs of GaN grown at Cl/Ga ratio 2 and 3 on c- Al_2O_3 , GaN/c- Al_2O_3 , and Si at N/Ga = 250 without nitridation in N_2 .

To judge the effects of nitridation and carrier gas selection, a 15 min nitridation at 850 °C was carried out using NH_3 and H_2 was used as the carrier gas instead of N_2 . Two HCl flow rates of 8.0 sccm (Cl/Ga = 2.5) and 8.8 sccm (Cl/Ga = 2.75) were used to see the Cl/Ga ratio effect while keeping TMGa and NH_3 flows constant at 3.2 and 800 sccm, respectively. The SEM micrograph results are shown in Figure 7-2. It is observed again that a GaN film completely covered the GaN/c- Al_2O_3 substrate, while GaN was non-

uniformly deposited on the c-Al₂O₃ and Si substrates for both values of Cl/Ga. Well-faceted GaN microrods were observed on c-Al₂O₃ and Si(111) substrates, while more film-like morphology was viewed on GaN substrate at Cl/Ga = 2.5. Short and often faceted GaN crystals are seen on the c-Al₂O₃ and Si(111) substrates at Cl/Ga ratio = 2.75 with more exposed surface area, whereas more film-like uniform coverage was detected on the GaN/c-Al₂O₃ substrate.

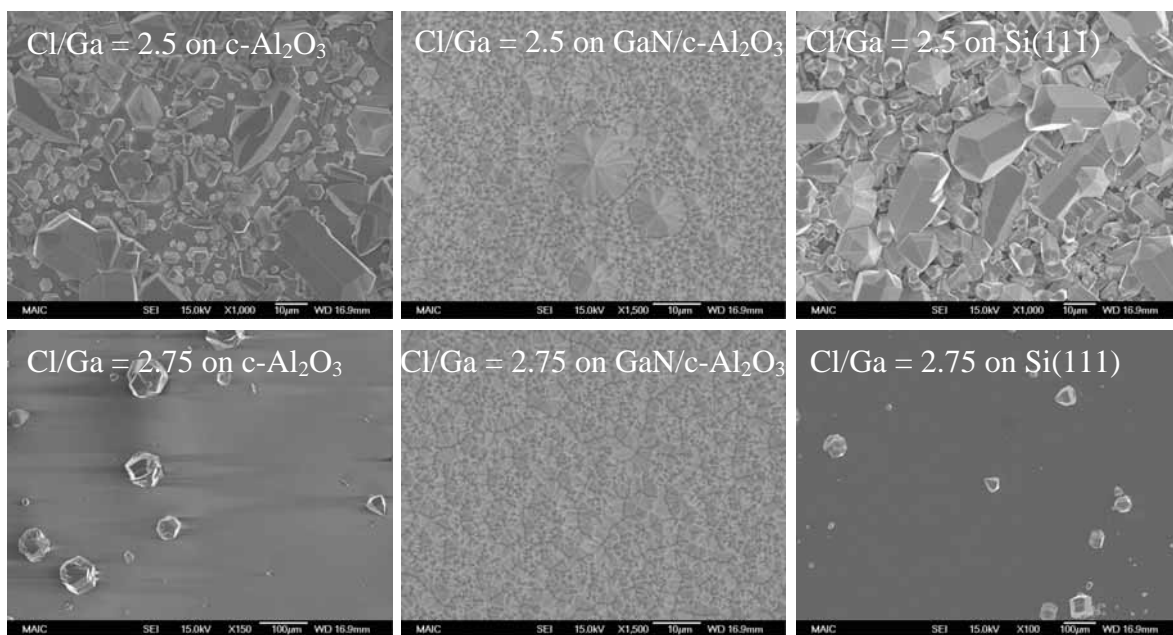


Figure 7-2. SEM micrographs of GaN grown at Cl/Ga ratio of 2.5 and 2.75, N/Ga = 250, and in H₂ with nitridation.

It appeared that a nitridation step may be needed to assist nucleating GaN nanorods on Si(111). It is known that GaN film is not to grow on Si₃N₄. However, if Si₃N₄ deposited non-uniformly on Si, it will act as *in situ* mask that can facilitate nucleation of GaN nanorods in small opening windows. The overall growth rate can be lowered by also decreasing the Ga flux, which might facilitate nucleation of smaller nuclei. Therefore, a 15 min nitridation was carried out at 850 °C and TMGa flow was decreased 3.2 to 1.6 sccm, while maintaining the N/Ga ratio at 250 by decreasing NH₃ flow rate in

the range 800 to 400 sccm. The Cl/Ga ratio was then changed in the range 2 to 6 by increasing the HCl flow rate in the range 3.2 to 9.6 sccm while keeping TMGa flow at 1.6 sccm.

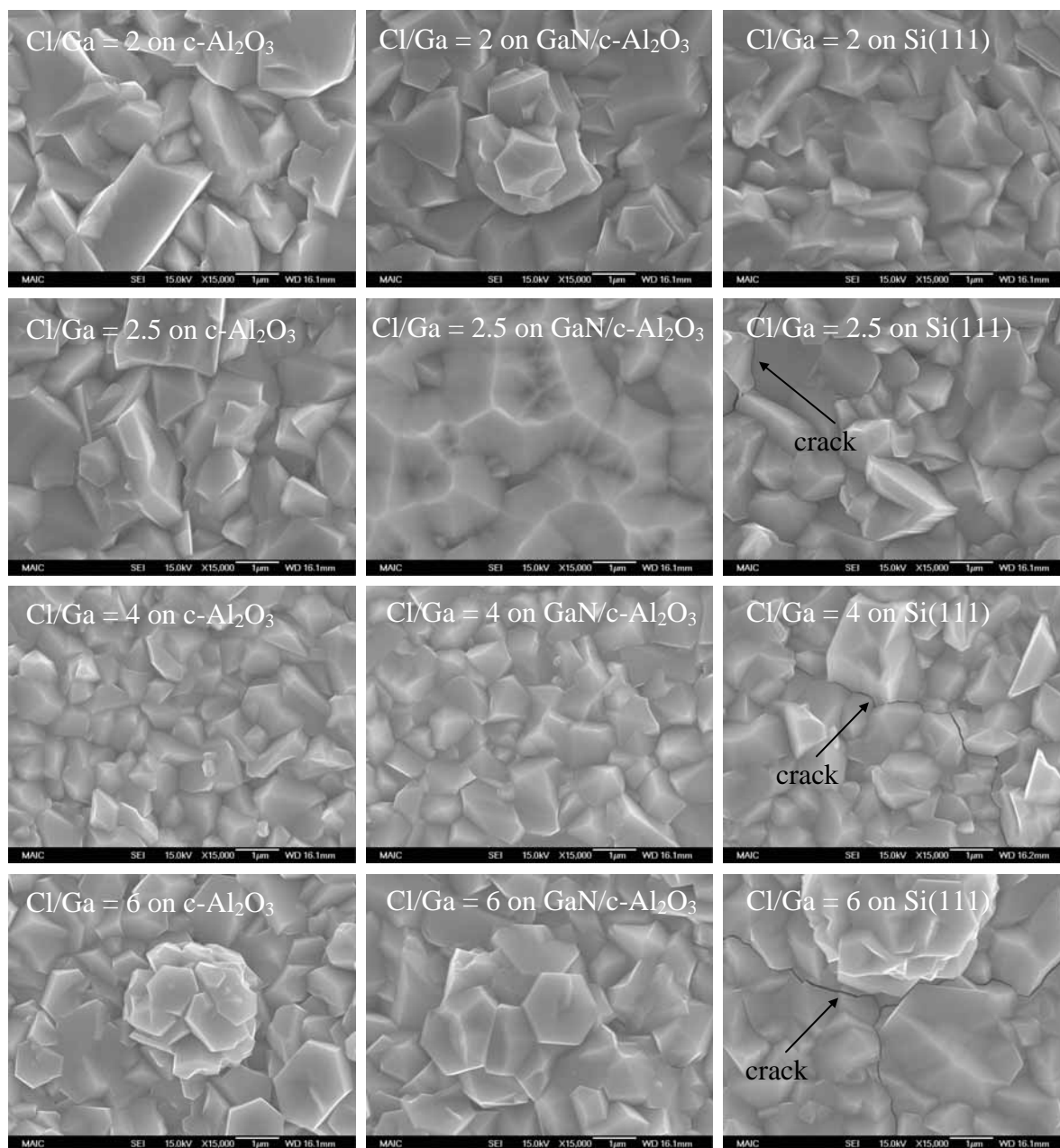


Figure 7-3. SEM plan-view of GaN with Cl/Ga ratio 2, 2.5, 4, and 6 on c-Al₂O₃, GaN/c-Al₂O₃, and Si(111).

Figure 7-3 shows SEM micrographs of grown with variation of the Cl/Ga ratio: Cl/Ga = 2, 2.5, 4, and 6 in N₂ carrier gas. Because of the nitridation process, complete

coverage of GaN/c-Al₂O₃ was observed, regardless of the substrate. No significant differences were found in this experimental set, although it appeared that more hexagonal-plate structures were found at high Cl/Ga = 6 conditions and more film-like features were observed on GaN/c-Al₂O₃ at Cl/Ga = 2.5. Although the surface was very rough, GaN film on Si(111) substrates occasionally showed cracks just as in the case of growing thick GaN film.

A higher Cl/Ga ratio (> 6) was apparently required to grow GaN nanostructures. It should be noted that the maximum flow rate of HCl was 10.0 sccm because of the MFC limit. Therefore, the TMGa flow rate was decreased from 1.6 to 0.5 sccm while keeping the HCl flow near the maximum allowable value at 9.6 sccm (Cl/Ga = 19) and NH₃ flow at 400 sccm (N/Ga = 800).

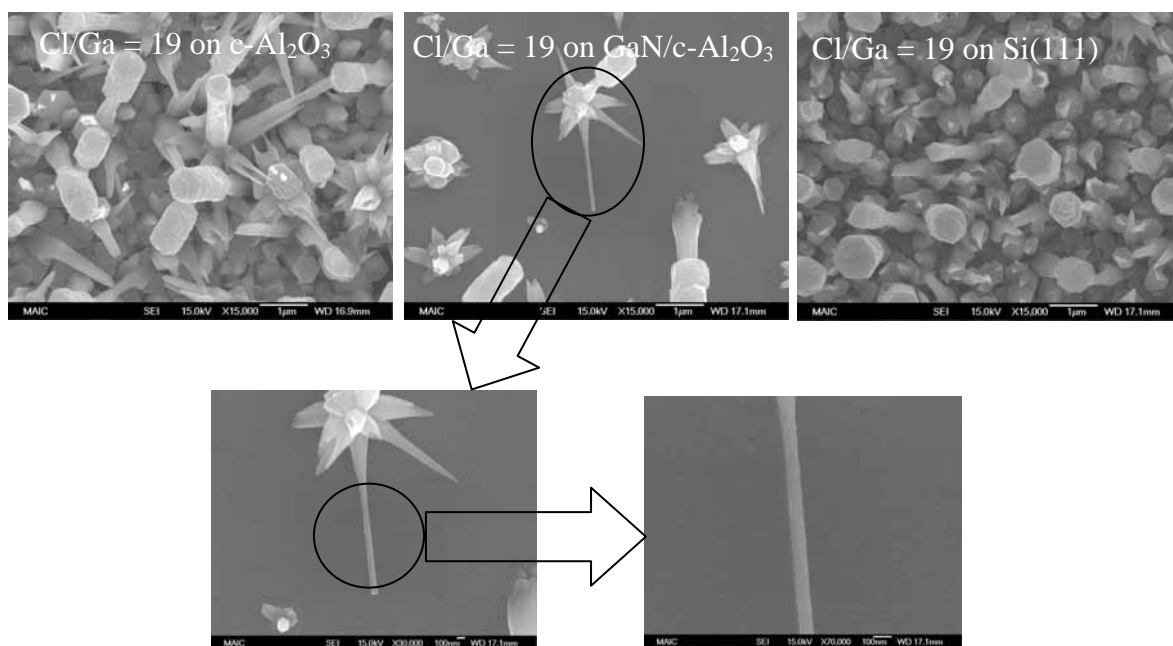


Figure 7-4. SEM plan-view of GaN at Cl/Ga = 19, N/Ga = 800, T = 850 °C on various substrates.

Interesting columnar structures were observed in this case, as shown in Figure 7-4. The denoted Cl/Ga ratio of 19, however, may have a large uncertainty since the TMGa

flow rate of 0.5 sccm may be wrong. When TMGa flow rate (F_{TMGa}) was determined, following formula was used:

$$F_{TMGa}(sccm) = \frac{P_{TMGa}^{vap}(Torr)}{P_{TMGa}^{vap}(Torr) + P_{bubbler}^{out}(Torr)} \times F_{N_2}(sccm) \quad (1)$$

where $P_{TMGa}^{vap}(Torr)$ is the vapor pressure of TMGa, $P_{bubbler}^{out}(Torr)$ is the pressure of the bubbler, and F_{N_2} is the flow rate of the N₂ carrier gas through the bubbler. The vapor pressure of TMGa is a strong function of bubbler temperature and is given by the following equation [provided by Epichem]:

$$\text{Log}_{10} P(Torr) = 8.07 - \frac{1703}{T(K)} \quad (2)$$

Since the TMGa bubbler was used at room temperature (20 °C), $P_{TMGa}^{vap} = 182$ Torr was calculated from the above equation. The bubbler pressure is higher than the total reactor pressure (760 – 800 Torr) to if it delivers the stream. It was customary to set the pressure at $P_{bubbler}^{out}(Torr) = 882$ Torr by adjusting the needle valve at the bubbler exit line. Thus, the flow rate of TMGa became $F_{TMGa}(sccm) = 0.17 \times F_{N_2}(sccm)$. To make $F_{TMGa} = 0.5$ sccm, F_{N_2} should be 3 sccm. It is known that when the flow rate is less than 10 % of MFC maximum, the flow rate may not be accurate. The maximum MFC flow rate of N₂ carrier gas through the bubbler was 50 sccm and thus at $F_{N_2} < 5$ sccm may be correlate error in the flow rate. In addition, when a very low flow rate, such as 3 sccm, was used, it was now difficult to control bubbler pressure since the pressure is not sensitive to the aperture of the needle valve. Hence, maintaining the bubbler out line pressure at $P_{bubbler}^{out}(Torr) = 882$ Torr was a challenge, and it was often questionable how accurately the

pressure was being maintained. Therefore, the actual TMGa flow rate and Cl/Ga ratio may not be correct. To avoid this problem, one should lower the bubbler temperature and increase the N₂ flow rate accordingly or obtain new MFCs.

7.3 Conclusions

An exploratory growth study of GaN nanorods was carried out by changing growth conditions such as Cl/Ga molar ratio, substrate nitridation, and N₂/H₂ carrier gases on GaN/c-Al₂O₃, c-Al₂O₃ and Si(111) substrates. More uniform coverage was observed on GaN/c-Al₂O₃ than c-Al₂O₃ or Si(111) substrates when no nitridation was carried out or when H₂ carrier gas was used. When nitridation was performed and N₂ carrier gas was used, complete coverage of GaN was achieved, regardless of the substrate. Although GaN nanorods were not successfully grown, the morphology changes suggest that GaN nanorods could be grown at a high Cl/Ga ratio (> 6).

CHAPTER 8 FUTURE WORK AND RECOMMENDATIONS

8.1 Nucleation and Growth Mechanism Studies of InN Nanorods

Although controlled syntheses of InN nanorods were achieved by H-MOVPE without external catalyst or template, the nucleation and growth mechanism of nanorods are unclear at this point. Interestingly, vertical alignments of nanorods were sometimes observed on GaN/c-Al₂O₃; however, the results were not consistent.

Initial stage of growth can be studied by taking the sample after several short runs. This may show the nucleation mechanism of nanorods. The attempts were not successful since no growth was observed in 10 min run, and a number of nanorods were observed after 15 min run although the deposition was non-uniform.

The interface between nanorods and substrates needs to be characterized by TEM. The challenge is how to prepare the sample without damaging the interface. This will elucidate the growth mechanism more clearly.

8.2 Self-aligned InN Nanorods as Buffer Material for GaN on Si

Crack-free, thick GaN films were successfully grown on Si (111) using InN nanorods as a buffer material. The GaN films, however, were polycrystalline, perhaps because the growth axis was non-uniform because of the random arrangement of the underlying InN nanorods. Self-aligned InN nanorods were also grown on GaN substrates. If self-aligned InN nanorods could be grown on GaN/Si templates, the overgrown thick GaN may have an aligned growth axis that is essential for single crystal growth. The schematic of this procedure is proposed as in Figure 8-1.

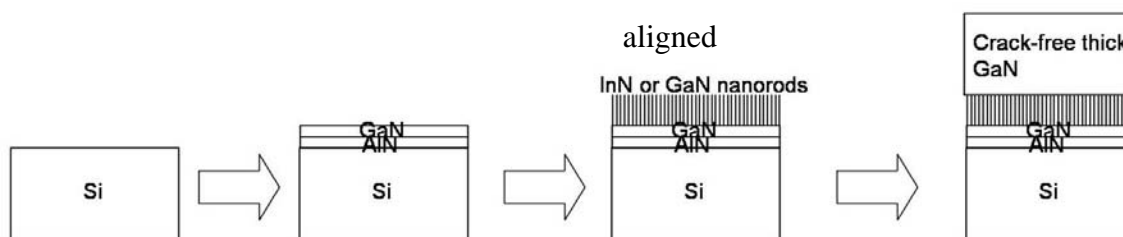


Figure 8-1. Schematic of crack-free GaN growth on Si substrate using self-aligned InN or GaN nanorods.

8.3 Buffer Layer Optimization for GaN growth on Si Substrate

The lack of suitable substrates has been a longstanding problem for Group III nitride growth. It is obvious that buffer layer optimization including the selection of buffer layer material, growth conditions, and thickness, are very important to grow high quality film. It was observed that adequate use of such a buffer layer could compensate for lattice and thermal expansion mismatches. In addition, the buffer layer can change the surface properties by reducing the surface free energy. It turns out, however that there is no universal rules for specific buffer layer selection and growth, as by occasionally observing similar results for very different growth conditions. For example HT-AlN or LT-AlN buffer layers, and nitridation temperature, or nitridation time all give promising results, depending upon the recipes for growth of the buffer layer. Therefore, additional buffer layer optimization should be performed for H-MOVPE system especially on Si substrate.

Thick GaN was recently grown on Si using InN nanorods as an interface material. The film quality, however, was not satisfactory and no single crystal GaN has been grown on Si to date using InN nanorods interlayer approach. The proper growth and application of buffer layers will enhance material quality significantly.

8.4 Use of Negative Thermal Expansion Materials

The growth of thick/freestanding GaN is impeded by lack of suitable substrates. The bowing and cracking problems are troublesome because of the excessive stress caused mainly by thermal expansion differences between GaN the substrates. If the thermal expansion of the materials could be controlled, the bowing and cracking problem can be reduced. Here the use of negative thermal expansion materials as a buffer material was suggested.

Although most materials in nature expand when they are heated, there are several negative thermal expansion (NTE) materials as listed in Table 8-1.

Table 8-1. Lists of NTE materials.

NTE materials	Reference
ZrW ₂ O ₈	[Per98] [Eva97] [Yam01] [Mar96] [Eva96] [Pry96] [Sik04] [Dad97]
HfW ₂ O ₈	[Yam01] [Wit98]
ZrV ₂ O ₇	[Car01] [Mar96][Pry96]
ZrMo ₂ O ₈	[Car00]
Sc ₂ (WO ₄) ₃	[Sec02]
Lu ₂ (WO ₄) ₃	[Liu02]
Al ₂ (WO ₄) ₃	[Gar01]
Gd ₂ (MoO ₄) ₃	[Bri72] [Dmi03]
Sm ₂ (MoO ₄) ₃	[Dmi03]
Eu ₂ (MoO ₄) ₃	[Dmi03]
Sc ₂ (MoO ₄) ₃	[Jor99]

ZrW₂O₈ and HfW₂O₈ are the most well-studied compounds in this table. Figure 8-2 shows the lattice parameter changes of these NTE materials with increasing temperature [Yam01]. Cubic ZrW₂O₈ (a = 9.157 Å at room temperature) and HfW₂O₈ (a = 9.130 Å at room temperature) exhibits isotropic NTE from 0.3 to 1050 K with $\alpha = -8.8 \times 10^{-6} \text{ K}^{-1}$ [Eva97]. The lattice parameters of HfW₂O₈ and ZrW₂O₈ decreased linearly with temperature. It should be noted that the cubic crystal structures persisted during

heating, that the crystals shrink isotropically, and that no phase transform occurred up to the decomposition temperature. The decomposition temperature of ZrW_2O_8 is ~ 1050 K

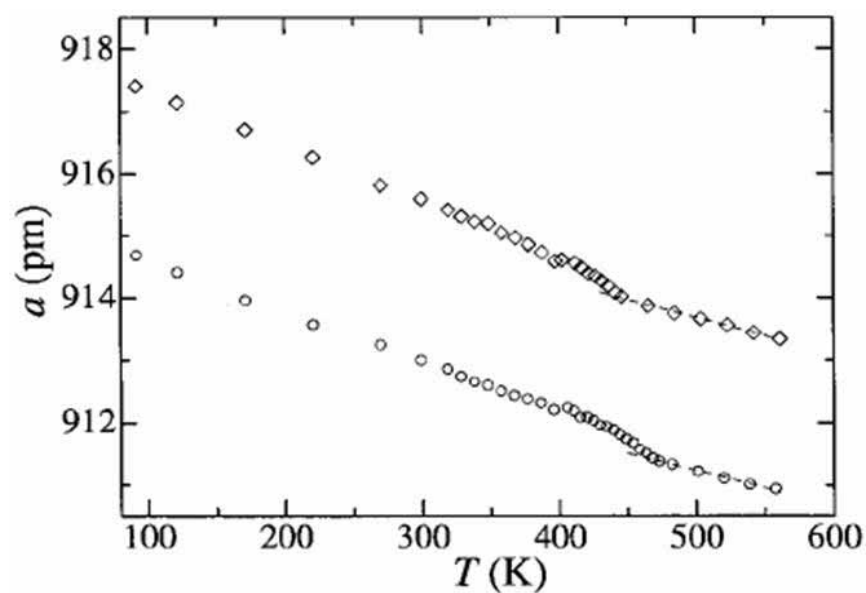


Figure 8-2. Lattice parameters of ZrW_2O_8 (◇) and HfW_2O_8 (○) as a function of temperature [Yam01].

The unit cell of ZrW_2O_8 is shown in Figure 8-3. The unit cell is composed of ZrO_6 octahedra and WO_4 tetrahedra.

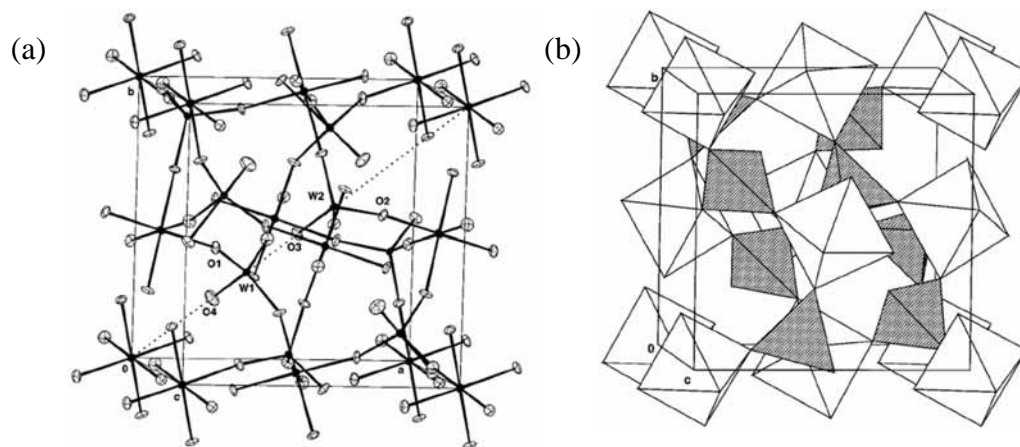


Figure 8-3. Crystal structures of NTE materials (a) Unit cell of ZrW_2O_8 , with 90% thermal ellipsoids drawn. (b) Polyhedral representation of the structure. ZrO_6 octahedra shown in white, WO_4 tetrahedra shaded [Eva96].

The NTE phenomenon is related to transverse thermal vibrations of bridging oxygen atoms, resulting in coupled rotations of the essentially rigid polyhedral blocks of the structure [Eva96]. The schematic of this phenomenon is shown in Figure 8-4 [Pry96].

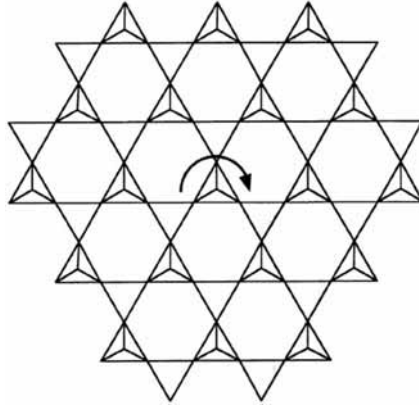


Figure 8-4. An array of linked triangles as found in tridymite. Rotation of one triangle causes the local environment to be pulled inwards [Pry96].

The appropriate mixture of NTE materials with Group III nitrides can create a crystal with a controllable thermal expansion coefficient. The use of NTE materials as a buffer layer for a III-V compound semiconductor has already been suggested [Lo01]. However, no experimental work was found using an NTE buffer layer. Since cracking usually occurs during the cooling of GaN grown on Si, proper use of NTE materials could reduce the excessive tensile stress. The lattice mismatch between GaN, NTE materials, and Si are not compared at this point since the structural and physical properties of most NTE materials are still not clearly defined. The synthesis of NTE material is usually done by dehydration of hydrated NTE material. For example, ZrW_2O_8 was synthesized by dehydration of $ZrW_2O_7(OH)_2 \cdot 2H_2O$ [Dad97]. The growth of NTE materials by conventional epitaxy (*i.e.*, MOVPE, MBE, or HVPE) was not reported to date. Thus, the deposition of NTE material on Si will be a challenging task.

8.5 Double-sided Growth of GaN on Si and Sapphire

The cracking of GaN occurs because of the excessive curvature generation during the cooling process as strong tensile stress creates concave bowing in GaN. Likewise, there will be strong convex bowing of thick GaN film grown on sapphire substrate due to the compressive stress generated during the cooling process. Double-sided growth could work as the stress would cancel out if growth on both sides were uniform. Potential problems with this process could be the non-uniformity with respect to growth axis, the role of edge growth, and backside deposition. Suspending the double-sided polished wafer and growing simultaneously on both sides may work; however, a creative wafer-holding design would be necessary.

APPENDIX
THERMOCHEMICAL DATA FOR AL-IN-GA-C-H-CL-N SYSTEM

Table A-1. Gas Phase

Species	ΔH°_{298} (J/mole)	S°_{298} (J/mole K)	T(K) Range	C_p (J/mol K) = A + B*T + C*T ² + D*T ²				Ref #
				A	B	C	D	
Al	330000	164.6	298.14 - 4300	20.859	-9.133E-05	2.365E-08	4.855E+04	[SUB94]
			4300 - 8200	17.789	-1.364E-04	1.147E-07	2.956E+07	
			8200 - 10000	-22.242	6.992E-03	-2.429E-07	4.073E+08	
AlC	682283	225.9	298.14 - 1200	35.167	3.691E-03	-1.222E-06	-2.628E+05	[SUB94]
			1200 - 3300	37.843	-1.696E-03	1.187E-06	1.979E+05	
			3300 - 6000	-12.912	2.097E-02	-1.662E-06	7.627E+07	
AlC ₂	675623	252.9	298.14 - 1100	42.790	2.347E-02	-8.394E-06	-1.100E+05	[SUB94]
			1100 - 6000	61.350	3.652E-04	-3.535E-08	-4.050E+06	
AlCl	-51007	228.0	298.14 - 2400	37.039	7.829E-04	-2.009E-08	-2.341E+05	[SUB94]
			2400 - 5700	43.137	-3.051E-03	6.447E-07	-4.397E+06	
			5700 - 6000	-25.513	1.512E-02	-7.052E-07	2.847E+08	
AlHCl	10522	257.2	298.14 - 1000	37.509	2.568E-02	-9.584E-06	-2.044E+05	[SUB94]
			1000 - 4300	53.579	2.334E-03	-1.386E-07	-2.376E+06	
			4300 - 6000	60.309	1.046E-03	-1.099E-07	-3.423E+07	
AlH ₂ Cl	-106345	251.1	298.14 - 900	36.497	5.907E-02	-2.280E-05	-4.062E+05	[SUB94]
			900 - 2800	74.982	4.877E-03	-8.180E-07	-6.497E+06	
			2800 - 6000	82.866	7.087E-05	-5.189E-09	-1.277E+07	
AlCl ₂	-240874	290.4	298.14 - 1500	56.336	2.460E-03	-8.675E-07	-4.847E+05	[SUB94]
			1500 - 5800	56.504	4.837E-04	4.193E-08	1.210E+06	

Table A-1. Continued

			5800 – 6000	1.860	1.368E-02	-8.623E-07	2.875E+08	
AlHCl ₂	-351279	288.8	298.14 – 1100	61.863	2.578E-02	-9.340E-06	-7.312E+05	[SUB94]
			1100 – 6000	82.017	4.078E-04	-3.944E-08	-4.961E+06	
AlCl ₃	-584505	314.4	298.14 – 800	75.053	1.589E-02	-8.866E-06	-6.337E+05	[SUB94]
			800 – 6000	83.082	2.294E-05	-2.118E-09	-1.280E+06	
AlH	249250	187.9	298.14 – 1000	22.302	1.962E-02	-7.025E-06	1.637E+05	[SUB94]
			1000 – 2900	40.276	-2.855E-03	1.125E-06	-3.486E+06	
			2900 - 5400	-27.458	2.753E-02	-2.689E-06	9.496E+07	
			5400 - 6000	151.983	-2.006E-02	8.637E-07	-6.651E+08	
AlH ₂	276774	213.3	298.14 - 1000	23.058	4.018E-02	-1.383E-05	1.750E+05	[SUB94]
			1000 - 4900	51.217	3.467E-03	-2.858E-07	-4.819E+06	
			4900 - 6000	63.237	3.110E-04	-5.827E-08	-5.331E+07	
AlH ₃	128894	206.6	298.14 - 800	16.480	8.353E-02	-3.208E-05	1.353E+05	[SUB94]
			800 - 1800	59.098	1.900E-02	-4.354E-06	-5.461E+06	
			1800 - 6000	81.991	3.523E-04	-2.997E-08	-1.626E+07	
AlN	438829	228.4	298.14 - 1200	34.111	3.121E-03	1.457E-06	-2.456E+05	[SUB94]
			1200 - 2800	36.908	5.852E-03	-1.070E-06	-3.751E+06	
			2800 - 6000	32.862	4.698E-03	-4.939E-07	1.790E+07	
Al ₂	509200	243.0	298.14 - 900	41.640	-4.993E-03	2.943E-06	-1.708E+05	[SUB94]
			900 - 2800	38.855	4.500E-04	5.694E-08	1.057E+04	
Al ₂ C ₂	544985	284.6	298.14 - 1100	63.487	2.883E-02	-1.042E-05	-3.121E+05	[SUB94]

Table A-1. Continued

			1100 - 6000	86.053	4.518E-04	-4.371E-08	-5.045E+06	
Al ₂ Cl ₆	-1295534	475.6	298.14 - 600	161.452	4.981E-02	-3.353E-05	-1.372E+06	[SUB94]
			600 - 3300	182.438	3.002E-04	-4.955E-08	-2.572E+06	
			3300 - 6000	182.950	-1.474E-05	1.507E-09	-2.904E+06	
C	716680	158.1	298.14 - 3400	20.975	-3.996E-04	2.008E-07	-3.361E+03	[SUB94]
			3400 - 10000	23.051	1.209E-04	-4.046E-09	-1.712E+07	
			10000 - 20000	19.445	3.079E-04	3.692E-10	1.124E+08	
C ₁₀ N	1460000	442.6	298.14 - 1200	154.819	1.104E-01	-3.438E-05	-1.382E+06	[SUB94]
			1200 - 1600	219.829	3.021E-02	-6.437E-06	-1.430E+07	
			1600 - 2200	466.590	-1.378E-01	2.577E-05	-1.648E+08	
			2200 - 4000	256.726	1.735E-03	-1.715E-07	-2.659E+07	
C ₁₀ N ₂	1200000	447.4	298.14 - 1200	167.995	1.202E-01	-3.667E-05	-1.586E+06	[SUB94]
			1200 - 1600	237.757	3.529E-02	-7.527E-06	-1.579E+07	
			1600 - 2200	520.417	-1.572E-01	2.942E-05	-1.881E+08	
			2200 - 4000	280.848	2.011E-03	-1.989E-07	-3.032E+07	
C ₁₁ NH	1270000	454.7	298.14 - 1200	176.833	1.356E-01	-4.157E-05	-2.097E+06	[SUB94]
			1200 - 1600	253.664	4.071E-02	-8.505E-06	-1.741E+07	
			1600 - 2100	690.115	-2.597E-01	4.964E-05	-2.799E+08	
			2100 - 4000	303.357	2.876E-03	-2.892E-07	-3.466E+07	
C ₁₁ N	1500000	467.9	298.14 - 1300	170.519	1.148E-01	-3.384E-05	-1.490E+06	[SUB94]
			1300 - 1600	239.209	3.322E-02	-6.659E-06	-1.598E+07	

Table A-1. Continued

			1600 - 2200	531.517	-1.642E-01	3.088E-05	-1.965E+08	
			2200 - 4000	279.296	3.787E-03	-4.181E-07	-3.142E+07	
C ₁₂ H ₂₆	-290872	622.6	298.14 - 500	-268.693	1.952E+00	-1.244E-03	6.916E+06	[SUB94]
			500 - 800	105.945	8.242E-01	-2.882E-04	-5.539E+06	
			800 - 1000	107.947	7.745E-01	-2.427E-04	0	
CCl	439560	224.6	298.14 - 1100	31.548	9.313E-03	-3.749E-06	-1.550E+05	[SUB94]
			1100 - 5200	35.444	1.565E-03	-1.190E-07	1.432E+05	
			5200 - 6000	43.872	4.413E-04	-1.305E-07	-6.230E+07	
CHCl	308280	234.9	298.14 - 800	30.466	2.977E-02	-1.093E-05	-1.466E+05	[SUB94]
			800 - 2500	44.262	6.562E-03	1.354E-07	-1.626E+06	
			2500 - 4900	53.024	8.112E-03	-1.014E-06	-3.571E+07	
			4900 - 6000	105.080	-8.257E-03	4.266E-07	-1.903E+08	
CH ₂ Cl	116872	243.5	298.14 - 900	31.585	4.981E-02	-1.589E-05	-1.660E+05	[SUB94]
			900 - 2300	56.273	1.680E-02	-3.059E-06	-4.518E+06	
			2300 - 6000	81.106	5.609E-04	-4.383E-08	-2.269E+07	
CH ₃ Cl	-81870	234.4	298.14 - 700	10.683	1.086E-01	-4.137E-05	1.205E+05	[SUB94]
			700 - 1500	42.093	5.199E-02	-1.237E-05	-2.831E+06	
			1500 - 4000	96.339	4.656E-03	-5.241E-07	-2.509E+07	
			4000 - 6000	107.137	2.036E-04	-1.270E-08	-4.380E+07	
CNCl	137947	236.3	298.14 - 1200	43.592	2.088E-02	-6.386E-06	-3.531E+05	[SUB94]
			1200 - 3600	60.119	2.170E-03	-1.339E-07	-4.790E+06	

Table A-1. Continued

			3600 – 6000	61.563	1.360E-03	-1.740E-08	-5.294E+06	
CCl ₂	226230	265.0	298.14 – 800	47.759	1.869E-02	-9.555E-06	-5.351E+05	[SUB94]
			800 – 3500	60.402	-2.951E-03	1.035E-06	-1.887E+06	
			3500 – 6000	29.466	1.225E-02	-9.923E-07	2.944E+07	
CHCl ₂	73895	277.8	298.14 – 700	45.180	4.939E-02	-2.188E-05	-4.718E+05	[SUB94]
			700 – 2300	66.827	1.084E-02	-2.080E-06	-2.612E+06	
			2300 – 6000	82.131	2.785E-04	-2.175E-08	-1.271E+07	
CH ₂ Cl ₂	-95000	270.4	298.14 – 700	28.619	9.983E-02	-4.252E-05	-3.264E+05	[SUB94]
			700 – 1800	66.799	3.066E-02	-6.758E-06	-3.899E+06	
			1800 – 6000	104.520	1.076E-03	-9.072E-08	-2.356E+07	
CCl ₃	80000	300.3	298.14 – 800	62.886	3.551E-02	-1.789E-05	-8.211E+05	[SUB94]
			800 – 6000	82.821	1.304E-04	-1.361E-08	-2.788E+06	
CHCl ₃	-102700	296.4	298.14 – 700	52.487	8.638E-02	-3.671E-05	-7.247E+05	[SUB94]
			700 – 2300	89.033	2.025E-02	-2.395E-06	-4.189E+06	
			2300 - 6000	106.825	7.968E-03	1.706E-09	-1.595E+07	
CCl ₄	-95600	309.5	298.14 - 800	87.051	3.741E-02	-1.904E-05	-1.214E+06	[SUB94]
			800 - 6000	107.797	1.175E-04	-1.227E-08	-3.195E+06	
CH	597370	183.0	298.14 - 900	28.318	-4.643E-04	4.419E-06	5.437E+04	[SUB94]
			900 - 2800	21.902	1.186E-02	-1.793E-06	3.455E+05	
			2800 - 6400	32.139	5.016E-03	-5.756E-07	-4.571E+06	
			6400 - 12000	79.927	-6.695E-03	2.178E-07	-2.232E+08	

Table A-1. Continued

			12000 - 20000	28.186	-5.528E-04	1.154E-08	8.923E+08	
CHN_HCN	132000	201.8	298.14 - 1600	32.577	2.324E-02	-5.310E-06	-2.832E+05	[SUB94]
			1600 - 5600	58.835	1.581E-03	-1.180E-07	-1.280E+07	
			5600 - 10000	74.573	-2.429E-03	1.743E-07	-8.950E+07	
CHN_HNC	194328	205.2	298.14 - 1400	37.443	1.657E-02	-3.271E-06	-1.815E+05	[SUB94]
			1400 - 4500	55.585	2.519E-03	-2.635E-07	-8.741E+06	
			4500 - 6000	61.803	1.154E-04	-7.045E-09	-2.073E+07	
CH ₂	390421	194.9	298.14 - 900	27.632	1.579E-02	2.326E-07	1.251E+05	[SUB94]
			900 - 2200	29.137	1.978E-02	-3.693E-06	-1.422E+06	
			2200 - 6000	57.017	9.725E-04	-8.901E-08	-2.055E+07	
CH ₃	146300	194.0	298.14 - 1600	25.844	4.249E-02	-9.520E-06	6.653E+04	[SUB94]
			1600 - 4400	73.421	3.551E-03	-3.672E-07	-2.222E+07	
CH ₄	-74600	186.4	298.14 - 1000	2.235	9.693E-02	-2.603E-05	6.109E+05	[SUB94]
			1000 - 2000	47.229	4.222E-02	-7.068E-06	-8.634E+06	
			2000 - 6000	101.131	5.369E-03	1.417E-07	-4.481E+07	
CN	440287	202.6	298.14 - 1000	23.312	1.363E-02	-3.673E-06	1.883E+05	[SUB94]
			1000 - 2800	32.866	1.388E-03	5.860E-07	-1.382E+06	
			2800 - 5500	35.625	4.582E-03	-4.432E-07	-2.986E+07	
			5500 - 9800	49.663	-1.094E-03	1.036E-07	-1.052E+07	
			9800 - 19000	26.035	3.298E-03	-1.090E-07	8.617E+07	
			19000 - 20000	70.671	-4.074E-04	-2.351E-08	-1.757E+09	

Table A-1. Continued

CN ₂ CNN	633484	232.1	298.14 – 1500	37.081	2.479E-02	-5.990E-06	-1.455E+05	[SUB94]
			1500 – 6000	69.647	-1.800E-03	1.302E-07	-1.465E+07	
CN ₂ NCN	500535	226.2	298.14 – 700	22.682	7.464E-02	-3.710E-05	6.882E+04	[SUB94]
			700 – 1900	65.882	-1.608E-04	-3.596E-07	-4.263E+06	
			1900 – 6000	64.096	-5.036E-04	4.123E-08	-6.875E+05	
C ₂	830457	197.1	298.14 – 500	97.481	-1.641E-01	1.184E-04	-1.381E+06	[SUB94]
			500 – 4300	30.083	5.243E-03	-4.986E-07	1.737E+06	
			4300 – 12000	27.970	3.882E-03	-1.934E-07	4.476E+07	
			12000 – 20000	86.667	-3.128E-03	4.369E-08	-1.209E+09	
C ₂ Cl	534090	241.9	298.14 – 1200	42.931	2.171E-02	-7.231E-06	-3.314E+05	[SUB94]
			1200 – 6000	61.288	3.761E-04	-3.562E-08	-4.829E+06	
C ₂ HCl	213802	242.0	298.14 – 1000	55.080	2.749E-02	-7.582E-06	-7.354E+05	[SUB94]
			1000 – 2400	69.587	1.046E-02	-1.805E-06	-3.992E+06	
			2400 – 6000	85.868	3.755E-04	-2.795E-08	-1.733E+07	
C ₂ H ₃ Cl	23000	264.0	298.14 – 600	19.098	1.453E-01	-6.540E-05	-2.608E+05	[SUB94]
			600 – 1400	60.174	5.961E-02	-1.488E-05	-3.088E+06	
			1400 – 3900	118.581	5.935E-03	-6.913E-07	-2.479E+07	
			3900 – 6000	131.940	2.372E-04	-1.503E-08	-4.641E+07	
C ₂ H ₅ Cl	-112257	275.9	298.14 – 600	6.880	2.137E-01	-9.322E-05	2.930E+04	[SUB94]
			600 – 1300	61.711	9.916E-02	-2.568E-05	-3.729E+06	
			1300 – 3200	148.486	1.431E-02	-1.940E-06	-3.177E+07	

Table A-1. Continued

			3200 – 4000	173.732	1.522E-03	-1.353E-07	-6.056E+07	
C ₂ Cl ₂	209618	272.0	298.14 – 1000	64.347	2.679E-02	-9.646E-06	-5.242E+05	[SUB94]
			1000 – 3000	83.063	2.331E-03	-3.613E-07	-4.065E+06	
			3000 – 6000	87.130	4.102E-05	-2.820E-09	-7.872E+06	
C ₂ H ₂ Cl ₂ _1_1C ₂ H ₂ Cl ₂	2300	288.2	298.14 – 700	49.260	1.051E-01	-4.482E-05	-8.464E+05	[SUB94]
			700 – 1900	90.822	3.056E-02	-6.535E-06	-4.824E+06	
			1900 – 6000	129.565	1.025E-03	-8.504E-08	-2.618E+07	
C ₂ H ₂ Cl ₂ _CIS	4100	289.6	298.14 – 700	42.911	1.173E-01	-5.142E-05	-7.510E+05	[SUB94]
			700 – 1900	90.630	3.076E-02	-6.588E-06	-5.213E+06	
			1900 – 6000	129.578	1.021E-03	-8.471E-08	-2.662E+07	
C ₂ H ₂ Cl ₂ _TRANS	6100	290.0	298.14 – 700	42.225	1.184E-01	-5.191E-05	-5.665E+05	[SUB94]
			700 – 1900	90.578	3.081E-02	-6.601E-06	-5.097E+06	
			1900 – 6000	129.578	1.021E-03	-8.470E-08	-2.652E+07	
C ₂ H ₄ Cl ₂	-130122	305.2	298.14 – 600	29.966	1.940E-01	-8.817E-05	-3.244E+05	[SUB94]
			600 – 1400	85.860	7.776E-02	-1.977E-05	-4.196E+06	
			1400 – 4000	161.491	7.209E-03	-8.548E-07	-3.150E+07	
C ₂ Cl ₃	190279	328.2	298.14 – 800	70.711	5.920E-02	-2.776E-05	-8.790E+05	[SUB94]
			800 – 4800	106.394	7.494E-04	-8.679E-08	-5.126E+06	
			4800 – 6000	108.823	-1.813E-04	1.252E-08	-1.084E+07	
C ₂ HCl ₃	-19100	325.0	298.14 – 700	64.821	9.766E-02	-4.527E-05	-8.768E+05	[SUB94]
			700 – 2300	111.494	1.454E-02	-2.828E-06	-5.432E+06	

Table A-1. Continued

			2300 – 6000	131.800	3.386E-04	-2.646E-08	-1.841E+07	
C ₂ H ₃ Cl ₃	-142298	320.1	298.14 – 700	61.517	1.576E-01	-7.049E-05	-8.827E+05	[SUB94]
			700 – 2000	129.253	3.521E-02	-7.349E-06	-7.260E+06	
			2000 – 4000	172.401	2.301E-03	-2.410E-07	-3.028E+07	
C ₂ Cl ₄	-12427	343.4	298.14 – 600	75.246	1.116E-01	-6.589E-05	-6.321E+05	[SUB94]
			600 – 1300	117.746	1.674E-02	-5.321E-06	-3.283E+06	
			1300 – 6000	132.786	3.686E-05	2.361E-09	-7.206E+06	
C ₂ H ₂ Cl ₄	-149369	356.0	298.14 – 700	76.342	1.505E-01	-6.799E-05	-1.093E+06	[SUB94]
			700 – 1900	143.958	3.085E-02	-7.407E-06	-7.738E+06	
			1900 – 4000	181.342	-7.737E-04	6.853E-08	-2.320E+07	
C ₂ Cl ₅	39000	396.5	298.14 – 700	124.213	6.121E-02	-3.502E-05	-1.829E+06	[SUB94]
			700 – 6000	154.083	-1.046E-04	1.074E-08	-3.848E+06	
C ₂ HCl ₅	-145603	381.5	298.14 – 700	103.110	1.242E-01	-5.979E-05	-1.493E+06	[SUB94]
			700 – 1500	150.772	3.083E-02	-8.381E-06	-5.178E+06	
C ₂ Cl ₆	-141500	398.6	298.14 – 800	139.890	7.572E-02	-3.826E-05	-2.025E+06	[SUB94]
			800 – 6000	182.258	2.664E-04	-2.778E-08	-6.169E+06	
C ₂ H	569000	209.7	298.14 – 1000	39.083	1.139E-02	2.563E-06	-2.715E+05	[SUB94]
			1000 – 2100	28.122	3.126E-02	-6.686E-06	7.655E+04	
			2100 – 6400	77.129	-3.728E-03	2.647E-07	-2.723E+07	
			6400 – 10000	63.159	-1.206E-04	5.032E-09	3.479E+07	
C ₂ NH	610438	240.6	298.14 – 1000	49.550	3.850E-02	-1.276E-05	-5.046E+05	[SUB94]

Table A-1. Continued

			1000 – 3200	75.742	5.872E-03	-8.461E-07	-5.981E+06	
			3200 – 6000	86.604	1.665E-04	-1.148E-08	-1.775E+07	
C ₂ H ₂	227400	200.9	298.14 – 1700	43.333	3.194E-02	-6.585E-06	-7.339E+05	[SUB94]
			1700 – 4700	83.176	1.701E-03	5.040E-08	-2.274E+07	
			4700 – 9200	55.556	6.419E-03	-8.416E-08	1.634E+08	
			9200 – 10000	-13.730	1.823E-02	-6.453E-07	8.536E+08	
C ₂ H ₃	260000	232.8	298.14 – 700	7.990	1.121E-01	-4.332E-05	1.722E+05	[SUB94]
			700 – 1500	40.616	5.243E-02	-1.233E-05	-2.801E+06	
			1500 – 3900	94.926	5.278E-03	-6.030E-07	-2.527E+07	
			3900 – 6000	106.963	2.447E-04	-1.551E-08	-4.563E+07	
C ₂ H ₄	52400	219.3	298.14 – 600	-1.510	1.593E-01	-6.691E-05	2.528E+05	[SUB94]
			600 – 1300	36.420	8.033E-02	-2.049E-05	-2.366E+06	
			1300 – 3000	104.259	1.404E-02	-1.977E-06	-2.423E+07	
			3000 – 6000	130.538	6.132E-04	-4.348E-08	-5.492E+07	
C ₂ H ₅	107000	250.5	298.14 – 700	-6.535	1.754E-01	-6.480E-05	5.870E+05	[SUB94]
			700 – 1400	40.091	9.217E-02	-2.263E-05	-3.852E+06	
			1400 – 3300	126.700	1.229E-02	-1.599E-06	-3.522E+07	
			3300 – 6000	151.468	5.557E-04	-3.808E-08	-6.853E+07	
C ₂ H ₆	-84000	229.2	298.14 – 700	-2.384	1.924E-01	-6.902E-05	3.223E+05	[SUB94]
			700 – 1400	45.037	1.083E-01	-2.658E-05	-4.260E+06	
			1400 – 3200	145.619	1.528E-02	-2.028E-06	-4.044E+07	

Table A-1. Continued

			3200 – 6000	175.852	6.958E-04	-4.818E-08	-7.984E+07	
C ₂ N ₂ CCN	804806	239.0	298.14 – 900	36.285	3.625E-02	-1.505E-05	-1.059E+05	[SUB94]
			900 – 5300	59.166	1.393E-03	-7.918E-09	-3.094E+06	
			5300 – 6000	54.098	3.192E-03	-1.816E-07	8.302E+06	
C ₂ N ₂ CNC	684924	233.8	298.14 – 800	35.193	4.199E-02	-1.922E-05	-8.578E+04	[SUB94]
			800 – 4000	60.762	8.025E-04	-1.076E-07	-3.195E+06	
			4000 – 6000	62.406	-1.348E-05	1.016E-09	-5.053E+06	
C ₂ N ₂	309100	242.2	298.14 – 1300	52.476	3.471E-02	-9.851E-06	-4.324E+05	[SUB94]
			1300 – 6000	84.877	1.590E-03	-2.865E-08	-1.049E+07	
C ₃	839958	237.6	298.14 – 1000	32.216	2.910E-02	-1.067E-05	2.006E+05	[SUB94]
			1000 – 2800	59.940	-5.083E-03	1.525E-06	-5.539E+06	
			2800 – 5100	-7.286	2.097E-02	-1.204E-06	1.174E+08	
			5100 – 8000	60.731	9.544E-03	-8.308E-07	-3.892E+08	
			8000 – 10000	211.874	-1.840E-02	6.183E-07	-1.688E+09	
C ₃ H	630000	241.9	298.14 – 900	48.296	4.083E-02	-1.441E-05	-5.736E+05	[SUB94]
			900 – 1600	62.911	1.749E-02	-3.808E-06	-2.353E+06	
			1600 – 2100	200.713	-7.828E-02	1.501E-05	-8.447E+07	
			2100 – 4000	83.754	1.205E-03	-1.207E-07	-1.055E+07	
C ₃ NH	380000	251.7	298.14 – 1300	62.591	4.404E-02	-1.206E-05	-8.946E+05	[SUB94]
			1300 – 1600	85.867	1.739E-02	-3.441E-06	-6.296E+06	
			1600 – 2000	362.317	-1.756E-01	3.441E-05	-1.691E+08	

Table A-1. Continued

			2000 – 4000	107.372	1.695E-03	-1.735E-07	-1.461E+07	
C ₃ H _{4_1}	192129	244.0	298.14 – 600	10.206	1.907E-01	-9.046E-05	0	[SUB94]
			600 – 1350	49.160	9.737E-02	-2.733E-05	-2.051E+06	
C ₃ H _{4_2}	185435	248.2	298.14 – 600	17.229	1.679E-01	-7.440E-05	0	[SUB94]
			600 – 1350	43.111	1.040E-01	-2.988E-05	-1.272E+06	
C ₃ H ₆	20418	266.7	298.14 – 700	5.297	2.209E-01	-8.349E-05	5.983E+04	[SUB94]
			700 – 1400	65.858	1.114E-01	-2.731E-05	-5.566E+06	
			1400 – 3400	171.676	1.427E-02	-1.822E-06	-4.429E+07	
			3400 – 4000	199.650	1.069E-03	-8.232E-08	-8.139E+07	
C ₃ H _{6_1}	53304	237.6	298.14 – 500	-238.356	1.027E+00	-8.058E-04	5.323E+06	[SUB94]
			500 – 1350	47.235	1.457E-01	-4.106E-05	-3.758E+06	
C ₃ H _{6_2}	20418	267.0	298.14 – 600	-11.349	2.677E-01	-1.202E-04	5.443E+05	[SUB94]
			600 – 1350	41.168	1.476E-01	-4.207E-05	-2.545E+06	
C ₃ H ₈	-103847	270.0	298.14 – 600	-21.526	3.444E-01	-1.597E-04	5.840E+05	[SUB94]
			600 – 1000	49.099	1.782E-01	-4.895E-05	-3.304E+06	
			1000 – 1473.09	72.225	1.300E-01	-2.721E-05	0	
			1473.09 – 2200	-217.225	3.025E-01	-5.204E-05	1.937E+08	
			2200 – 2800	-2.181	1.193E-01	-1.388E-05	2.094E+08	
			2800 – 3400	-2055.691	9.570E-01	-1.097E-04	3.808E+09	
			3400 – 4000	188.615	2.092E-02	0	0	

Table A-1. Continued

C ₃ N	609000	252.1	298.14 – 1600	53.750	2.905E-02	-5.781E-06	-4.842E+05	[SUB94]
			1600 – 1900	618.579	-3.745E-01	7.518E-05	-3.212E+08	
			1900 – 4000	102.028	-2.584E-03	7.465E-08	-2.887E+07	
C ₄	1033918	252.9	298.14 – 2500	53.395	2.800E-02	-4.956E-06	-3.620E+05	[SUB94]
			2500 – 7000	106.174	-3.328E-03	2.418E-07	-4.381E+07	
			7000 – 10000	92.452	5.378E-04	-4.244E-08	-1.517E+07	
C ₄ H _{10_1}	-126148	310.2	298.14 – 500	-116.904	7.514E-01	-4.922E-04	3.033E+06	[SUB94]
			500 – 1000	52.283	2.540E-01	-7.632E-05	-3.081E+06	
			1000 – 1600	293.778	-1.134E-02	7.926E-06	-6.351E+07	
			1600 – 2200	268.317	6.969E-03	4.634E-06	-5.173E+07	
			2200 – 3000	423.048	-6.055E-02	1.164E-05	-2.457E+08	
			3000 – 3500	188.341	6.067E-02	-5.726E-06	0	
C ₄ H _{10_2}	-134516	294.7	298.14 – 500	-184.144	9.895E-01	-7.170E-04	4.419E+06	[SUB94]
			500 – 1350	62.001	2.403E-01	-7.081E-05	-3.848E+06	
C ₄ H ₂	472792	250.1	298.14 – 500	21.763	2.252E-01	-1.717E-04	0	[SUB94]
			500 – 1350	75.170	5.027E-02	-1.270E-05	-1.418E+06	
C ₄ H ₄	304595	279.5	298.14 – 600	23.517	2.097E-01	-1.023E-04	-3.325E+05	[SUB94]
			600 – 1350	68.631	1.010E-01	-2.821E-05	-2.699E+06	
C ₄ H _{6_1}	162214	293.1	298.14 – 700	9.680	2.650E-01	-1.125E-04	1.292E+05	[SUB94]
			700 – 1350	32.197	1.993E-01	-6.410E-05	0	
C ₄ H _{6_2}	110165	278.8	298.14 – 500	-98.099	6.577E-01	-4.803E-04	2.156E+06	[SUB94]

Table A-1. Continued

			500 – 1350	76.018	1.357E-01	-3.848E-05	-3.731E+06	
C ₄ H ₈	-152591	265.5	298.14 – 1500	21.681	2.600E-01	7.727E-05	1.839E+06	[SUB94]
C ₄ H _{8_1}	-126	305.7	298.14 – 500	-99.938	6.617E-01	-4.458E-04	2.485E+06	[SUB94]
			500 – 1350	53.292	2.069E-01	-6.129E-05	-3.001E+06	
C ₄ N	790000	285.0	298.14 – 1100	66.110	4.971E-02	-1.630E-05	-6.063E+05	[SUB94]
			1100 – 1600	93.493	1.395E-02	-3.074E-06	-5.497E+06	
			1600 – 2300	175.665	-4.194E-02	7.688E-06	-5.567E+07	
			2300 – 4000	110.391	5.997E-04	-5.737E-08	-1.124E+07	
C ₄ N ₂	533460	290.1	298.14 – 1000	77.196	6.461E-02	-2.131E-05	-7.699E+05	[SUB94]
			1000 – 2100	117.116	1.349E-02	-2.631E-06	-8.239E+06	
			2100 – 6000	136.050	3.163E-04	-2.447E-08	-2.046E+07	
C ₅	1050942	271.7	298.14 – 900	62.972	6.340E-02	-2.458E-05	-3.726E+05	[SUB94]
			900 – 3500	106.597	2.957E-03	-4.243E-07	-7.496E+06	
			3500 – 10000	112.171	1.322E-05	-6.633E-10	-1.313E+07	
C ₅ HN	600000	303.0	298.14 – 1300	92.087	6.513E-02	-1.855E-05	-1.187E+06	[SUB94]
			1300 – 1600	127.558	2.345E-02	-4.767E-06	-8.931E+06	
			1600 – 2000	493.195	-2.323E-01	4.547E-05	-2.237E+08	
			2000 – 4000	156.227	2.051E-03	-2.096E-07	-1.938E+07	
C ₅ H _{8_1}	32928	289.8	298.14 – 500	-470.127	1.873E+00	-1.509E-03	1.074E+07	[SUB94]
			500 – 800	7.450	3.324E-01	-1.211E-04	-2.769E+06	
			800 – 1350	4.770	3.171E-01	-1.046E-04	0	

Table A-1. Continued

C ₅ N	830000	304.6	298.14 – 1100	67.079	9.244E-02	-3.357E-05	-2.755E+05	[SUB94]
			1100 – 1600	135.934	3.636E-03	-1.306E-06	-1.264E+07	
			1600 – 4000	141.655	-2.127E-03	2.719E-07	-1.228E+07	
C ₆ H ₅ Cl	52773	297.4	298.14 – 1500	179.992	1.596E-02	0	-7.792E+06	[SUB94]
C ₆ H ₆	82927	269.3	298.14 – 500	-182.327	9.542E-01	-6.880E-04	3.619E+06	[SUB94]
			500 – 1350	58.568	2.359E-01	-8.006E-05	-4.823E+06	
C ₆ N	1010000	337.5	298.14 – 1200	96.197	6.881E-02	-2.166E-05	-8.885E+05	[SUB94]
			1200 – 1600	136.761	1.825E-02	-3.895E-06	-8.791E+06	
			1600 – 2300	255.584	-6.182E-02	1.133E-05	-8.213E+07	
			2300 – 4000	159.212	9.606E-04	-9.347E-08	-1.643E+07	
C ₆ N ₂	750000	342.6	298.14 – 1200	108.875	7.920E-02	-2.420E-05	-1.081E+06	[SUB94]
			1200 – 1600	155.202	2.287E-02	-4.869E-06	-1.054E+07	
			1600 – 2200	341.228	-1.038E-01	1.942E-05	-1.240E+08	
			2200 – 4000	183.123	1.329E-03	-1.320E-07	-1.991E+07	
C ₇ NH	820000	353.6	298.14 – 1200	119.937	8.952E-02	-2.674E-05	-1.475E+06	[SUB94]
			1200 – 1600	167.892	3.078E-02	-6.424E-06	-1.118E+07	
			1600 – 2100	483.179	-1.863E-01	3.565E-05	-2.007E+08	
			2100 – 4000	205.569	2.196E-03	-2.204E-07	-2.491E+07	
C ₇ N	1060000	363.2	298.14 – 1200	113.429	7.583E-02	-2.354E-05	-1.118E+06	[SUB94]
			1200 – 1600	158.283	2.067E-02	-4.393E-06	-1.011E+07	
			1600 – 2300	293.904	-7.063E-02	1.295E-05	-9.390E+07	

Table A-1. Continued

			2300 – 4000	183.774	1.095E-03	-1.073E-07	-1.875E+07	
C ₈ N	1240000	390.1	298.14 – 1200	125.526	8.959E-02	-2.800E-05	-1.136E+06	[SUB94]
			1200 – 1600	178.856	2.370E-02	-5.024E-06	-1.172E+07	
			1600 – 2200	377.032	-1.110E-01	2.078E-05	-1.328E+08	
			2200 – 4000	207.862	1.394E-03	-1.380E-07	-2.134E+07	
C ₈ N ₂	980000	395.1	298.14 – 1200	138.689	9.935E-02	-3.031E-05	-1.338E+06	[SUB94]
			1200 – 1600	196.805	2.875E-02	-6.109E-06	-1.322E+07	
			1600 – 2200	430.872	-1.305E-01	2.443E-05	-1.560E+08	
			2200 – 4000	232.070	1.633E-03	-1.609E-07	-2.521E+07	
C ₉ NH	1050000	403.9	298.14 – 1200	148.372	1.126E-01	-3.416E-05	-1.787E+06	[SUB94]
			1200 – 1600	210.770	3.575E-02	-7.463E-06	-1.429E+07	
			1600 – 2100	586.995	-2.233E-01	4.269E-05	-2.405E+08	
			2100 – 4000	254.482	2.527E-03	-2.537E-07	-2.981E+07	
Cl	121302	165.2	298.14 – 800	23.686	1.000E-05	-1.412E-06	-1.540E+05	[SUB94]
			800 – 3400	22.633	-9.689E-04	1.415E-07	3.847E+05	
			3400 – 10000	20.835	-8.310E-06	4.021E-10	2.260E+06	
GaCl	-69622	240.3	298.14 – 4100	37.589	1.823E-04	1.360E-07	-1.750E+05	[SUB94]
			4100 – 6000	25.418	2.980E-03	-3.342E-09	5.102E+07	
HCl	-92310	186.9	298.14 – 800	29.017	-1.963E-03	4.705E-06	2.588E+04	[SUB94]
			800 – 2400	25.299	7.871E-03	-1.320E-06	-1.616E+05	
			2400 – 6000	31.673	2.508E-03	-1.856E-07	-3.868E+05	

Table A-1. Continued

InCl	-72148	248.3	298.14 – 3900	37.682	1.040E-04	1.936E-07	-1.448E+05	[SUB94]
			3900 – 6000	14.971	6.635E-03	-3.069E-07	7.373E+07	
Cl ₂	0	223.1	298.14 – 1500	36.246	1.913E-03	-4.635E-07	-2.527E+05	[SUB94]
			1500 – 3300	40.693	-3.208E-03	1.101E-06	-8.928E+05	
			3300 – 5600	12.227	1.468E-02	-1.649E-06	-7.633E+06	
			5600 – 10000	109.552	-1.331E-02	5.566E-07	-3.130E+08	
GaCl ₂	-220979	302.9	298.14 – 2300	58.245	-4.760E-04	3.134E-07	-3.834E+05	[SUB94]
			2300 – 6000	50.476	3.846E-03	-3.312E-07	6.173E+06	
Ga ₂ Cl ₂	-220973	353.5	298.15 – 6000	83.100	2.245E-05	-2.684E-09	-3.018E+05	[SUB94]
InCl ₂	-201484	314.2	298.14 – 3600	58.201	-3.802E-04	2.872E-07	-2.910E+05	[SUB94]
			3600 – 6000	56.463	2.071E-03	-1.861E-07	-1.269E+07	
In ₂ Cl ₂	-232177	372.4	298.15 – 6000	83.122	1.125E-05	-1.345E-09	-2.165E+05	[SUB94]
GaCl ₃	-432625	324.5	298.14 – 2300	82.177	9.538E-04	-2.397E-07	-6.855E+05	[SUB94]
			2300 – 6000	83.139	1.589E-06	-1.281E-10	-8.867E+05	
InCl ₃	-369693	339.2	298.15 – 6000	82.938	1.042E-04	-1.248E-08	-5.613E+05	[SUB94]
GaCl ₄	-602327	419.7	298.15 – 6000	132.773	1.302E-04	-1.560E-08	-9.029E+05	[SUB94]
In ₂ Cl ₄	-579126	456.0	298.15 – 6000	132.848	9.229E-05	-1.106E-08	-6.844E+05	[SUB94]
Ga ₂ Cl ₆	-962464	492.7	298.14 – 3800	182.038	5.920E-04	-9.666E-08	-1.464E+06	[SUB94]
			3800 – 6000	182.909	3.208E-06	-2.970E-10	-1.770E+06	
In ₂ Cl ₆	-882340	527.7	298.15 – 6000	182.554	1.835E-04	-2.198E-08	-1.198E+06	[SUB94]
Ga	272000	169.0	298.14 – 600	38.711	-2.108E-02	5.921E-06	-6.770E+05	[SUB94]

Table A-1. Continued

			600 – 1400	30.750	-1.075E-02	3.279E-06	3.019E+05	
			1400 – 6000	21.983	-6.385E-04	8.778E-08	1.984E+06	
			6000 – 10000	9.704	9.028E-04	6.806E-08	1.368E+08	
GaH	214323	199.8	298.14 – 1000	22.503	2.007E-02	-7.377E-06	1.424E+05	[SUB94]
			1000 – 3400	36.596	5.827E-04	3.138E-07	-2.151E+06	
			3400 – 5800	35.170	6.243E-03	-8.725E-07	-4.964E+07	
			5800 – 6000	94.036	-9.534E-03	3.057E-07	-2.849E+08	
Ga ₂	433600	267.1	298.14 – 1100	33.729	1.874E-02	-4.577E-06	3.904E+04	[SUB94]
			1100 – 2500	40.336	8.371E-03	-1.608E-07	-6.242E+05	
H	217999	114.7	298.15 – 6000	20.786	0	0	0	[SUB94]
InH	215016	207.7	298.14 – 900	22.573	2.164E-02	-8.679E-06	1.177E+05	[SUB94]
			900 – 3300	35.333	1.954E-03	-8.363E-08	-1.506E+06	
			3300 – 6000	53.482	-9.479E-04	-2.567E-07	-7.437E+07	
NH	358433	181.2	298.14 – 900	29.254	-2.267E-03	4.316E-06	2.116E+04	[SUB94]
			900 – 2600	26.349	6.226E-03	-7.612E-07	-4.852E+05	
			2600 – 6000	16.433	8.307E-03	-6.415E-07	2.451E+07	
			6000 – 16500	78.442	-4.553E-03	1.061E-07	-3.990E+08	
			16500 – 20000	41.987	-1.226E-03	2.052E-08	9.200E+08	
N ₃ H	294000	239.3	298.14 – 800	31.620	5.719E-02	-2.100E-05	-2.304E+05	[SUB94]
			800 - 2100	57.402	1.744E-02	-3.349E-06	-3.613E+06	

Table A-1. Continued

			2100 – 6000	81.038	8.198E-04	-1.461E-08	-1.877E+07	
H ₂	0	130.7	298.14 – 1000	31.357	-5.518E-03	4.478E-06	-1.132E+05	[SUB94]
			1000 – 2100	17.849	1.168E-02	-1.888E-06	2.560E+06	
			2100 – 6000	32.051	2.146E-03	-6.857E-08	-7.122E+06	
NH ₂	190000	195.0	298.14 – 900	27.174	1.655E-02	-3.012E-07	1.583E+05	[SUB94]
			900 – 2200	30.778	1.703E-02	-2.630E-06	-1.582E+06	
			2200 – 6000	45.494	6.385E-03	-4.552E-07	-1.037E+07	
N ₂ H _{2_1_1} N ₂ H ₂	283962	228.2	298.14 – 700	11.294	7.922E-02	-3.040E-05	3.581E+05	[SUB94]
			700 – 1700	37.418	3.308E-02	-7.209E-06	-2.187E+06	
			1700 – 6000	76.059	2.407E-03	-1.934E-07	-2.176E+07	
N ₂ H ₂ _CIS	247885	218.4	298.14 – 800	10.046	7.712E-02	-2.664E-05	4.207E+05	[SUB94]
			800 – 1700	39.212	3.247E-02	-7.158E-06	-3.368E+06	
			1700 – 5300	78.695	4.766E-04	2.085E-07	-2.181E+07	
			5300 – 6000	52.960	8.505E-03	-4.837E-07	5.199E+07	
N ₂ H ₂ _TRANS	211859	218.3	298.14 – 800	8.430	7.959E-02	-2.795E-05	4.766E+05	[SUB94]
			800 – 1700	39.063	3.215E-02	-6.990E-06	-3.423E+06	
			1700 – 4500	71.814	3.506E-03	-1.227E-08	-1.561E+07	
			4500 – 6000	57.776	9.540E-03	-6.898E-07	-3.415E+06	
NH ₃	-45940	192.8	298.14 – 1100	21.218	4.574E-02	-1.085E-05	1.534E+05	[SUB94]
			1100 – 2600	45.828	1.963E-02	-2.846E-06	-6.582E+06	
			2600 – 6000	76.177	2.454E-03	-8.429E-08	-3.612E+07	

Table A-1. Continued

N ₂ H ₄	95180	238.5	298.14 - 600	9.501	1.451E-01	-6.574E-05	1.336E+05	[SUB94]
			600 - 1600	51.478	5.589E-02	-1.231E-05	-2.639E+06	
			1600 - 4200	112.895	5.963E-03	-6.336E-07	-3.186E+07	
			4200 - 6000	127.366	3.171E-04	-1.953E-08	-5.990E+07	
In	240700	173.8	298.14 - 600	15.352	1.054E-02	2.390E-06	1.890E+05	[SUB94]
			600 - 1100	8.405	3.137E-02	-1.327E-05	2.213E+05	
			1100 - 2900	41.363	-1.043E-02	1.516E-06	-5.674E+06	
			2900 - 8400	30.106	-3.387E-03	3.487E-07	-2.187E+05	
			8400 - 10000	-55.474	1.108E-02	-3.416E-07	8.985E+08	
In ₂	418800	285.1	298.14 - 1800	35.821	1.310E-02	-1.224E-07	4.027E+04	[SUB94]
			1800 - 3000	41.188	1.183E-02	-4.893E-07	-6.095E+06	
N	472687	153.3	298.14 - 2950	20.894	-1.691E-04	6.011E-08	-5.578E+03	[SUB94]
			2950 - 6000	16.376	4.567E-04	1.674E-07	1.512E+07	
N ₂	0	191.6	298.14 - 800	27.223	2.520E-03	3.236E-06	7.665E+04	[SUB94]
			800 - 2200	28.424	6.379E-03	-1.240E-06	-8.339E+05	
			2200 - 6000	37.550	1.232E-05	2.535E-08	-6.855E+06	
N ₃	436000	223.1	298.14 - 800	24.402	5.021E-02	-2.048E-05	-1.233E+05	[SUB94]
			800 - 2200	52.350	7.104E-03	-1.439E-06	-3.739E+06	
			2200 - 6000	61.965	1.111E-04	-8.863E-09	-9.310E+06	

Table A-2. Gas Phase (Metalorganics, Adducts, Oligomers, etc)

Component	T (K) range	ΔH_{298}° (J/mol)	S_{298}° (J/mol K)	C_p (J/mol K) = $A + B*T + C*T^2 + D*T^3 + E*T^{-2}$					Ref
				A	B	C	D	E	
AlCH ₃	298.15-3000	70000	239.2	35.039	7.017E-02	-2.651E-05	3.625E-09	-3.492E+05	[Prz98]
Al(CH ₃) ₃	298.15-3000	-87864	345.0	67.035	2.236E-01	-8.632E-05	1.206E-08	-1.996E+06	[Prz98]
Al ₂ (CH ₃) ₆	298.15-3000	-268000	499.3	153.819	4.582E-01	-1.788E-04	2.521E-08	-4.421E+06	[Prz98]
GaCH ₃	298.15-3000	79000	250.9	33.365	7.271E-02	-2.783E-05	3.853E-09	-5.996E+05	[Prz98]
Ga(CH ₃) ₃	298.15-3000	-45100	354.6	56.520	2.506E-01	-1.101E-04	1.900E-08	-1.247E+06	[Prz98]
InCH ₃	298.15-3000	215000	256.3	37.027	6.639E-02	-2.449E-05	3.282E-09	-4.696E+05	[Prz98]
In(CH ₃) ₃	298.15-3000	207000	367.5	75.349	2.121E-01	-8.065E-05	1.112E-08	-1.933E+06	[Prz98]
Al·NH ₃	298.15-3000	250000	257.6	41.860	5.102E-02	-1.546E-05	1.701E-09	4.237E+04	[Prz98]
(Al·N) ₃	298.15-3000	-525000	300.3	108.730	3.436E-02	-1.743E-05	2.986E-09	-3.663E+06	[Prz98]
MMA·NH	298.15-3000	-190000	286.2	61.619	8.466E-02	-3.058E-05	3.995E-09	-5.076E+05	[Prz98]
(MMA·NH) ₃	298.15-3000	-750000	506.7	202.220	2.815E-01	-1.080E-04	1.508E-08	-7.674E+06	[Prz98]
TMA·NH ₃	298.15-3000	-246000	399.5	112.231	2.546E-01	-9.317E-05	1.267E-08	-3.771E+06	[Prz98]
(DMA·NH ₂) ₃	298.15-3000	-760000	587.4	324.353	4.812E-01	-1.742E-04	2.341E-08	-1.257E+07	[Prz98]
Ga·NH ₃	298.15-3000	200000	265.6	40.799	5.281E-02	-1.635E-05	1.842E-09	5.339E+04	[Prz98]
(Ga·N) ₃	298.15-3000	-360000	322.0	122.283	1.554E-02	-8.002E-05	1.386E-08	-3.307E+06	[Prz98]
MMG·NH	298.15-3000	-130000	293.9	60.265	8.687E-02	-3.168E-05	4.174E-09	-3.669E+05	[Prz98]
(MMG·NH) ₃	298.15-3000	-520000	526.9	213.634	2.695E-01	-1.027E-04	1.421E-08	-7.327E+06	[Prz98]
TMG·NH ₃	298.15-3000	-170000	400.4	87.982	2.934E-01	-1.125E-04	1.557E-08	-1.451E+06	[Prz98]
(DMG·NH ₂) ₃	298.15-3000	-525000	573.7	264.909	5.836E-01	-2.304E-04	3.301E-08	-9.659E+06	[Prz98]
GaCl ₃ ·NH ₃	298.15-3000	-619000	376.1	99.906	7.306E-02	-2.672E-05	3.543E-09	-6.737E+05	[Prz98]
GaH ₂	298.15-3000	261000	225.1	27.738	3.792E-02	-1.757E-05	2.814E-09	-1.971E+05	[Prz98]
GaH ₃	298.15-3000	140000	217.3	25.648	7.203E-02	-3.346E-05	5.366E-09	1.415E+05	[Prz98]
InH ₂	298.15-3000	301000	234.3	30.939	3.490E-02	-1.652E-05	2.694E-09	-3.536E+05	[Prz98]
InH ₃	298.15-3000	226000	228.6	36.024	5.894E-02	-2.743E-05	4.417E-09	-7.673E+05	[Prz98]

Table A-3. Liquid Phase

Species	ΔH_{298}° (J/mole)	S_{298}° (J/mole K)	T(K) Range	C_p (J/mol K) = A + B*T + C*T ² + D*T ³				Ref#
				A	B	C	D	
AlCl ₃ (l)	-670277	185.2	298.14 - 465.69	64.929	8.787E-02	0	0	[SUB94]
			465.69 - 2000	125.520	0	0	0	
Al(l)	10711	39.8	298.14 - 700	24.367	3.769E-03	5.266E-06	-1.482E+05	[SUB94]
			700 - 933.39	38.584	-3.706E-02	3.459E-05	-1.482E+05	
			933.39 - 2900	31.748	0	0	0	
CCl ₄ (l)	-128005	216.4	298.14 - 500	123.989	2.611E-02	0	0	[SUB94]
C ₆ H ₅ Cl (l)	11698	194.1	298.14 - 410	59.932	2.938E-01	0	0	[SUB94]
NH ₄ Cl(l)	-300018	116.8	298.14 - 457.69	132.065	1.840E-02	-7.288E-05	-3.967E+06	[SUB94]
			457.69 - 793.2	26.736	1.303E-01	-1.226E-05	4.184E+05	
			793.2 - 1000	121.336	0	0	0	
InCl(l)	-170080	131.0	298.14 - 393	35.146	4.184E-02	0	0	[SUB94]
			393 - 498	58.576	0	0	0	
			498 - 900	62.760	0	0	0	
GaCl ₃ (l)	-513168	167.9	298.14 - 351	118.407	0	0	0	[SUB94]
			351 - 600	128.030	0	0	0	
InCl ₃ (l)	-503000	173.5	298.14 - 856	90.923	3.045E-02	1.528E-08	-2.951E+02	[SUB94]
			856 - 1200	117.000	-1.345E-15	2.684E-19	-4.159E-07	
In ₂ Cl ₃ (l)	-506264	306.4	298.14 - 598	93.722	9.707E-02	0	0	[SUB94]
			598 - 1000	146.440	0	0	0	
In ₃ Cl ₄ (l)	-673624	455.6	298.14 - 538	125.102	1.703E-01	0	0	[SUB94]
			538 - 1000	205.016	0	0	0	
In ₄ Cl ₇ (l)	-1188256	655.5	298.14 - 531	188.280	2.738E-01	0	0	[SUB94]
			531 - 1000	322.168	0	0	0	
Ga(l)	5590	59.2	200 - 302.89	108.229	-4.543E-01	7.115E-04	-8.799E+05	[SUB94]
			302.89 - 4000	26.069	-3.012E-04	2.410E-07	2.367E+05	
In(l)	3283	65.3	298.14 - 429.69	21.839	1.145E-02	1.272E-05	4.581E+04	[SUB94]
			429.69 - 3800	27.456	-1.092E-03	5.020E-07	4.234E+05	
AlCl ₃ (l)	-670277	185.2	298.14 - 465.69	64.929	8.787E-02	0	0	[SUB94]
			465.69 - 2000	125.520	0	0	0	
Al(l)	10711	39.8	298.14 - 700	24.367	3.769E-03	5.266E-06	-1.482E+05	[SUB94]
			700 - 933.39	38.584	-3.706E-02	3.459E-05	-1.482E+05	

Table A-3. Continued

			933.39 - 2900	31.748	0	0	0	
CCl ₄ (l)	-128005	216.4	298.14 - 500	123.989	2.611E-02	0	0	[SUB94]
C ₆ ClH ₅ (l)	11698	194.1	298.14 - 410	59.932	2.938E-01	0	0	[SUB94]
NH ₄ Cl(l)	-300018	116.8	298.14 - 457.69	132.065	1.840E-02	-7.288E-05	-3.967E+06	[SUB94]
			457.69 - 793.2	26.736	1.303E-01	-1.226E-05	4.184E+05	
			793.2 - 1000	121.336	0	0	0	
InCl(l)	-170080	131.0	298.14 - 393	35.146	4.184E-02	0	0	[SUB94]
			393 - 498	58.576	0	0	0	
			498 - 900	62.760	0	0	0	
GaCl ₃ (l)	-513168	167.9	298.14 - 351	118.407	0	0	0	[SUB94]
			351 - 600	128.030	0	0	0	
InCl ₃ (l)	-503000	173.5	298.14 - 856	90.923	3.045E-02	1.528E-08	-2.951E+02	[SUB94]
			856 - 1200	117.000	-1.345E-15	2.684E-19	-4.159E-07	
In ₂ Cl ₃ (l)	-506264	306.4	298.14 - 598	93.722	9.707E-02	0	0	[SUB94]
			598 - 1000	146.440	0	0	0	
In ₃ Cl ₄ (l)	-673624	455.6	298.14 - 538	125.102	1.703E-01	0	0	[SUB94]
			538 - 1000	205.016	0	0	0	
In ₄ Cl ₇ (l)	-1188256	655.5	298.14 - 531	188.280	2.738E-01	0	0	[SUB94]
			531 - 1000	322.168	0	0	0	
Ga(l)	5590	59.2	200 - 302.89	108.229	-4.543E-01	7.115E-04	-8.799E+05	[SUB94]
			302.89 - 4000	26.069	-3.012E-04	2.410E-07	2.367E+05	
In(l)	3283	65.3	298.14 - 429.69	21.839	1.145E-02	1.272E-05	4.581E+04	[SUB94]
			429.69 - 3800	27.456	-1.092E-03	5.020E-07	4.234E+05	

Table A-4. Solid Phase

Species	ΔH°_{298}	S°_{298}	T(K) Range	$C_p \text{ (J/mol K)} = A + B*T + C*T^2 + D*T^{-2}$				Ref #
	(J/mole)	(J/mole K)		A	B	C	D	
AlCl ₃ (s)	-705632	109.3	298.14 - 465.69	64.929	8.787E-02	0	0	[SUB94]
			465.69 - 2000	125.520	0	0	0	
AlH ₃ (s)	-11400	30.0	298.14 - 500	49.383	2.408E-02	6.330E-07	-1.459E+06	[SUB94]
AlN(s)	-317984	20.2	298.14 - 500	-56.593	3.221E-01	-2.772E-04	1.364E+06	[SUB94]
			500 - 1300	43.974	1.181E-02	-5.001E-06	-2.010E+06	
			1300 - 1900	21.657	2.379E-02	-5.375E-06	1.045E+07	
			1900 - 3000	55.534	-2.407E-03	4.190E-07	-7.645E+06	
Al ₄ C ₃ (s)	-206900	89.0	298.14 - 2500	148.741	3.346E-02	3.921E-10	-3.728E+06	[SUB94]
Al(s)	0	28.3	298.14 - 700	24.367	3.769E-03	5.266E-06	-1.482E+05	[SUB94]
			700 - 933.39	38.584	-3.706E-02	3.459E-05	-1.482E+05	
			933.39 - 2900	31.748	0	0	0	
NH ₄ Cl(s)	-314553	94.9	298.14 - 457.69	132.065	1.840E-02	-7.288E-05	-3.967E+06	[SUB94]
			457.69 - 793.2	26.736	1.303E-01	-1.226E-05	4.184E+05	
			793.2 - 1000	121.336	0	0	0	
InCl(s)	-186188	95.0	298.14 - 393	35.146	4.184E-02	0	0	[SUB94]
			393 - 498	58.576	0	0	0	
			498 - 900	62.760	0	0	0	
InCl ₂ (s)	-362753	122.2	298.14 - 509	58.576	5.021E-02	0	0	[SUB94]
GaCl ₃ (s)	-524674	135.1	298.14 - 351	118.407	0	0	0	[SUB94]
			351 - 600	128.030	0	0	0	
InCl ₃ (s)	-530000	142.0	298.14 - 856	90.923	3.045E-02	1.528E-08	-2.951E+02	[SUB94]
			856 - 1200	117.000	-1.345E-15	2.684E-19	-4.159E-07	
In ₂ Cl ₃ (s)	-548104	236.4	298.14 - 598	93.722	9.707E-02	0	0	[SUB94]
			598 - 1000	146.440	0	0	0	
In ₃ Cl ₄ (s)	-736384	338.9	298.14 - 538	125.102	1.703E-01	0	0	[SUB94]
			538 - 1000	205.016	0	0	0	
In ₄ Cl ₇ (s)	-1271936	497.9	298.14 - 531	188.280	2.738E-01	0	0	[SUB94]
			531 - 1000	322.168	0	0	0	
Diamond	1828	2.4	298.14 - 700	-10.399	6.646E-02	-3.708E-05	0	[SUB94]

Table A-4. Continued

			700 - 2500	21.052	3.224E-03	-4.524E-07	-2.515E+06	
			2500 - 5700	23.836	1.116E-03	-1.692E-08	-3.989E+06	
			5700 - 6000	22.672	1.202E-03	0	0	
Ga(s)	0	40.7	200 - 302.89	108.229	-4.543E-01	7.115E-04	-8.799E+05	[SUB94]
			302.89 - 4000	26.069	-3.012E-04	2.410E-07	2.367E+05	
In(s)	0	57.6	298.14 - 429.69	21.839	1.145E-02	1.272E-05	4.581E+04	[SUB94]
			429.69 - 3800	27.456	-1.092E-03	5.020E-07	4.234E+05	

Table A-5. Carbon (Graphite)

Species	ΔH_{298}° (J/mol)	S_{298}° (J/mol K)	T(K) Range	$C_p = A + B*T + C*T^2 + D*T^3 + E*T^4$					Ref #
				A	B	C	D	E	
C(s)	0	5.7	298.14 - 6000	24.300	9.446E-04	-5.125E+06	1.586E+09	-1.440E+11	[SUB94]

Table A-6. GaN and InN

Species	ΔH_{298}° (J/mole)	S_{298}° (J/mole K)	T(K) Range	C_p (J/mol K) = $A + B*T + C*T^2 + D*T^3 + E*T^4$					Ref
				A	B	C	D	E	
GaN(s)	-156800	30	298 - 4000	32.532	1.867E-02	-2.335E-06	-3.307E+05	0	[Unl03]
InN(s)	-71000	42.5	298 - 4000	43.886	8.194E-03	0	-1.007E+06	8.353E+07	[Lei04]

LIST OF REFERENCES

- [Abe93] C. R. Abernathy, S. J. Pearton, F. Ren, and P. W. Wisk, *J. Vac. Sci. Technol. B* 11, 179 (1993).
- [Abl05] A. Able, W. Wegscheider, K. Engl and J. Zweck, *J. Cryst. Growth* 276 (2005) 415.
- [Aco04] J.D. Acord, S. Raghavan, D.W. Snyder and J.M. Redwing, *J. Cryst. Growth* 272 (2004) 65.
- [Ade01] J. Aderhold, V. Yu. Davydov, F. Fedler, H. Klausning, D. Mistele, T. Rotter, O. Semchinova, J. Stemmer, and J. Graul, *J. Cryst. Growth* 222, 701 (2001).
- [Age97] J. Ager, T. Suski, S. Ruvinov, J. Krueger, G. Conti, E. Weber, M. Bremser, R. Davis, and C. Kuo, *Materials Research Society Symposium Proceedings*, 449, 775 (1997).
- [Alb98] J.D. Albrecht, R.P. Wang, P.P. Ruden, M. Farahmand, K.F. Brennan, *J. Appl. Phys.* 83 (1998) 4777.
- [Alm92a] M.J. Almond, C.A. Jenkins, D.A. Rice, *J. Organomet. Chem.* 439 (1992) 251.
- [Alm92b] M.J. Almond, M.G.B. Drew, C.E. Jenkins, D.A. Rice, *J. Chem. Soc. Dalton Trans.* (1992) 5.
- [Ama86] H. Amano, N. Sawaki, I. Akasaki, Y. Toyada, *Appl. Phys. Lett.* 48 (1986) 353.
- [Ama89] H. Amano, M. Kito, K. Hiramatsu, I. Akasaki, *Jpn. J. Appl. Phys.* 28 (1989) L2112.
- [Amb96] O. Ambacher, M. Brandt, R. Dimitrov, T. Metzger, M. Stutzmann, R. Fisher, A. Miehr, A. Bergmayer, G. Dollinger, *J. Vac. Sci. Technol. B* 14 (1996) 3532.
- [And05] P.A. Anderson, C.E. Kendrick, R.J. Kinsey, A. Asadov, W. Gao, R.J. Reeves, S.M. Durbin, *Phys. Status Solidi c* (2005), 2(7), 2320-2323.
- [And74] A.F. Andreevya and O.J. Elisejeva, *Z. Neorg. Chim.* 13, 185 (1974).
- [As00] D.J. As, T. Frey, D. Schikora, K. Lischka, V. Cimalla, J. Pezoldt, R. Goldhahn, S. Kaiser, and W. Gebhardt, *Appl. Phys. Lett.* 76 (2000) 1686.
- [Ban72] V.S. Ban, *J. Electrochem. Soc.* 119 (1972) 762.

- [Bar93] I. Barin, Thermochemical Data of Pure Substances, 2nd ed, VCH, Weinheim, 1993.
- [Bec02] F. Bechstedt, J. Furthmuller, *J. Cryst. Growth* 246 (2002) 315.
- [Ben02] M. Benyoucef, M. Kuball, D. D. Koleske, A. E. Wickenden, R. L. Henry, M. Fatemi and M. E. Twigg, *Mater. Sci. Eng. B*, 93 (2002) 15.
- [Bhu02] A.G. Bhuiyan, T. Tanaka, A. Yamamoto, A. Hashimoto, *Phys. Status Solidi a* 194, 502 (2002).
- [Bhu03] A.G. Bhuiyan, T. Tanaka, K. Kasashima, A. Hashimoto, A. Yamamoto, 5th International Conference on Nitride Semiconductors (ICNS-5), Nara, Japan, May 25–30, 2003.
- [Bi04] Z.X. Bi, R. Zhang, Z.L. Xie, X.Q. Xiu, Y.D. Ye, B. Liu, S.L. Gu, B. Shen, Y. Shi, Y.D. Zheng, *Mater. Lett.* 58 (2004) 3641.
- [Bil26] W. Biltz, W. Klemm. *Z. Zammah, Anorg. Chem.* 152 (1926) 276.
- [Bin02] M. Binnewies, E. Milke, Thermochemical Data of Elements and Compounds, second ed, Wiley-VCH, Weinheim, 2002.
- [Bok00] T.H. Bok, J.H. Ye, S.F.Y. Li, *J. Vac. Sci. Technol. A* 18 (2000) 2542.
- [Bon98] J.-M. Bonard, J.-P. Salvetat, T. Stockli, W.A. de Heer, L. Forro, and A. Chatelain, *Appl. Phys. Lett.* 73 (1998) 918.
- [Bra96] O. Brandt, H. Yang, H. Kostal, K. Ploog, *Appl. Phys. Lett.* 69 (1996) 2707.
- [Bre97] E. Bretschneider, diss. University of Florida 1997.
- [Bri03] O. Briot, B. Maleyre, S. Ruffenach, C. Piquier, F. Demangeot, and J. Frandon, *Phys. Status Solidi(c)* 0, No. 7, (2003) 2851.
- [Bri04] O. Briot, B. Maleyre, S. Ruffenach, B. Gil, C. Piquier, F. Demangeot, J. Frandon, *J. Cryst. Growth* 269 (2004) 22.
- [Bri72] L.H. Brixner, *Mater. Res. Bull.* 7 (1972) 879.
- [Bru89] T.R. Brumleve, S.A. Mucklejohn, N.W. O'Brien, *J. Chem. Thermodyn.*, 21 (1989) 1193.
- [Bu93] Y. Bu, L. Ma, M.C. Lin, *J. Vac. Sci. Technol. A* 11 (6) (1993) 2931.
- [Bur97] J. Burm, K. Chu, W. Davis, W.J. Schaff, L.F. Eastman, T.J. Eustis, *Appl. Phys. Lett.* 70 (1997) 464.

- [But02] K.S.A. Butcher, M. Wintrebert-Fouquet, P.P.-T. Chen, T.L. Tansley, S. Sriheaw, Mater. Res. Symp. Proc. 693 (2002) 341.
- [But05a] K.S.A. Butcher, M. Wintrebert-Fouquet, P.P.-T. Chen, K.E. Prince, H. Timmers, S.K. Shrestha, T.V. Shubina, S.V. Ivanov, R. Wuhler, M.R. Phillips, B. Monemar, Phys. Status Solidi c 2 (2005) 2263.
- [But05b] K.S.A. Butcher, T.L. Tansley, Superlatt. Microstructures 38 (2005) 1.
- [Cad01] R. Cadoret, A. Trassoudaine, E. Aujol, Phys. Status Solidi a 183 (2001) 5.
- [Cad97] R. Cadoret, E. Gil-Lafon, J. Phys. I France 7 (1997) 889.
- [Cad99] R. Cadoret, J. Cryst. Growth 205 (1999) 123.
- [Car00] S. Carlson and A.M.K. Andersen, Phys. Rev. B 61 (2000) 11209.
- [Car01] S. Carlson and A.M.K. Andersen, J. Appl. Crystallogr. 34 (2001) 7.
- [Cha04] C.-A. Chang, C.-F. Shih, N.-C. Chen, P.-H. Chang, and K.-S. Liu, Phys. Status Solidi(c) 1, 2559 (2004).
- [Cha05] C.-Y. Chang, G.-C. Chi, W.-M. Wang, L.-C. Chen, K.-H. Chen, F. Ren, S. J. Pearton, Appl. Phys. Lett. 87, 093112 (2005).
- [Cha06] C.H. Chang, M. Akilian, M.L. Schattenburg, Applied Optics 45 (2006) 432.
- [Cha94] J.F.Chang, H.H. Kuo, I.C. Leu and M.H. Hon, Sens Actuators B84 258 (1994).
- [Che04] J. Chen, A. Béré, G. Nouet and P. Ruterana, Superlatt. Microstructures, 36 (2004) 369.
- [Che05a] S.-C. Chen, S.-K. Lin, K.-T. Wu, C.-P. Huang, P.-H. Chang, N.C. Chen, C.-A. Chang, H.-C. Peng, C.-F. Shih, K.-S. Liu, Microelectronics Journal 36 (2005) 428.
- [Che05b] J.W. Chen, Y.F. Chen, H. Lu, and W.J. Schaff, Appl. Phys. Lett. 87 (2005) 041907.
- [Che06] T.P. Chen, C. Thomidis, J. Abell, W. Li, T.D. Moustakas, Journal of Crystal Growth 288(2) (2006) 254-260. .
- [Che91] Q. Chen and P. D. Dapkus, J. Electrochem. Soc., 138, 2821 (1991).
- [Che97] Y. Chen, D.E. Laughlin, X. Ma, M. Kryder, J. Appl. Phys. 81 (1997) 4380.
- [Chu98] S.N.G. Chu, J. Electrochem. Soc. Vol. 145 (1998) 3621.
- [Clo04] R. Clos, A. Dadgar and A. Krost, Phys. Status Solidi a 201 (2004) R75.

- [Cra02] M. D. Craven, S. H. Lim, F. Wu, J. S. Speck, S. P. DenBaars, *Appl. Phys. Lett.* 81 (2002) 469.
- [Dad03] A. Dadgar, M. Poschenrieder, A. Reiher, J. Bläsing, J. Christen, A. Krtschil, T. Finger, T. Hempel, A. Diez, and A. Krost, *Appl. Phys. Lett.*, 82 (2003) 28.
- [Dad04] A. Dadgar, F. Schulze, T. Zettler, K. Haberland, R. Clos, G. Straßburger, J. Bläsing, A. Diez and A. Krost, *J. Cryst. Growth*, 272 (2004) 72.
- [Dad97] M.S. Dadachov, R.M. Lambrecht, *J. Mater. Chem.* 7 (1997) 1867.
- [Dav01] A.V. Davydov, W.J. Boettinger, U.R. Kattner, and T.J. Anderson, *Phys. Status Solidi a* 188, 407 (2001).
- [Dav02a] V.Yu Davydov, A.A. Klochikhin, V.V. Emtsev, S.V. Ivanov, V.V. Vekshin, F. Bechstedt, J. Furthmuller, H. Harima, A.V. Mudryi, A. Hashimoto, A. Yamamoto, A.J. Aderhold, J. Graul, E.E. Haller, *Phys. Status Solidib* 230 (2002) R4.
- [Dav02b] V.Yu. Davydov, A.A. Klochikhin, V.V. Emtsev, D.A. Kurdyukov, S.V. Ivanov, V.A. Vekshin, F. Bechstedt, J. Furthmuller, J. Aderhold, J. Graul, A.V. Mudryi, H. Harima, A. Hashimoto, A. Yamamoto and E.E. Haller, *Phys. Status Solidib* 234, No. 3, 787 (2002).
- [Dav02c] V.Yu. Davydov, A.A. Klochikhin, R.P. Seisyan, V.V. Emtsev, S.V. Ivanov, F. Bechstedt, J. Furthmüller, H. Harima, A.V. Mudryi, J. Aderhold, O. Semchinova, J. Graul, *Phys. Status Solidib* 229 (2002) R1.
- [Dav03] E. A. Davis, S. F. J. Cox, R. L. Lichti, and C. G. Van de Walle, *Appl. Phys. Lett.* 82 592 (2003).
- [Dav97] V. Y. Davydov, N. S. Averkiev, I. N. Goncharuk, D. K. Nelson, I. P. Nikitina, A. S. Polkovnikov, A. N. Smirnov, M. A. Jacobsen, and O. K. Semchinova, *J. Appl. Phys.* 82, 5097 (1997).
- [Dav98a] A.V. Davydov, T. J. Anderson, *Electrochem. Soc. Proc.* 98-118 (1998) 38.
- [Dav98b] V.Yu. Davydov, Yu. E. Kitaev, I.N. Goncharuk, A.N. Smirnov, J. Graul, O. Semchinova, D. Uffmann, M.B. Smirnov, A.P. Mirgorodsky, R.A. Evarestov, *Phys. Rev. B* 58, 12899 (1998).
- [Dav99] V.Yu. Davidov, V.V. Emtsev, I.N. Goncharuk, A.N. Sminov, V.D. Petrikov, V.V. Mamutin, V.A. Vekshin, S.V. Ivanov, M.B. Smirnov, and T. Inushima, *Appl. Phys. Lett.* 75 (1999) 3297.
- [Deb05] P. Deb, H. Kim, V. Rawat, M. Oliver, S. Kim, M. Marshall, E. Stach, and T. Sands, *Nano Lett.*, Vol. 5, No. 9, (2005) 1847.

- [Dem96] F. Demangeot, J. Frandon, M. A. Renucci, O. Briot, B. Gil, R.-L. Aulombard, MRS Internet J. Nitride Semicond. Res. 1, 23(1996).
- [Det01] T. Detchprohm, M. Yano, S. Sano, R. Nakamura, S. Mochiduki, T. Nakamura, H. Amano and I. Akasaki, Jpn. J. Appl. Phys. Vol. 40 (2001) L16.
- [Det92] T. Detchprohm, K. Hiramatsu, K. Itoh, I. Akasaki, Jpn. J. Appl. Phys. 31, L1454-L1456 (1992).
- [Dim04] E. Dimakis, G. Konstantinidis, K. Tsagaraki, A. Adikimenakis, E. Iliopoulos, A. Georgakilas, Superlatt. Microstructures 36 (2004) 497.
- [Dim05] E. Dimakis, K. Tsagaraki, E. Iliopoulos, Ph. Komninou, Th. Kehagias, A. Delimitis and A. Georgakilas, J. Cryst. Growth, 278(2005) 367.
- [Din04] Y. Ding, P. X. Gao, Z. L. Wang, J. Am. Chem. Soc. 126 (2004) 2066.
- [Dmi03] V. Dmitriev et al., J. Phys. Chem. Solids 64 (2003) 307.
- [Dra04] M. Drago, T. Schmidling, C. Werner, M. Pristovsek, U.W. Pohl and W. Richter, J. Cryst. Growth 272 (2004) 87.
- [Dra06] M. Drago, P. Vogt, W. Richter, Phys. Status Solidi a 203 (2006) 116.
- [Edg97] J.H. Edgar, C.H. Wei, D.T. Smith, T.J. Kistenmacher, W.A. Bryden, J. Mater. Sci. 8 (1997) 307.
- [Edw98] N.V. Edwards, M.D. Bremser, R.F. Davis, A.D. Batchelor, S.D. Yoo, C.F. Karan, and D.E. Aspnes, Appl. Phys. Lett. 73, 2808 (1998).
- [Eip05] E. Eiper, A. Hofmann, J.W. Gerlach, B. Rauschenbach and J. Keckes, J. Cryst. Growth, 284 (2005) 561.
- [Etz01] E. V. Etzkorn and D. R. Clarke, J. Appl. Phys. 89 (2001) 1025.
- [Eva97] J.S.O. Evans, T.A. Mary and A.W. Sleight, Physica B, 1997, 241, 311-316.
- [Flo97] J.A. Floro, E. Chason, S.R. Lee, R.D. Twisten, R.Q. Hwang and L.B. Freund, J. Electron. Mater. 26 (1997) 969.
- [Gao03] L. Gao, Q. Zhang, J. Li, J. Mater. Chem. 13 (2003) 154.
- [Gar01] N. Garg et al. 2001 Solid State Phys. 39.
- [Gil00] D.R. Gilbert, A. Novikov, N. Patrin, J.S. Budai, F. Kelly, R. Chodelka, R. Abbaschian, S.J. Pearton, R. Singh, Appl. Phys. Lett.(2000), 77, 4172.
- [Gor77] S.P. Gordienko, B.V. Fenochka, Zh. Fiz. Khim. 51 (1977) 530.

- [Got95] W. Gotz, N.M. Johnson, J. Walker, D.P. Bour, H. Amano, I. Akasaki, *Appl. Phys. Lett.* 67 (1995) 2606.
- [Gra05] J. Grandal, M.A. Sanchez-Garcia, *J. Cryst. Growth* 278 (2005) 373.
- [Gri59] H. Grimmeiss and Z. H- Koelmans, *Nature (London)* 14a, 264 (1959).
- [Guo93] Q. Guo, O. Kato, *J. Appl. Phys.* 73 (1993) 7969.
- [Guo98] Q. X. Guo, M. Nishio, and H. Ogawa, A. Wakahara and A. Yoshida, *Phys. Rev. B* 58 (1998) 15304.
- [Guo99] Q. Guo, M. Nishio, H. Ogawa, A. Yoshida, *Jpn. J. Appl. Phys.* 38 (1999) L490.
- [Had03] D.B. Haddad, J.S. Takur, V.M. Naik, G.W. Auner, R. Naik, L.E. Wenger, *Mater Res. Soc. Symp. Proc.* 743 (2003) 701.
- [Had04] D.B. Haddad, H. Dai, R. Naik, C. Morgan, V.M. Naik, J.S. Thakur, G.W. Auner, L.E. Wenger, H. Lu, W.J. Schaff, *Mater. Res. Soc. Symp. Proc.* 798 (2004) Y12.7.1.
- [Hag03] P.R. Hageman, V. Kirilyuk, W.H.M. Corbeek, J.L. Weyher, B. Lucznik, M. Bockowski, S. Porowski and S. Müller, *J. Cryst. Growth* 255 (2003) 241.
- [Hah40] H. Hahn, R. Juza, *Z. Anorg. Allgem. Chem.* 244 (1940) 111.
- [Han97] W. Han, S. Fan, Q. Li, Y. Hu, *Science* 277 (1997) 1287.
- [Har95] H.L. Hartnagel, A.L. Dawar, A.K. Jain and C. Jagadish, *Semiconducting Transparent Thin Films (IOP Publishing, Bristol, 1995)*.
- [He06] J.H. He, R. Yang, Y.L. Chueh, L.J. Chou, L.J. Chen, Z.L. Wang, *Adv. Mater* 18 (2006) 650.
- [Hea99] S. Hearne, E. Chason, J. Han, J.A. Floro, J. Figiel, J. Hunter, H. Amano and I.S.T. Song, *Appl. Phys. Lett.* 74 3 (1999) 356.
- [Hel92] K. H. Hellwege, A. M. Hellwege, and D. F. Nelson, *Landolt-Börnstein Numerical Data and Functional Relationships in Science and Technology (Springer, Berlin, 1979, 1992), Vols. III:11, III:29*.
- [Hig02] M. Higashiwaki, T. Matsui, *Jpn. J. Appl. Phys.* 41 (2002) L540.
- [Hos90] M. Hoshino, *J. Appl. Phys.*, 68 (1990) 2538.
- [Hov72] H.J. Hovel and J.J. Cuomo, *Appl. Phys. Lett.* 20 (1972) 71.
- [Hua01] M.H. Huang, S. Mao, H. Feick, H.Q. Yan, Y.Y. Wu, H. Kind, E. Weber, R. Russo, P.D. Yang, *Science* 292 (2001) 1897.

- [Hua03] M. Huang, diss. University of Florida (2003).
- [Hua05a] Y. Huang, H. Wang, Q. Sun, J. Chen, D.Y. Li, Y.T. Wang and H. Yang, J. Cryst. Growth 276 (2005) 13.
- [Hua05b] Y. Huang, H. Wang, Q. Sun, J. Chen, J.F. Wang, Y.T. Wang and H. Yang, J. Cryst. Growth 281 (2005) 310.
- [Hul69] F. Hulbert, J. Br. Ceram. Soc. 6 (1969) 11.
- [Hur04] T.-B. Hur, I.J. Lee, H.L. Park, Y.-H. Hwang and H.-K. Kim, Solid State Comm. 130 (2004) 397.
- [Hwa04] J. Hwang, diss., University of Florida 2004.
- [Iga92] O. Igarashi, Jpn. J. Appl. Phys. 31 (1992) 2665.
- [IIIV03] III-Vs Review, Elsevier Ltd., Vol 16, No 6, August 2003.
- [Im98] J.S. Im, H. Kollmer, J. Off, A. Sohmer, F. Scholz and A. Hangleiter, Phys. Rev. B 57, (1998) R9435.
- [Inu01] T. Inushima, V. V. Mamutin, V. A. Vekshin, S. V. Ivanov, T. Sakon, M. Motokawa and S. Ohoya, J. Cryst. Growth, 227-228 (2001) 481.
- [Jac63] M.G. Jacko, S.J.W. Price, Can. J. Chem. 41 (1963) 1560.
- [Jai04] A. Jain, S. Raghavan, J.M. Redwing, J. Cryst. Growth 269 (2004) 128.
- [Jam05] M. Jamil, J. R. Grandusky, V. Jindal, F. Shahedipour-Sandvik, S. Guha and M. Arif, Appl. Phys. Lett. 87 (2005) 082103.
- [JCP93] Inorganic Powder Data, 33, Joint Committee for Powder Diffraction Standards (JCPDS), International Centre for Diffraction Data (ICDD), USA, 1162, (1993).
- [JCP96] Joint Committee for Powder Diffraction Standards (JCPDS), International Centre for Diffraction Data (ICDD). (1996).
- [Jes67] W.A. Jesser, D. Kuhlmann-Wilsdorf, Phys. Status Solidi 19, (1967) 95.
- [Ji05] X.H. Ji, S.P. Lau, H.Y. Yang, S.F. Yu, Nanotechnology 16 (12) (2005) 3069-3073.
- [Joh02] J.C. Johnson, H.Q. Yan, R.D. Schaller, P.B. Petersen, P.D. Yang, R.J. Saykally, Nano Lett. 2 279 (2002).
- [Joh04a] M.C. Johnson, C.J. Lee, E.D. Bourret-Courchesne, S.L. Konsek, S. Aloni, W.Q. Han, and A. Zettl, Appl. Phys. Lett. 85 (2004) 5670.

- [Joh04j] M.C. Johnson, S.L. Konsek, A. Zettl, E.D. Bourret-Courchesne, *J. Cryst. Growth* 272 (2004) 400.
- [Jon87] R.D. Jones, K. Rose, *J. Phys. Chem. Solids* 48 (1987) 587.
- [Jor99] J.D. Jorgensen, Z. Hu, S. Teslic, D.N. Argyriou, S. Short, J.S.O. Evans and A.W. Sleight, *Phys. Rev. B* 59 (1999) 215.
- [Jot01] R. Jothilingam, M.W. Koch, J.B. Posthill, G.W. Wicks, *Journal of Electronic Materials*, Vol 30, No 7 (2001) 821.
- [Juz38] R. Juza and H. Hahn, *Z. Anorg. Allg. Chem.* 239, 282 (1938).
- [Juz56] R. Juza and A. Rabenau, *Z. Anorg. Allg. Chem.* 285, 212 (1956).
- [Kan04] S.W. Kang, diss., University of Florida 2004.
- [Kat94] Y. Kato, S. Kitamura, K. Hiramatsu, N. Sawaki, *J. Cryst. Growth* 144 (1994) 133.
- [Kee04] K. Keem, H. Kim, G.T. Kim, J.S. Lee, B. Min, K. Cho, M.Y. Sung and S. Kim, *Appl. Phys. Lett.* 84 4376 (2004).
- [Kel00] S. Keller, I. Ben-yaacov, S.P. Denvers, and U.K. Mishra, *Proceedings of the International Workshop on Nitride Semiconductors (IWN' 2000)*, Nagoya, Japan, September 24–27, 2000, IPAP conference series 1, p.233.
- [Kha93] M.A. Khan, J.N. Kuznia, A.R. Bhattarai, and D.T. Olsen, *Appl. Phys. Lett.* 62, 1786 (1993).
- [Kih00] M. Kihara, T. Sasaki, T. Tsuchiya, and H. Sakaguchi, *Proc. Int. Workshop on Nitride Semiconductors*, IPAP Conf. Series 1, pp. 117-120 (2000).
- [Kim03] H.-M. Kim, W.C. Lee, T.W. Kang, K.S. Chung, C.S. Yoon, C.K. Kim, *Chemical Physics Letters* 380 (2003) 181.
- [Kim03c] H.-M. Kim, W.C. Lee, T.W. Kang, K.S. Chung, C.S. Yoon, C.K. Kim, *Chemical Physics Letters* 380 (2003) 181.
- [Kim05] J-H. Kim, J.A. Freitas, Jr., P.B. Klein, S. Jang, F. Ren, and S.J. Pearton, *Eletroch. Sol-St. Lett.* 8 (2005) G345.
- [Kim06] T.W. Kim, diss., University of Florida 2006.
- [Kim94] S.H. Kim, H.S. Kim, J.S. Hwang, J.G. Choi, P.J. Chong, *Chem. Mater.* 6 (1994) 278.
- [Kim99] C. Kim, I. K. Robinson, J. Myoung, K-H Shim, K. Kim, *J. Appl. Phys.* 85 (1999) 4040.

- [Kis96] C. Kiselowski, J. Kruger, S. Ruvimov, T. Suski, J. W. Ager III, E. Jones, Z. Liliental-Weber, M. Rubin, E. R. Weber, M. D. Bremser, and R. F. Davis, *Phys. Rev. B* 54, (1996) 745.
- [Kle00] C.A. Klein, *J. Appl. Phys.* 88 (2000) 5487.
- [Kol98] J.W. Kolis, S. Wilcenski, R.A. Laudise, *Mater. Res. Soc. Symp. Proc.* 495 (1998) 367.
- [Kos04] R. Kosiba, G. Ecke, V. Cimalla, L. Spieß, S. Krischok, J.A. Schaefer, O. Ambacher, W.J. Schaff, *Nuclear Instruments and Methods in Physics Research B* 215 (2004) 486–494.
- [Kou05] A. Koukitu, J. Kikuchi, Y. Kangawa and Y. Kumagai, *J. Cryst. Growth* 281 (2005) 47.
- [Kou98] A. Koukitu, S. Hama, T. Taki, H. Seki, *Jpn. J. Appl. Phys. PART 1- 37 (3A):* 762-765 (1998).
- [Kri04] S. Krischok, V. Yanev, O. Balykov, M. Himmerlich, J.A. Schaefer, R. Kosiba, G. Ecke, I. Cimalla, V. Cimalla, O. Ambacher, H. Lu, W.J. Schaff, L.F. Eastman, *Surface Science* 566–568 (2004) 849–855.
- [Kro03] A. Krost, A. Dadgar, G. Strassburger, and R. Clos, *Phys. Status Solidi a* 200 (2003) 26.
- [Kro05] A. Krost, A. Dadgar, F. Schulze, J. Bläsing, G. Strassburger, R. Clos, A. Diez, P. Veit, T. Hempel and J. Christen, *J. Cryst. Growth*, 275(2005) 209.
- [Kry05] O. Kryliouk, H.J. Park, H.T. Wang, B.S. Kang, T.J. Anderson, F. Ren and S.J. Pearton, *J. Vac. Sci. Technol. B*, 23(5), 1891(2005).
- [Kry06] O. Kryliouk, H. J. Park, T. Anderson, to be published.
- [Kry99a] O. Kryliouk, M. Reed, T. Dann, T. Anderson and B. Chai, *Mat. Sci. Eng. B* 59, 116-119 (1999).
- [Kry99b] O. Kryliouk, M. Reed, T. Dann, T. J. Anderson and B. Chai, *Mat. Sci. Eng. B*, 66, 26 (1999).
- [Kub89] K. Kubota, Y. Kobayashi, and K. Fujimoto, *J. Appl. Phys.* 66, 2984 (1989).
- [Kum01] Y. Kumagai, K. Takemoto, A. Koukitu, H. Seki, *J. Cryst. Growth* 222 (2001) 118.
- [Kum02] M. Senthil Kumar, G. Sonia, V. Ramakrishnan, R. Dhanasekaran and J. Kumar, *Physica B: Condensed Matter*, 324 (2002) 223.

- [Kum04] Y. Kumagai, J. Kikuchi, Y. Matsuo, Y. Kangawa, K. Tanaka, A. Koukitu, *J.Cryst. Growth* 272 (2004) 341.
- [Kur01] E. Kurimoto, H. Harima, A. Hashimoto, and A. Yamamoto, *phys.stat.sol.(b)* 228, No.1, 1–4 (2001).
- [Kur04a] K. Kuriyama, T. Tokumasu, H. Sano and M. Okada, *Solid State Communications*, 131 (2004) 31.
- [Kur04b] E. Kurimoto, M. Hangyo, H. Harima, M. Yoshimoto, T. Yamaguchi, T. Araki, Y. Nanishi, K. Kisoda, *Appl. Phys. Lett.* 84 (2004) 212.
- [Kuy04] T. Kuykendall, P.J. Pauzauskie, Y. Zhang, J. Goldberger, D. Sirbuly, J. Denlinger, and P. Yang, *Nature materials* 3 (2004) 524.
- [Lan04] Z.H. Lan, W.M. Wang, C.L. Sun, S.C. Shi, C.W. Hsu, T.T. Chen, K.H. Chen, C.C. Chen, Y.F. Chen, L.C. Chen, *J. Cryst. Growth* 269 (2004) 87.
- [Lar88] C.A. Larsen, N.I. Buchan, and G.B. Stringfellow, *Appl. Phys. Lett.*, 52, 480 (1988).
- [Lar90] C.A. Larsen, N.I. Buchan, S.H. Li, and G.B. Stringfellow, *J. Cryst. Growth* 102 (1990) 103.
- [Leb00] V. Lebedev, J. Jinschek, U. Kaiser, B. Schroter, W. Richter, *Appl. Phys. Lett.* 76 (2000) 2029.
- [Lee04] I.J. Lee, J.-Y. Kim, H.-J. Shin, H.-K. Kim, *J. Appl. Phys.* 95 (2004) 5540.
- [Lei03] J. Leitner, A. Strejc, D. Sedmidubský, K. Ružicka, *Thermochimica Acta* 401 (2003) 169.
- [Lei04] J. Leitner, P. Marsík, D. Sedmidubsky, K. Ruzicka, *Journal of Physics and Chemistry of Solids* 65 (2004) 1127.
- [Lei65] A. Leib, M. T. Emerson, J. P. Oliver, *Inorg. Chem.* 4 (1965) 1825.
- [Lei96] J. Leitner, J. Stejskal, P. Vonka, *Mater. Lett.* 28 (1996) 197. .
- [Les96] M. Leszczynski, H. Teisseyre, T. Suski, I. Grzegory, M. Bockowski, J. Jun, S. Porowski, K. Pakula, J. M. Baranowski, C. T. Foxon, T. S. Cheng, *Appl. Phys. Lett.* 69, 73-75 (1996).
- [Li04] Q.H. Li, Q. Wan, Y.X. Liang and T.H. Wang, *Appl. Phys. Lett.* 84 (2004) 4556.
- [Li06] J.-B. Li, J. Liang, G. Rao, Y. Zhang, G.Y. Liu, J. Chen, Q. Liu and W. Zhang, *Journal of Alloys and Compounds*, In Press, Corrected Proof, Available online 18 January 2006. (<http://www.elsevier.com/locate/jallcom>).

- [Li94] X. Li, B. Zhou, K.S.A. Butcher, E. Florido, N. Syakir, and T.L. Tansley, Proceedings of the Australian Compound Optoelectronic Materials Devices Conference, Sydney, Australia, December 12–14, 1994, p. 43.
- [Lia00] H.M. Liaw, R. Venugopal, J. Wan, R. Doyle, P.L. Fejes and M.R. Melloch, *Solid-State Electronics* 44 (2000) 685.
- [Lia01] H.M. Liaw, R. Venugopal, J. Wan and M.R. Melloch, *Solid-State Electronics* 45 (2001) 1173.
- [Lia02] C.H. Liang, L.C. Chen, J.S. Hwang, K.H. Chen, Y.T. Hung and Y.F. Chen, *Appl. Phys. Lett.* 81, 22 (2002).
- [Liu02] H. Liu et al. *Solid State Commun.* 121 (2002) 177.
- [Liu78] S. Liu and D.A. Stevenson, *J. Electrochem. Soc.* 125 (1978) 1161.
- [Lo01] Y.-H. Lo, F. Ejeckman, Z. Zhu, US Pat. 20010042503A1.
- [Los04] M. Losurdo and G. Bruno, conference proceedings of the ICNS-6, Bremen (2005); see otherwise: T. Ive, Brandt, M. Ramsteiner, M. Giehler, H. Kostial, and K. Ploog, *Appl. Phys. Lett.* 84, 1671 (2004).
- [Lu01] H. Lu, W.J. Schaff, J. Hwang, H. Wu, G. Koley, and L.F. Eastman, *Appl. Phys. Lett.*, Vol. 79, No. 10, 3 September (2001) 1489.
- [Lu02a] H. Lu, W. J. Schaff, L. F. Eastman, J. Wu, W. Walukiewicz, K. M. Yu, J. W. Auger III, E. E. Haller, and O. Ambacher, Abstract of the 44th Electronic Material Conference, Santa Barbara, CA, June 26–28, 2002; *J. Electron. Mater.* (to be published); W. J. Schaff (private communication, Cornell University, Ithaca, N.Y.).
- [Lu02b] H. Lu, W.J. Schaff, L.F. Eastman, and C. Wood, *Mater. Res. Soc. Symp. Proc.* 693, 9 (2002).
- [Lu04a] H. Lu, W.J. Schaff, L.F. Eastman, *J. Appl. Phys.* 96 (2004) 3577.
- [Lu04b] Y.Lu, J. Li, H.T. Ng, C. Binder, C. Partridge and M. Meyyapan, *Chem. Phys. Lett.* 391 (2004) 344.
- [Luo05] S. Luo, W. Zhou, Z. Zhang, L. Liu, X. Dou, J. Wang, X. Zhao, D. Liu, Y., L. Song, Y. Xiang, J. Zhou, S. Xie, *small* 1 (2005) 1004.
- [Mac70] J.B. MacChesney, P.M. Bridenbaugh, P.B. O'Connor, *Mater. Res. Bul.* 5 (1970) 783.
- [Mal04a] B. Maleyre, O. Briot, and S. Ruffenach, *J. Cryst. Growth* 269, 15 (2004).
- [Mal04b] B. Maleyre, S. Ruffenach, O. Briot, B. Gil and A. Van der Lee, *Superlatt. Microstructures* 36 (2004) 517.

- [Mal05] B. Maleyre, S. Ruffenach, O. Briot, B. Gil, and A. van der Lee, *Phys. Status Solidi c* 2, 2309 (2005).
- [Mar01] H. Marchand, L. Zhao, N. Zhang, B. Moran, R. Coffie, U. K. Mishra, J. S. Speck, S. P. DenBaars, and J. A. Freitas, *J. Appl. Phys.* 89 (2001) 7846.
- [Mar02] D. Martin, J.F. Carlin, V. Wagner, H.J. Buhlmann, M. Ilegems, *Phys. Status Solidib* 194 (2002) 520.
- [Mar03] I.V. Markov, *Crystal Growth for Beginners*, World Scientific, 2nd ed. p 422 (2003).
- [Mar69] H.P. Maruska and J.J. Tietjen, *Appl. Phys. Lett.* 15, 327 (1969).
- [Mar77] L.A. Marasina, I.G. Pichugin, and M. Tlaczala, *Krist. Tech.* 12, 541 (1977).
- [Mar96] T.A. Mary, J.S.O. Evans, T. Vogt and A.W. Sleight, *Science*, 1996, 272, 90-92.
- [Mas01] M. Mastro, diss. University of Florida 2001.
- [Mas06a] M.A. Mastro, C.R. Eddy, Jr., D.K. Gaskill, N.D. Bassim, J. Casey, A. Rosenberg, R.T. Holm, R.L. Henry and M.E. Twigg, *J. Cryst. Growth* 287 (2006) 610.
- [Mas06b] M.A. Mastro, O.M. Kryliouk and T.J. Anderson, *Mater. Sci. Eng. B* 127 (2006) 91.
- [Mat02] T. Matsuoka, H. Okamoto, M. Nakao, H. Harima, E. Kurimoto, *Appl. Phys. Lett.* 81 (2002) 1246.
- [Mat75] J.W. Matthews, *Epitaxial Growth Part B* (1975), Academic Press, Inc.
- [Mat87] E.N. Matthias, B.M. Allen, *IEEE Trans. Electron Devices*, ED-34 (1987) 257.
- [Mat89] T. Matsuoka, H. Tanaka, T. Sasaki, and A. Katsui, *Proceedings of the Sixteenth International Symposium on GaAs and Related Compounds*, Karuizawa, Japan, September 25–29, 1989 (Institute of Physics, Bristol, 1990), p. 141.
- [Mat97] T. Matsuoka, in *GaN and Related Materials*, edited by S. J. Pearton, Gordon and Breach, New York, 1997, pp. 53–59.
- [Maz89] D. Mazzaresse, A. Tripathi, W. C. Conner, K. A. Jones, L. Calderon, D. W. Eckart, *J. of Electronic Materials* 18, 3 (1989) 369.
- [Mel97] Yu.V. Melnik, K.V. Vassilevski, I.P. Nikitina, A.I. Babanin, V. Yu. Davydov, V.A. Dmitriev, *MRS Internet J. Nitride Semicond. Res.* 2, 39(1997).
- [Mer50] J.H. van der Merwe, *Proceedings: Physical Society London*, A63, 616 (1950).

- [Mer63] J.H. van der Merwe, *J. Appl. Phys.* 34, No1 (1963) 117.
- [Mes05] V.N. Bessolov, V.Y. Davydov, Y.V. Zhilyaev, E.V. Konenkova, G.N. Mosina, S.D. Raevskii, S.N. Rodin, S. Sharofidinov, M.P. Shcheglov, H.S. Park, M. Koike, *Technical Physics Letters* 31 (2005) 915.
- [Mey83] G. Meyer, R. Blachnik, *Anorg. Allg. Chem.*, 503 (1983) 126.
- [Mey84] D.J. Meyer, diss., University of Florida 1984.
- [Min04] T. Minegishi, T. Suzuki, C. Harada, H. Goto, M.-W. Cho and T. Yao, *Current Applied Physics*, 4, (2004) 685.
- [Mit03] K.D. Mitzner, J. Sternhagen and D.W. Galipeau, *Sens Actuators B* 93 92 (2003).
- [Mit98] P. Mitra, A.P. Chatterjee and H.S. Maiti, *Mater.Lett.* 35 (1998) 33.
- [Mor73] Y. Morimoto, K. Uchino and S. Ushio: *J. Electrochem. Soc.* 120 (1973) 1783.
- [Mot02a] K. Motoki, T. Okahisa, S. Nakahata, N. Matsumoto, H. Kimura, H. Kasai, K. Takemoto, K. Uematsu, M. Ueno, Y. Kumagai, A. Koukitu, H. Seki, *J. Cryst. Growth* 237–239 (2002) 912.
- [Mot02b] K. Motoki, T. Okahisa, S. Nakahata, N. Matsumoto, H. Kimura, H. Kasai, K. Takemoto, K. Uematsu, M. Ueno, Y. Kumagai, A. Koukitu and H. Seki, *Mater. Sci. Eng. B* 93, (2002) 123.
- [Mot02c] Motlan, E.M. Goldys, T.L. Tansley, *J. Cryst. Growth* 241 (2002) 165.
- [Mot18] W.R. Mott, *Trans. Am. Electrochem. Soc.*, 34 (1918) 287.
- [Mou93] T. J. Mountziaris, S. Kalyanasundaram, N. K. Inge, *J. Crystal Growth* 131 (1993) 283.
- [Mur02] A.K. Murali, A.D. Barve, S.H. Risbud, *Mater. Sci. Eng. B* 96 (2002) 111.
- [Nak92] S. Nakamura, T. Muskai, M. Senoh, N. Iwasa, *Jpn. J. Appl. Phys.* 31 (1992) L139.
- [Nak94] S. Nakamura, T. Mukai, M. Senoh, *Appl. Phys. Lett.* 64 (1994) 1687.
- [Nak95a] S. Nakamura, T. Muskai, M. Senoh, *Appl. Phys. Lett.* 67 (1995) 1868.
- [Nak95b] S. Nakamura, M. Senoh, N. Iwasa, S. Nagahama, T. Yamada, T. Muskai, *Jpn. J. Appl. Phys.* 10B (1995) L1332.
- [Nak96a] S. Nakamura, M. Senoh, S.I. Nagahama, N. Iwasa, T. Yamada, T. Matsushita, H. Kiyoku, Y.S. Ugimoto, *Jpn. J. Appl. Phys.* 35 (1996) L217.

- [Nak96b] S. Nakamura, M. Senoh, S.I. Nagahama, N. Iwasa, T. Yamada, T. Matsushita, H. Kiyoku, Y.S. Ugimoto, *Appl. Phys. Lett.* 68 (1996) 2105.
- [Nak97] S. Nakamura, M. Senoh, S. Hagahama, H. Iwasa, T. Yamada, T. Matsushita, Y. Sugimoto, and H. Kiyoku, *Appl. Phys. Lett.* 70 (1997) 1417.
- [Nak98] S. Nakamura, M. Senoh, S.I. Nagahama, N. Iwasa, T. Yamada, T. Matsushita, H. Kiyoku, Y.S. Ugimoto, T. Kozaki, H. Umemoto, M. Sano, K. Chocho, *Appl. Phys. Lett.* 72 (1998) 211.
- [Nao03] H. Naoi, M. Narukawa, H. Miyake and K. Hiramatsu, *J. Cryst. Growth* 248, (2003) 573.
- [Nat80] B.R. Natarajan, A.H. Eltoukhy, J.E. Greene, T.L. Barr, *Thin Solid Films* 69 (1980) 201.
- [Nik99] A. Nikolaev, I. Nikitina, A. Zubrilov, M. Mynbaeva, Y. Melnik, and V. Dmitriev MRS 1999 Fall Proceedings W6.5.
- [Nis83] J. Nishizawa, T. Kurabayashi, *J. Electrochem. Soc.* 130 (1983) 413.
- [Nou04] G. Nouet, P. Ruterana, J. Chen, B. Lei, H. Ye, G. Yu, M. Qi and A. Li, *Superlatt. Microstructures*, 36 (2004) 417.
- [Now99] R. Nowak, M. Pessa, M. Suganuma, M. Leszczynski, I. Grzegory, S. Porowski, F. Yoshida, *Appl. Phys. Lett.* 75 (1999) 2070.
- [Oka98] Y. Okamoto, *J. Crystal Growth* 191 (1998) 405.
- [Ole98] S.K. O'Leary, B.E. Foutz, M.S. Shur, U.V. Bhapkar, L.F. Eastman, *J. Appl. Phys.* 83 (1998) 826.
- [Oli03] R.A. Oliver, C. Norenberg, M.G. Martin, M.R. Castell, L. Allers, G.A.D. Briggs, *Surface Science* 532–535 (2003) 806.
- [Ond02] B. Onderka, J. Unland, and R. Schmid-Fetzer, *J. Mater. Res.* 17 (2002) 3065.
- [Osa72] K. Osamura, K. Nakajima, Y. Murakami, H. P. Shingu, and A. Ohtsuki, *Solid State Commun.* 11, 617 (1972).
- [Osa75] K. Osamura, S. Naka, and Y. Murakami, *J. Appl. Phys.* 46, 3432 (1975).
- [Oto03] Y. Otoki, M. Kihara, T. Tanaka, K. Takano, T. Kikkawa and T. Igarashi, *The International Conference on Compound Semiconductor Manufacturing Technology* 13.3 (2003).
- [Pan94] J.I. Pankove, S.S. Chang, H.C. Lee, R. Molnar, T.D. Moustakas, and B. Van Zeghbrock, *Tech. Dig. Int. Electron Devices Meet.* 94, 389 (1994).

- [Pan99] Y.C. Pan, W.H. Lee, C.K. Shu, H.C. Lin, C.I. Chiang, H. Chang, S.D. Lin, M.C. Lee, W.K. Chen, *J. Appl. Phys.* 38 (1999) 645.
- [Par01] H. Parala, A. Devi, F. Hipler, E. Maile, A. Birkner, H.W. Becker, R.A. Fischer, *J. Cryst. Growth* 231 (2001) 68.
- [Par03] C. Park, S. Han, C. Doh, S. Yeo, D. Yoon, S.-K. Hwang, K.-H. Lee, and T. Anderson, *Chemical Vapor Deposition XVI (CVD-VXI) and EURO-CVD 14*, M. Allendorf, F. Maury, and F. Teyssandier, Eds., Vol. 2003-08, 92-97 (2003).
- [Par05] C. Park, J. Kim, D. Yoon, S. Han, C. Doh, S. Yeo, K. Lee, T. Anderson, *Journal of The Electrochemical Society*, 152 (2005) C298.
- [Pas01] R. Paszkiewicz, B. Paszkiewicz, R. Korbutowicz, J. Kozłowski, M. Tlaczala, L. Bryja, R. Kudrawiec, J. Misiewicz, *Cryst. Res. Technol.*, 36 (2001), 971.
- [Pas04] T. Paskova, P.P. Paskov, E. Valcheva, V. Darakchieva, J. Birch, A. Kasic, B. Arnaudov, S. Tungasmita, B. Monemar, *Phys. Status Solidi(a)* 201 (2004) 2265.
- [Pas63] J. Pastrnak and L. Souckova, *Phys. Status Solidi* 3, K71 (1963).
- [Per92] P. Perlin, C. J. Carrilon, J. P. Itie, A. S. Miguel, I. Grzegory, and A. Polian, *Phys. Rev. B*, 45, 83 (1992).
- [Per97] W.G. Perry, T. Zheleva, M.D. Bremser, R.F. Davis, W. Shan, and J.J. Song, *J. Electron. Mater.* 26, 224 (1997).
- [Per98] C.A. Perottani and J.A.H. da Jornada *Science* 280 (1998) 886.
- [Plo99] K.H. Ploog, O. Brandt, H. Yang, A. Trampert, *J. Vac. Sci. Technol. B* 16 (1999) 2229.
- [Pol96] A. Polian, M. Grimsditch, and I. Grzegory, *J. Appl. Phys.*, 79, 3343 (1996).
- [Por95] S. Porowski, High pressure crystallization of III-V nitrides, *Acta Physica Polonica*. 87 (2) (1995) 295.
- [Por99] S. Porowski, *MRS Internet J. Nitride Semicond. Res.* 4S1, G1.3 (1999).
- [Pra69] G. L. Pratt, *Gas Kinetics*, Wiley, London (1969).
- [Pri95] D.M. Price, *J. Therm. Anal.*, 45 (1995) 1285.
- [Prz98] I.N. Przhivalskii, S. Yu. Karpov, Yu.N. Makarov, *MRS Internet J. Nitride Semicond. Res.* 3, 30 (1998).
- [Puy76] N. Puychevriev and M. Menoret, *Thin Solid Films* 36, 141 (1976).

- [Qia05] Z. Qian, S. Hou, J. Zhang, R. Li, Z. Shen, X. Zhao, Z. Xue, *Physica E* 30 (2005) 81.
- [Raa93] I.J. Raaijmakers, J. Yang, *Appl. Surf. Sci.* 73 (1993) 31-41.
- [Rag02] B. Raghathamachar, W.M. Vetter, M. Dudley, R. Dalmau, R. Schelessner, Z. Sitar, E. Michaels, J.W. Kolis, *J. Cryst. Growth* 246 (2002) 271.
- [Rag04] S. Raghavan and J.M. Redwing, *J. Cryst. Growth* 261 (2004) 294.
- [Ran00] M.R. Ranade, F. Tessier, A. Navrotsky, V.J. Leppert, S.H. Risbud, F.J. DiSalvo, C.M. Balkas, *J. Phys. Chem. B* 104 (2000) 4060.
- [Ran01] M.R. Ranade, F. Tessier, A. Navrotska, R. Marchand, *J. Mater. Res* 16 (2001) 2824.
- [Ree02] M. Reed, diss., University of Florida 2002.
- [Rei03] A. Reiher, J. Bläsing, A. Dadgar, A. Diez and A. Krost, *J. Cryst. Growth* 248 (2003) 563.
- [Rei87] R.C. Reid, J.M. Prausnitz, B.E. Poling, *The Properties of Gases and Liquids*, McGraw Hill, New York (1987).
- [Ren58] T. Renner, *Z. Anorg. Allg. Chem.* 298, 28 (1958).
- [Rie96] W. Rieger, T. Metzger, H. Angerer, R. Dimitrov, O. Ambacher, and M. Stutzmann, *Appl. Phys. Lett.* 68, 970 (1996).
- [Rob36] C. Robert, *Helv. Phys. Acta*, 9 (1936) 418.
- [Rod95] D.L. Rode, D.K. Gaskill, *Appl. Phys. Lett.* 66 (1995) 1972.
- [Saf97] S.A. Safvi, J.M. Redwing, M.A. Tischler, T.F. Kuech, *J. Electrochem. Soc.* 144, 5 (1997) 1789.
- [Sam69] G.V. Samsonov, *Nitridy Kiev*, 1969.
- [San99] S.I. Sandler, *Chemical and Engineering Thermodynamics*, 3rd ed, John Wiley & Sons, Inc. (1999).
- [Sar05] K. Sardar, F.L. Deepak, A. Govindaraj, M.M. Seikh, and C.N.R. Rao, *small* 1 (2005) 91.
- [Sat94] Y. Sato and S. Sato, *J. Cryst. Growth* 144, 15 (1994).
- [Sat95] Y. Sato, S. Sato, *J. Cryst. Growth* 146 (1995) 262.
- [Sat97] M. Sato, *Jpn. J. Appl. Phys., Part 2* 36, L658 (1997).

- [Sav78] V.A. Savastenko and A.U. Sheleg, *Phys. Status Solidi a*, 48, K135 (1978).
- [Say05] I. Sayago, E. Terrado, E. Lafuente, M.C. Horillo, W.K. Maser, A.M. Benito, R. Navarro, E.P. Urriolabeita, M.T. Martinez and J. Gutierrez, *Synth. Metals* 148, 15 (2005).
- [Sch00] W.J. Schaff, H.Lu, J. Hwang, and H. Wu, *Proceedings of the Seventeenth Biennial IEEE/Cornell Conference on Advanced Concepts in High Performance Devices*, August 7–9, 2000, p. 225.
- [Sch04a] B. Schwenzer, L. Loeffler, R. Seshadri, S. Keller, F.F. Lange, S.P. DenBaars and U.K. Mishra, *J. Mater. Chem.* 14 (2004), 637.
- [Sch04b] F. Schulze, A. Dadgar, J. Blaosing, A. Krost, *J. Crystal Growth* 272 (2004) 496.
- [Sch06] F. Schulze, A. Dadgar, J. Bläsing, T. Hempel, A. Diez, J. Christen and A. Krost, *J. Cryst. Growth* 289 (2006) 485.
- [Sec02] R.A. Secco, *J. Phys. Chem. Solids* 63 (2002) 425.
- [Sed06] D. Sedmidubsky and J. Leitner, *J. Cryst. Growth* 286 (2006) 66.
- [Seg04] A.S. Segal, A.V. Kondratyev, S.Yu. Karpov, D. Martin, V. Wagner, M. Ilegems, *J. Cryst. Growth* 270 (2004) 384.
- [She02] J. Shen, S. Johnston, S. Shang and T. Anderson, *J. Cryst. Growth* 240 (2002) 6.
- [She06] J. Shen, Research Institute for Non-ferrous Metals, Beijing, China, personal communications (2006).
- [Shi05] C.F. Shih, N.C. Chen, P.H. Chang and K.S. Liu, *J. Cryst. Growth* 281 (2005) 328.
- [Sin04] P. Singh, P. Ruterana, M. Morales, F. Goubilleau, M. Wojdak, J.F. Carlin, M. Ilegems and D. Chateigner, *Superlatt. Microstructures* 36 (2004) 537.
- [Smi68] W.R. Smith, R.W. Missen, *Canad. J. of Chem. Eng.* 46 (1968) 269.
- [Smo01] I.P. Smorchkova, L. Chen, T. Mates, L. Shen, S. Heikman, B. Moran, S. Keller, S.P. DenBaars, J.S. Speck and U.K. Mishra, *J. Appl. Phys.* 90 (2001) 5196.
- [Spe06] P. Specht, J.C. Ho, X. Xu, R. Armitage, E.R. Weber, E. Erni, C. Kisielowski, *J. Cryst. Growth* 288 (2006) 225.
- [Sta02] E. Starikov, P. Shiktorov, V. Gruzinskis, L. Reggiani, L. Varani, J.C. Vaissiere, Jian H. Zhao, *Physica B* 314 (2002) 171.
- [Sto06] T. Stoica, R. Meijers, R. Calarco, T. Richter, and H. Luth, *J. Cryst. Growth* 290 (2006) 241.

- [Sto09] G. Stoney, Proc. R. Soc. London, Ser. A 82, 172 (1909).
- [Str99] G.B. Stringfellow, Organometallic Vapor Phase Epitaxy, Academic Press (San Diego, CA) 2nd Ed. (1999) 192.
- [SUB94] Thermo-Calc version K database. Stockholm Technology Park Björnnäsvägen 21 SE-113 47 Stockholm, Sweden.
- [Sug03] K. Sugita, H. Takatsuka, A. Hashimoto, and A. Yamamoto, Phys. Status Solidib 240, 421 (2003).
- [Sul88] B.T. Sullivan, R.R. Parsons, K.L. Westra, M.J. Brett, J. Appl. Phys 64 (1988) 144.
- [Sun85] B. Sundman, B. Jansson, J.O. Andersson, Calphad 9 (1985) 153.
- [Sun96] H. Sunakawa, A. Yamaguchi, A. Kimura, and A. Usui, Jpn. J. Appl. Phys., Part 2 35, L1395 (1996).
- [Suz96] T. Suzuki, T. Ohmura, Phil. Mag. A 74 (1996) 1073.
- [Tab96] A. Tabata, R. Enderlein, J. R. Leite, S.W. da Silva, J.C. Galzerani, D. Schikora, M. Kloidt and K. Lischka, J. Appl. Phys. 79, 4137 (1996).
- [Tak04] N. Takahashi, A. Niwa, T. Nakamura, J. Phys. Chem. Solids 65 (2004) 1259.
- [Tak96] Y. Takagi, M. Ahart, T. Azuhata, T. Sota, K. Suzuki, S. Nakamura, Physica B 219-220 (1996) 547.
- [Tak97a] N. Takahashi, J. Ogasawara, and A. Koukitu, J. Cryst. Growth 172, 298 (1997).
- [Tak97b] N. Takahashi, R. Matsumoto, A. Koukitu, and H. Seki, Jpn. J. Appl. Phys., Part 2 36, L743 (1997).
- [Tan04] T. Tang, S. Han, W. Jin, X. Liu, C. Li, D. Zhang, C. Zhou, B. Chen, J. Han, and M. Meyyapan, J. Mat. Res. 19 423 (2004).
- [Tan05] T. Tanaka, K. Takano, H. Fujikura, T. Mishima, Y. Kohji, H. Kamogawa, T. Meguro and Y. Otoki, The International Conference on Compound Semiconductor Manufacturing Technology 4.1 (2005).
- [Tan86] T.L. Tansley, C.P. Foley, J. Appl. Phys. 59 (1986) 3241.
- [Tho96] A. Thon and T.F. Kuech, Appl. Phys. Lett. 69 (1996) 55.
- [Tou77] Y.S. Touloukian, R.K. Kriby, R.E. Taylor, and P.D. Desai, Thermophysical Properties of Matter, 12 (1977) 298.
- [Tra74] J.W. Trainor and K. Rose, J. Electron. Mater. 3, 821 (1974).

- [Tsu05] A. Tsuyuguchi, K. Teraki, T. Koizumi, J. Wada, T. Araki, Y. Nanishi, H. Naoi, Institute of Physics Conference Series (2005), 184 (Compound Semiconductors 2004), 239-242.
- [Tya77] V.A. Tyagai, A.M. Evstigneev, A.N. Krasiko, A.F. Andreeva, V.Ya. Malakhov, Sov. Phys. Semicond. 11 (1977) 1257.
- [Unl03] J. Unland, B. Onderka, A. Davydov, R. Schmid-Fetzer, J. Cryst. Growth 256 (2003) 33.
- [Usu97] A. Usui, H. Sunakawa, A. Sakai, and A. Yamaguchi, Jpn. J. Appl. Phys. 36 (1997) L899.
- [Vad05] S. Vaddiraju, A. Mohite, A. Chin, M. Meyyappan, G. Sumanasekera, B. W. A, and M.K. Sunkara, Nano lett. 2005 Vol. 5, No. 8 1625.
- [Ven05] S. Venkataraj, H. Kittur, R. Drese and M. Wuttig, Thin Solid Films 514 (2006) 1. .
- [Ven99] P. Vennegues and B. Beaumont, Appl. Phys. Lett. 75, 4115 (1999).
- [Vor71] A.M. Vorobev, G.V. Evseeva, L.V. Zenkevich, Zh. Fiz. Khim. 45 (1971) 2650.
- [Vor73] A.M. Vorobev, G.V. Evseeva, L.V. Zenkevich, Zh. Fiz. Khim. 47 (1973) 2885.
- [Wak89] A. Wakahara and A. Yoshida, Appl. Phys. Lett. 54, 709 (1989).
- [Wak90] A. Wakahara, T. Tsuchiya, and A. Yoshida, J. Cryst. Growth 99, 385 (1990).
- [Wal04] W. Walukiewicz, S.X. Li, J. Wu, K.M. Yu, J.W. Ager III, E.E. Haller, H. Liu, W.J. Schaff, J. Cryst. Growth 269 (2004) 119.
- [Wal99] P. Waltereit, O. Brandt, A. Trampert, M. Ramsteiner, M. Reiche, M. Qi, and K. H. Ploog, Appl. Phys. Lett. 74 (1999) 3660.
- [Wan03] J.Y. Wang, S. Hofmann, A. Zalar, E.J. Mittemeijer, Thin Solid Films 444 (2003) 120.
- [Wan04] Q. Wan, Q.H. Li, Y.J. Chen, T.H. Wang, X.L. He, J.P.Li and C.L. Lin, Appl. Phys. Lett. 84 3654(2004).
- [Wan05] C.-L. Wang, J.-R. Gong, W.-T. Liao, C.-K. Lin and T.-Y. Lin, Thin Solid Films 493 (2005) 135.
- [Wan06] X. Wang, S.-B. Che, Y. Ishitani, A. Yoshikawa, Journal of Applied Physics (2006) 99(7), 073512/1.
- [Wee03] T.W. Weeks, Jr., E.L. Piner, T. Gehrke, K.J. Linthicum, United States Patent 6,617,060 September 9, 2003.

- [Wes88] K.L. Westra, R.P.W. Lawson, M.J. Brett, *J. Vac. Sci. Technol. A* 6 (1988) 1730.
- [Wet94] C. Wetzel, D. Volm, B.K. Meyer, K. Pressel, S. Nilsson, E.N. Mokhov, P.G. Baranov, *Appl. Phys. Lett.* 65 (1994)1033.
- [Wit05] H. Witte, A. Krtschil, E. Schrenk, K. Fluegge, A. Dadgar, and A. Krost, *J. Appl. Phys.* 97, 043710 (2005).
- [Wit98] R. L. Withers, J. S. O. Evans, J. Hanson and A. W. Sleight, *J. Solid State Chem.*, 1998, 137, 161-167.
- [Wu02a] J. Wu, W. Walukiewicz, K.M. Yu, J.W. Ager III, E.E. Haller, H. Lu, W.J. Schaff, Y. Saito, Y. Nanishi, *Appl. Phys. Lett.*, 80 (2002) 3967.
- [Wu02b] J. Wu, W. Walukiewicz, W. Shan, K.M. Yu, J.W. Ager III, E.E. Haller, Hai Lu, W.J. Schaff, *Phys. Rev. B* 66 (2002) 201403.
- [Wu06] C.-L. Wu, C.-H. Shen, H.-Y. Chen, S.-J. Tsai, H.-W. Lin, H.-M. Lee, S. Gwo, T.-F. Chuang, H.-S. Chang, T. M. Hsu, *Journal of Crystal Growth* 288 (2006) 247. .
- [Xu03] K. Xu and A. Yoshikawa, *Appl. Phys. Lett.* 83, (2003)14.
- [Yam00] S. Yamaguchi, M. Kariya, S. Nitta, H. Amano and I. Akasaki, *Applied Surface Science*, 159-160 (2000) 414.
- [Yam01a] A. Yamamoto, Y. Murakami, K. Koide, M. Adachi, and A. Hashimoto, *Phys. Status SolidiB* 228, 5 (2001).
- [Yam01b] A. Yamamoto, M. Adachi, A. Hashimoto, *J. Cryst. Growth* 230 (2001) 351.
- [Yam02] A. Yamamoto T. Tanaka, K. Koide, and A. Hashimoto, *phys. stat. sol. (a)* 194, 510 (2002).
- [Yam04] A. Yamamoto K. Sugita, H.Takatsuka, A. Hashimoto, V. Yu. Davydov, *J. Cryst. Growth* 261, 275 (2004).
- [Yam05] A. Yamamoto, T. Kobayashi, T. Yamauchi, M. Sasase, A. Hashimoto, and Y. Ito, *Phys. Status Solidi(c)* 2, 2281(2005).
- [Yam06] A. Yamamoto, H. Miwa, Y. Shibata, and A. Hashimoto, *phys. stat. sol. (c)* 3, No. 6, 1527–1530 (2006).
- [Yam94a] A. Yamamoto, M. Tsujino, M. Ohkubo and A. Hashimoto, *J. Cryst. Growth* 137 (1994) 415.
- [Yam94b] A. Yamamoto, M. Tsujino, M. Ohkubo, A. Hashimoto, *Sol. Energy Mater. Sol. Cells* 35 (1994) 53.

- [Yam97] A. Yamamoto, Y. Yamauchi, M. Ohkubo, A. Hashimoto and T. Saitoh, *Solid-State Electronics* 41 (1997) 149.
- [Yam98] A. Yamamoto, T. Shin-ya, T. Sugiura, A. Hashimoto, *J. Cryst. Growth* 189/190 (1998) 461.
- [Yam99] S. Yamaguchi, M. Kariya, S. Nitta, T. Takeuchi, C. Wetzel, H. Amano, I. Akasaki, *J. Appl. Phys.* 85 (1999) 7682.
- [Yan02a] F.-H. Yang, J.-S. Hwang, K.-H. Chen, Y.-J. Yang, T.-H. Lee, L.-G. Hwa, and L.-C. Chen, *Thin Solid Films* 405 (2002) 194.
- [Yan02b] W. Yang, P. Wang, F. Li and K.W. Cheah, *Nanotechnology* 13 (2002) 65.
- [Yin04] L. Yin, Y. Bando, D. Golberg, M. Li, *Adv. Mater.* 16 (2004) 1833.
- [Yon02] I. Yonenaga, *MRS Internet J. Nitride Semicond. Res.* 7, 6(2002).
- [Yoo97] S.F. Yoon, X.B. Li, and M.Y. Kong, *J. Cryst. Growth* 180, 27 (1997).
- [Yos03] M. Yoshimoto, H. Yamamoto, W. Huang, H. Harima, J. Saraie, A. Chayahara, Y. Horino, *Appl. Phys. Lett.* 83 (2003) 3480.
- [Yos83] S. Yoshida, S. Misawa, and S. Gonda, *Appl. Phys. Lett.* 42, 427 (1983).
- [You00] W.T. Young, S.R.P. Silva, J.V. Anguita, J.M. Shannon, K.P. Homewood and B.J. Sealy, *Diamond and Related Materials*, 9 (2000) 456.
- [Yu05] H.Q. Yu, L. Chen, R. Zhang, X. Xiu, Z.L. Xie, Y.D. Ye, S.L. Gu, B. Shen, Y. Shi, Y.D. Zheng, *Materials Science Forum* 475-479 (2005) 3783.
- [Yu06] J.W. Yu, H.C. Lin, Z.C. Feng, L.S. Wang, S. Tripathy and S.J. Chua, *Thin Solid Films* 498 (2006) 108.
- [Yum81] M. Yumura, T. Asaba, *Symp. Int. Combust. Proc.* 18 (1981) 863.
- [Zam01] S. Zamir, B. Meyler, and J. Salzman, *Appl. Phys. Lett.* 78 (2001) 288.
- [Zam02] S. Zamir, B. Meyler, J. Salzman, *J. Cryst. Growth* 243 (2002) 375.
- [Zao81] A. Zaouk, E. Salvetat, J. Sakaya, F. Maury, G. Constant, *J. Crystal Growth* 55 (1981) 135.
- [Zha02] J. Zhang, L. Zhang, X. Peng and X. Wang, *J. Mater. Chem* (2002) 12, 802.
- [Zha05] J.X. Zhang, Y. Qu, Y.Z. Chen, A. Uddin and Shu Yuan, *J. Cryst. Growth* 282 (2005) 137.

BIOGRAPHICAL SKETCH

Hyun Jong Park was born on October 25, 1973, in Seoul, Korea. He is the son of Jong Soo Park and Sun Kyoung Kim, and has an elder sister, Soo Kyung Park. He graduated from Yongsan High school in 1992 where he had an opportunity to perform various chemistry experiments as a member of the Yongsan Chemistry Club. His dream of becoming a scientist started then. Following high school, he attended Hanyang University, graduating with a Bachelor of Science degree in chemical engineering in February 1999. Between 1994 and 1997, he served as an artillery vehicle driver while performing military duty in Korea. In 1998, he attended the English Language Institute at the University of Florida in Gainesville where he met his lovely wife, Catherine. After graduating from Hanyang University, he attended the Japanese Language Institute of Asuka Gakuin in Yokohama, Japan, in 1999.

He returned to Gainesville and began a graduate program at the University of Florida, pursuing his doctoral degree in chemical engineering in 2000. He married Catherine Jaewon Park in 2002, and had two sons, David Sangjin and Justin Sanghyun Park, in 2003 and 2005. While doing research in Dr. Anderson's group, his interests were the growth of gallium nitride and indium nitride films and nanostructured materials by Hydride-Metalorganic Vapor Phase Epitaxy.